Characterization of the elastic properties of rocks at different scales : link between seismic, sonic and ultrasonic wave velocities

Ariel Gallagher

PSL UNIVERSITÉ PARIS

THÈSE DE DOCTORAT
DE L'UNIVERSITÉ PSL

Préparée à l'École Normale Supérieure de Paris

Caractérisation des propriétés élastiques des roches à différentes échelles. Lien entre les vitesses des ondes sismiques, soniques et ultrasoniques.

Soutenue par

Ariel GALLAGHER

Le 20 Juin 2022

Ecole doctorale n° 560

Sciences de la Terre et de l'Environnement et Physique de l'Univers, Paris (STEP'UP)

Spécialité

Sciences de la Terre et de l'Environnement

Composition du jury :

Alexandre, SCHUBNEL Dr, École Normale Supérieure de Paris	*Président du jury*
Daniel, BRITO Pr, Université de Pau et des Pays de l'Adour	*Rapporteur*
YVES, LEROY Pr, Imperial College London	*Rapporteur*
Beatriz, QUINTAL Dr, Université de Lausanne	*Examinateur*
Jérôme, FORTIN Dr, École Normale Supérieure de Paris	*Directeur de thèse*
Jan, BORGOMANO Dr, Modis	*Invité*

ENS | PSL

STEP'UP ÉCOLE DOCTORALE

cnrs

TotalEnergies

“An experiment is a question which science poses to Nature, and a measurement is the recording of Nature’s answer.”

-Max Planck, Scientific Autobiography and Other Papers

ACKNOWLEDGEMENTS

First and foremost, I need to thank my supervisor, Jérôme Fortin. He was always very patient, efficient and insightful guide for the moments where moving forward seemed all but possible. His optimism and intelligence were a great source of inspiration.

When I first arrived in Paris, Jan Borgomano introduced me to the experimental setup which would become the focal point of all my research. His knowledge in experimental rock physics and frequency effect helped me hit the ground running and I'm forever grateful for him for showing patience while teaching the ins and outs of this setup. I also want to thank Sam Chapman. His door was always open to talk and I am very grateful for his expertise.

I very much appreciate and would like to thank Daniel Brito and Yves LeRoy for having accepted to be reporters for my thesis, as well as, Alexandre Schubnel and Beatriz Quintal for having accepted to be examiners for my thesis.

I feel a great privilege being able to complete my doctoral studies at the Geophysics laboratory in ENS Paris. The community which is fostered here is a constant source of encouragement, knowledge and inspiration and made me feel very fortunate to have ended up here.

A big thank you to friends and family who through conversation, food and collective experiences have shaped me into the person I am today. Finally, thank you to my wife Annika.

RÉSUMÉ

Quelle est la principale différence entre l'étude d'un échantillon de roche en laboratoire, à l'échelle centimétrique, et l'étude d'un affleurement rocheux sur le terrain, à l'échelle kilométrique ? Un affleurement rocheux peut inclure des hétérogénéités qui ne seront pas présentes dans un échantillon de roche, comme des fractures, des paramètres hétérogènes variables ou même des couches rocheuses complètement différentes, pour ne mentionner que quelques exemples. Dans quelle mesure les propriétés déterminées à l'échelle centimétrique peuvent-elles être utilisées pour trouver des propriétés à l'échelle du terrain ? Pour aider à répondre à cette question, plusieurs tests de laboratoire sont développés et réalisés pour mieux caractériser les fractures et les hétérogénéités mésoscopiques, ce qui permettra d'appliquer les données extrapolées du laboratoire aux paramètres à l'échelle du terrain.

ABSTRACT

What is the main difference between studying a rock sample in the lab, at the centimeter scale, and studying a rock outcrop in the field, at the kilometer scale? A rock outcrop can include heterogeneities that will not be present in a rock sample, such as fractures, varying heterogeneous parameters or even completely different rock layers, to name a few. How than can properties determined at the centimeter scale be used to find properties at the field scale? To help answer this question, multiple laboratory tests are developed and performed to better characterize fractures and mesoscopic heterogeneities, which will allow data extrapolated from the laboratory to be applied to field scale parameters.

CONTENTS

LIST OF FIGURES

LIST OF TABLES

Introduction Générale

"Comment extrapoler les propriétés des roches mesurées en laboratoire, qui sont déterminées sur des échantillons de taille centimétrique, à des problèmes de terrain mesurés au kilomètres ? ” il s’agit d’une citation du livre d'Yves Guéguen et Victor Palciauskas intitulé "Introduction à la physique des roches" publié il y a 20 ans. C'est une question toujours d’actualité. En science, toute solution théorique doit être testée expérimentalement pour être validée. Par conséquent, il est essentiel de comprendre les différents mécanismes qui peuvent survenir lors d’un changement d’échelle. Dans cette thèse, j’étudie la vitesse des ondes élastiques en condition *in situ*. En particulier je me focalise sur la manière dont différentes hétérogénéités peuvent modifier la façon dont les ondes élastiques se propagent à travers un milieu poreux saturé.

Trois séries d'essais en laboratoire ont été réalisées à l'aide d'une cellule triaxiale qui permet de reproduire les conditions *in situ*. On utilise des méthodes d'oscillations forcées et des propagations d’onde ultrasoniques pour extraire les propriétés élastiques à différentes fréquences.

La première série de tests a été effectué sur trois échantillons de carbonate. L'un de ces échantillons est homogène et sert d’échantillon de comparaison. Les deux autres échantillons sont hétérogènes. En étudiant les propriétés élastiques dans la gamme de fréquence apparente (10^{-2} à 10^{5}–10^{6}), deux pics d'atténuation ont été observés. Un pic a été observé dans les trois échantillons et s'est produit à une fréquence d'environ 40 kHz. Ce mécanisme d'atténuation est lié à l’écoulement de fluide dans les pores, qui se produit au niveau microscopique ; il est principalement contrôlé par le facteur de forme des fissures préexistantes présentes dans les trois échantillons. Le deuxième pic d'atténuation a été observé dans les échantillons hétérogènes, autour de 100 Hz. Ce mécanisme d'atténuation est lié à l’écoulement mésoscopique de fluide entre des régions de porosité variable. En utilisant la diffusivité hydraulique de l'échantillon et la fréquence de coupure observée, la longueur de diffusion a été calculée, qui est en accord avec les observations de tomographies de

densité des échantillons. Un modèle numérique 3D a également été développé et a confirmé les résultats expérimentaux.

Ensuite, des essais d'oscillation hydrostatique à basse fréquence ont été réalisés sur des échantillons de carbonate de Rustrel intacts et fracturés, à trois pressions effectives dans des conditions sèches et saturées en eau. Le module d'incompressibilité et l'atténuation ont été mesurée en fonction de la fréquence. Dans le cas sec, il n'y a ni dispersion ni atténuation, ainsi que dans la roche intacte et saturée. Lorsque l'échantillon est fracturé, on observe une dispersion. Par ailleurs le déphasage entre contrainte et déformation est négatif. Cette dispersion s'atténue avec la pression de confinement. Un modèle analytique 1D et un modèle numérique 3D ont été développés, qui expliquent les observations expérimentales, soulignant les paramètres critiques (raideur de la fracture et géométrie de la fracture) contrôlant la dispersion, le mécanisme sous-jacent étant de la diffusion de la pression du fluide de la fracture vers l'espace poreux.

Enfin, deux fractures perpendiculaires ont été créées dans un échantillon de calcaire de Solnhofen. L'échantillon fracturé a été testé, dans une gamme de fréquences de 0,2 à 40 Hz, dans des conditions non drainées et saturées en glycérine, à plusieurs pressions effectives. Le module de Young normalisé et l'atténuation ont été extraits, ce qui a mis en évidence un pic d'atténuation à la fréquence de 2 Hz, ayant une amplitude maximale de 0,07 à la pression effective la plus faible de 5 MPa. Un modèle numérique 3D a été développé et utilisé, confirmant les données expérimentales. Le mécanisme sous-jacent pour cette dispersion étant de la diffusion de pression de fluide de fracture à fracture.

General Introduction

"How do we extrapolate laboratory – measured rock properties which are determined on centimeter-sized samples, to field-scale problems measured in kilometers?" is a quote from Yves Guéguen and Victor Palciauskas book the "Introduction to the physics of rocks" published 20 years ago. It is an

interesting question, as usually in science any theoretical solution should be tested experimentally to be validated. This can be quite challenging when there are no labs that can test to scale phenomenon which are studied in the field in geosciences. Therefore, it becomes crucial to understand the different mechanics which can arise when upscaling. Here I will focus on the elastic wave properties under in situ condition, and in particular I focus on how different heterogeneities (mesoscopic and fractures) can alter the way elastic waves propagate through a saturated porous media - rock.

Three sets of laboratory tests were conducted using a triaxial cell which allows for dry, water, brine and glycerin saturated sample conditions, under pressure while forced oscillation and ultrasonic transmission methods were used to extract elastic properties from the samples being tested.

The first barrage of tests was performed on three carbonate samples. One of these samples is homogeneous and is used as a comparison. The other two samples were heterogeneous. When studying the elastic properties within the apparent frequency range (10^{-2} to 10^{5} and 10^{6} Hz), two distinct attenuation peaks were observed in the heterogeneous samples and only one was observed in the homogeneous sample. The peak observed in all three samples occurred at a frequency around 40 kHz. This attenuation mechanism was related to squirt flow, which occurs at the microscopic level and is related to the aspect ratio of the pre-existing cracks present in all three samples. The second attenuation peak was observed around 100 Hz. This attenuation mechanism was related to mesoscopic flow between regions of varying porosity. Using the hydraulic diffusivity of the sample and cut-off frequency observed, the length of diffusion was calculated which was in good agreement with what was seen in the CT scans. A 3D numerical model was also developed and corroborated the experimental results.

Next, low frequency (0.04 to 1 Hz frequency range) hydrostatic oscillation tests were performed on intact and fractured carbonate Rustrel samples, at three effective pressures in dry and water saturated conditions. The apparent bulk modulus and attenuation were extracted along the whole frequency range showing no dispersion in the dry case or in the intact case. However, there was negative phase shift between stress and strain in the fractured case in water saturated conditions at lower effective pressures which disappeared at the highest effective pressure. A 1D analytical model and 3D numerical model were developed, which explained the behavior, underlining the critical parameters (fracture compliance and fracture geometry) relevant to the local negative phase shift associated to fracture to pore space fluid pressure diffusion (FPD).

Finally, two perpendicular saw cut fractures were made in a Solnhofen limestone sample, then the saw cut sample was tested, within a frequency range of 0.2 to 40 Hz, in undrained glycerin saturated

conditions using the axial oscillation test performed at multiple effective pressures. The normalized Young's modulus and attenuation were extracted, which highlighted an attenuation peak at 2 Hz frequency, having a maximum amplitude of 0.07 at the lowest effective pressure of 5 MPa, interpreted as a fracture to fracture fluid pressure diffusion. A 3D numerical model was developed and used which corroborated the experimental data.

1. Introduction

In this chapter, a quick overview of the basics of elastic and porelasticity theory is explained, which is essential for the interpretation of laboratory measurements as well as for seismic inversion. Following this, the concepts of dispersion and attenuation of velocity are described as well as the multiple mechanisms behind the attenuation/dispersion which can be present in rocks at different scales.

1.1 Rocks

Rocks have unique properties depending on the mineral composition and grain size as well as its physical structure. Granite and rhyolite have the same mineral composition, however due to the different cooling rates in which they were created, they will have varying grain size and therefore unique properties. It is also interesting to note that samples with matching mineral composition and grain size can vary in properties as well due to their porous structure. This is seen, for example, in the change in p- and s-wave velocities between Fontainebleau sandstone samples with identical porosities (Gomez et al., 2010).

1.1.1 Carbonate rocks

All experiments described in this paper were performed on carbonate rocks. Carbonate rocks are composed mainly of minerals which come from organic or inorganic sources. These rocks are heterogeneous in nature mostly due to the numerous processes that create them: Carbonates are a product of i) sedimentation depending on physical-chemical-biological processes, depositional environment, paleogeography, climate, etc. and ii) diagenesis inducing numerous post-depositional microstructural changes (mineralogical changes, cementation, dissolution, recrystallization, etc.) during burial due to fluid migrations, fluid-rock interaction and temperature evolution (Bohacs et al., 2000; Riding, 2000; Freytet and Verrecchia, 2002; Alonso-Zarza and Tanner, 2009; Pace et al., 2016).

All these geological processes control the microstructure of carbonates and their resulting physical properties (Anselmetti,1994; Anselmetti and Eberli, 1993, 1999, 2001; Eberli et al., 2003; Bailly et al., 2019a, 2022).

1.2 Scale

The definition of scale is an important concept in rock mechanics. For example, at the smaller scales, the bulk modulus (measure of stiffness) of a calcite mineral is calculated to be around 77 GPa, however some of the dry samples measured in this thesis have a calcite content hovering around ~98% calcite and usually have bulk moduli around 25 GPa. The reduction of stiffness when going up to a sample scale is expected, as the sample is made up of not only calcite, but also pores filled by fluid.

1.2.1 Representative elementary volume

The representative elementary volume (REV) is defined as the volume which is needed to always measure the same physical properties (Bear, 1972). As rocks are composed of solid rock matrix and pore space which can be filled with fluid, gas or a mixture of these, it is important to include an unbiased representation of each of these components. Figure 1.1 shows a representation of this phenomenon. If the scale one uses is too small, it is possible that either there are too few pores (A) and the stiffness of the sample will be overestimated, or there are too many pores (B) and the stiffness of the sample will be underestimated. Once a large enough volume is used to always measure the same property value during a test, the beginning of the REV is reached (C). In theory, if the rock sample were forever homogeneous as the volume increases, the REV domain would continue in perpetuity (D). In reality, heterogeneities will appear at different scale, at which point the physical properties would change. An example of heterogeneity is fractures (E).

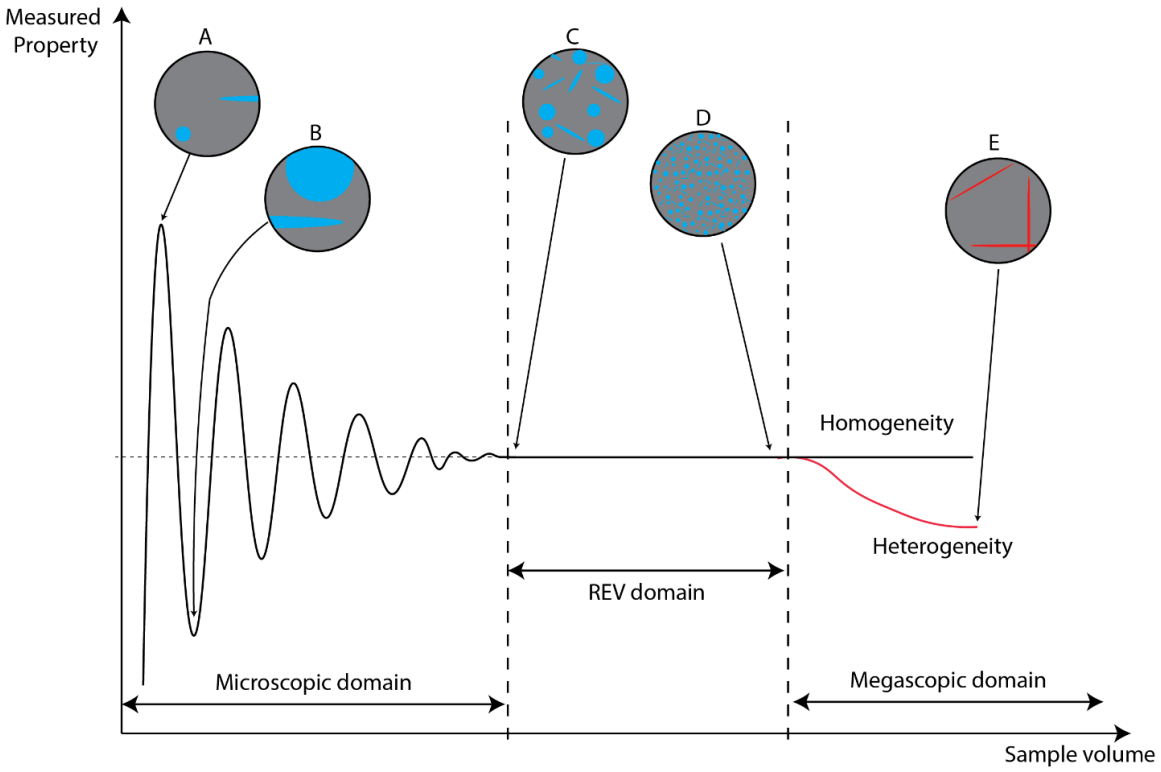

Figure 1.1: Volume versus measured property description of the REV domain (modified after Bear, 1972). In the microscopic scale (A, B), the volume is too small to adequately represent all the pore space. Within the REV the measured properties are constant (C, D). In the megascopic domain, other heterogeneous features appear which change the measured properties (E).

1.2.2 Concept of different scales

Different scales have been defined by Haldorsen and Lake (1984) which i) include microscopic (pore scale - μm to mm), ii) macroscopic (plug scale – cm), iii) megascopic (m to dm) and iv) gigascopic (km) scales. Bailly et al. (2019b) studied the different effects that upscaling has on the elastic properties of lacustrine carbonate found in Samos. This was done by comparing p-wave velocity data compiled at the different scales and frequencies on 5 cm samples with 500 kHz frequency, 20 and 40 cm outcrops with a frequency of 250 kHz and 54 kHz, respectively, and ~15 m outcrops at a frequency of 100 Hz. The results showed that as the scale was increased, the p-wave velocity decreased. Although the experiments were limited to dry samples, it still shows that using solely ultrasonic measurements in the lab may be insufficient to determine subsurface reservoir properties because of the presence of heterogeneities.

1.3 Elastic behavior

Different types of responses are presented in figure 1.2 which shows three examples of stress strain behaviors, when loading and unloading a rock. The first (A) is a linear elastic loading and unloading path and can be defined as perfectly elastic. The second (B) shows non-linear elastic loading and unloading path, which is typical of viscoelastic materials. Finally, a non-elastic behavior (C) is shown, where there is irreversible strain during the loading/unloading cycles.

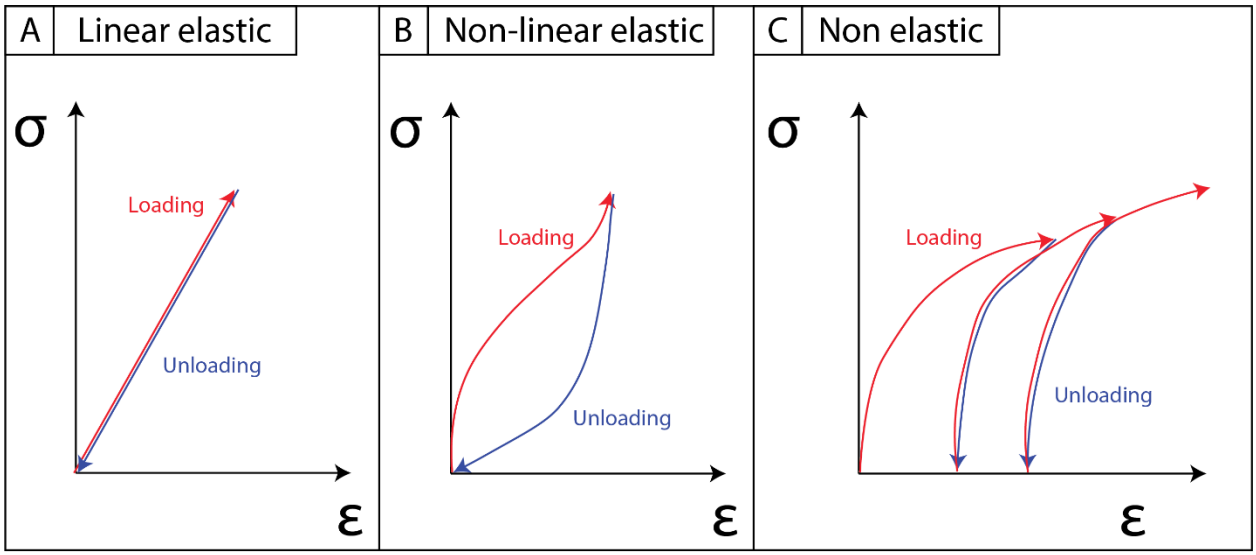

Figure 1.2: Stress strain paths during the loading and unloading of linear, non-linear and non-elastic samples;

In the linear elastic case, the mechanical behavior can be well described using the theory of elasticity, or Hooke's law:

$$\sigma = M.\varepsilon \qquad \ldots (1.1)$$

where M is a fourth rank tensor of the elastic moduli, σ is the stress tensor and ε is the strain tensor. If we assume isotropy, the fourth rank tensor of the elastic moduli can be described with two independent elastic moduli. Equation 1.1 can be reduced to:

$$\varepsilon_{ij} = \frac{1+\nu}{E}\sigma_{ij} - \frac{\nu}{E}\sigma_{ij}\delta_{ij}, \qquad \ldots (1.2)$$

where E and ν are the Young's modulus and Poisson's ratio, respectively, and δ_{ij} is the Kronecker's symbol, where $\delta_{ij} = 0$ if $i \neq j$ and $\delta_{ij} = 1$ if $i = j$. If an isotropic sample is loaded uniaxially (σ_{zz}), the Young's modulus and Poisson's ratio can be determined, as follows:

$$E = \frac{\sigma_{zz}}{\varepsilon_{zz}} \text{ and} \quad \ldots (1.3)$$

$$\nu = -\frac{\varepsilon_{xx}}{\varepsilon_{zz}} = -\frac{\varepsilon_{yy}}{\varepsilon_{zz}} . \quad \ldots (1.4)$$

The bulk (K) and shear (G) modulus can also be used to fully define the elastic constants of an isotropic sample. The bulk modulus is described using a hydrostatic compression such that:

$$\varepsilon_{kk} = \frac{P}{K} , \quad \ldots (1.5)$$

where ε_{kk} is the volumetric strain ($\varepsilon_{xx} + \varepsilon_{yy} + \varepsilon_{zz}$) and P is the hydrostatic pressure defined as $P=-\frac{\sigma_{xx}+\sigma_{yy}+\sigma_{zz}}{3}$. The shear modulus is described using a shear deformation such that:

$$\varepsilon_{ij} = \frac{\sigma_{ij}}{2G} . \quad \ldots (1.6)$$

The bulk and shear are commonly used in geophysics, whereas the Young and Poisson ratio are more often use in rock mechanics. Therefore, it is important to compare the bulk and shear modulus to the Young's modulus and Poisson's ratio.

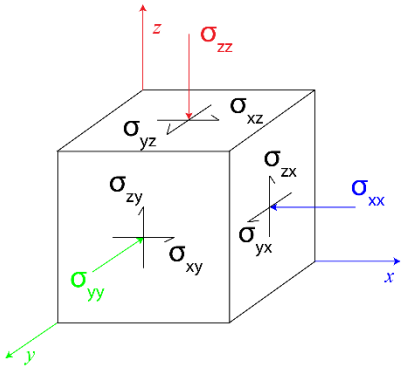

Figure 1.3: Infinitesimal isotropic cube with confining stresses applied;

If three uniaxial stresses, σ_{xx}, σ_{yy} and σ_{zz}, are applied to an infinitesimal isotropic cube, then:

$$\varepsilon_{xx} = \frac{\sigma_{xx}}{E} - \nu\frac{\sigma_{yy}}{E} - \nu\frac{\sigma_{zz}}{E} . \quad \ldots (1.7)$$

The strain in the y and z directions can be defined similarly. Knowing the strain in the three principal directions as well as the definition of the hydrostatic stress and strain:

$$E\varepsilon_{kk} = \sigma_{kk}(1 - 2\nu) . \quad \ldots (1.8)$$

The bulk modulus can now be compared to the Young's modulus and Poisson's ratio through equations 1.5 and 1.8:

$$K = \frac{E}{3(1-2\nu)}. \quad \ldots (1.9)$$

The shear modulus can be solved, in E and ν, by showing a 2D shear stress applied to a square and resolving it into its principal directions X' and Y'. Figure 1.4A shows a 2D stress field with a shear stress (σ) and no stress in the X or Y directions. Figure 1.4B shows the shear stress in A resolved into the X' and Y' directions. This produces a positive stress (σ) in the X' direction and a negative stress (σ) in the Y' direction.

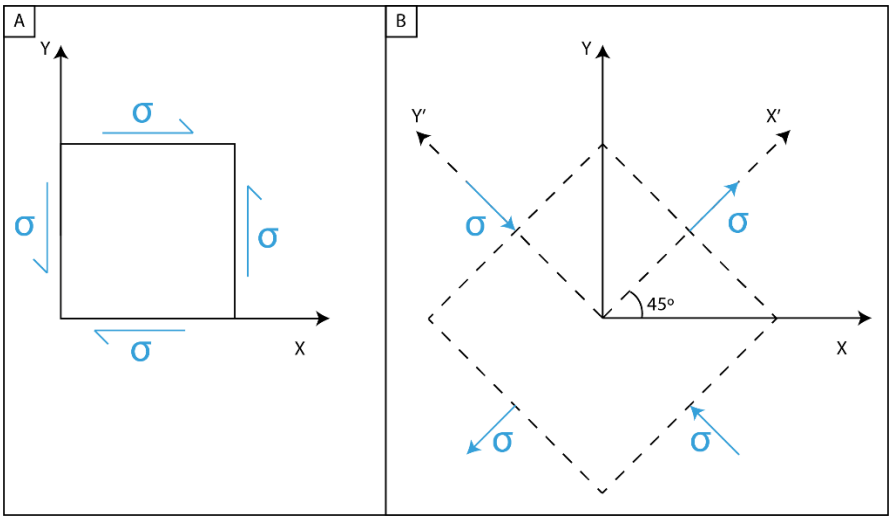

Figure 1.4: (A) 2D representation of shear stress field; (B) Same shear stress representation resolved into its principal directions;

Following the X' direction and using equation (1.7):

$$E\varepsilon_{x'x'} = \sigma_{x'x'} - \nu\sigma_{y'y'} \quad \ldots (1.10)$$

,with $\sigma_{x'x'} = \sigma$, $\sigma_{y'y'} = -\sigma$ and $\varepsilon_{x'x'} = \varepsilon$.

Then combining equation 1.6 and 1.10, the shear modulus can be defined as:

$$G = \frac{E}{2(1+\nu)}. \quad \ldots (1.11)$$

It is also important to relate the bulk and shear moduli to the compressional and shear wave velocities, or p- and s-wave velocities for short.

A p-wave can be defined as a wave traveling along z using a displacement vector, $u_z(z,t) = e^{i(kz-\omega t)}$, for a wave with phase velocity $V_p = \omega/k$. The p-wave, in the z direction, is defined to have a strain $\varepsilon_{zz} = \frac{\partial u_z}{\partial z}$, with all other strain ε_{ij} equal to 0. Knowing that all internal forces are in equilibrium and assuming zero external body forces, the dynamic equilibrium equation:

$$\frac{\partial \sigma_{zz}}{\partial z} = \rho \frac{\partial^2 u_z}{\partial t^2}, \quad \ldots (1.12)$$

can be solved with equation 1.7, where ρ is the density.

Knowing $\varepsilon_{xx} = \varepsilon_{yy} = 0$ and $\sigma_{xx} = \sigma_{yy}$ due to isotropy, equation 1.7 can be re-written:

$$\sigma_{xx} = \sigma_{yy} = \frac{\nu}{1-\nu}\sigma_{zz} \text{ and} \quad \ldots (1.13)$$

$$\sigma_{zz} = \frac{\varepsilon_{zz} E(1-\nu)}{(1+\nu)(1-2\nu)}. \quad \ldots (1.14)$$

Using equation 1.14, the dynamic equilibrium equation turns into:

$$\left[\frac{E(1-\nu)}{(1+\nu)(1-2\nu)}\right]\frac{\partial^2 u_z}{\partial z^2} = \frac{\partial^2 u_z}{\partial t^2}. \quad \ldots (1.15)$$

Now, the displacement vector can be used to solve the p-wave velocity:

$$V_p = \frac{\omega}{k} = \sqrt{\frac{E(1-\nu)}{(1+\nu)(1-2\nu)\rho}} = \sqrt{\frac{K+\frac{4}{3}G}{\rho}}. \quad \ldots (1.16)$$

An s-wave can be defined as a shear deformation traveling along z using a displacement vector, $u_y(z,t) = e^{i(kz-\omega t)}$, for a wave with phase velocity $V_s = \omega/k$. By definition $\varepsilon_{zy} = \frac{1}{2}\frac{\partial u_y}{\partial z}$ and $\sigma_{zy} = G\frac{\partial u_y}{\partial z}$. Similarly to the p-wave, the dynamic equilibrium equation can be solved $\frac{\partial \sigma_{zy}}{\partial z} = \rho \frac{\partial^2 u_y}{\partial t^2}$ such that $G\frac{\partial^2 u_y}{\partial z^2} = \frac{\partial^2 u_y}{\partial t^2}$, leading to:

$$V_s = \sqrt{\frac{G}{\rho}}. \quad \ldots (1.17)$$

This is a very powerful tool as the bulk and shear modulus of isotropic mediums can be calculated by measuring its p- and s-wave velocities. This can be used to quickly and easily measure bulk and shear modulus in the lab, or it can be used to estimate the elastic properties of rock in situ.

Next, the effects that different pore fluids have on the elastic properties of a rock will be discussed using the drained, undrained and unrelaxed rock conditions.

1.3.1 Drained conditions

Rocks are a porous medium, as they are composed of a solid mineral structure and pore space. The compressibility of a rock is therefore related to not only what minerals it is composed of but to its pore space. The dry compressibility (inverse of K_{dry}) of a rock can be written as (Mavko et al.,2009):

$$\frac{1}{K_{dry}} = \frac{1}{K_m} + \frac{\phi}{K_\phi}, \quad \ldots (1.18)$$

where K_m is the bulk modulus of the mineral matrix and ϕ is the porosity. The K_ϕ is the effective dry pore-space compressibility, which is defined as the ratio of the fractional change in pore volume V_p, to an increment of applied external hydrostatic stress, at constant pore pressure:

$$K_\phi = \frac{V_p}{\partial V_p / \partial P \big|_{p_f}}. \quad \ldots (1.19)$$

As rocks are fluid saturated, one needs to define the effective pressure as:

$$P^{eff} = P - \alpha p_f,$$

where P is the mean pressure applied at the boundary, p_f is the pore pressure and α is the Biot's coefficient (Biot, 1941; Rice and Cleary, 1976). The Biot coefficient is defined as:

$$\alpha = 1 - K_d / K_m \quad \ldots (1.20)$$

Where, K_d is the drained bulk modulus. In drained conditions, there is a constant fluid pressure, which allows for the pore volume to vary. In this case, Hooke's law is written as:

$$\sigma_{ij} = \left(K_d - {}^2/_3\, G\right)\varepsilon_{kk}\delta_{ij} + 2G\varepsilon_{ij} - \alpha p_f \delta_{ij}. \quad \ldots (1.21)$$

Note that the drained moduli are equal to the dry ones.

1.3.2 Undrained conditions

Undrained conditions are met when the pore space in a rock is filled with fluid, and the pore fluid mass is constant. In these conditions, the pore pressure can build up when a stress is applied at the boundaries of the sample. The relationship between the increase in pore pressure and confining pressure is given by the Skempton's coefficient (B) (Mavko et al. ,2009):

$$B = \frac{dp_f}{dP}\Big|_{undrained} = \left[1 + \phi\left(\frac{1}{K_f} - \frac{1}{K_m}\right)\left(\frac{1}{K_d} - \frac{1}{K_m}\right)^{-1}\right]^{-1}, \quad \ldots (1.22)$$

where K_f is the fluid's bulk modulus. The bulk modulus of the undrained sample (K_{und}) can be deduced using Biot-Gassmann's equation (Gassmann,1951):

$$K_{und} = K_d + \frac{\left(1-\frac{K_d}{K_m}\right)^2}{\frac{\phi}{K_f} - \frac{1-\phi}{K_m} - \frac{K_d}{{K_m}^2}}. \quad \ldots (1.23)$$

Biot-Gassmann's equation assumes that (i) the pores are fully filled with no isolated pores, (ii) the pore pressure is isobaric at a REV scale, (iii) there is no chemical weakening of the sample.

In the laboratory, it can be hard to create undrained boundary conditions due to the hydraulic tubing that is connected to the sample, creating volumes of water at the inlet and outlet of the sample, which act as excess pore pressure absorbers (Pimienta et al., 2016b). These volumes associated to the hydraulic tubing or any excess volume which can be added experimentally, are called dead volumes.

When a stress oscillation is applied at the boundaries of the sample, if the frequency is low enough, there is time for the pore fluid to migrate from the sample to the dead volume. At high enough frequencies, there is not enough time for the pore fluid to flow, and the masse of fluid is constant in the sample. The cut-off frequency between the undrained and drained frequency regimes due to the dead volume is related to the permeability, k, and dry bulk modulus and inversely related to the dynamic viscosity η of the pore fluid as well as half the length of the sample, L, (Cleary, 1978):

$$f_{undrained} = \frac{kK_d}{\eta L^2}, \quad \ldots (1.24)$$

Purely undrained conditions are met in this manuscript by using micro valves which are placed near the inlet and outlet, removing the dead volume associated with the drained-undrained transition (Borgomano et al., 2020). The micro valves allow undrained conditions to be reached even at low frequencies, as the pore fluid mass is constant. In this manuscript, all tests are performed using the closed microvalves, therefore the cut-off frequency between the undrained and drained frequency is not investigated.

1.3.3 Unrelaxed conditions

The drained-undrained frequency regimes occur due to the time dependence for the fluid to move at the sample scale (equation 1.24). The undrained-unrelaxed frequency regimes occur due to the time dependence for fluid to move at the pore scale. This FPD mechanism resulting from flow between a

relatively compliant and stiff pore at the pore scale is referred to as squirt flow (Mavko and Nur, 1975, 1979). Figure 1.5 (modified after Murphy et al., 1986) shows an example of the pore pressure distribution between low (A) and high (B) frequencies. At low frequencies, the pore fluid in the compliant pore has time to go back and forth between the compliant and stiff pores during the compression and dilation of the compliant pore. However, at high frequencies, the fluid in the compliant pore does not have time to flow and is effectively stuck, with the consequence of a pore pressure build up higher in the compliant pores than in the stiff pore.

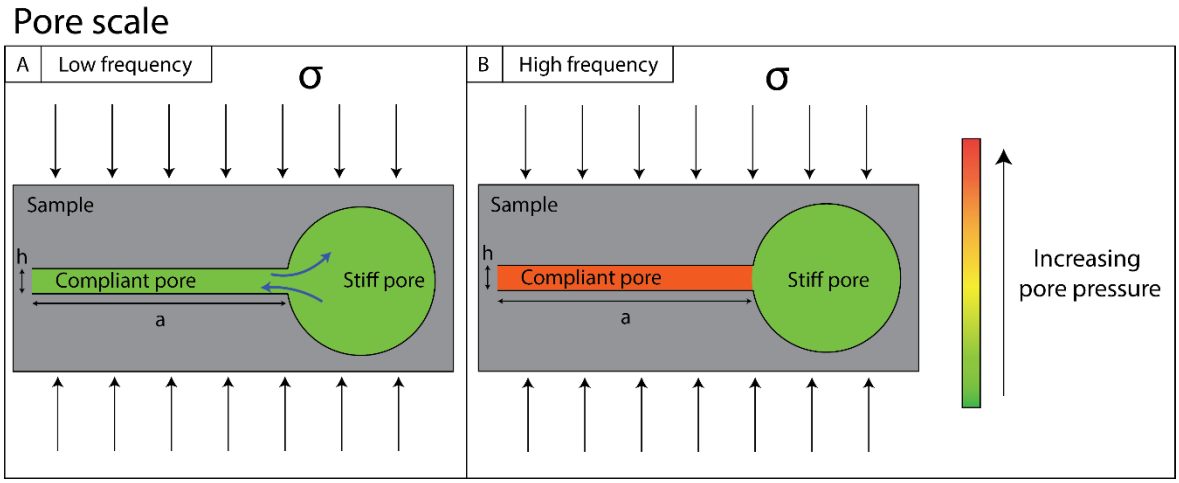

Figure 1.5: At the pore scale (A) Relaxed frequency regime where pore fluid has time to flow back and forth from the compliant and stiff pore; (B) Unrelaxed frequency regime where the fluid in the compliant pore is stuck with increase in pore pressure;

Many theoretical models of squirt-flow have been developed by analyzing the effect the aspect ratio (aperture/radius assuming a geometry of penny shape for the compliant pore), at the pore scale, has on the attenuation mechanism (O'Connell and Budiansky, 1977; Mavko and Nur, 1979; Palmer and Traviolia, 1980). These models are reviewed as a whole by Jones (1986). Other models assumed a binary structure with the majority of the porosity attributed to stiff pores and a small amount attributed to compliant pores, which are responsible for the frequency dependence of the elastic modulus at the pore scale (Walsh, 1965; Mavko and Jizba, 1991; Shapiro, 2003). Dvorkin et al. (1995) considered the sample to be a granular structure at the pore scale, with stiff pores compromising the intergranular structure and the compliant pores compromising the intragranular structure. A reformulation of this model was completed by Pride et al. (2004) and corroborated that the high-frequency limit is consistent with the well-established predictions of Mavko and Jizba (1991).

To summarize, figure 1.6 shows a visual representation of a sample with dead volumes (A), with a representation of their effects on the bulk modulus of a sample (B). In the drained regime, the pore fluid pressure cannot develop and does not add any stiffness to the sample, the drained bulk modulus

is equal to the dry modulus. In the undrained regime, there is an isobaric pore pressure at the REV scale which develops in the sample, in this case, the pore fluid adds stiffness to the system and there is a increase in bulk modulus ($K_{und} > K_d$) due to the increase in frequency. Finally, there is the unrelaxed regime, which shows a pore pressure gradient at the microscopic scale, related to the difference in compliance between the pores, and $K_{unr} > K_{und}$. This high frequency regime can not be interpreted in the framework of the poroelasticity (the assumption of isobaric pore pressure at the REV scale is not valid), but can be interpreted using the framework of effective medium model (Fortin and Guéguen, 2021). The change in elastic properties, due to a change in frequency is called dispersion. As shown in figure 1.6, during the dispersion, an associated attenuation occurs which is related to a loss of energy between the changes of stable regimes.

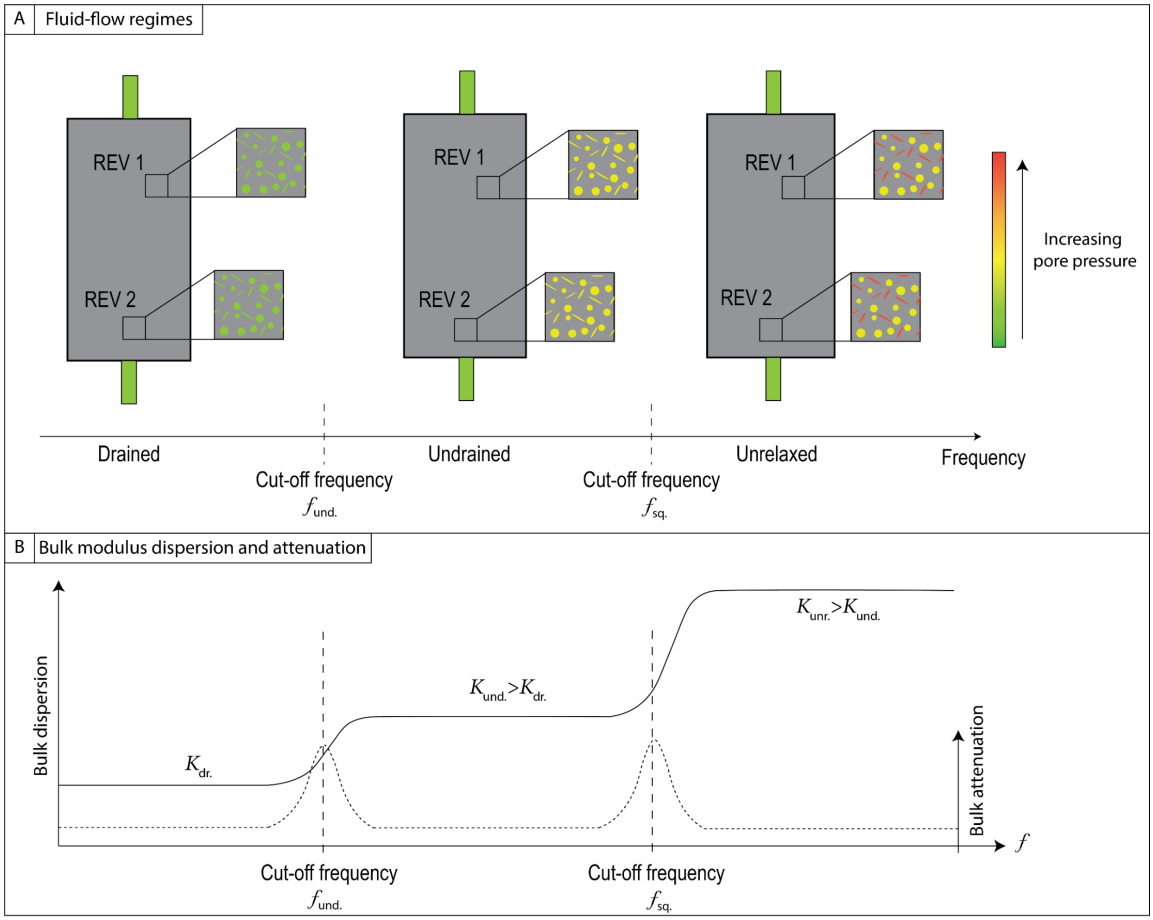

Figure 1.6: (A) Drained, undrained and unrelaxed fluid flow regimes; (B) Bulk modulus dispersion and attenuation caused by the fluid flow regimes;

1.4 Dispersion and attenuation

The elastic modulus (M) of a sample can be written in the form of a complex number (O'Connell and Budiansky, 1977):

$$M = M_R + M_I \,, \qquad \ldots (1.25)$$

where M_R is the real part and M_I is the imaginary part. If the rock is perfectly elastic (figure 1.2A), there is no phase shift between stress and strain. However, if there is a non-linear elastic response (figure 1.2B), the stress and strain will not have the same phase, or will be out of sync. This non-linear elastic response can be described by assuming a viscoelastic medium. As the stress is the cause of the strain, the strain phase can only be equal or lag behind the stress phase.

The attenuation of a sample is measured experimentally by (i) measuring the phase shift between the stress and the strain or (ii) by relating the maximum elastic energy stored in one cycle (E) to the elastic energy dissipated (ΔE) during that cycle (O'Connell and Budiansky, 1978):

$${Q_M}^{-1} = \tan(\Delta\phi) = \frac{1}{2\pi}\frac{\Delta E}{E} = \frac{M_I}{M_R} \,, \qquad \ldots (1.26)$$

Where $\Delta\phi$ is the phase shift between the stress phase, ϕ_σ and the strain phase ϕ_ε.

For a modulus M, a body wave of angular frequency ω can be described by using the propagation equation along the z-axis:

$$u = u_0 e^{-az} e^{i\omega(t-\frac{z}{V_o})} \,, \qquad \ldots (1.27)$$

where V_o is the wave velocity and a is the attenuation coefficient of the sample. The wave's energy decreases along the z-axis according to e^{-az}. The ${Q_M}^{-1}$ and a can be related by (O'Connell and Budiansky, 1978):

$$a = \frac{{Q_M}^{-1}\omega}{V_o} \,. \qquad \ldots (1.28)$$

A first method to determine the attenuation, is to measure the phase shift between stress and strain. This can be done by fitting a sinusoidal wave to match the data or by applying a fast Fourier transform (FFT) to the data.

Another method requires the determination of the elastic energy stored and dissipated in one cycle. This can be determined using figure 1.2 with the elastic energy dissipated equal to the area within

the stress-strain cycle and the elastic energy stored as the area underneath the stress-strain curve, following (Tisato and Madona, 2012):

$$\Delta E = \sum_{n=1}^{N-1} \frac{(\sigma_{n+1}-\sigma_n)(\varepsilon_{n+1}-\varepsilon_n)}{2N_c} \quad \text{and} \quad \mathrm{E}_m = \sum_{n=1}^{N} \frac{\sigma_n \varepsilon_n}{2N} \qquad \ldots (1.29)$$

where N is the total number of data points, N_c is the total number of cycles collected, with σ_n and ε_n being the stress and strain at a particular data point n.

All three methods have been used and compared by Borgomano (2018), and the author showed that the method of applying an FFT to determine the phase shift and the determination of the elastic energy lost always matched well, whereas the sinusoidal fitting method is not precise enough. As the FFT method is straightforward and reliable to implement, it is always used in the manuscript.

1.5 Other mechanisms of dispersion and attenuation induced by fluid pressure

1.5.1 Mesoscopic flow

Partial saturation can be the cause of mesoscopic FPD. This was first studied analytically by White (1975) assuming bi phasic pore space, with a spherical pocket saturated with a very compressible gas and the surrounding volume saturated with liquid (concentric spheres). White's model couples body waves and fluid flow. The body waves induce fluid flow generating a pore pressure gradient between the gas and liquid. Using measured velocities in unconsolidated packed sand, p-wave velocities were calculated and shown to increase by ~18% with saturation with matching attenuation peaks. It was also shown that although bulk modulus is frequency dependent, the shear modulus was not. Other analytical solutions have been developed to describe mesoscopic FPD through fluid heterogeneities (Johnson, 2001; Kobayashi & Mavko, 2016; Pride et al., 2004).

Numerical models have also been developed to solve FPD due to partial saturation by solving Biot's (1941) quasi-static consolidation equations (Quintal et al., 2011) and Biot's (1962) dynamic poroelastic equations (Carcionne et al., 2003; Rubino et al., 2009) which match well with analytic solutions.

Experimentally, there have been two main methods to introduce bi-phasic fluid distribution to a sample. The first is the imbibition and drainage technique (Alemu et al.,2013; Nakagawa et al.,

2013a; Zhang et al., 2015). The second is the exsolution of a gas from a fluid (Johnston and Toksöz, 1980; Blanchard and Delommot, 2015; Tisato et al., 2015; Spencer and Shine, 2016; Chapman et al., 2017; Chapman et al., 2021). The most comprehensive of these was probably conducted by Chapman et al. (2021) as they managed to test a large frequency range while simultaneously having a good understanding of the fluid distribution. A Berea sandstone cylindrical sample, with a diameter of 40 mm and a height of 80 mm, was saturated with a water-CO2 mixture. The first part of the experiment followed a strict CO2 gas exsolution process which was monitored using a X-ray scanner, allowing for a 3D representation of fluid distribution. The second part of the experiment had the process repeated on the sample, in a triaxial cell, where axial oscillation tests were performed at a large frequency range. Dispersion and attenuation were observed which were consistent with the analytical and 3D numerical models. The rate of the fluid pressure decline was also observed to have an effect on the dispersion and attenuation, showing a shift of the attenuation peak to higher frequencies during slow pressure declines.

Another cause of mesoscopic FPD can be caused by a heterogeneous sample, with varying solid matrix properties. Pride et al. (2004) made a double porosity analytical model in the framework of the poroelasticity (Biot, 1962), where a consolidate sandstone (phase 1) host rock contains thin lenses of another rock type (phase 2). It was found that the magnitude of the attenuation measured was controlled by the difference of elastic properties of the two phases as well as the shape of the inclusions. Indeed, the two phases needed to have a significant difference in properties to generate pore fluid pressure gradients. It is interesting to note that a change in permeability alone did not create an attenuation peak. Carcione and Picotti (2006) develop also a mesoscopic FPD numerical model using the laws of poroelasticity (Biot, 1962), and in their case the heterogeneities were in the form of stratified layers.

1.5.2 Fracture to pore space flow

Fractures are not routinely tested in the laboratory, as a sample with a fracture, is hard to test and would introduce a heterogeneity (no longer in the REV domain). However, fractures can have large effects on reservoir parameters such as permeability (Walsh, 1981; Paillet et al. 1987) and elastic properties (Matonti et al., 2015; Bailly et al., 2019b) as well as having an effect on the dispersion and attenuation as it provides a FPD mechanism between the compliant fracture and the pore space around it.

A common method for modelling fractures is to assume a saturated host rock with aligned parallel fractures. This method was successfully used by Thomsen (1995) and Chapman (2003), showing

dispersion and attenuation. Using a host porous medium (phase 1) with aligned thin layers (phase 2) placed periodically, Brajanovski et al. (2005) elegantly solved for the p-wave modulus as a function of frequency knowing the phase 1 properties and the normal compliance of the fracture. In this case, the thin layers had a large porosity, permeability and compliance, to mimic a fracture. Experimentally, there has been little work. However, Nakagawa (2013b) completed uniaxial stress test on a jacketed fractured sample with a slight vacuum applied to the pore pressure to prevent fluid from moving between the jacket and the sample. The oscillations were performed normal to the fracture at a frequency range between 1 and 100 Hz, and attenuation was measured with a peak around 1 Hz frequency. Amalokwu et al. (2014) were able to synthesize sandstone samples with and without aligned penny-shaped voids. These were tested at an effective pressure of 40 MPa at a frequency of 650 kHz showing more attenuation in the samples with aligned fractures.

The largest advancements in the effect of fracture on dispersion and attenuation have come from numerical modeling as this method can more easily take into account more complex geometries. For example, a mesoscopic 2D fracture was simulated by Rubino et al. (2013), by representing the fracture as a much more compliant media within the host rock. This is similar to what is laid out by Brajanovski et al. (2005), however, here the fracture has a more complicated geometry. Rubino et al. (2013) were also interested in the effect that another fracture perpendicularly placed to the first fracture would have on the dispersion and attenuation. A second attenuation peak at higher frequencies was observed and is related to the two fractures being connected, changing the frequency dependence completely. When the fractures were not connected, there was only one attenuation peak at a lower frequency associated to the fracture to matrix FPD mechanism.

Rubino et al. (2014) continued their work, by changing sample and fracture characteristics and looking at the changes in the p-wave modulus frequency dependence. They show that the attenuation related to the fracture to fracture FPD mechanism was sensitive to the vertical and horizontal fracture length and the angle of intersection. Quintal et al. (2014) followed a similar methodology looking at these effects on s-wave attenuation mechanisms. It was found that the s-wave attenuation caused by FPD between fractures is also connected to the angle of intersection. An interesting finding was that s-wave attenuation is much more sensitive to the fracture inclination than the p-wave modulus in both the unconnected and connected formats.

To summarize, there are two main FPD mechanisms occurring due to fractures which are (i) FPD between the fracture and pore space of the matrix and (ii) the FPD between two interconnected fractures. The FPD from the fracture to the pore space of the matrix is presented in figure 1.7. At low enough frequencies (A), there is a constant pore pressure throughout the sample (matrix and fracture). At higher frequencies (B), there is no time for the pore fluid in the fracture to flow to the pore space, a pore pressure higher in the fracture than in the matrix is developed. The critical frequency for this mechanism is (Brajanovski et al., 2005):

$$f \sim \frac{D}{L^2}, \qquad \ldots (1.30)$$

where D is the hydraulic diffusivity $D = kBK_d/(\alpha\eta)$ and L is half of the distance between two fractures.

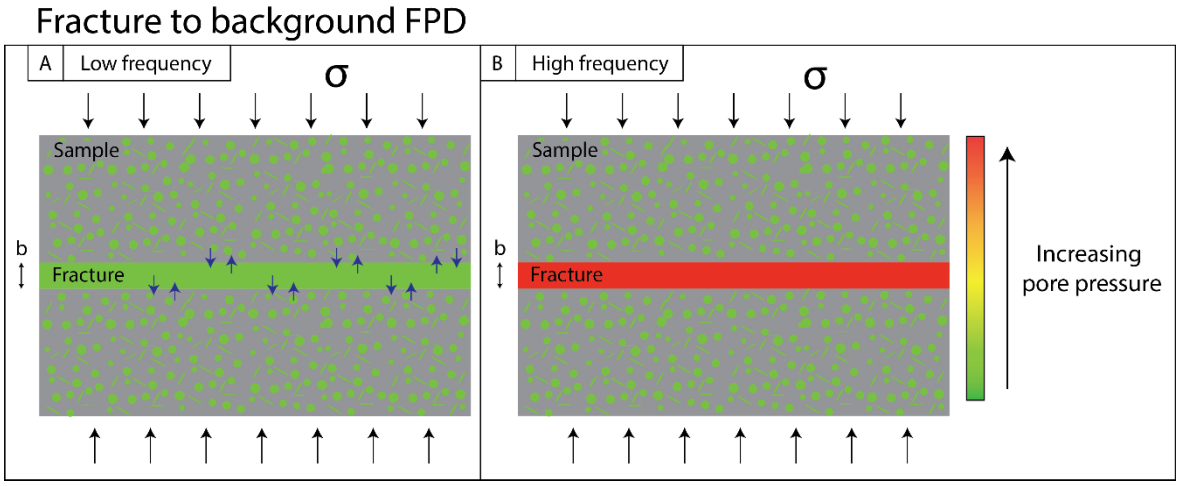

Figure 1.7: (A) low frequency regime where fracture fluid has time to flow back and forth from the stresses horizontal fracture to the sample pore space; (B) high frequency regime where the fluid in the stressed horizontal fracture is stuck with an increase in pore pressure;

The FPD due to fracture to fracture flow is presented in figure 1.8. At low frequencies (A), again, the pore fluid has time to equilibrate between both fractures. At higher frequencies (B), the horizontal fracture will have an increased pore pressure.

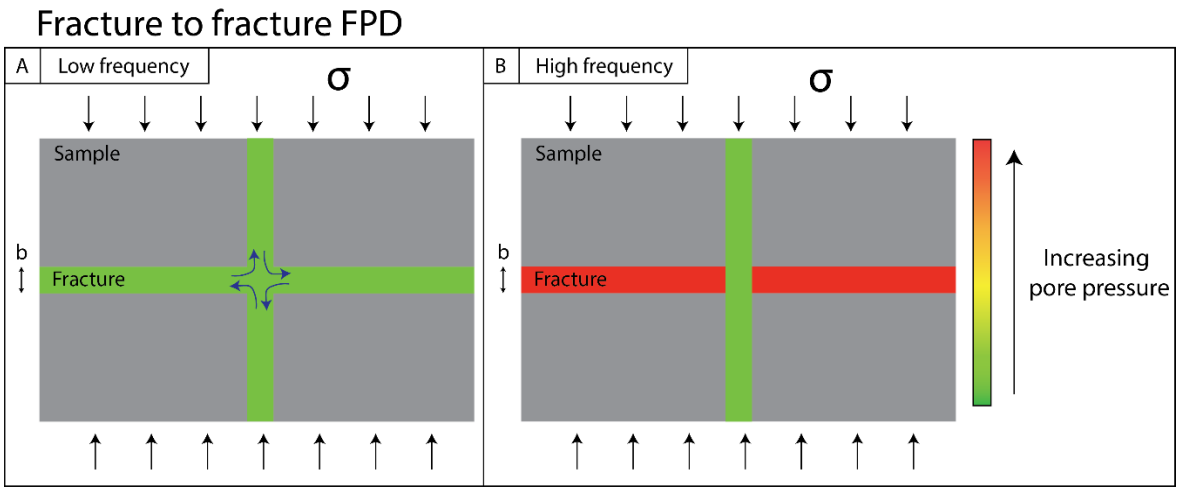

Figure 1.8: (A) low frequency regime where fracture fluid has time to flow back and forth from the stresses horizontal fracture to the "dead volume" vertical fracture; (B) high frequency regime where the fluid in the stressed horizontal fracture is stuck with an in increase in pore pressure;

Lissa et al. (2020) continued through this vein of work, by following the same methodology and adding a 3D aspect, looking at the effect the roughness of the fracture would have on the attenuation. Before their work, it was assumed that fractures have a constant aperture, when fractures are rough by nature and develop contact areas as the samples effective pressure is increased. When contact areas are taken into account, the stiffness of the fracture increases making for a smaller attenuation amplitude, with the attenuations peak frequency increasing.

1.6 Thesis outline

The goal of this chapter is to explain the main mechanisms, which are observed experimentally in the rest of this manuscript. Chapters 2 to 5 are written as independent articles which are published in peer-reviewed journals related to rock mechanics. For this reason, they conform to the typical article structure with abstract, introduction, experimental methods, results, discussion and conclusion. As they are independent articles they can stand alone, however the theme within the thesis is to study the heterogeneous aspects of rock mechanics through experimental work which is corroborated by analytical and/or numerical methods. Each chapter is shortly summarized below.

Chapter 2 is a machine paper published in the "Review of Scientific Instruments" journal. This machine paper, published in 2020, underlines the working of the triaxial cell which is used for all the elastic property tests performed in this manuscript. The cell is outfitted to perform hydrostatic

oscillation tests at a frequency range of 10^{-2} to 1.3 Hz and axial oscillations tests at a frequency range of 10^{-2} Hz to 1 kHz. Different pore fluids can be used, such as water, brine and glycerin. Innovative micro valves were installed in the bottom and top cap, to allow undrained conditions to be met, which was shown to work on a Vosges sandstone sample.

Chapter 3 focusses on the frequency dependent results on three carbonate samples. Forced oscillation methods are used to test samples in dry, brine and glycerin saturated condition, reaching apparent frequency range is between 7 10^{-2}Hz to 100 kHz and 1 MHz. Two attenuation peaks were observed. The first is at a frequency of around 100 Hz, and is associated to mesoscopic FPD caused by the heterogeneous nature of the samples tested. The sample which was determined to be isotropic, did not have this first attenuation peak. The second peak is at a frequency around 40 kHz and was measured in all three samples. This peak is assumed to be caused by squirt-flow as it is pressure dependent. Also, the first peak had no attenuation in shear, however the second did, which is consistent with theory.

Chapter 4 is a paper under press in the "Rock Mechanics and Rock Engineering" journal. In this paper, hydrostatic oscillation tests (frequency range of 0.04 to 1 Hz) are performed on an intact and saw cut Rustrel sample, at three effective pressures, in dry and water saturated conditions. An interesting local negative phase shift between the stress and strain, was measured in the saw-cut water saturated conditions, in the low effective pressures. A 1D analytical model and 3D numerical model were made, which corroborated the results and showed FPD between the fracture and the pore space.

Chapter 5 focuses on dispersion related to fracture to fracture FPD. In this paper, axial oscillation tests (frequency range of 0.2 to 40 Hz) were performed on a saw-cut Solnhofen limestone in glycerin saturated conditions at multiple effective pressures. An innovative eddy gauge sensor was used to measure the global axial strain. An attenuation peak in the Young's modulus was observed at 2 Hz which decreased while the effective pressure was increased. The attenuation is associated to fracture to fracture FPD, as the permeability of the matrix is too low to allow for fracture to pore space fluid flow.

Chapter 6 provides concluding remarks on the work accomplished on measuring elastic properties on heterogeneous samples in the lab. A discussion is also started on what the future entails with the new developments which are made experimentally.

2. An apparatus to measure elastic dispersion and attenuation using hydrostatic- and axial-stress oscillations under undrained conditions.

This chapter is a published machine paper in Review of Scientific Instruments: Borgomano, J. V., Gallagher, A., Sun, C., & Fortin, J. (2020). An apparatus to measure elastic dispersion and attenuation using hydrostatic-and axial-stress oscillations under undrained conditions. *Review of Scientific Instruments*, *91*(3), 034502.

Abstract

An experimental apparatus is described for the investigation of the frequency dispersion, and related attenuation, of fluid-saturated rocks under confining pressure and undrained boundary conditions. The forced-oscillation method is performed on cylindrical samples. The measurement of stress and strain under hydrostatic oscillations allows the dynamic bulk modulus to be inferred, while axial oscillations give access to the dynamic Young's modulus and Poisson's ratio. We present calibration measurements for dispersion and attenuation on standard materials such as glass, plexiglass and gypsum. Results show that for strain amplitudes below 10^{-5}, robust measurements can be achieved up to 1 kHz and 1.3 Hz, respectively for axial and hydrostatic oscillations. A new experimental design of the endplatens (sample holders) allows control of drained or undrained boundary conditions using microvalves. The microvalves were tested on a porous Vosgian sandstone. In addition, numerical modelling confirms that the resonances of the apparatus only affect frequencies above 1 kHz, with little sensitivity to the sample's stiffness.

2.1 Introduction

Dispersion (i.e. frequency-dependence) of the elastic properties of subsurface rocks constitute a major challenge when trying to link seismic (~100 Hz) or sonic (~10 kHz) field surveys to laboratory standard ultrasonic measurements (~1 MHz). Through the causality principle, well expressed with Kramers-Kronig relationships, an elastic dispersion is conjugated with an elastic dissipation, often named "attenuation" (Q^{-1}) by analogy to viscoelastic solids (O'Connell and Budiansky, 1978).

Wave induced fluid flows (WIFF) are thought to be among the principal mechanisms for attenuation in subsurface rocks (Pride et al., 2004). Each of the various mechanisms within WIFF have a corresponding theoretical or modelling solution (e.g., Winkler and Nur, 1979; Müller et al., 2010; Sarout, 2012). It is therefore essential to verify experimentally these models in controlled and comparable conditions to reliably interpret field measurements.

In fully saturated conditions, one major mechanism at play may be the squirt-flow between compliant cracks and stiff pores. The characteristic frequency ($f \sim \xi^3 K_S/\eta$) is dependent on the crack aspect ratio (ξ), the skeleton bulk modulus (K_S), and the fluid's dynamic viscosity (η) (Mavko et al., 2009). Therefore, for reservoir rocks with $\xi \sim 0.001, K_S \sim 40$ GPa and $\eta \sim 0.001 - 0.1$ Pa.s, the squirt-flow attenuation may affect the frequency range from 400 Hz to 40 kHz.

In order to investigate these dispersive mechanisms, specific devices have been developed to measure the complex elastic moduli over broadband frequencies under the kHz range using the forced-oscillation method. In most apparatus, if we ignore resonant bar techniques which measure narrow frequency bands in the sonic range (5 to 20 kHz), the Young's modulus or Poisson's ratio is accessible in a large broadband (1 mHz to 1 kHz) through axial oscillations generated by piezoelectric actuators or dynamic shakers (e.g., Spencer, 1981; Batzle et al., 2006; Mikhaltsevitch et al., 2011; Tisato and Madonna, 2012; Szewczyk et al., 2016; Sun et al., 2018). The apparatus developed by Jackson and Paterson (1993) is able to measure the shear modulus and the Young's modulus up to 1 Hz, through torsional and flexural oscillations respectively (Jackson et al., 2011). The previous apparatus at the Ecole Normale Supérieure of Paris (Pimienta et al., 2015a, 2015b, 2016a) was able to measure a bulk modulus up to 0.4 Hz with pure hydrostatic oscillations, and Young's modulus/Poisson's ratio up to 100 Hz through axial oscillations.

The new apparatus presented in this paper is able to measure the complex bulk modulus up to 1 Hz, and Young's modulus and Poisson's ratio up to 1 kHz using forced-oscillation methods, under either drained or undrained boundary conditions, and for temperatures between 20 and 100°C. The frequencies of the viscous-driven WIFF (such as squirt-flow) for a water-saturated rock may be shifted to lower frequencies with the use of more viscous pore fluids, such as glycerin (Batzle et al., 2006). This enables us to extend the "apparent frequency" range of the apparatus (e.g. Borgomano et al., 2017). We have recently reported some experimental results on carbonates or sandstones (Chapman et al., 2018; Borgomano et al., 2019b; Yin et al., 2019). We wish here to present the apparatus itself and the related calibrations.

2.2 Pressure vessel

A standard hydraulic triaxial cell from Top Industrie company (Figure 2.1) was modified in order to investigate the frequency dependence of the dynamic moduli of cylindrical samples, of 80 mm length and 40 mm diameter. The cell is auto-compensated (*i.e.* the piston is hydraulically compensated for the confining pressure), and can reach a maximum confining pressure of 100 MPa and a maximum axial stress of 700 MPa, using servo-controlled hydraulic pumps. Initial experiments were conducted at room temperature (controlled at 20°C). A servo-controlled heating collar located around the confinement cell, enables heating and temperature control (through a PID controller) to a maximum of 100°C (Figure 2.1). The temperature feedback is provided by a thermocouple (type K) located inside the confining oil. The sample is jacketed in a neoprene sleeve to separate the confining oil from the pore fluid, and is maintained in between a top and a bottom endplaten, respectively made out of steel and aluminum.

A piezoelectric actuator from PI (PICA Stack P-056-20P) is installed above the top endplaten, and under a cylindrical steel rod that can be put in contact with the axial piston (Figure 2.1). A neoprene sleeve isolates the actuator from the confining oil. The axial piston is either not in contact with the top endplaten for pure hydrostatic conditions, or in contact to apply a deviatoric stress.

The top and bottom endplaten, which contain the pore-fluid lines, are both equipped with two P- and S-ultrasonic transducers of 10 mm diameter and 1 mm height from PI Ceramics (type PIC255/ref PRYY+0.111), allowing for time travel measurements of P- and S-waves of 1 MHz in the axial direction of the sample. They are also equipped with hydraulically piloted microvalves, which enables us to switch between axially drained or undrained conditions for a saturated porous sample (Figure 2.1).

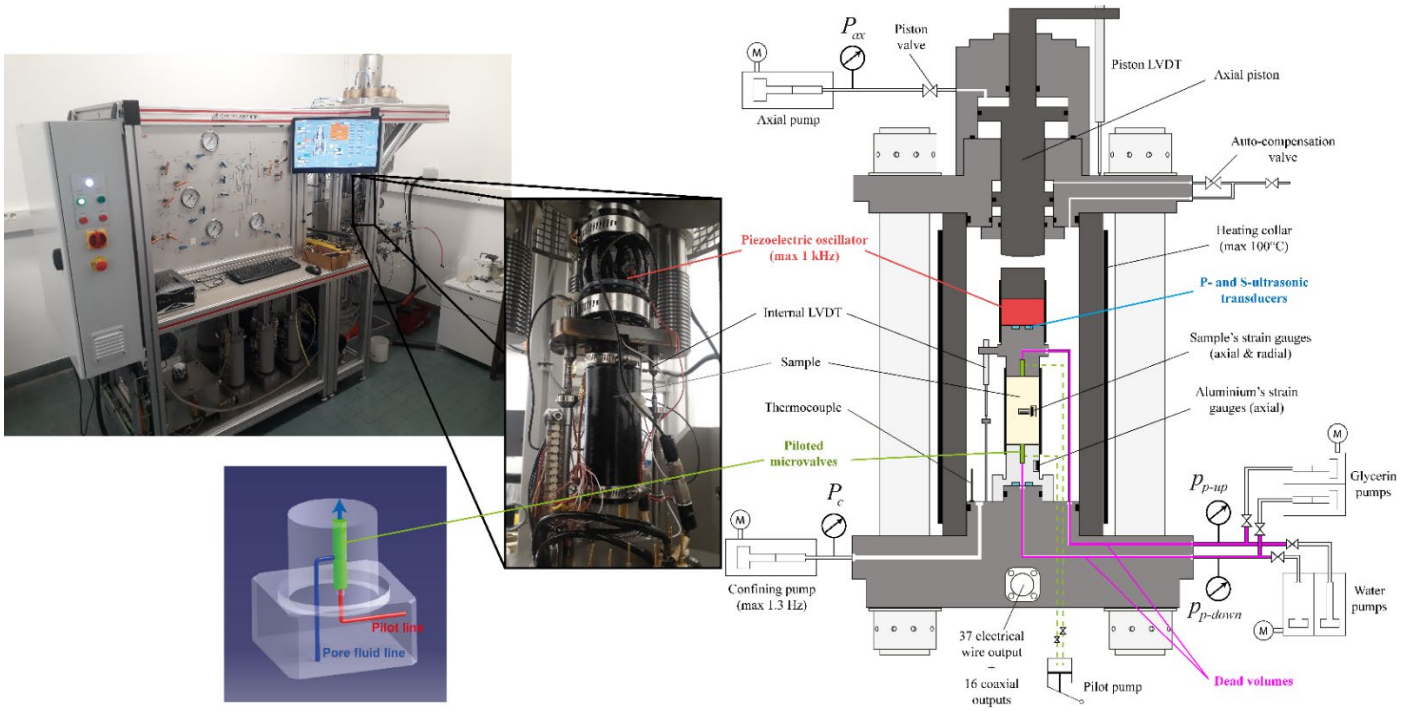

Figure 2.1: Photo and schematics of the experimental apparatus. The sample is a cylinder of 80 mm length and 40 mm diameter, isolated from the confining oil by a neoprene jacket. A piezoelectric actuator is used to induce axial-stress oscillations (maximum 1 kHz), with the axial piston in contact with a small deviatoric stress of maximum 1.5 MPa. The confining pump is used to perform hydrostatic oscillations while the axial piston is not in contact (maximum 1.3 Hz). P- and S-wave ultrasonic transducers (1 MHz) are mounted in the top and bottom endplatens. Drained or undrained boundary conditions of the sample can be achieved through the two hydraulically piloted microvalves installed in the top and bottom endplatens.

The deformations of the sample can be measured with two internal LVDTs, which can measure the global strain in the axial direction with a resolution of 10^{-5}, and with axial and radial strain gauges directly glued on the sample (at mid-height), which can measure local strains with a maximum resolution of 0.3×10^{-7} (Figure 2.1). The strain results reported here were acquired with TML 350 ohms foil strain gauges (FCB-6-350-11). Up to 14 strain gauges, connected in quarter bridge, can be connected to the data acquisition system. Four axial strain gauges are reserved for the bottom aluminum endplaten in order to deduce axial stresses (Figure 2.1).

2.3 Methodology

The technique used to characterize the frequency dispersion and attenuation of the elastic moduli of a sample is the forced-oscillations method (or stress-strain method). This method applies an oscillatory stress to the sample, and records the subsequent axial and radial strains (e.g., Spencer, 1981; Paffenholz and Burkhardt, 1989; Jackson and Paterson, 1993; Batzle et al., 2006; Adelinet et al., 2010; Mikhaltsevitch et al., 2011; Takei et al., 2011; David et al., 2013; Madonna and Tisato, 2013; Pimienta et al., 2015a). All the signals are analyzed using Fast Fourier Transform method to

extract amplitudes and phases. The apparatus enables us to perform two modes of stress-oscillations: (i) hydrostatic, using the confining pump; (ii) axial, using the piezoelectric actuator.

For hydrostatic oscillations (Figures 2.2a & 2.2b), the confining pressure oscillates with an amplitude (ΔP_c) of about 0.2 MPa around a mean value to induce strain oscillation amplitude in the order of 10^{-6}. Below 0.1 Hz, the confining pump regulates from the feedback of the confining pressure transducer (Figure 2.1). Above 0.1 Hz, the confining pump regulates solely in position. Depending on the bulk modulus of the sample, the pressure oscillation can be adjusted so that the strains meet the previous condition. For an isotropic sample, the volumetric strain (ε_{vol}) can be calculated by (i) $\varepsilon_{vol} = \varepsilon_{ax} + 2\varepsilon_{rad}$, where ε_{ax} and ε_{rad} are the mean values of all the strain gauges glued at mid-height on the sample in the axial and the radial directions respectively (Figure 2.2), or by (ii) $\varepsilon_{vol} = 3\varepsilon_{mean}$, where ε_{mean} is the mean values of all the strain gauges regardless of direction. In theory, for an isotropic sample, both calculations should give the same result. However, the second method gives a slightly lower uncertainty, since the error on average decreases with increasing number of strain gauges used. Moreover, relation (ii) gives equal importance to the axial and radial directions, whereas the uncertainty in relation (i) is primarily controlled by the radial directions. The bulk modulus K is then calculated by:

$$K = -\frac{\Delta P_c}{\varepsilon_{vol}}, \qquad \ldots (2.1)$$

with the convention that strains are negative in compression (Figure 2.2a). For a perfectly homogenous sample, no significant discrepancy between the different strain gauges are expected. For rocks however, small discrepancies between the strain gauges may arise from the intrinsic heterogeneity or anisotropy of the sample. An associated uncertainty can therefore be calculated when averaging the strain gauges. From Equation 1, the uncertainty on K (δK) depends on the uncertainty of the confining pressure ($\delta P \approx 0.001$ MPa) and the uncertainty on the average of the strains ($\delta\varepsilon$). The relative uncertainty on K is then deduced by $\delta K/K = \delta P/P_c + \delta\varepsilon/\varepsilon_{vol}$. The error on the strain average can be calculated by $\delta\varepsilon = std/\sqrt{n}$, where *std* is the standard deviation between the strain amplitudes, and n is the number of strain gauges considered.

For axial oscillations (Figures 2.2c & 2.2d), the piezoelectric actuator between the piston and the sample's top endplaten induces axial stress oscillations. A small deviatoric stress (maximum 1.5 MPa) is constantly applied by the piston to preload the actuator and ensure a good coupling with the sample, while avoiding stress induced anisotropy. In order to limit the displacement of the piston

when the actuator is oscillating, the auto-compensation valve is closed. The oscillating axial stress ($\Delta\sigma_{ax}$) (around the mean value) generated by the actuator is measured from the axial strain gauges (ε_{alu}) glued on the lower endplaten (Figure 2.2) made out of aluminum by $\Delta\sigma_{ax} = E_{alu}\varepsilon_{alu}$, where E_{alu} is the associated Young's modulus of the endplaten that is to be calibrated with standard samples. The Young's modulus (E) and the Poisson's ratio (ν) of the sample can then be calculated by:

$$E = \frac{\sigma_{ax}}{\varepsilon_{ax}} \quad \text{and} \quad \nu = -\frac{\varepsilon_{rad}}{\varepsilon_{ax}}\,. \qquad \ldots (2.2)$$

A total of 4 axial strain gauges are glued on the lower aluminum endplaten, at diametrical opposite locations. Due to the geometry of the endplaten and the position of the strain gauges, we demonstrate later that $E_{alu} = 78$ GPa. In addition, this configuration helps control that the vertical alignment is good and that the axial stress is homogeneous on the sample, as any tilt would result in different strain readings on the aluminum endplaten. Similarly to K, the uncertainty on the strain averages ($\delta\varepsilon$) can be calculated as previously, and propagated to the moduli relative uncertainties by $\delta E/E = \delta\varepsilon_{alu}/\varepsilon_{alu} + \delta\varepsilon_{ax}/\varepsilon_{ax}$ and $\delta\nu/\nu = \delta\varepsilon_{rad}/\varepsilon_{rad} + \delta\varepsilon_{ax}/\varepsilon_{ax}$.

The inverse of the quality factor (Q^{-1}) measures the elastic energy dissipation within the sample during the oscillating cycles. In the following text, the term attenuation refers to the factor Q^{-1}. For a purely elastic material $Q^{-1} = 0$. When dissipation occurs, the rheology of the sample may be considered analogue to a viscoelastic material (O'Connell and Budiansky, 1977). The stress-strain curve presents an elliptic shape that highlights the non-elastic behavior (e.g. Figures 2.2b & 2.2d). The slope of the big axis is given by the elastic modulus, while the surface represents the amount of elastic energy dissipated (e.g. Tisato & Madonna, 2012). This elliptic shape is the result of the phase shift between the applied stress (of phase φ_σ) and the induced strain (of phase φ_ε). The attenuation is then given by (O'Connell and Budiansky, 1977):

$$Q^{-1} = \tan(\varphi_\sigma - \varphi_\varepsilon)\,. \qquad \ldots (2.3)$$

The attenuation related to K and E are therefore calculated by:

$$Q_K^{-1} = \tan(\varphi_{P_c} - \varphi_{\varepsilon_{vol}}) \quad \text{and} \quad Q_E^{-1} = \tan\left(\varphi_{\sigma_{ax}} - \varphi_{\varepsilon_{ax}}\right). \qquad \ldots (2.4)$$

Because the lower endplaten is assumed perfectly elastic (as confirmed by the calibration on standard samples), we consider that $\varphi_{\sigma_{ax}} = \varphi_{\varepsilon_{alu}}$.

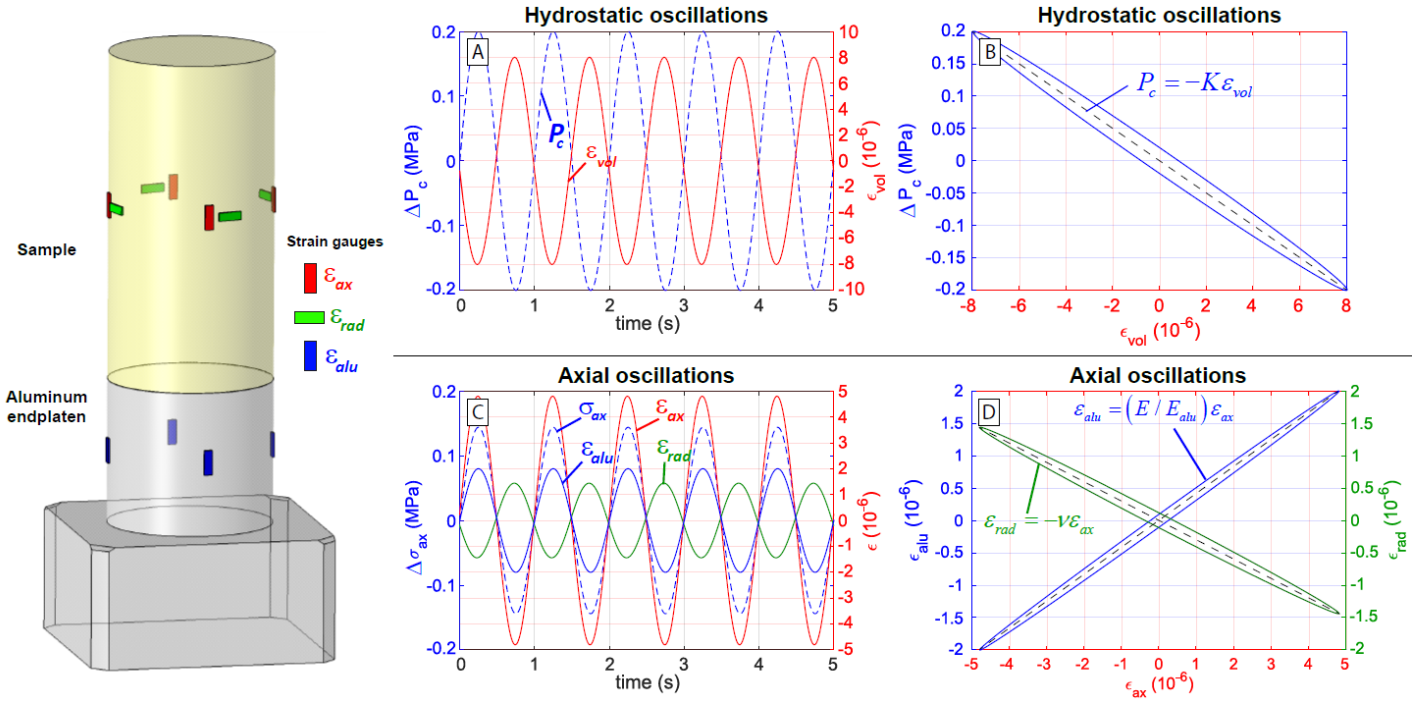

Figure 2.2: Strain gauge positions (left) and typical stress-strain recordings of hydrostatic (a & b) and axial (c & d) oscillations (around mean values) on a viscoelastic material (modified from (Borgomano et al., 2017)). The strains (ε_{ax}, ε_{rad}, ε_{alu}) are each averaged from 4 strain gauges around the circumference of the sample/endplaten at mid-height. The axial stress oscillation ($\Delta\sigma_{ax}$) is deduced from the aluminum endplaten axial strain (ε_{alu}) and its calibrated Young's modulus of 78 GPa.

2.4 Generation of stress oscillations and strain measurements

The controller program of the confining pump has been modified to perform hydrostatic oscillations. Under 0.2 Hz, the program works in controlled pressure mode, and imposes a perfect sinusoidal function to the confining pressure. Above 0.2 Hz, and to a maximum of 1.3 Hz, the program works in controlled flow-rate mode, with a constant injection rate between pump-volume bounds. In order to maximize the frequency range, the volume of the confining cell has to be as small as possible (here 4L), with a high flow-rate confining pump (here 70mL/min). Due to the limited flow-rate of the pump and the cell volume, there is a compromise between the frequency and the amplitude of the pressure oscillation. Figure 2.3 represents the maximum amplitude reachable in this apparatus for a given frequency and the corresponding volumetric strain for different bulk moduli. At a low frequency of 10^{-3} Hz and at maximum flow-rate, the pump can achieve oscillations with an

amplitude of 10 MPa (Figure 2.3a). The amplitude decreases to about 0.1 MPa at 1 Hz. Due to the intrinsic inertia and joint friction in the pump, any frequency higher than 1.3 Hz cannot be performed.

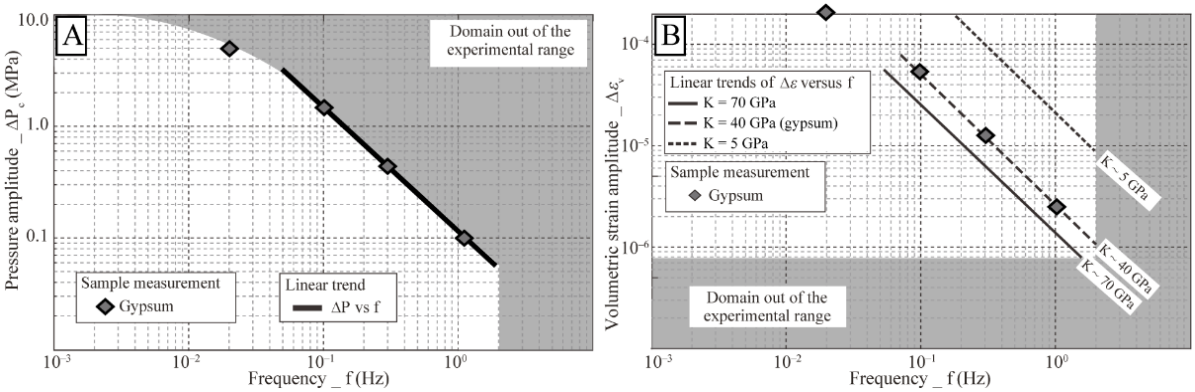

Figure 2.3: (a) Maximum amplitude of the hydrostatic-stress oscillations achievable with the confining pump as a function of frequency, tested with a gypsum sample of bulk modulus K≈40 GPa. (b) Corresponding volumetric strain for various theoretical bulk moduli. For a given bulk modulus, the volumetric strain can have values equal or lower than the lines shown;

The piezoelectric actuator (PI PICA Stack P-056-20P) is controlled through a programmable function generator (TTi TG1010A) and an electric amplifier (PI PICA E-482). The amplifier can deliver a maximum voltage of 1150V with a voltage gain of 100V/V. The actuator can tolerate stresses up to 30 MPa (blocking stress), over which there is a risk of depolarization and permanent damage. Figure 2.4 shows the amplitudes of axial-stress oscillations obtained with a glass sample for constant voltage inputs of 200, 400 and 600V, and on a plexiglass (PMMA) sample for a voltage of 600V. The axial stress (σ_{ax}) is deduced from the aluminum endplaten average strain (ε_{alu}) and considering a Young modulus of $E_{alu} = 78$ GPa. The axial stress amplitudes are stable over the frequency range up to 10^3 Hz, although there does seem to be a little decrease in amplitude above 200 Hz when the voltage input is 600V. The results on the plexiglass and on the glass, of very contrasting Young's moduli of around 5 GPa and 80 GPa respectively, are fairly similar with an input voltage of 600V. This shows that the stress produced by the piezoactuator is solely proportional to the input voltage, with little effect of the sample present between the actuator and the endplaten. The voltage can then be adjusted to the Young's modulus of the sample in order to obtain the desired strain amplitude.

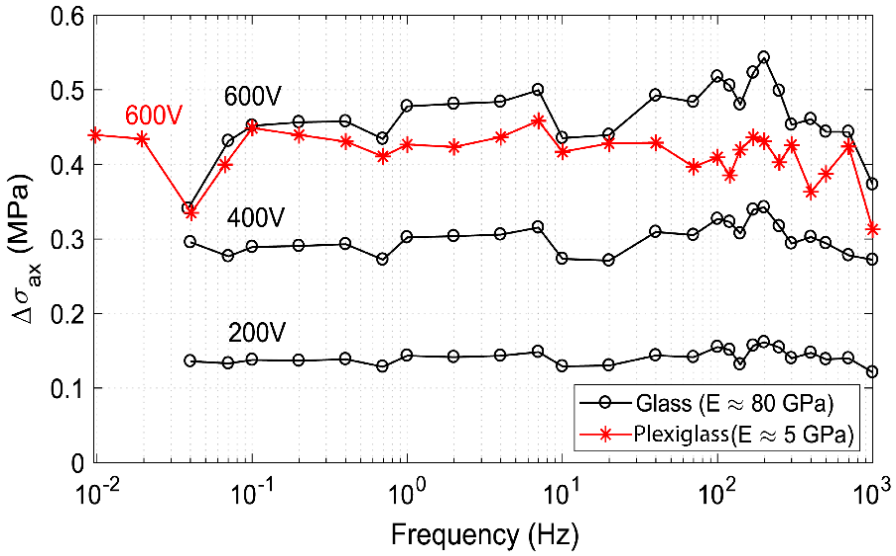

Figure 2.4: Amplitude of stress during axial-stress oscillations using the piezoelectric oscillator under oscillating voltages of 200V, 400V and 600V on a glass sample, and 600V on a plexiglass (PMMA) sample. The axial oscillations were performed on the samples at a confining pressure of 5 MPa and a deviatoric stress of 1 MPa. The axial stress (σ_{ax}) is deduced from the aluminum endplaten average strain (ε_{alu}) and considering a Young modulus of E_{alu} = 78 GPa;

The current data acquisition system (DAQ) used both for the pressure transducers and the strain gauges (1/4 bridge) can record with a sampling frequency up to 4 kHz. It is composed of four measurement modules provided by Gantner instruments. The pressure transducers are connected to two universal Q.bloxx A107 universal modules, while the strain gauges are connected in ¼ bridge configuration to two Q.bloxx A166 multichannel modules. The maximum recordable frequency without aliasing being under the Nyquist frequency of 2 kHz, we limit our measurements to a maximum of 1 kHz. In order to manage the size of the output files, the sampling frequency is adjusted depending on the frequency of the measurement. The sampling frequencies are always chosen to be at least 20 times greater than the frequency of the stress oscillation. This rule is of course violated for frequencies between 200 Hz and 1 kHz, but the uncertainty on the Fourier transform is then lowered by acquiring a greater number of periods. For both hydrostatic and axial stress oscillations, we record at least 50 periods of the signal to perform the FFT. For frequencies above 1 Hz, the number of recorded periods can be reasonably increased without substantially penalizing the total duration of the experiment. For frequencies between 2 and 20 Hz, we measure at least 400 periods, and above 20 Hz at least 1200 periods.

2.5 Protocol

Measurements can be done at various effective pressures on homogenous materials (mainly for calibration), and principally on natural cored porous rocks. The top and bottom surfaces of the plug are necessarily rectified to be perfectly parallel (tolerance of 1 μm). Once the sample is installed in the cell, it runs through several hydrostatic seasoning cycles, in order to minimize nonlinear cycling effects caused by microcracks (Hart and Wang, 1995). The confining pressure varies several times between 0.2 and 30 MPa, which is the maximum pressure tolerable of the piezoelectric actuator. The strain gauges and the internal axial LVDTs (Figure 2.1) are monitored until the final cycles are repeatable. The static bulk modulus, during loading and unloading (tangent modulus for a given confining pressure), may be deduced from the last cycle.

For a given effective pressure, either for rocks or non-porous materials, the hydrostatic and axial oscillations are performed in sequence, followed by ultrasonic measurements of P- and S-wave travel times between the top and bottom end platen (Figure 2.1), and eventually permeability measurements using the Darcy flow method. The effective pressure is then changed, generally by changing the confining pressure, allowing enough time to equilibrate the pore pressure through the sample.

After measurements are performed on oven-dry porous rock, the sample can be fully saturated in the cell following a specific procedure. A vacuum is generated throughout the whole sample from a vacuum pump connected on the top pore-line. The pore fluid is then injected from the bottom of the sample with one of the pore-fluid pumps, with a pressure of at least 2 MPa. The vacuum pump is connected to the top pore line via a transparent tube which enables us to see the fluid that has crossed the sample. Moreover, the volume injected by the fluid pumps can be monitored. A volume of fluid of at least 2 to 3 times the pore volume, at high pressure, is drained through the sample to ensure absence of air bubbles. The sample's unconfined porosity is measured prior to the installation in the cell, via the triple weight method. Porosity variations with effective pressure may eventually be deduced from the volume of fluid ejected from the sample, which can be measured with the fluid pumps.

Throughout the experimental surveys on saturated porous media, the pore fluid is maintained at a minimum pressure of 2 MPa, also limiting the presence of air bubbles. A second pair of pore-fluid pumps containing another fluid can be connected to the pore lines (Figure 2.1). Up to now, two pore-fluids have been used in rocks: glycerin and water, due to their viscosity contrast (ratio 1000:1). Since glycerin dissolves in water, the sample and the tubings will first be saturated by the glycerin.

For low permeability rocks, the saturation with glycerin can be accelerated by heating the cell, which decreases the glycerin's viscosity. Prior to the installation in the cell and the first 'dry' measurements, all the samples are generally oven dried at 80°C for at least 1 day to remove potential moisture effects.

2.6 Calibration of dispersion and attenuation

Calibration measurements of the forced-oscillation method have been performed on three standards at room temperature (20°C): gypsum, glass and plexiglass (PMMA). The gypsum is the same sample used by Pimienta et al. 2015a, 2015b for the calibration of another apparatus. The glass sample is a borosilicate glass that was used in the studies of Mallet et al. (2013, 2015). It was synthesized by the French Atomic Energy Commission (CEA) laboratory by a reproducible method, under conditions of slow cooling that prevent any crack formation. The plexiglass was provided by abaqueplast company (France).

The hydrostatic and axial forced-oscillation methods were applied at a low confining pressure of 5 MPa and of 30 MPa, the maximum pressure allowed by the piezoactuator. Consistently with uncracked media, the three calibrating sample's exhibited no dependence on confining pressure (Figure 2.5). The bulk moduli dispersion and attenuation inferred from hydrostatic oscillations are presented in Figures 2.5a and 2.5b respectively. For the pure elastic materials, there was consistently no dispersion of the bulk moduli, with constant values around 58 GPa and 44 GPa for glass and gypsum respectively, in the frequency range 0.004 to 1.3 Hz. In this frequency range, the bulk attenuation (Q_K^{-1}) for glass and gypsum can be considered negligible, although the results seem to scatter between 0 and 0.02 (Figure 2.5b). For the plexiglass, although dispersion is difficult to observe on the bulk modulus (Figure 2.5a), which is about 5 GPa, an attenuation around 0.04 was observed between 0.004 and 1.3 Hz (Figure 2.5b) with a maximum around 1 Hz.

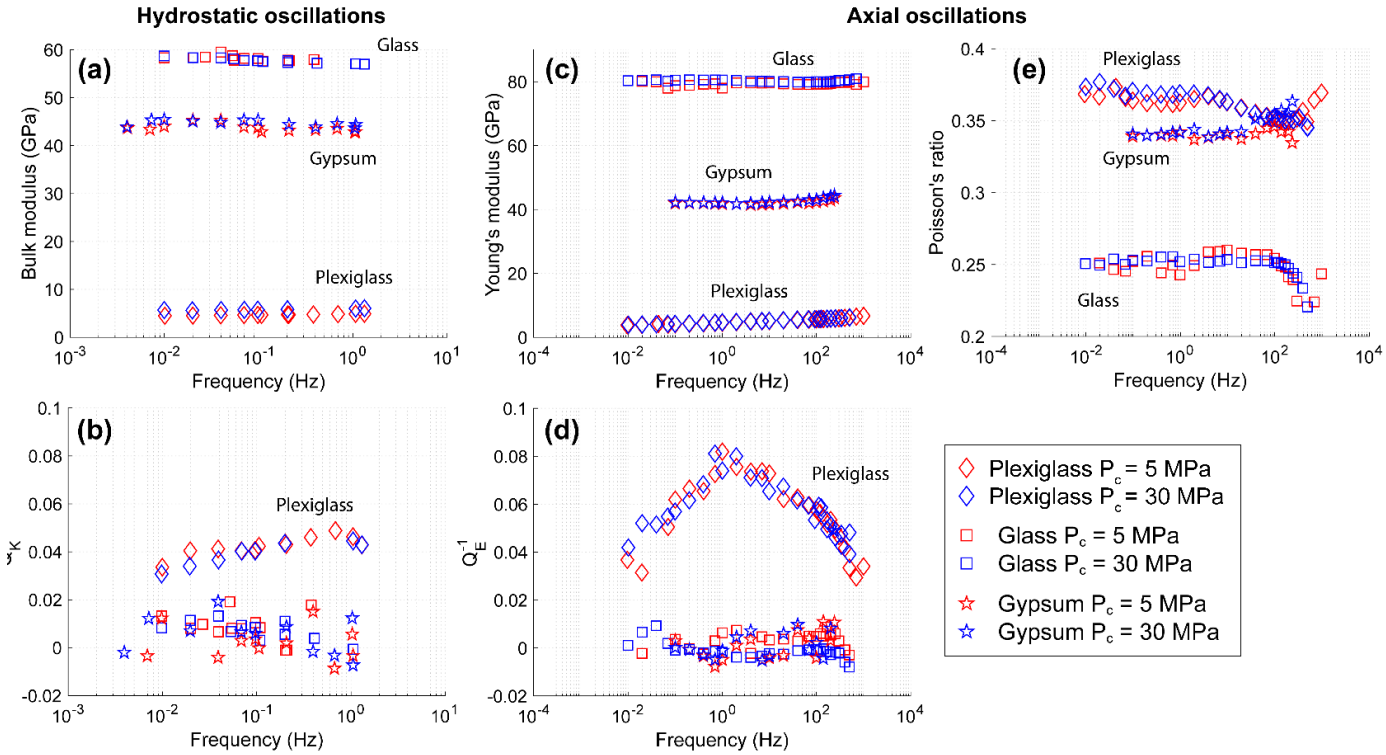

Figure 2.5: Calibration results of plexiglass (PMMA), glass and gypsum, for confining pressures 5 and 30 MPa at room temperature (20°C). Bulk modulus dispersion (a) and attenuation (b) are inferred from hydrostatic oscillations. Young's modulus dispersion (c) and attenuation (d), and Poisson's ratio dispersion (e), are inferred from axial oscillations. Relative uncertainties for* K, E, *ν are respectively 0.3%, 2%, 3% for PMMA, 2%, 5%, 6% for gypsum and 1%, 4%, 5% for glass;

The Young's modulus dispersion and attenuation inferred from the axial-stress oscillations are presented Figures 2.5c & 2.5d. For glass and gypsum, again, no dispersion of E is visible in the frequency range 0.01 Hz to 1 kHz, with constant values of 80 GPa and 42 GPa respectively (Figure 2.5c). Consistently, the related attenuation (Q_E^{-1}) is negligible, with scattered points between -0.01 and 0.01 (Figure 2.5d). However, for the plexiglass, a noticeable attenuation peak ($Q_E^{-1} = 0.08$) centered between 1 and 2 Hz was observed (Figure 2.5d), with a very low Young's modulus increasing from 2.5 GPa to 5 GPa between 0.01 Hz and 1 kHz (Figure 2.5c). This behavior is consistent with the results obtained on bulk modulus, and with previous experimental observations at room temperature on plexiglass (PMMA) (Batzle et al., 2006; Tisato and Madonna, 2012; Madonna and Tisato, 2013; Pimienta et al., 2015b).

The Poisson's ratio dispersion, deduced from the axial oscillations, is presented in Figure 2.5e. For the non-dispersive glass and gypsum samples, ν seems to be constant around 0.25 and 0.34, respectively, up to 100 Hz. At higher frequencies, the Poisson's ratio seems to abruptly diverge either up or down (Figure 2.5e). This is an error issued from the Fourier transform on the low amplitude radial strains, which decrease above 100 Hz as axial stress decreases (as seen in Figure 2.4), reaching the strain gauge's uncertainty limit. Over the frequency range of 0.01 to 100 Hz for the plexiglass, a

slight decrease with increasing frequency is observed (Figure 2.5e), as was previously observed in the study of Pimienta et al. (2016a).

Overall, these calibration results ensure the apparatus is capable of reliably measuring elastic or viscoelastic dispersion and attenuation using forced-oscillation methods up to 1.3 Hz for the bulk modulus, up to 1 kHz for Young's modulus, and up to 100 Hz for Poisson's ratio.

2.7 Controlling the undrained boundary conditions

In forced-oscillation experiments on saturated rocks, controlling the pore-fluid's boundary conditions in the sample may prove to be essential to control the wave induced fluid flow (WIFF) in and out of the sample. If the boundary conditions are drained (opened), then a dispersive transition between a drained and undrained fluid-flow regime will appear. This mechanism has been pointed out first by Dunn (1987) for radial flow out of unjacketed samples under axial-stress oscillations (no confinement) and named the "Biot-Gardner effect". In our apparatus, the samples are jacketed radially, but the mechanism may still occur axially through the endplatens and pore-fluid lines (Figure 2.1). This transition was regularly defined as the drained/undrained transition in previous studies and is a significant contributor to elastic dispersion and attenuation in broadband studies (e.g., Pimienta et al., 2015a, 2016b; Borgomano et al., 2017; Chapman et al., 2018). It bears a characteristic frequency (f_c), equal to (Cleary, 1978):

$$f_c = \frac{4kK_d}{\eta L^2}, \qquad \ldots (2.5)$$

where k is the permeability, K_d is the "drained bulk modulus", η is the dynamic viscosity of the pore-fluid and L is the length of the sample.

Closing the valves on the top and bottom pore-fluid lines (necessarily located outside the confining cell) does not achieve purely undrained conditions as small dead volumes of about 3 mL remain (purple in Figure 2.1). The storage capacity of these dead volumes are large enough to still generate a drained/undrained dispersive transition (Pimienta et al., 2016b; Borgomano et al., 2017), which may be misinterpreted as a local WIFF mechanism like squirt-flow between cracks and pores.

In the past, few studies proposed a poroelastic model to take into account these dead-volumes. Pimienta et al. (2016b) proposed a 1D poroelastic model, accounting for a vertical global flow, which solves the pressure diffusion equation accounting for different boundary conditions with the presence

of dead-volumes. The boundary conditions were then defined as "experimentally undrained" with the dead-volume as an input parameter. One can deduct from the previous model that near drained conditions can be achieved when the cumulated dead-volumes (top and bottom) are at least 10 times larger than the pore volume of the sample (Pimienta et al., 2016b), which can easily be achieved by adding the internal volumes of the fluid pumps (Borgomano et al., 2017). The model can further be extended to 3D using finite element methods to verify the possible effect of radial flow, especially near the pore lines in the endplatens, which has the main effect to shift the transition to lower frequencies (e.g. Borgomano, 2018; Sun et al., 2019).

Although the drained/undrained transition may be of interest to verify the applicability of Biot-Gassmann's equations (e.g., Borgomano et al., 2017; Yin et al., 2019), it may be problematic when investigating other dispersive mechanisms (e.g. squirt-flow), especially when the characteristic frequencies of each mechanism overlap (e.g., Pimienta et al., 2015a). In order to remove the drained/undrained effect, we developed piloted microvalves settled in the endplatens (Figure 2.1), that enable to impose either open or closed boundary conditions. The microvalves being very close to the sample, we limit the dead volume to a maximum of 20µL for each side. By default, the microvalves are opened, but can be closed by applying pressure through a pilot line (Figure 2.1).

The microvalves were first tested on a Bleurswiller sandstone, a 25% porosity Vosgian sandstone, which is composed by ~60% quartz, ~30% feldspars and ~10% clays (Fortin et al., 2006, 2007; Baud et al., 2015). The permeability was measured to be around 200 mD (2×10^{-13} m²) using Darcy flow at an effective pressure of $P_{eff} = 5$ MPa. Hydrostatic oscillations between 0.01 and 1.3 Hz were performed under oven-dry and fully-saturated conditions with pure glycerin (Figure 2.6). In the saturated case, the microvalves were kept either open or closed during the whole oscillation sequence, with very large dead volumes connected to them (>200 mL). One experiment was performed without any microvalve installed to compare with the open configuration.

From the bulk modulus dispersion and attenuation results (Figure 2.6a & 2.6b, respectively), we can clearly observe that there is no dispersion/attenuation for both the dry and the closed microvalve cases, whereas a strong dispersion is observed for the open configuration (Figure 2.6a). In the open configuration, we clearly observe that the bulk modulus at 0.01 Hz is consistent with the "dry" condition, then progressively increases to the "closed" configuration values at 1 Hz (Figure 2.6a). From Equation 5, the theoretical characteristic frequency of the drained/undrained transition was evaluated to be $f_c = 0.75$ Hz, taking $K_d = 6$ GPa, $k = 2.10^{-13}$ m², $\eta = 1$ Pa.s and $L = 8.10^{-2}$ m. This frequency is consistent with the observed transition and the center of the attenuation peak (Figure 2.6b), supporting the evidence of the drained/undrained transition. Moreover, the bulk

moduli value for both drained (6 GPa) and undrained (16 GPa) configurations are consistent with Biot-Gassmann's equations (horizontal dashed lines in Figure 2.6a), when using an skeleton modulus (solid without pores) of 39 GPa (from a Voigt-Reuss-Hill average of the mineral composition, Mavko et al., 2009), and a glycerin bulk modulus of $K_f = 4.36$ GPa.

Therefore, these microvalves enable us to suppress the drained/undrained transition and achieve pure undrained conditions regardless of the permeability of the sample. The good agreement between the open configuration results and the results without microvalves (Figure 2.6a) imply that they do not affect the connectivity of the pore lines, which is essential in order to not affect permeability measurements using the steady state flow rate method (Darcy flow).

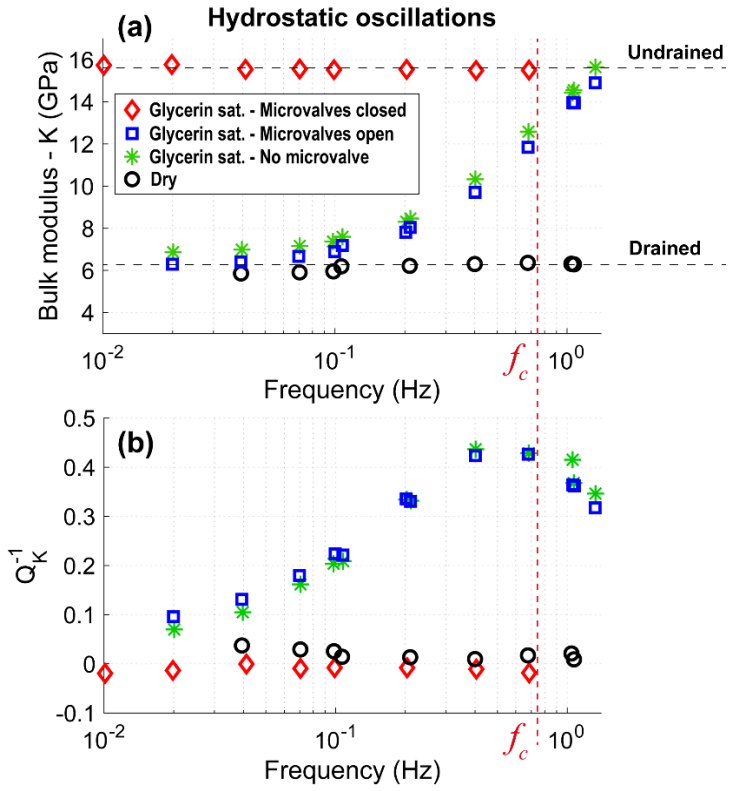

Figure 2.6: Results of bulk modulus dispersion (a) and attenuation (b) under dry and glycerin-saturated conditions from hydrostatic oscillations on a Bleurswiller sandstone at P_{eff} = 5 MPa. Relative uncertainty on* K *is around 3%. In glycerin saturated conditions, the endplatens' microvalves were either open to achieve axially drained boundary conditions, or closed to test undrained boundary conditions. The theoretical drained/undrained characteristic frequency ($f_c = 0.75$ Hz) was calculated using Equation 5. The horizontal dashed lines correspond to Biot-Gassmann's equations;

2.8 Numerical investigation of resonant frequencies

One major concern when developing dynamic oscillatory setups is the possibility of resonant frequencies disrupting the results. A simple method to verify the frequency ranges affected by the resonances of the machine can be computed through numerical solutions. Here, we used Comsol Multiphysics to model the relevant parts of the apparatus (Figure 2.7a), and simulate its dynamic response. Since we expect resonant frequencies to be in the kHz range according to the size of the apparatus, we only focused on the axial-stress oscillations performed by the piezoelectric actuator that may reach these frequencies.

The main body and piston of the triaxial cell are made out of a quenched and tempered (+QT900) 1.4418 stainless steel ($E = 200$ GPa, $\nu = 0.28$, $\rho = 7700$ kg.m^{-3}). In the axial column, the piezoelectric actuator (PZT) is made out of PIC151 piezoceramic ($E_{11} = 55$ GPa,$\nu_{12} = 0.38$, in polarized state, Fett et al., 2002). The top endplaten is again made out of stainless steel and the lower endplaten of aluminum 2017A ($E = 72.5$ GPa, $\nu = 0.33$, $\rho = 2790$ kg.m^{-3}). The piston load chamber at the top of the cell was modeled with the properties of Therminol SP mineral oil ($K = 1.9$ GPa, $G = 0$ GPa, $\rho = 898$ kg.m^{-3}). Finally, we tested 3 virtual samples with varying Young's modulus ($E_S = 9, 36, 90$ GPa) for the same Poisson's ratio ($\nu_S = 0.2$) and density ($\rho_S = 2500$ kg.m^{-3}). The materials are all considered purely elastic in the model.

The stack of pieces in the vertical column can freely expand radially, with continuous boundaries between each other (Figure 2.7a). Only the bottom of the lower endplaten is fixed. The top of the piston is radially fixed on an axially mobile surface that can compress the oil (no radial displacement). The piston slides without friction in the upper part of the cell's frame. Since the piston is auto-compensated for the confining pressure, we did not simulate the contribution of the latter, but simply added a deviatoric pre-stress in the vertical column (1.5 MPa). For the finite element calculation, a free tetrahedral mesh was applied to the whole geometry (Figure 2.7b). An oscillatory boundary load of +/- 1 MPa were simulated on the top and bottom surfaces of the piezoactuator and the displacements of all the nodes were calculated in the frequency domain. Analogous to the real experimental conditions, the sample's axial and radial strains were deduced from the nodes displacements at mid-height on the surface of the sample, averaged on a grid surface equivalent to the experimental strain gauges (6x2 mm). Similarly, the aluminum axial strains (deducing the axial stresses) are inferred from a surface grid at mid-height on the bottom endplaten.

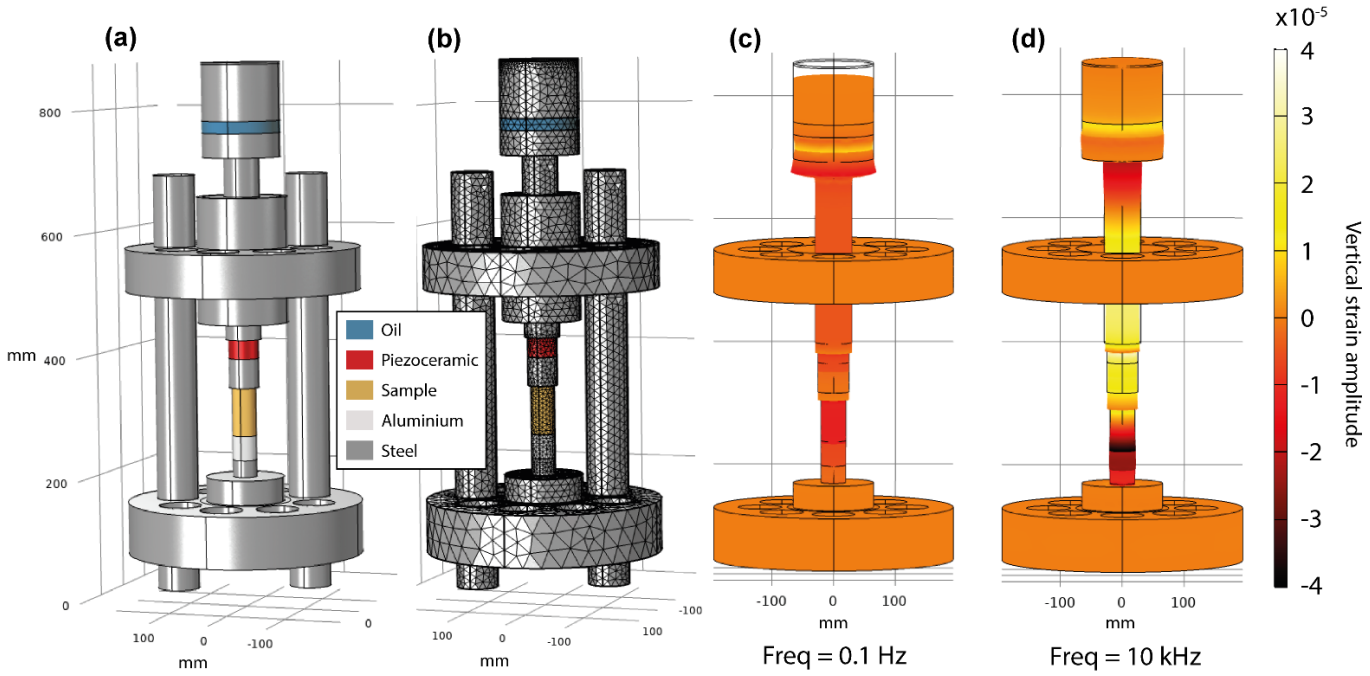

Figure 2.7: Numerical model of the experimental setup, with the definitions of materials (a) and the free tetrahedral mesh (b). The materials are all purely elastic and isotropic. The system is solved in frequency domain for axial oscillations of amplitude 0.2 MPa, and the maximum vertical strains are represented here for 0.1 Hz (c) and 10 kHz (d) (illustrated here for the sample with E_S = 36 GPa);

The frequency range of the simulations goes from 10^{-5} to 10^{4} Hz, and were applied to the three samples of varying Young's modulus (E_s = 9, 36, 90 GPa). The strain amplitude results, inferred from the virtual strain gauges, are presented Figure 2.8a. Negative values represent compressive strains. The strain amplitudes are not affected by resonances for frequencies up to 600 Hz. It seems that the axial strains of the sample start to diverge at slightly lower frequencies than the radial or aluminum strains (Figure 2.8a). Moreover, the stiffening of the sample would seem to increase slightly the frequency upon which the phenomenon appears.

When converted to Young's modulus dispersion ($E = (\varepsilon_{alu}/\varepsilon_{ax})E_{alu}$) and attenuation Q_E^{-1} (using Kramers-Kronig relationships, (O'Donnell et al., 1981)), and Poisson's ratio ($\nu = -\varepsilon_{rad}/\varepsilon_{ax}$) as would be measured experimentally in the cell (Figure 2.8), it seems that E becomes significantly affected only above 2 kHz, while ν may start to diverge at 1 kHz, but insignificantly in terms of absolute value. The moduli result at low frequency are consistent with the sample's input (Figures 2.8b & 2.8d). Although the materials used in the model are purely elastic, the resonances above 3 kHz seem to result in an apparent attenuation on E, with potential increasing or decreasing dispersion of E, which may appear non-physical for purely elastic materials. This is related to our experimental configuration and our method to calculate the different moduli. The non-homogenous stress field in the vertical column at a resonance frequency (Figure 2.7d) induces an apparent phase shift between

the strains on the sample and the strains on the aluminum endplaten (used as the axial stress reference), resulting in an apparent dispersion/attenuation of the sample's Young's modulus. Therefore, it is highly probable that changing the vertical distance between the sample's and aluminum's strain gauges will affect the apparent dispersion/attenuation results of E (Figures 2.8b & 2.8c). This also explains why Poisson's ratio (Figure 2.8d) is much less affected (in absolute value) since the radial and axial strain gauges nearly coincide.

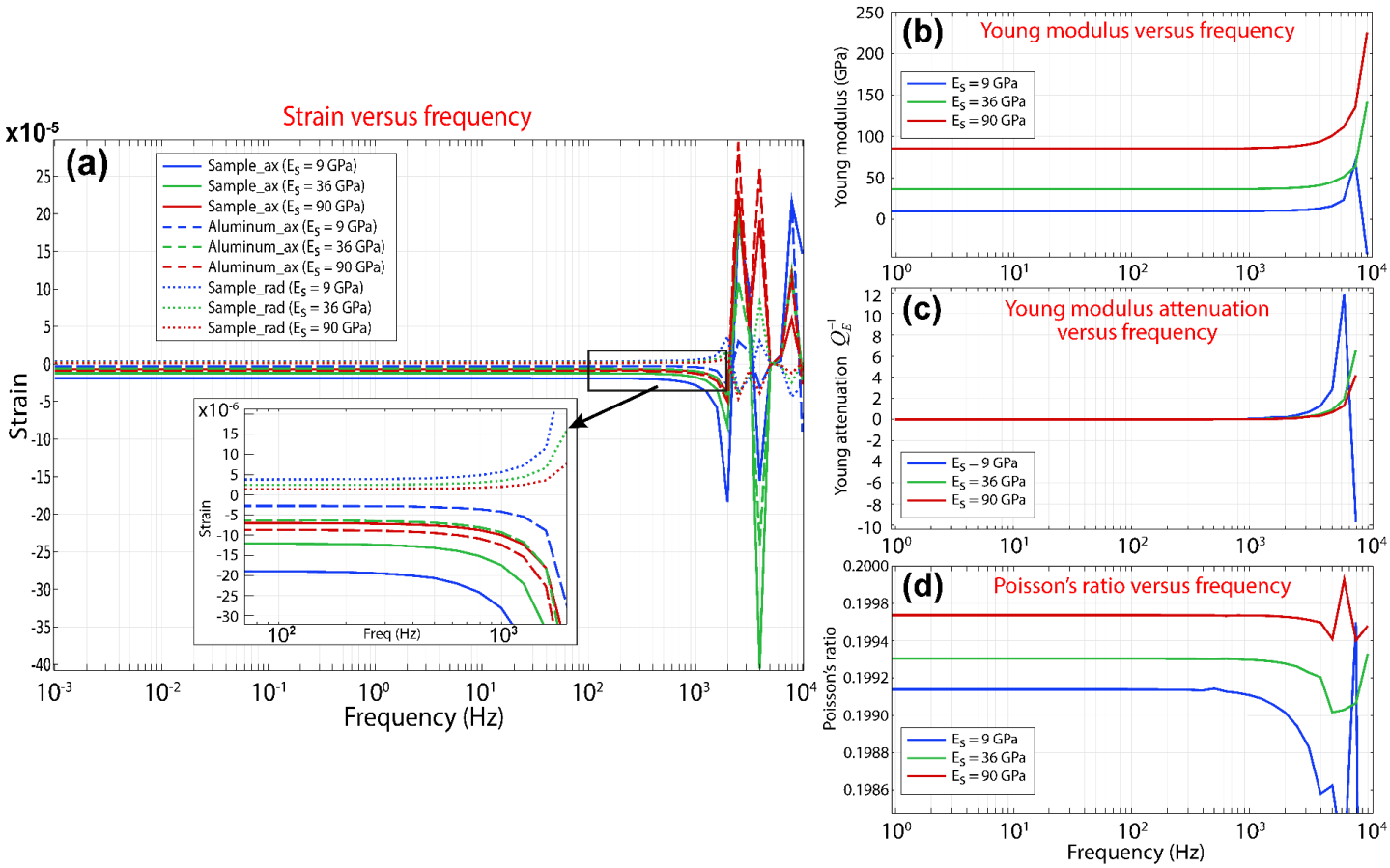

Figure 2.8: (a) Results of the numerical simulation for axial, radial and aluminum endplaten strains (positions shown in Figure 2.2); and the induced (b) Young's modulus, (c) Young attenuation Q_E^{-1} and (d) Poisson's ratio as function of frequency, as would be interpreted from the strain gauges. Simulations were performed here for 3 samples of Young's moduli E_s = 9, 36, 90 GPa, Poisson's ratio $\nu_S = 0.2$ and length L = 80 mm;

Although the Poisson's ratio of the glass standard (Figure 2.5e) seemed to diverge and decrease in the similar manner as the model (Figure 2.8c), we do not believe it to be related to a resonance problem but due to the lower-amplitude limit of the radial strain gauges, since for stiff materials the resonances seem to affect higher frequencies (2-3 kHz, Figure 2.8c) and with negligible amplitude

for ν. Nevertheless, the numerical model suggests that the apparatus should not be affected by resonance frequencies below 1 kHz, allowing use of the forced-oscillation method up to that frequency. However, such triaxial cell designs will inevitably be affected by resonant frequencies above 1 kHz.

2.9 Applications

The apparatus was first employed on fluid-saturated low-permeability limestones (pure calcitic), prior to the installation of the microvalves (Borgomano et al., 2019b). The drained/undrained transitions were at relatively low frequency allowing study of potentially higher frequency squirt-flow effects. Similarly to the results on a dual-porosity oolitic limestone (Borgomano et al., 2017), little or no squirt-flow dispersion was observed for the Indiana limestone (bioclastic & cemented) or a Rustrel limestone (rudist grainstone & cemented). However, thermal cracking on the Indiana sample generated sufficiently low aspect ratio cracks, mainly located in the intergranular cement, to generate squirt-flow dispersion affecting seismic frequencies (~100 Hz)(Borgomano et al., 2019a). In addition, a coquina sample (detritical), cored from a deep offshore well, seemed to present some squirt-flow dispersion at sonic frequencies (~10 kHz). The main interpretation proposed for this sample was that, similarly to sandstones, the squirt-flow originated from the uncemented grain-to-grain contacts, as opposed to the cracked Indiana sample(Borgomano et al., 2019b). Consistently with "crack" closure, the squirt-flow phenomenon disappeared with increasing effective pressure above 15-20 MPa for both latter samples. For all samples, drained to undrained transitions were well in accordance with Biot-Gassmann's equations.

Forced-oscillation measurements were then performed on a glycerin-saturated Berea sandstone (Chapman et al., 2018), again to investigate the squirt-flow mechanism, and compare with the dispersion/attenuation results on a similar Berea sandstone in another apparatus (Mikhaltsevitch et al., 2016). This comparison under similar pressure conditions confirmed the very high sensitivity of the squirt-flow mechanism to variations in the characteristic aspect ratios of the cracks, as the dispersive frequency ranges appeared quite different in both these studies (Mikhaltsevitch et al., 2016; Chapman et al., 2018).

More recently, using the benefit of the drained/undrained transition, fluid substitution and shear weakening at seismic frequencies were investigated in a clay-bearing sandstone (Yin et al., 2019). It was shown that the shear-weakening in water-saturated conditions, due to the reduction in surface free energy in the clays, affected mainly the shear modulus at seismic frequencies (<100 Hz), while

seemingly not affecting the ultrasonic results (1 MHz).The observation at high frequency (1 MHz) was interpreted as a combination of shear weakening due to clays that decreases *G* over the full frequency range, and squirt-flow in cracks that re-increases *G* at high frequency (Yin et al., 2019).

2.10 Conclusion

A new apparatus was developed to perform both hydrostatic- and axial-stress oscillations on saturated rock samples, enabling to characterize the dispersion and attenuation of the elastic moduli over a large frequency range (0.004 Hz to 1 kHz). The cylindrical samples can have selectively drained or undrained boundary conditions at the top and bottom with the use of microvalves, while the lateral surface is jacketed. The various conditions were tested on a porous sandstone, demonstrating the effect of the microvalves on the drained/undrained fluid-flow regimes. The apparatus has been successfully tested on known elastic and viscoelastic materials, such as glass, gypsum and plexiglass (PMMA). The complex Young's modulus can safely be characterized up to 1 kHz, while the Poisson's ratio measurements seems to be reliable up to 100 Hz, using axial-stress oscillations. The complex bulk modulus, inferred from hydrostatic oscillations, can reliably be measured up to 1.3 Hz. The dynamic limits of the apparatus were investigated through a numerical model, showing that frequencies above 1 kHz will undoubtedly be affected by resonance.

3. An experimental study of seismic wave attenuation and dispersion in fluid saturated homogenous and heterogeneous pre salt carbonates

3.1 Introduction

Compressional and shear wave velocities (v_p, v_s), in fluid saturated porous media, are dispersive from low frequency (seismic – 0.1 to 1 Hz), medium frequency (sonic log – 1 to 10 kHz) to high frequency (ultrasonic – 1 MHz) measurements. There are multiple reasons for the dispersion of the elastic modulus, such as partial saturation (King et al., 2000; Pride et al. 2004; Müller et al., 2010) , the presence of multiple pore fluids (White, 1975; Johnson, 2001; Masson and Pride, 2011; Quintal, 2012; Quintal et al., 2012), inertial effects as described by Biot at higher frequency regimes (Biot, 1956), pore fluid pressure diffusion (FPD) mechanisms which are typically categorized by mesoscopic or microscopic heterogeneities (Batzle et al.,2006 ; Müller et al.,2010 ; Sarout et al.,2012) ,as well as, dispersion which can arise due to the scattering of elastic waves whose wave length are close to the size of the heterogeneities (Morlet et al., 1982; Murai et al., 1995; Gurevich et al., 1998).

At the microscopic scale, the microporous structure can be thought of as intact, with thin compliant pores and stiff round pores interspersed throughout. At higher frequencies, elastic wave propagation does not allow time for the fluid in the thin compliant pores to flow to the stiff round pores, creating none uniform pore fluid pressures in the representative elementary volume (REV), with high fluid pressure in the compliant pores and lower pressure in the stiff pores (O'Connell and Budiansky, 1977; Dvorkin et al.,1995; Gurevich et al.,2010). The higher pressure in the compliant pores has an effect of increasing the overall stiffness of the sample. Experimentally, this phenomenon has been shown to have a larger effect at low effective pressures as the micro cracks are open (Adelinet et al., 2010).

Mesoscopic FPD is analogous to squirt flow, at a larger scale, in terms of having zones of differing fluid mobility ($M = k/\eta$) (Batzle et al.,2006), which lead to the creation of none uniform pore fluid pressure profiles. These heterogeneous zones can be created due to partial saturation (White, 1975; Lee and Collet, 2009; Adam et al., 2009), due to fractures (Parra, 2000; Brajanovski et al. 2010;

Amalokwu et al.,2014), or due to samples with distinct zones with varying permeability, porosity and elastic properties (Brajanovski et al.,2005; Rubino and Holliger, 2012).

Other FPD mechanisms are related to experimental setups, such as the drained to undrained cut-off frequency that was shown by Pimienta et al. (2016b) to happen between the saturated sample and dead volume, which was well described by a simple 1D analytical model. A setup, using innovative microvalves, is used in this work to remove the dead volume, creating undrained boundary conditions, and ensuring that the attenuation measured is not due to fluid flow between the sample and the dead volume. Borgomano et al. (2020) showed that with these microvalves, undrained elastic moduli are directly reached, as the mass pore fluid in the sample is kept constant; as a consequence, in these experiments the drained-undrained critical frequency does not exist.

In the experiments presented in this paper, carbonate samples were chosen to investigate mesoscopic and microscopic FPD mechanisms, in order to try to better understand the key characteristics which define these mechanisms. Carbonates have heterogeneous pore types and complex microstructures (Lucia, 1995), which makes them ideal to study these mechanisms.

Three different carbonate samples were tested at varying effective pressures. The elastic properties, at a large apparent frequency range ($7\ 10^{-2}$ to $10^{5} – 10^{6} – 5.5\ 10^{8}$ Hz), were measured in a triaxial cell using hydrostatic and axial stress oscillations. Ultrasonic sensors were also used to deduce the p- and s-wave ultrasonic velocities. Two distinct attenuation peaks were observed, which were attributed to mesoscopic and microscopic FPD. These two transitions where interpreted in the light of analytical and numerical models. Finally, our experimental data is compared to borehole data that was available.

The three carbonate samples that were tested in this study come from a pre salt formation. They will be referred to as granular #1, #2 and shrub #1. The granular samples were cored from the same well and have similar chemical compositions, mostly made up of calcite, with some pockets of quartz (table 3.1), which was measured using X-ray Powder Diffraction (XRD). Shrub 1 comes from a second well and is composed predominantly of calcite and quartz, with some dolomite and to a lesser extent clay (table 3.1). The porosity of the samples was measured using the triple weight method and was in the range of 0.14 to 0.17 (table 3.1). The permeability was measured using a nitrogen gas permeameter, with a correction taking into account Klinkenberg gas slippage, and was in the range of 1 to 16 mD. Details of the sample properties are listed in table 3.1.

Samples	granular 1	granular 2	shrub 1
Porosity	0.14	0.17	0.15
Permeability (m^2)	$4\ 10^{-15}$	$16\ 10^{-15}$	$1\ 10^{-15}$
Dry density (kg/m^3)	2247.18	2177.92	2223.61
Quartz (% of Mineral)	4.7	2.2	38.3
Calcite (% of Mineral)	95.3	97.8	45.5
Dolomite (% of Mineral)	0.0	0.0	15.2
Wetclay (% of Mineral)	0.0	0.0	1.1
Mineral bulk (K_{min})	75.1	76.1	62.4

Table 3.1: Three carbonate samples properties and chemical composition;

Figure 3.1 shows the thin sections of all three samples. Granular #1 shows sub rounded to rounded carbonate grains of moderate sorting, intergranular porosity and can be defined as *spherulitic grainstone*. Granular #2 shows sparitic carbonate grains with some grains fused, again of moderate sorting, and can be defined as *spherulitic grainstone*. Shrub #1 has rounded sparitic carbonate grains with sizes ranging from ~200 μm to up to 1 -2 mm, together with quartz grain and dolomite crystals and can be defined as *spherulitic grainstone with quartz grains and dolomite*.

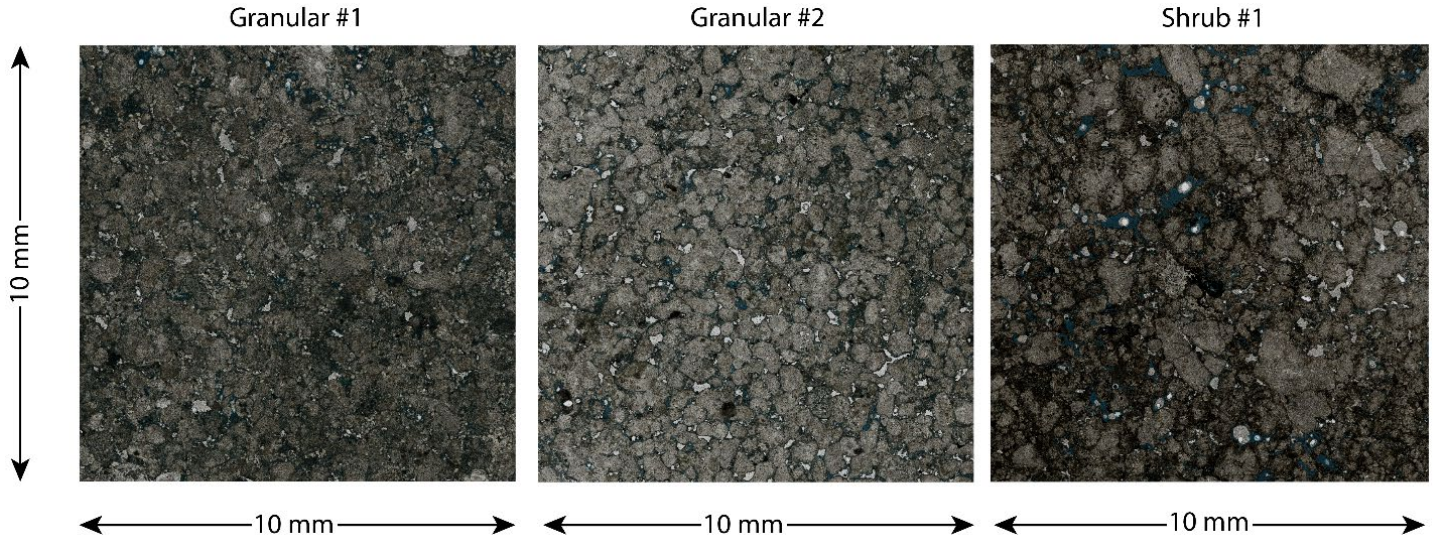

Figure 3.1: Thin section (1 cm X 1cm) of three carbonate samples studied;

Figure 3.2 shows the three samples CT scan put into greyscale and binarized (rock matrix versus porosity) using a threshold which was chosen to have a porosity closest to the value calculated using the triple weight method. Granular #1 shows a relatively homogeneous distribution of the porosity. Granular #2 shows a much more heterogeneous porosity distribution with higher porosity near the top of the sample. Shrub #1 shows a heterogeneous porosity distribution, with a high porosity near the lower middle part of the sample.

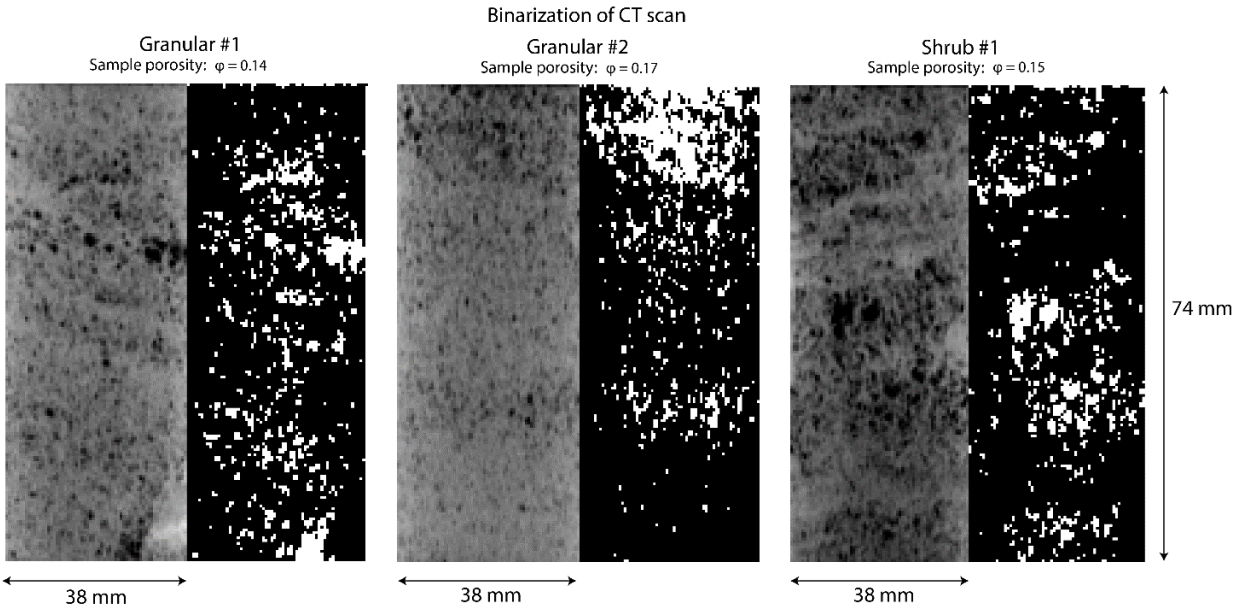

Figure 3.2: Grey scale CT scans (left) with binarized picture (right) side-by-side;

Figure 3.3 shows the evolution of the p- and s-wave ultrasonic velocities versus pressure for the three samples. For the three samples, the velocities increase as pre-existing cracks (or compliant pores) are closed (Walsh, 1965). The ultrasonic velocities reach a plateau at a pressure of 25 MPa. The closure pressure at which cracks closed is $P_{close} = \frac{\pi \xi E}{4(1-\nu^2)}$ (Walsh 1965; Jaeger, 2009) where E is the Young modulus (GPa), ξ the mean crack aspect ratio and ν the Poisson's ratio. Assuming ν = 0.3, this leads to $P_{close} \simeq 0.86\xi E$, assuming E~50 GPa, this lead to mean crack aspect 0.7-0.8 10^{-3} in agreement with previous preexisting crack aspect ratio reported in the literature on carbonate rocks (Baud et al., 2000; Nicolas et al., 2016; Panza et al., 2019).

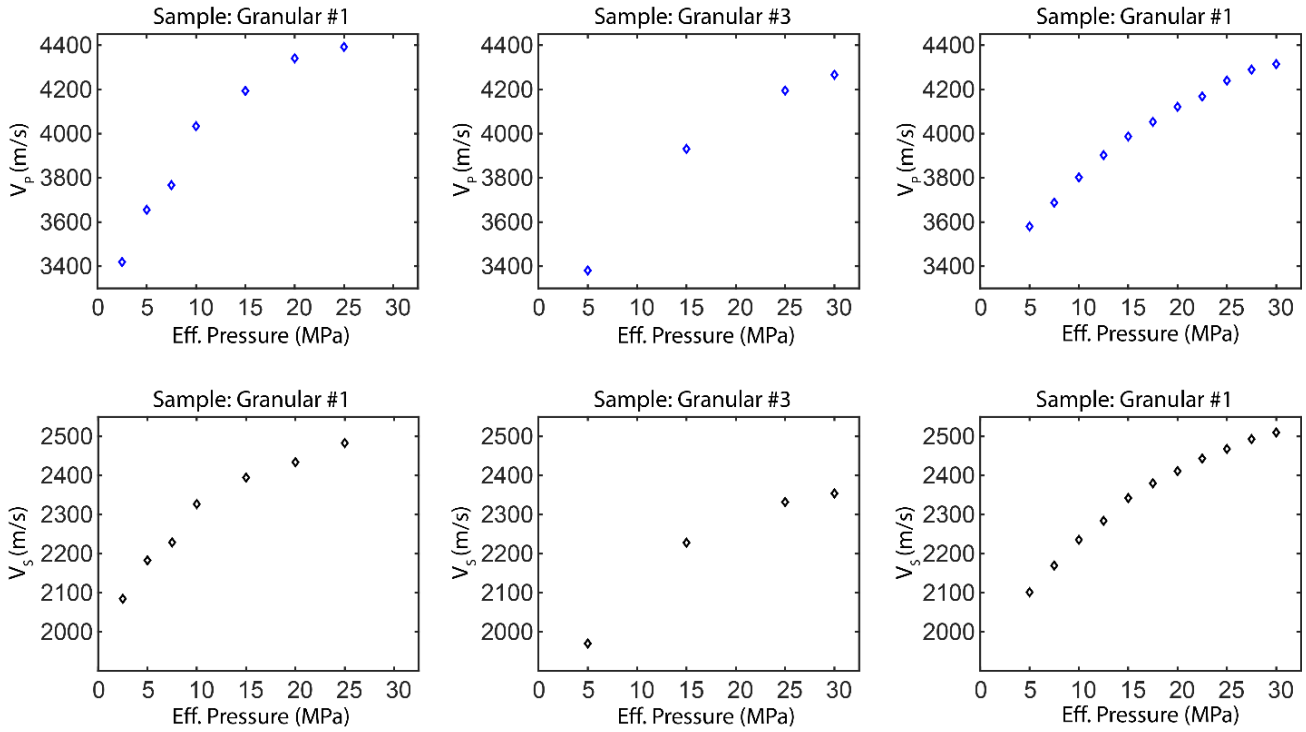

Figure 3.3: P- and s-wave velocities of all three samples, in dry conditions, dependent on effective pressure;

3.2 Methodology

A TOP Industries triaxial cell, outfitted with four pumps, was used for all experimental data presented in this paper. Two pumps are oil filled and are used to control the cell pressure and axial piston, respectively. The other two pumps are Quizix (QX1500HC model) dual piston precision pumps, used to control pore pressure at the inlet and outlet of the sample, one of these is used for glycerin, the other for brine. Unique to this setup are microvalves which reduce dead volume to ~ 20 µl and allow undrained conditions to be reached even at low frequencies (Borgomano et al., 2020).

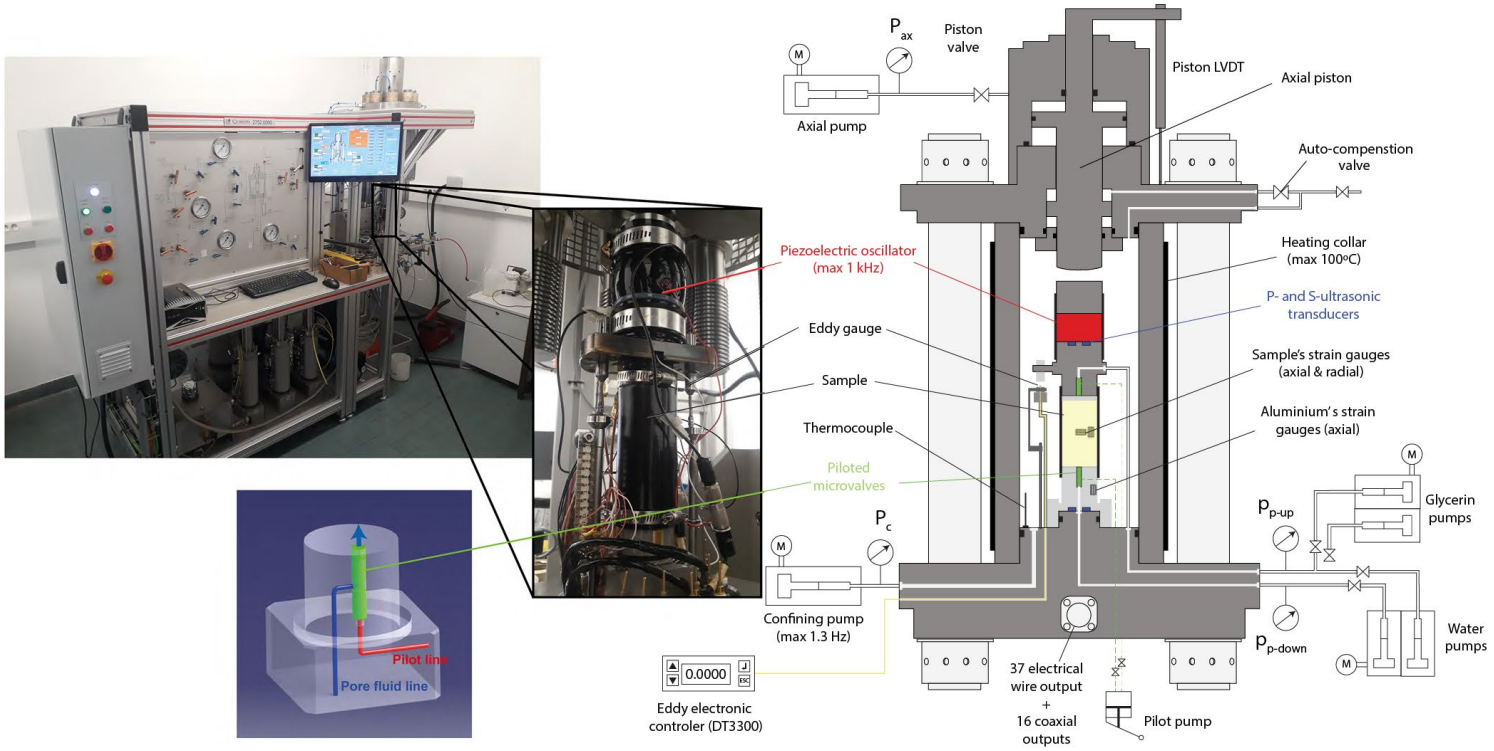

Figure 3.4: Picture of triaxial cell (left); Schematic of microvalve (bottom left); Jacketed sample (middle); Schematic of triaxial cell; [adapted from Borgomano et al. (2020)];

3.2.1 Sample preparation

The cylindrical samples are machined to a length of 74 mm and a diameter of 38 mm. Four orthogonal biaxial strain gauge pairs are epoxied at 90^0 from each other at mid height (figure 3.5). The strain gauge pairs were acquired from Tokyo Measuring Instruments Lab and are referenced as type FCB-5-350-11-F. The strain gauge pairs have an axial and radial component, with a resistance of 350 Ω and have a gauge length of 5 mm. A neoprene jacket is used to isolate the sample from the pressurized oil in the cell.

Two pore fluids were used for the experiments. The first is 98% glycerin with product specification as Glycérol ≥98%, GPR RECTAPUR® provided by VWR Chemicals. The second is a brine mixture prepared with distilled water (1L) and a mixture of sodium chloride (222 g), calcium chloride dihydrate (20.7 g), potassium chloride (8.7g) and magnesium chloride hexahydrate (4.7 g). The sample was first tested in glycerin saturated conditions, then in brine saturated conditions. Knowing that the brine mixture has a salt concentration of around 250 000 PPM, the dynamic viscosity and

bulk modulus of the brine mixture can be estimated as 0.0015 Pa*s and 3.5 GPa, respectively, following the work by Batzle and Wang (1992). As the glycerin is hydrophilic, the dynamic viscosity was calculated knowing the permeability of the sample and by conducting a continuous flow rate permeability test. The dynamic viscosity of the glycerin was found to be 0.825 Pa*s, with the bulk modulus at 4.3 GPa.

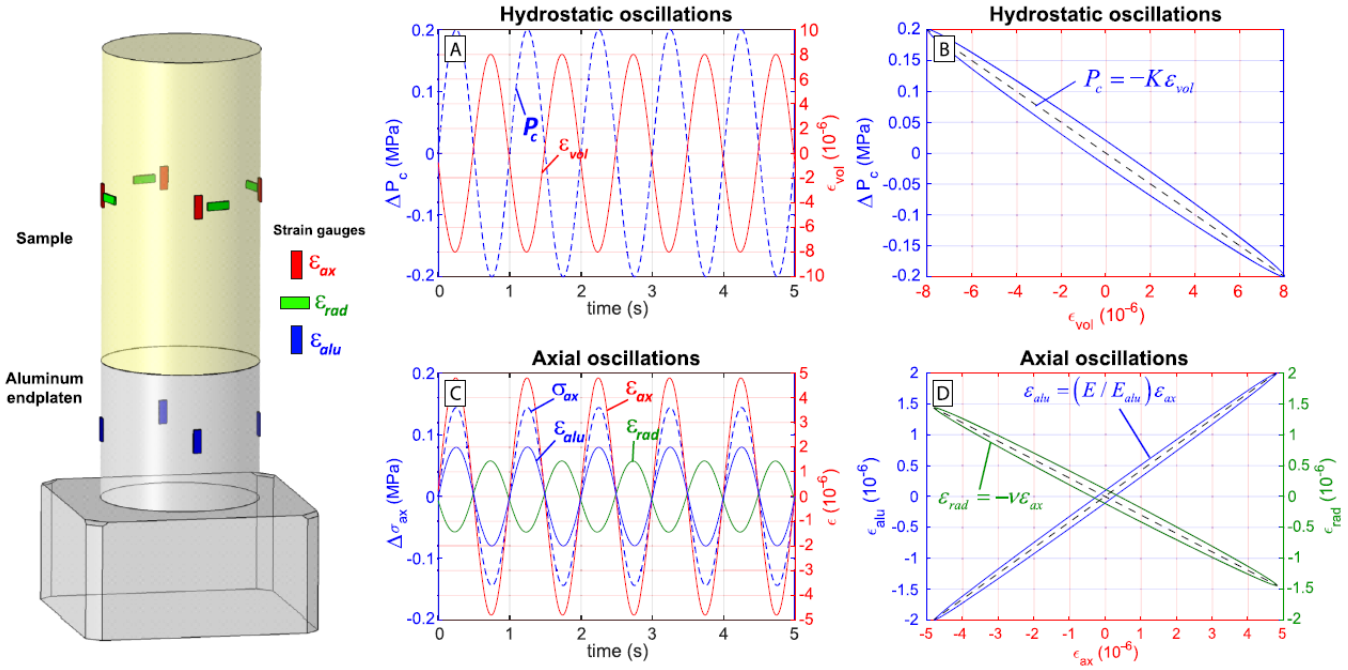

Figure 3.5: Strain gauge positions (left) and typical stress-strain recordings of hydrostatic[(a) and (b)] and axial [(c) and (d)] oscillations (around mean values) on a viscoelastic material. The strains (ε_{ax}, ε_{rad}, ε_{alu}) are each average from four strain gauges around the circumference of the sample/endplaten at mid-height. The axial-stress oscillation ($\Delta\sigma_{ax}$) is deduced from the aluminum endplaten axial strain (ε_{alu}) and is calibrated Young's modulus of 78 GPa [taken from Borgomano et al. (2020)];

3.2.2 Elastic property measurements

The triaxial cell is outfitted to measure three independent sets of elastic data on the samples at different frequency ranges. The first is a hydrostatic-stress oscillation test, the second is an axial-stress oscillation test and the third is an ultrasonic measurement test. When a sample is brought to required effective conditions, all three tests are completed to explore the effect the whole frequency range has on the elastic properties of the sample.

3.2.2.1 Hydrostatic oscillations

The hydrostatic oscillation test uses the cell pressure pump that controls the confining pressure of the sample. The cell pressure pump can oscillate around a mean value at a frequency of 0.007 to 1.3 Hz with a magnitude of 0.2 MPa to ensure that the strain is within the linear elastic range (ε ~ 10^{-6}) (Winkler and Murphy III, 1995). The confining stress is measured using a pressure sensor with a precision of 0.001 MPa. The volumetric strain is calculated as $2\varepsilon_{rad} + \varepsilon_{axial}$, where ε_{rad} and ε_{axial} are the mean values of all strain gauges glued at mid-height on the sample in the axial and radial directions, respectively (figure 3.5 – A&B). The bulk modulus is calculated using equation (3.1), where $-\Delta P_c$ is the magnitude of the effective confining pressure , ε_{vol} is the induced volumetric strain and K_{Hydro} is the bulk modulus.

$$K_{Hydro} = \frac{\Delta P_c}{\varepsilon_{vol}} \quad \ldots (3.1)$$

The effective pressure, ΔP_c, is defined by the difference between the cell pressure and the pore pressure in the sample. Using a MATLAB program, fast fourier transforms (FFTs) are used to determine the pressure and strain amplitude for each signal and averaged over all strain gauges for the volumetric strain.

3.2.2.2 Axial Oscillations

For a given confining pressure, the axial piston is put in contact with the sample column with a small deviatoric stress (<2 MPa), applied to ensure contact. Within the sample column, there is a piezoelectric actuator that induces an oscillatory axial stress (figure 3.5). The frequency range is between 10^{-2} and 10^{3} Hz. The magnitude of the axial stress oscillation is then computed using the strain gauges installed in the aluminum (AU4G) bottom cap, the known elastic modulus ($E_{alu(AU4G)}$ = 72 GPa), and:

$$\sigma_{axial} = E^{alu}{\varepsilon_{axial}}^{alu} \quad . \quad \ldots (3.2)$$

Using the axial stress inferred from equation 3.2 and the strain measured on the sample the elastic Young's modulus and Poisson's ratio of the sample can be calculated using:

$E = \frac{\sigma_{axial}}{\varepsilon_{axial}}$ and $\nu = -\frac{\varepsilon_{radial}}{\varepsilon_{axial}}$. . . . (3.3)

The samples are placed so that the strain gauges on the sample and the aluminum bottom cap are aligned axially. FFTs are used to determine the axial stress and strain.

The bulk and shear modulus can be estimated assuming the samples are isotropic and using:

$K_{axial} = \frac{E}{3(1-2\nu)}$ and $G_{axial} = \frac{E}{2(1+\nu)}$. . . . (3.4)

K_{axial} (equation 3.4) and K_{hydro} (equation 3.1) are then compared to each other and should match if the sample is isotropic.

3.2.2.3 Ultrasonics

Two ultrasonic sensors (p-wave and s-wave) are installed in the bottom end platen and top end platen (see figure 3.5). The eigen frequency of the sensor is 10^6 Hz. One of these is active and sends an ultrasonic pulse (Birch, 1960). The other is passive and receives the pulse. The time it takes for the signal to go from the active to passive ultrasonic ceramic is then determined by analyzing the signal and handpicking the arrival time. The travel time in the top and bottom cap are constant, measured using a calibration sample and subtracted from total travel time of the waves. Using the travel time of the ultrasonic wave and the length of the sample, the p- and s-wave velocity is calculated (V=L/Δt). The high frequency bulk (K_{HF}) and shear moduli (G_{HF}) are obtained using:

$K_{HF} = \rho\left({V_p}^2 - \frac{4}{3}{V_s}^2\right)$ and $G_{HF} = \rho {V_s}^2$, . . . (3.5)

where ρ is the density of the medium, V_p and V_s are the p-wave and shear wave velocities, respectively.

3.2.3 Apparent frequency

The frequency band that can *directly* be studied in the triaxial cell used in this paper ranges from 10^{-2} to 10^3 Hz and 10^6 Hz. However, a larger spectrum can be reached when studying specific mechanisms which are affected due to fluid pressure diffusion, using an apparent frequency method (Batzle et al., 2006; Borgomano et al., 2017). The specific cut-off frequencies of interest are directly correlated to the dynamic viscosity of the pore fluid. An example of these mechanisms is

squirt flow characterized by the cut-off frequency f_{sq}(equation 3.6) (O'Connell and Budiansky, 1977) where, ξ is the aspect ratio of the crack (aperture over diameter of a penny shape crack), K_m is the bulk modulus of the matrix and η is the dynamic viscosity of the pore fluid.

$$f_{sq} = \frac{\xi^3 K_m}{\eta} \quad \ldots (3.6)$$

When using different pore fluids, only the dynamic viscosity changes. Therefore, the apparent frequency can be expanded by increasing or decreasing the pore fluids dynamic viscosity. In this case higher frequencies are sought, so glycerin is used which has a much higher dynamic viscosity than water. The apparent frequency f_f^* can be calculated as :

$$f^*{}_f = f\frac{\eta_f}{\eta_0} \quad \ldots (3.7)$$

where, η_f is the dynamic viscosity of glycerin and η_0 is the dynamic viscosity of brine.

In this paper, dry and brine saturated data will be plotted as function of frequency, whereas glycerin data will be plotted as a function apparent frequency relative to brine.

3.2.4 Dispersion and Attenuation (Q^{-1})

In the case of porous rocks, the skeleton of the rock itself is none dispersive. However, the pore fluid diffusion induced by a change in the stress field is time-dependent. This can cause dissipation of elastic energy within the sample, similar to that of the rheology of a viscoelastic material (O'Connell and Budiansky, 1977). This anelastic behavior is highlighted in figures 3.5 B and D, where the stress-strain curve forms an ellipse, which represents the energy lost. This attenuation can be characterized by calculating the phase shift between the stress and the strain, when expressed as a complex stress $\bar{\sigma} = \sigma e^{i(2\pi f t + \phi_\sigma)}$ and complex strain $\bar{\varepsilon} = \varepsilon e^{i(2\pi f t + \phi_\varepsilon)}$ for a dynamic oscillation of frequency f, where ϕ_σ and ϕ_ε are the stress and strain phases.

The stress is related to the strain through its complex modulus $\bar{M}$.

$$\bar{\sigma} = \bar{M}\bar{\varepsilon} \quad \ldots (3.8)$$

The attenuation factor ${Q_M}^{-1}$ of modulus $\bar{M}$ is then defined as follows (O'Connell and Budiansky, 1978):

$$Q_M{}^{-1} = \frac{Im(\bar{M})}{Re(\bar{M})} = \frac{Im(\bar{\sigma}/\bar{\varepsilon})}{Re(\bar{\sigma}/\bar{\varepsilon})} = \tan(\phi_\sigma - \phi_\varepsilon) \quad \ldots (3.9)$$

To calculate the $Q_M{}^{-1}$, fast Fourier transforms (FFTs) were applied, using MATLAB, to the stress and strain curves to extract the phases of each. Using equations 3.1, 3.3, 3.4 and 3.9, the attenuation of the different elastic moduli can be calculated as:

$$Q_{K_{hyd}}{}^{-1} = \tan(\phi_{-\Delta P_c} - \phi_{\varepsilon_{vol}}), \quad \ldots (3.10)$$

$$Q_E{}^{-1} = \tan(\phi_{\sigma_{ax}} - \phi_{\varepsilon_{ax}}), \qquad Q_\nu{}^{-1} = \tan(\phi_{\varepsilon_{ax}} - \phi_{\varepsilon_{rad}}), \quad \ldots (3.11)$$

$$Q_{K_{ax}}{}^{-1} = \tan(\phi_{\sigma_{ax}} - \phi_{\varepsilon_{ax}+2\varepsilon_{rad}}) \text{ and } Q_{G_{ax}}{}^{-1} = \tan(\phi_{\sigma_{ax}} - \phi_{\varepsilon_{ax}-\varepsilon_{rad}}) \quad \ldots (3.12)$$

It must be underlined that equation 3.12 is only valid assuming an isotropic sample.

Two other methods can be used to extract the attenuation. The first is fitting sine functions through the stress and strain to extract phase angles manually. While the second calculates the dissipative elastic energy using the stress-strain curve to compute the area of the ellipse (fig 4) which represents the energy lost per cycle. While all methods can be valid. The analysis using FFTs is robust, straightforward and was used for this paper.

3.2.5 Uncertainties

For the elastic properties and ultrasonic measurements, the uncertainty is calculated using relative uncertainty and assuming a normal distribution. For the attenuation of the elastic properties, the standard deviation is calculated in dry conditions assuming that the attenuation in dry conditions fits a log linear curve.

3.2.5.1 Hydrostatic Oscillation Error

For the hydrostatic oscillations, the relative uncertainty of the bulk modulus ($\delta K_{hyd}/K_{hyd}$) is dependent on the volumetric strain uncertainty ($\delta\varepsilon_v$) and the pressure measurements uncertainty (δP). The relative uncertainty can then be calculated using:

$$\frac{\delta K_{hyd}}{K_{hyd}} = \frac{\delta P}{P} + \frac{\delta\varepsilon_v}{\varepsilon_v} \ . \quad \ldots (3.13)$$

For the pressure measurement uncertainty, the pressure transducer that is used has a resolution of δP = 0.001 MPa, with the amplitude of the cell pressure amplitude being around 0.2 MPa. The relative uncertainty due to the pressure ($\frac{\delta P}{P}$) is calculated to be 0.005, which is negligible. The uncertainty for the volumetric strain is measured by adding the relative uncertainty of the axial ($\frac{\delta \varepsilon_{ax}}{\varepsilon_{ax}}$) and radial ($\frac{\delta \varepsilon_{r}}{\varepsilon_{r}}$) strain measurements. Oscillations are repeated at least 10 times per test and the standard deviation and mean is calculated by using a sample size of 5 tests. In dry conditions, for sample granular #1, at f = 0.04 Hz and P_{diff} = 15 MPa, the mean of the axial strain gauges is 11.72 $\mu m/m$ with a standard deviation (S_n) of 0.54 $\mu m/m$, which gives a relative uncertainty of 2.1% for the axial strain. The relative uncertainty for the radial strain gauge is found to be 2.9%. A 5.5 % relative uncertainty is found for the bulk modulus which gives a standard deviation of 1 GPa on the bulk modulus.

Note that the amplitudes of the different strain gauges glued at different location do vary due to small heterogeneities in the sample as well as the different quality of contact between the sample and the strain gauge, which is why an average of these are used and this is assumed to represent the whole sample.

3.2.5.2 Axial Oscillation Error

For the axial oscillations, the relative uncertainty for the elastic properties are calculated as follows:

$$\frac{\delta E}{E} = \frac{\delta \varepsilon_{alu}}{\varepsilon_{alu}} + \frac{\delta \varepsilon_{ax}}{\varepsilon_{ax}}, \frac{\delta \nu}{\nu} = \frac{\delta \varepsilon_{rad}}{\varepsilon_{rad}} + \frac{\delta \varepsilon_{ax}}{\varepsilon_{ax}}, \frac{\delta K_{ax}}{K_{ax}} = \frac{\delta \varepsilon_{rad}}{\varepsilon_{rad}} + \frac{\delta \varepsilon_{ax}}{\varepsilon_{ax}} \text{ and } \frac{\delta G}{G} = \frac{\delta \varepsilon_{alu}}{\varepsilon_{alu}} + \frac{\delta \varepsilon_{rad}}{\varepsilon_{rad}} \ . \qquad \ldots (3.14)$$

The relative uncertainty of these measurements are related to combination of the relative uncertainty of either the mean of the axial strain gauges on the sample, radial strain gauges on the sample or axial strain gauges on the aluminum end platen.

In dry conditions, for sample granular #2, at f = 0.1 Hz and P_{diff} = 15 MPa, the mean of the axial strain gauges is 7.23 $\mu m/m$ with a standard deviation (S_n) of 0.34 $\mu m/m$, which gives a relative uncertainty of 2.1% for the axial strain. The relative uncertainty for the radial strain gauge on the sample and axial strain gauge on the aluminum is 3.2 and 1.1%, respectively, using the same method. Since the strain on the aluminum is smaller, the error on the Poisson's ratio and bulk modulus are larger when compared to the Young's and shear modulus. This give an error of +/- 1.2,

1.1 and 0.4 GPa for the Young's, bulk and shear modulus, respectively, with an error of +/- 0.014 for the Poisson's ratio.

3.2.5.3 Attenuation on elastic properties

When plotting the attenuation data from the axial oscillation tests, in dry conditions, it shows a log linear trend around 0 with the frequency range, which is consistent with theory (no attenuation in dry conditions) and the variance of the data compared to the log linear line of best fit is used to calculate the random uncertainty. For sample Granular #2, at an effective pressure of 5 MPa, the standard deviation, for a normal distribution, of the bulk attenuation is found to be 0.0096. This standard deviation is used for the sample Granular #2 brine and glycerin data at 5 MPa.

3.2.5.4 Ultrasonic measurement errors

For the ultrasonic measurements, sample granular #2 will be used for an example. The velocity of the waves is calculated using V=L/Δt. The length of the sample is 74.9 +/- 0.01 mm. This gives a relative uncertainty that is negligible for the travel length. The handpicked arrival time of the P-wave gives a total travel time of 17.55+/- 0.1 µs. This gives a relative uncertainty of 0.6 %. The handpicked arrival time for the S-wave gives a total travel time of 31.82 +/- 0.4 µs. This gives a relative uncertainty of 1.3 %. Equations 3.5 is used to calculate the high frequency bulk and shear modulus. The density of glycerin used is 1250 kg/m^3 (Bosart and Snoddy, 1927), with a relative uncertainty of 1%. Therefore, the relative uncertainty of the product ρV_S^2 is of +/- 2.2%. The relative uncertainty of bulk $(\frac{\delta K}{K})$ and shear $(\frac{\delta G}{G})$ modulus can be calculated to be +/- 3.4% and +/- 2.2% respectively.

3.3 Results

The samples were tested at confining pressures ranging from 5 MPa to 30 MPa within a frequency range of 7 10^{-2} to 10^5, 10^6 and 10^9 Hz in dry, brine and glycerin saturated conditions. For these tests, the microvalves were closed, so the samples are in undrained conditions. The green, blue and pink data points show the results for the dry, brine and glycerin saturated tests, respectively. The x, square, diamond and circle shapes represent the axial oscillations at different effective pressures

of 5, 15, 25 and 30 MPa, respectively. The star shaped data points represent the ultrasonic measurements.

3.3.1 Dry hydro and axial measurement comparison

Figure 3.6 shows the hydrostatic and axial oscillation measurement results in dry conditions for all three samples. Clearly, there is no frequency effect on all dry bulk moduli, with no dispersion or attenuation, however, the bulk modulus does increase with an increase in effective pressure. For granular #1, the hydrostatic and axial measurements match well (figure 3.6), with the amplitude of the bulk modulus calculated to be 15, 20 and 22 GPa for effective pressures of 5, 15 and 25 MPa, respectively. However, for granular #2 bulk modulus obtained by axial oscillations give larger values than the ones obtained by hydrostatic oscillations. This bulk modulus difference between these two methods is of 3.5 GPa (difference of 17%) at 5 MPa of effective pressure. It increases to a difference of 4 GPa when at 30 MPa of effective pressure. For shrub #1, the hydrostatic oscillations give larger values for the bulk modulus than the ones deduced from axial oscillations. The discrepancy between both methods is of 3 GPa at 5 MPa of effective pressure (difference of 15%) and it increases to 4 GPa when at 30 MPa of effective pressure. Note the bulk modulus obtained by hydrostatic oscillations is a direct measurement, whereas the one obtained from axial oscillations (on a larger frequency band) assumes isotropy of the sample (equation 3.4). Thus, this assumption of isotropy is valid for Granular#1, but not really for the two other samples. As a consequence, in the following we will focus on the Young's modulus and Poisson's ratio, which are direct measurements obtained on the largest frequency band, when comparing these samples.

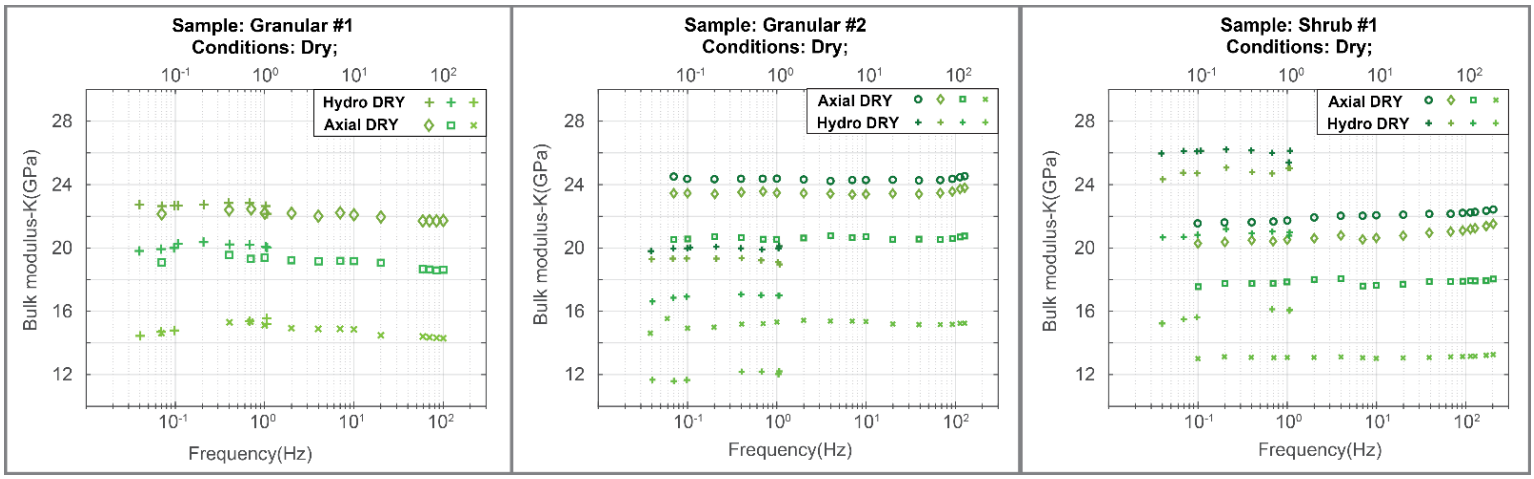

Figure 3.6: Bulk Modulus and Attenuation for all three samples in dry condition, obtained from i) confining pressure oscillations (+) and ii) deduced from axial oscillations (o) for 3 confining pressures of 5,15 and 25 MPa;

3.3.2 Frequency dependency in the fluid saturated sample "Granular #1"

Figure 3.7 shows the results for the axial oscillation tests of the Young's Modulus and attenuation, as well as, the Poisson's ratio and Poisson's attenuation, for sample Granular #1, in dry, brine and glycerin saturated conditions as a function of apparent frequency in the range of 7 10^{-2} to 10^{5} Hz and at effective pressures of 5, 15 and 25 MPa. In addition, the high frequency moduli obtained from ultrasonic measurements are shown.

The **dry** results are all frequency independent showing no attenuation in Young's Modulus or Poisson's ratio. However, the Young's Modulus is pressure dependent as it increases from 25 to 31 to 34 GPa, when the effective pressure is increased from 5 to 15 to 25 MPa, i.e. as preexisting cracks are closed. The same can be said about the Poisson's ratio, as it increases from 0.22 to 0.24 to 0.25, when the effective pressure is increased from 5 to 15 to 25 MPa.

The **brine** results (blue in figure 3.7) are frequency independent, as well, showing no attenuation in Young's Modulus or Poisson's ratio. The Young's Modulus is pressure dependent as it increases from 32 to 35 GPa, when the effective pressure is increased from 15 to 25 MPa. The Poisson's ratio, as well, however it decreases from 0.33 to 0.32 as the effective pressure is increased from 15 to 25 MPa.

At 5, 15 and 25 MPa effective pressure, in **glycerin** saturated conditions (pink in figure 3.7), the Young's modulus at low frequencies starts at 26.5, 31.5 and 35 GPa, respectively, and shows an increasing trend starting at around 30 kHz. This increase is highlighted in the Young's attenuation, which reaches a maximum amplitude of 0.06, 0.04 and 0.02 at a frequency of 8 10^4 Hz for effective pressures of 5, 15 and 25 MPa, respectively.

The Poisson's ratio results are frequency independent, in **glycerin** saturated conditions. There is no clear attenuation peak in the Poisson's attenuation. However, they are effective pressure dependent as the Poisson's ratio decreases from 0.34 to 0.33 to 0.32 when the effective pressure is increased from 5 to 15 to 25 MPa.

The ultrasonic measurements, in **brine** saturated conditions, are in line with the high frequency axial oscillations. The Young's modulus, in **glycerin** saturated conditions, from the ultrasonic data is 5.1 and 1.5 GPa larger in amplitude then the highest frequency in axial oscillations results, at an effective pressure of 5 and 25 MPa, respectively. The Poisson's ratio, in glycerin saturated conditions, shows good agreement with the high frequency axial oscillations.

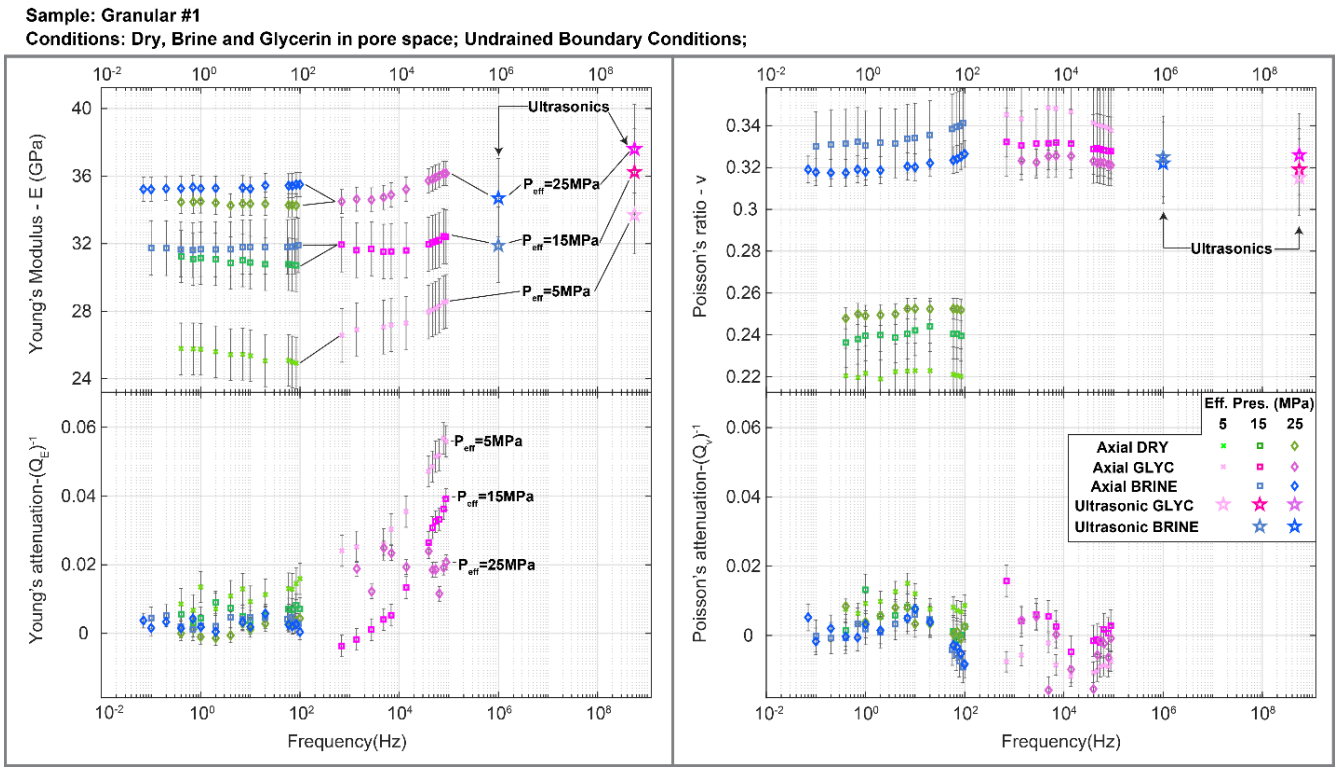

Figure 3.7: Young's modulus and Poisson's ratio, with their attenuation over a large frequency range (7 10^{-2} to 10^{5} – 10^{6} – 5.5 10^{8} Hz) in dry, brine and glycerin saturated conditions at 3 distinct effective pressures (5, 15 and 25 MPa) for sample Granular #1;

Figure 3.8 shows bulk and shear modulus, as well as, the bulk and shear attenuation for the granular sample #1 in dry, brine and glycerin saturated conditions, as a function of apparent frequency in the range of 7 10^{-2} to 9 10^{4} Hz, at effective pressures of 5, 15 and 25 MPa, using the data from figure 3.7, and equations 3.4 which assumes isotropy of the sample . In addition, the high frequency moduli are shown.

At 5, 15 and 25 MPa effective pressure, in **dry** conditions, the bulk modulus is constant throughout all frequencies tested at around 15, 20 and 23 GPa, respectively. At 5, 15 and 25 MPa effective pressure, in dry conditions, the shear modulus is constant throughout all frequencies at around 10.5, 12.5 and 13.7 GPa, respectively. The attenuation for these are close to 0, which is consistent with dry samples and are within the precision of our setup (<0.02) (Borgomano et al., 2020).

At 15 and 25 MPa effective pressure, in **brine** saturated undrained conditions, the bulk modulus is larger than in dry conditions at 31.1 and 32.2 GPa and constant throughout all frequencies tested. The shear modulus, in brine saturated undrained conditions is lower than in dry conditions and

constant throughout all frequencies tested. There is more shear weakening at low effective pressures which is consistent with other work on carbonates (Adam et al., 2006) and even clay-bearing sandstones (Yin et al.,2019). There is no significant attenuation bulk or shear attenuation.

At 5, 15 and 25 MPa effective pressure, in **glycerin** saturated conditions, the bulk modulus is mostly constant for frequencies < 10 kHz at around 30, 31.5 and 33 GPa, respectively, with a small amount of dispersion at frequencies >10 khz. There is an increase in bulk attenuation at around 80 kHz, to an amplitude of 0.04 at the lower two effective pressures of 5 and 15 MPa. The bulk modulus, at 25 MPa effective pressure, is also in line with the predicted undrained bulk modulus using Biot-Gassmann fluid substitution theory, which is showcased with the dotted line.

At 5, 15 and 25 MPa effective pressure, in **glycerin** saturated conditions, the shear modulus at low frequencies starts at 10, 12 and 13 GPa, respectively, and shows an increasing trend starting at around 30 kHz. This increase is highlighted in the shear attenuation, which reaches a maximum amplitude of 0.06, 0.04 and 0.03 at a frequency of 80 kHz for effective pressures of 5, 15 and 25 MPa, respectively. The decrease in attenuation with increase in pressure is consistent with the literature involving squirt flow (Adelinet al. 2011, Fortin et al 2014, Subramaniyan et al.,2015; Han et al., 2018), as the compliant cracks are closed at larger effective pressures, which leads to a decrease in crack density. It is also expected to have shear attenuation for squirt flow (Dvorkin et al., 1994), which is the case here.

The bulk modulus ultrasonic data, in **glycerin** saturated conditions, is 4.1 GPa larger in amplitude then the highest frequency axial oscillation results, at an effective pressure of 5 MPa. This difference in bulk modulus, in glycerin saturated conditions, decreases with increasing effective pressures and is equal to 0.9 GPa at 25 MPa effective pressure. The shear modulus ultrasonic data, in **glycerin** saturated conditions, is 2.5 GPa larger in amplitude then the highest frequency axial oscillation results, at an effective pressure of 5 MPa. This difference in bulk modulus, in glycerin saturated conditions, decreases with increasing effective pressures and is equal to 0.6 GPa at 25 MPa effective pressure.

In summary of the results on sample granular #1, shown in figures 3.7 and 3.8, the elastic properties for the dry and brine saturated conditions are frequency independent, whereas in glycerin saturated conditions, there is an attenuation peak at 80 kHz. This attenuation peak is pressure dependent with higher attenuation peaks at lower effective pressures. The low effective pressure

glycerin saturated ultrasonic results show more dispersion than the high effective pressure data, which is in line with crack density decreasing with an increase of effective pressure (Adelinet et al., 2011), and will be observed in all three samples. In addition, there is shear dispersion and attenuation in glycerin saturated conditions, all these observations suggest a mechanism of squirt flow that occurs at a frequency cut-off of 80 kHz.

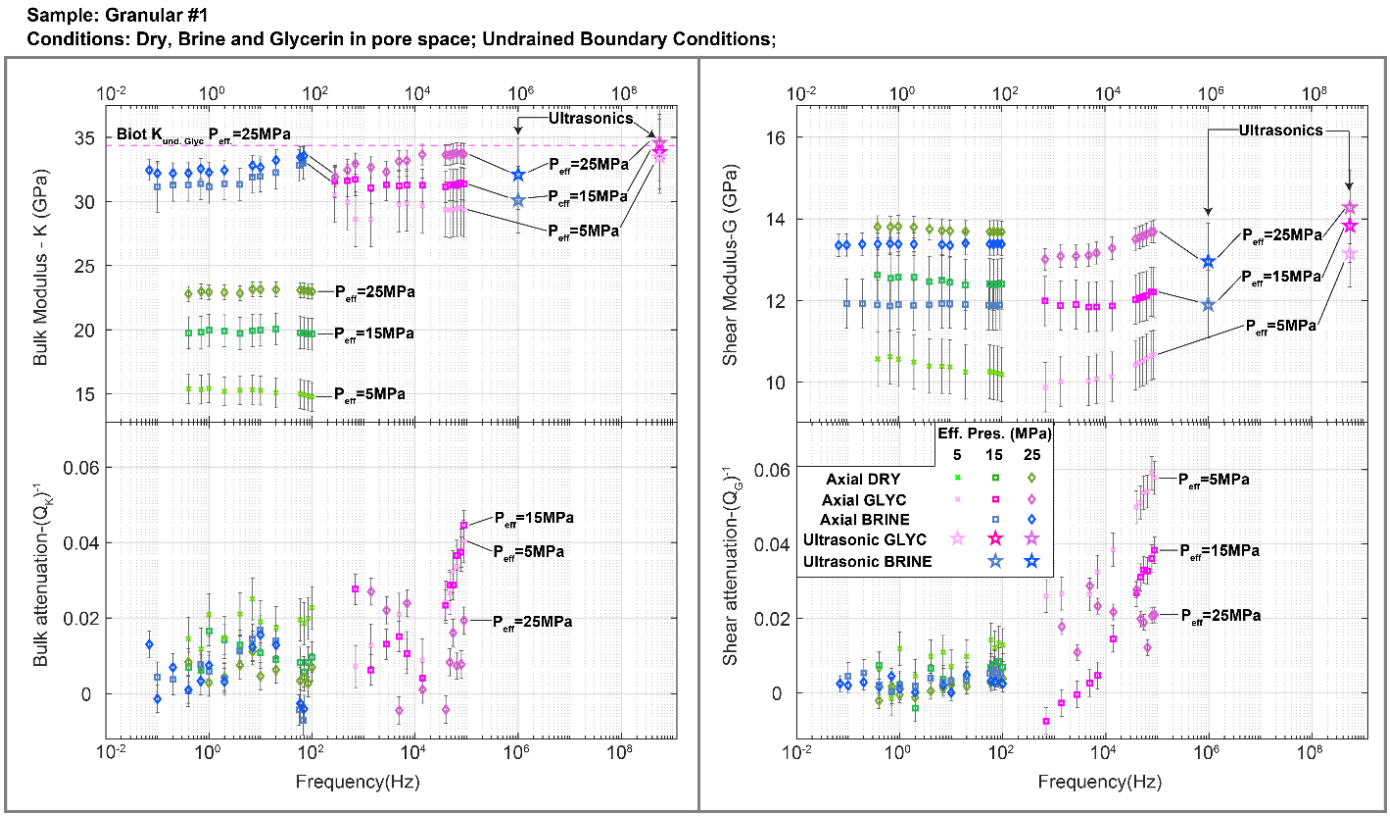

Figure 3.8: Bulk and shear modulus, with their attenuation over a large frequency range (7 10^{-2} to 10^{5} – 10^{6} – 5.5 10^{8} Hz) in dry, brine and glycerin saturated conditions at 3 distinct effective pressures (5, 15 and 25 MPa) for sample Granular #1;

3.3.3 Frequency dependency in the fluid saturated sample "Granular #2"

Figure 3.9 shows the results for the axial oscillation tests of the Young's modulus and attenuation, as well as, the Poisson's ratio and Poisson's attenuation, for sample Granular #2, in dry, brine and glycerin saturated conditions as a function of apparent frequency in the range of 7 10^{-2} to 10^{5} Hz and at effective pressures of 5, 15, 25 and 30 MPa. In addition, the high frequency moduli are shown.

For the dry and brine saturated sample, similar feature as those observed for "Granular # 1" can be observed. The **dry** results are all frequency independent showing no attenuation in Young's Modulus or Poisson's ratio. However, the Young's Modulus is pressure dependent as it increases from 23 to 29 to 31 to 31.8 GPa, when the effective pressure is increased from 5 to 15 to 25 to 30 MPa. The same can be said about the Poisson's ratio, as it increases from 0.245 to 0.265 to 0.275 to 0.275, when the effective pressure is increased from 5 to 15 to 25 to 30 MPa.

The Young's modulus, **brine** saturated results for 25 and 30 MPa effective pressures, are frequency independent and have amplitudes of 32 and 33 GPa, respectively, showing no attenuation peaks. However, the Young's attenuation, brine saturated results for 5 and 15 MPa effective pressure, shows a peak at around 40-100 Hz with an amplitude of 0.03, and a small increase of about 0.5 GPa in Young's modulus at an effective pressure of 15 MPa for the higher frequency.

The Poisson's ratio, **brine** saturated results for 25 and 30 MPa effective pressures are frequency independent and have amplitudes of 0.322 and 0.324, respectively, showing no attenuation peaks. However, as for the Young modulus, the Poisson's ratio brine saturated results, for 5 and 15 MPa effective pressure, both increase by about 0.01 with a small attenuation peak of 0.010 and 0.015, respectively at a frequency around 40-100 Hz.

At 5 MPa effective pressures in **glycerin** saturated conditions, the Young's modulus increases from 23.4 to 25 GPa, with two attenuations peaks of 0.029 and 0.047 at frequencies of 100 Hz and 40 kHz. At 15 MPa effective pressures in glycerin saturated conditions, the Young's modulus increases from 29.6 to 30.6 GPa, with two attenuation peaks of 0.012 and 0.022 at 100 Hz and 40 kHz. At 25 and 30 MPa effective pressures in glycerin saturated conditions, the Young's modulus stays constant at 33 and 34 GPa, with no attenuation peaks.

At 5 MPa effective pressure in **glycerin** saturated conditions, the Poisson's ratio increases from 0.352 to 0.382 with two attenuation peaks of 0.027 and 0.006 at 100 Hz and 10 kHz, respectively. At 15 MPa effective pressure in glycerin saturated conditions, the Poisson's ratio increases from 0.346 to 0.356 with two attenuation peak of 0.0158 and 0.0045 at the 60 Hz and 20 kHz, respectively. At 25 and 30 MPa effective pressures, the Poisson's ratio stays relatively constant two small attenuation peaks at 1 10^2 and 2 10^4 Hz, respectively.

For effective pressures under 25 MPa, the Young's modulus, in **brine** saturated conditions, from the ultrasonic data is larger in amplitude than the highest frequency brine saturated results. This difference is largest at lower effective pressures. At effective pressures of 25 and 30 MPa, the Young's modulus ultrasonic brine data is in line with the axial oscillation data. The Poisson's ratio, in brine saturated condition, calculated using the ultrasonic data is in agreement with the brine saturated axial oscillation data, at effective pressures of 15, 25 and 30 MPa.

The Young's modulus, in **glycerin** saturated conditions, from the ultrasonic data is 5.1, 2.3, 1.5 and 0.2 GPa larger in amplitude than the highest frequency in axial oscillations results, at an effective pressure of 5, 15, 25 and 30 MPa, respectively. The Poisson's ratio, in glycerin saturated conditions, shows good agreement with the high frequency axial oscillations, at effective pressures of 15, 25 and 30 MPa.

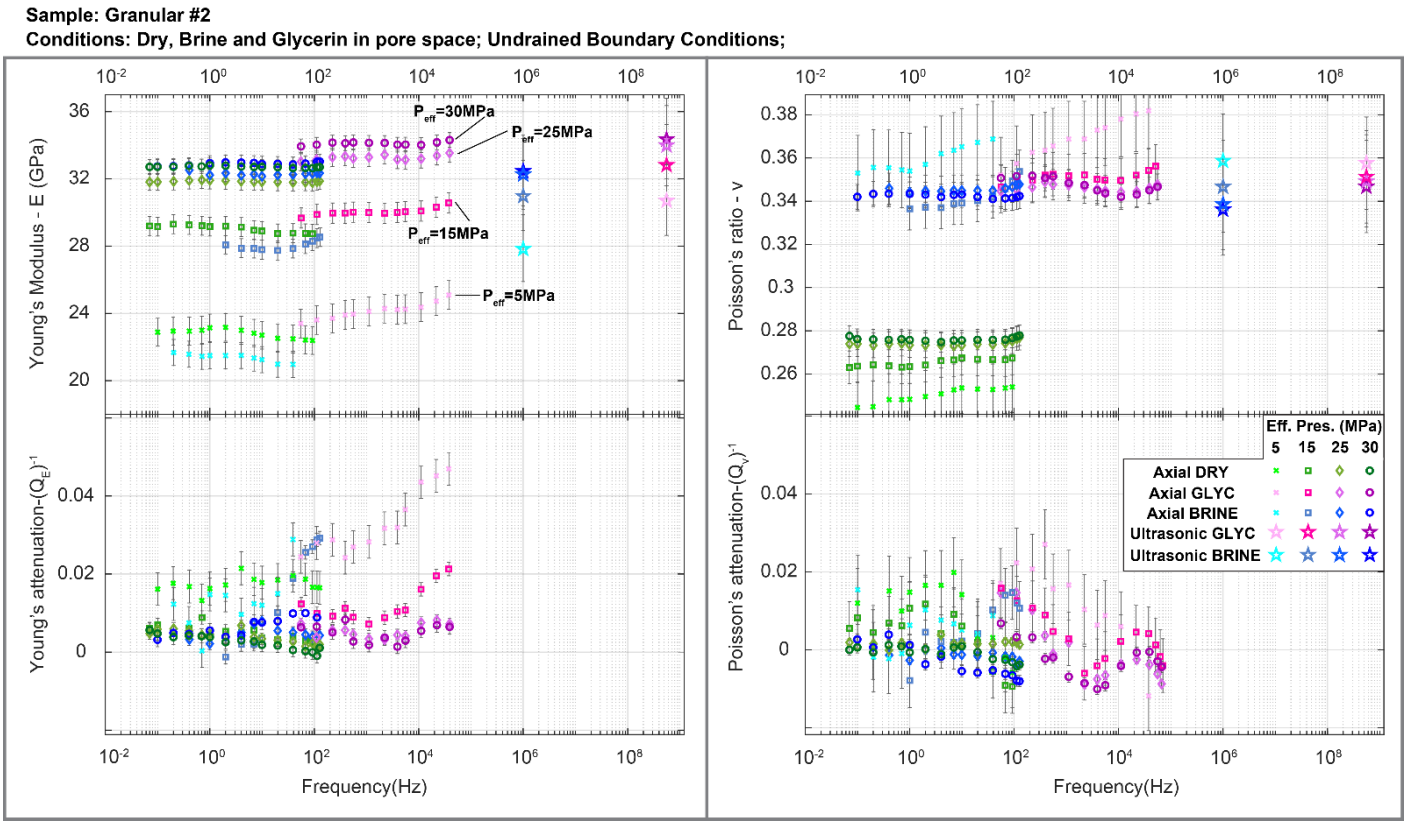

Figure 3.9: Young's modulus and Poisson's ratio, with their attenuation over a large frequency range (7 10^{-2} to 10^{5} – 10^{6} – 5.5 10^{8} Hz) in dry, brine and glycerin saturated conditions at 4 distinct effective pressures (5, 15, 25 and 30 MPa) for sample Granular #2;

The bulk and shear moduli, as well as their attenuation for the granular sample #2 in dry, brine and glycerin saturated conditions, is given in figure 3.10, using the data from figure 3.9, and equations 3.4 (assuming isotropy of the sample); although, it is known that the sample is slightly anisotropic.

At 5, 15, 25 and 30 MPa effective pressure, in **dry** conditions, the bulk modulus is constant throughout all frequencies tested at around 15, 20.5, 23.5 and 24.5 GPa, respectively. At 5, 15, 25 and 30 MPa effective pressure, in dry conditions, the shear modulus is constant throughout all frequencies at around 9, 11.5, 12.5 and 13 GPa, respectively. There is little to no dispersion in all dry conditions, with no attenuation.

At 5 MPa effective pressure, in **brine** saturated conditions, the bulk modulus increases from 25 to 27 GPa as the frequency is increased, with an attenuation peak at 0.05 at the highest frequency recorded of 40 Hz. At 15 MPa effective pressure, in brine saturated conditions, the bulk modulus increases from 29 to 31.3 GPa, with an attenuation peak of 0.06 at the highest frequency recorded

of 92 Hz. At 25 and 30 MPa frequency, the Bulk modulus is frequency independent, with no attenuation peaks.

At 5, 15, 25 and 30 MPa effective pressure, in **brine** saturated conditions, the shear modulus is found to be less frequency dependent over the frequency domain recorded. The shear attenuation at 5 and 15 MPa effective pressure, in brine saturated conditions show an amplitude increase with increase in frequency to around 0.026 at the higher frequencies.

At 5 MPa effective pressure, in **glycerin** saturated conditions, the bulk modulus increases from 24 GPa to 32.5 GPa, when going from a frequency of 100 Hz to 80 kHz. This dispersion is much less significant as the effective pressure is increased and is negligible at the highest effective pressure of 30 MPa. The bulk attenuation has two attenuation peaks at 100 and 40 kHz, with the first peak having a maximum amplitude, at an effective pressure of 5 MPa and 30 MPa, of 0.096 and 0.025, respectively. The second peak has a maximum amplitude, at an effective pressure of 5 MPa and 30 MPa, of 0.064 and ~0, respectively. The bulk modulus data is also in line with the predicted Biot-Gassmann undrained bulk modulus prediction, at the highest effective pressure of 25 MPa, i.e. when pre-existing cracks are closed.

At 5 MPa effective pressure, in **glycerin** saturated conditions, the shear modulus increases from 8.5 GPa to 9.4 GPa, when going from a frequency of 100 Hz to 80 kHz. This dispersion is much less significant as at an effective pressure of 15 MPa and is negligible at 25 and 30 MPa effective pressures. The shear attenuation has only one clear attenuation peaks at 40 kHz, for effective pressures of 5 and 15 MPa, with a maximum amplitude, at an effective pressure of 5 MPa and 15 MPa, of 0.058 and 0.02, respectively.

The bulk modulus ultrasonic data, in **glycerin** saturated conditions, is 3.5 GPa larger in amplitude then the highest frequency axial oscillation results, at an effective pressure of 5 MPa. This difference in bulk modulus, in glycerin saturated conditions, decreases with increasing effective pressures and is equal to 2 GPa at 30 MPa effective pressure. The shear modulus ultrasonic data, in **glycerin** saturated conditions, is the same amplitude when comparing the 30 MPa effective pressure results, however a discrepancy appears between the two measurements, at effective pressures of 5 and 15 MPa, which is larger at lower effective pressures.

To summarize, the results for the elastic properties on sample granular #2, presented in figures 3.9 and 10, show that there are two distinct attenuation peaks which appear around 100 and 40 kHz.

The first attenuation peak is seen in brine saturated conditions at low effective pressures, as well as, in the glycerin saturated conditions at all effective pressures. The second attenuation peak is observed around 40 kHz, in glycerin saturated conditions. Both of these mechanisms are pressure dependent. Only the second peak is associated with an attenuation and a dispersion of the shear modulus. The second peak is similar to the one observed for "granular # 1" and can be interpreted as a squirt flow mechanism. The first peak can be interpreted as a FPD at mesoscopic scale, and will be discussed more thoroughly in section 4.

Sample: Granular #2
Conditions: Dry and Glycerin in pore space; Undrained Boundary Conditions;

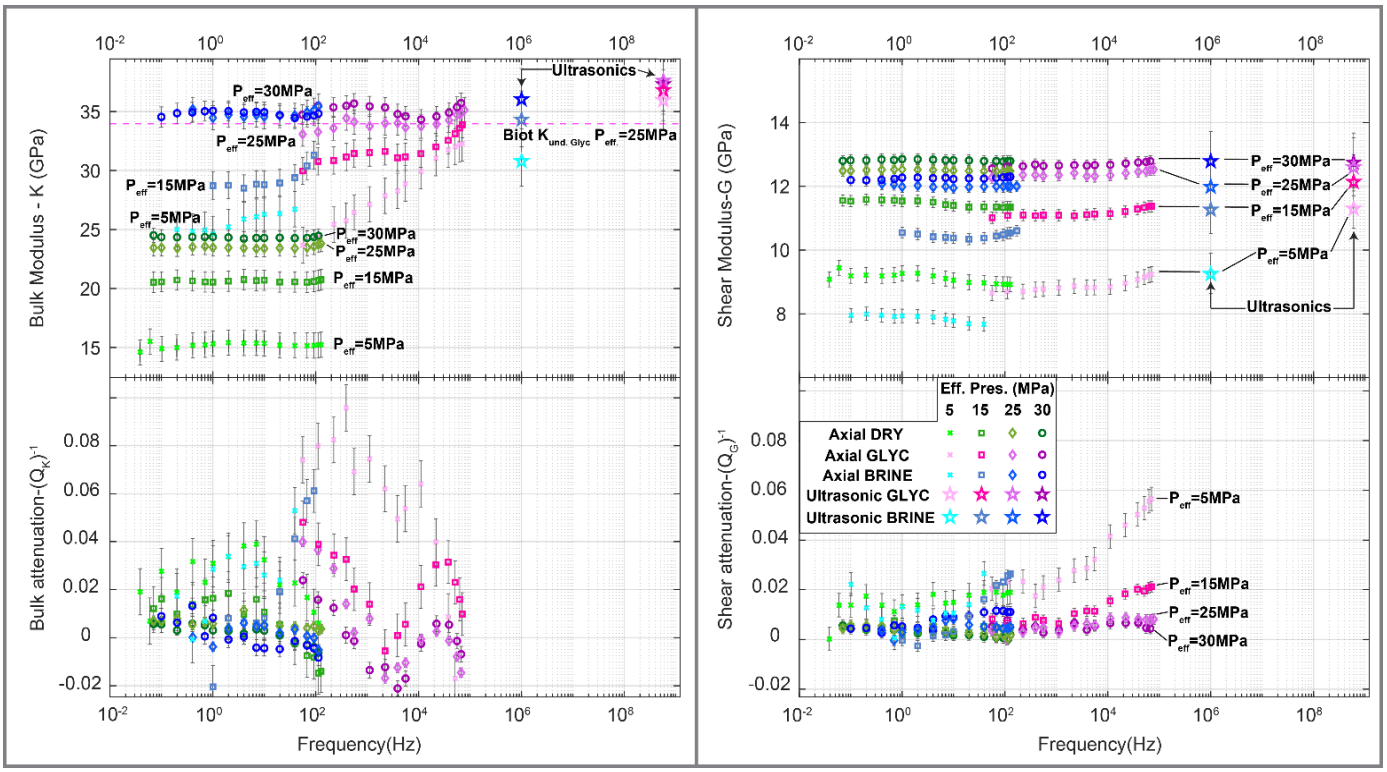

Figure 3.10: Bulk and shear modulus, with their attenuation over a large frequency range (7 10^{-2} to 10^{5} – 10^{6} – 5.5 10^{8} Hz) in dry, brine and glycerin saturated conditions at 4 distinct effective pressures (5, 15, 25 and 30 MPa) for sample Granular #2;

3.3.4 Frequency dependency in the fluid saturated sample "Shrub #1"

Figure 3.11 shows the results for the axial oscillation tests of the Young's modulus and attenuation, as well as, the Poisson's ratio and Poisson's attenuation, for sample Shrub #1.

Similar features as those observed for “Granular 2” can be observed. The **dry** results are all frequency independent showing no attenuation in Young’s Modulus or Poisson’s ratio. However, the Young’s Modulus is pressure dependent as it increases from 23.4 to 30.2 to 33.3 to 34.8 GPa, when the effective pressure is increased from 5 to 15 to 25 to 30 MPa. The same can be said about the Poisson’s ratio, as it increases from 0.203 to 0.218 to 0.229 to 0.234, when the effective pressure is increased from 5 to 15 to 25 to 30 MPa.

At 5 MPa effective pressure, in **glycerin** saturated conditions, the Young’s modulus increases from 20 GPa to 22 GPa, where it plateaus between attenuation peaks then it increases to 26 GPa, when going from a frequency of 100 Hz to 60 kHz. At 30 MPa effective pressure, there is an increase in Young’s modulus from 34.4 to 35.9 GPa, where again it plateaus between attenuation peaks then it increases again to 36.9 GPa when reaching 60 kHz frequency. The Young’s attenuation shows two attenuation peaks at 300 Hz and 40 kHz, with the first peak having a maximum amplitude of 0.036 and 0.029 at 5 MPa and 30 MPa effective pressures, respectively. The second peak has a maximum amplitude, at an effective pressure of 5 MPa and 30 MPa, of 0.070 and 0.023, respectively. An increase in effective pressure is related to a decrease in attenuation for both mechanisms.

At 5 MPa effective pressure, in **glycerin** saturated conditions, the Poisson’s ratio increases from 0.030 to 0.032, when going from a frequency of 100 Hz to 60 kHz, with two attenuation peaks at 300 and 40 kHz with magnitudes of 0.014. At 30 MPa effective pressure, in glycerin saturated conditions, the Poisson’s ratio increases with frequency from 0.028 to 0.030, with two attenuation peaks at 300 Hz, with a magnitude of 0.026, and at 40 kHz, with a magnitude of 0.012.

The Young’s modulus from the ultrasonic data is 8 GPa larger in amplitude than the highest frequency axial oscillation results, at an effective pressure of 5 MPa. This difference in Young’s modulus, between ultrasonic and axial oscillations, decreases with increasing effective pressures and is equal to 1.5 GPa at 30 MPa effective pressure. The Poisson’s ratio from the ultrasonic data is 0.01 larger in amplitude than the highest frequency axial oscillation data, at an effective pressure of 5 MPa. This difference increases with an increase of effective pressure to 0.026 at 30 MPa effective pressure.

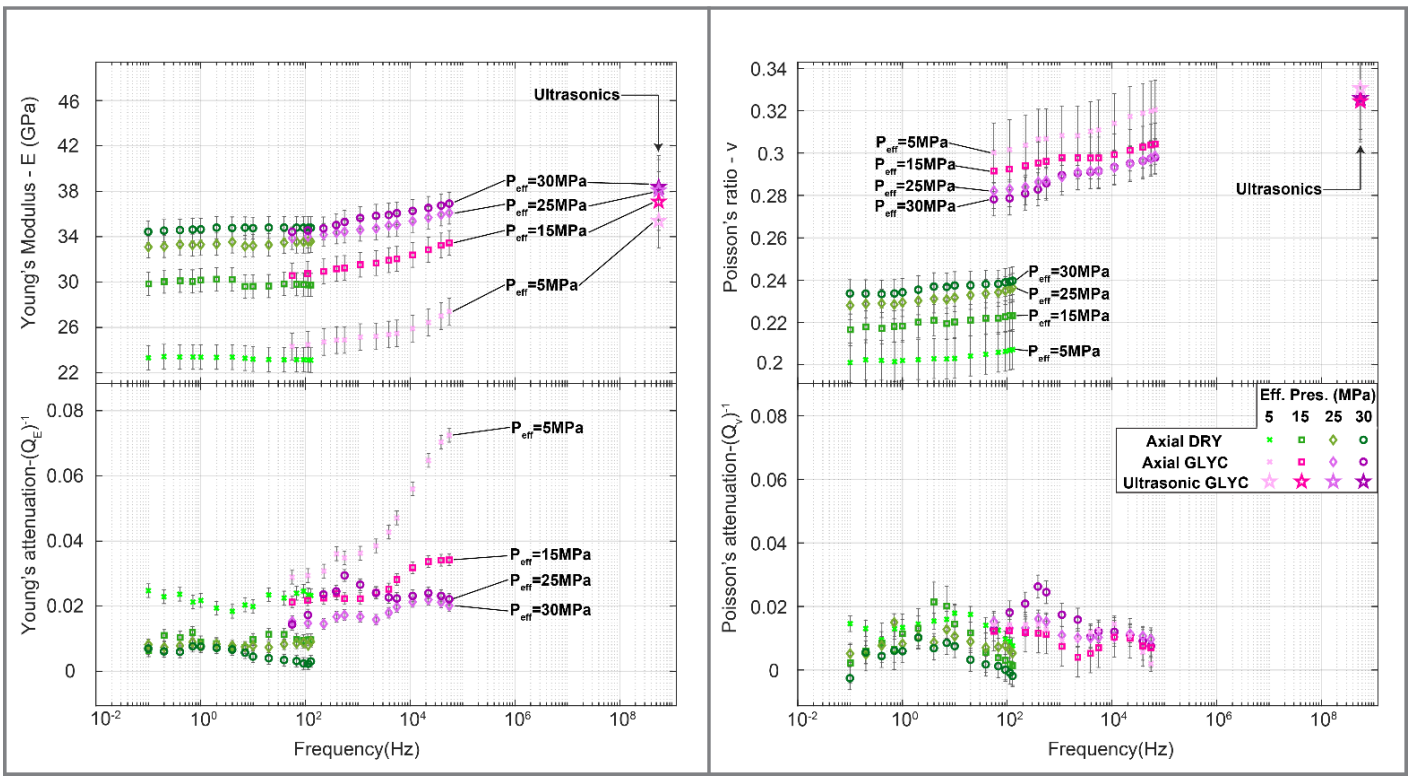

Figure 3.11: Young's modulus and Poisson's ratio, with their attenuation over a large frequency range (7 10^{-2} to 10^{5} – 10^{6} – 5.5 10^{8} Hz) in dry and glycerin saturated conditions at 4 distinct effective pressures (5, 15, 25 and 30 MPa) for sample Shrub #1;

Figure 3.12 shows the results for the axial oscillation tests of the bulk modulus and attenuation. Although, it is known that the sample does not behave isotropically, the bulk and shear moduli and attenuation are calculated indirectly as if it was isotropic, giving insight on the local elastic measurements. In addition, the high frequency moduli are shown.

At 5, 15, 25 and 30 MPa effective pressure, in **dry** conditions, the bulk modulus is constant throughout all frequencies tested at around 13, 17.7, 20.8 and 22 GPa, respectively. At 5, 15, 25 and 30 MPa effective pressure, in dry conditions, the shear modulus is constant throughout all frequencies at around 9.7, 12.3, 13.5 and 14 GPa, respectively. There is no bulk or shear attenuation.

At 5 MPa effective pressure, in **glycerin** saturated conditions, the bulk modulus increases from 20 GPa to 22 GPa, where it plateaus between attenuation peaks then it increases to 26 GPa, when going from a frequency of 100 Hz to 60 kHz. At 30 MPa effective pressure, there is an increase in

bulk modulus from 26 to 28 GPa, where it plateaus between attenuation peaks then it increases again to 30 GPa at the highest frequency of 60 kHz. The bulk attenuation reflects these results, with 2 attenuation peaks at 300 and 40 kHz, with the first peak having a maximum amplitude of 0.06 at both 5 MPa and 30 MPa effective pressures. The second peak has a maximum amplitude, at an effective pressure of 5 MPa and 30 MPa, of 0.08 and 0.04, respectively. The bulk modulus data at 25 MPa confining pressure is slightly smaller in amplitude when comparing with the Biot-Gassmann prediction, which is probably due to the anisotropy.

At 5 MPa effective pressure, in **glycerin** saturated conditions, the shear modulus increases from 9.3 GPa to 10.5 GPa with frequency. This dispersion is less significant at an effective pressure of 15 MPa and becomes even smaller at 25 and 30 MPa effective pressures. The shear attenuation at 5 MPa effective pressure, shows two attenuation peaks at around 300 Hz and 40 kHz, with maximum amplitudes of 0.033 and 0.07, respectively. The location of these peaks are the same for the other effective pressures, with lower peak amplitudes.

The bulk modulus ultrasonic data, in **glycerin** saturated conditions, is 8.4 GPa larger in amplitude than the highest frequency axial oscillation results, at an effective pressure of 5 MPa. This difference in bulk modulus decreases with increasing effective pressures and is equal to 4.2 GPa at 30 MPa effective pressure. The shear modulus ultrasonics is 4.3 GPa larger in amplitude then the highest frequency axial oscillation results, at an effective pressure of 5 MPa. The difference in shear modulus decreases with increasing effective pressure and is equal to 1.7 GPa at 30 MPa effective pressure.

The results for the elastic properties of sample shrub #1, presented in figures 3.11 and 3.12, first show the frequency independence when the sample is dry and also shows frequency dependence with two distinct attenuation peaks which appear around 300 and 40 kHz, when the sample is saturated with glycerin. The attenuation peaks are pressure dependent, with a decrease in attenuation, as the pressure is increased, however the higher frequency peak seems to be more sensitive to pressure change than lower frequency peak. These observations are similar to those observed on ‘Granular#2’.

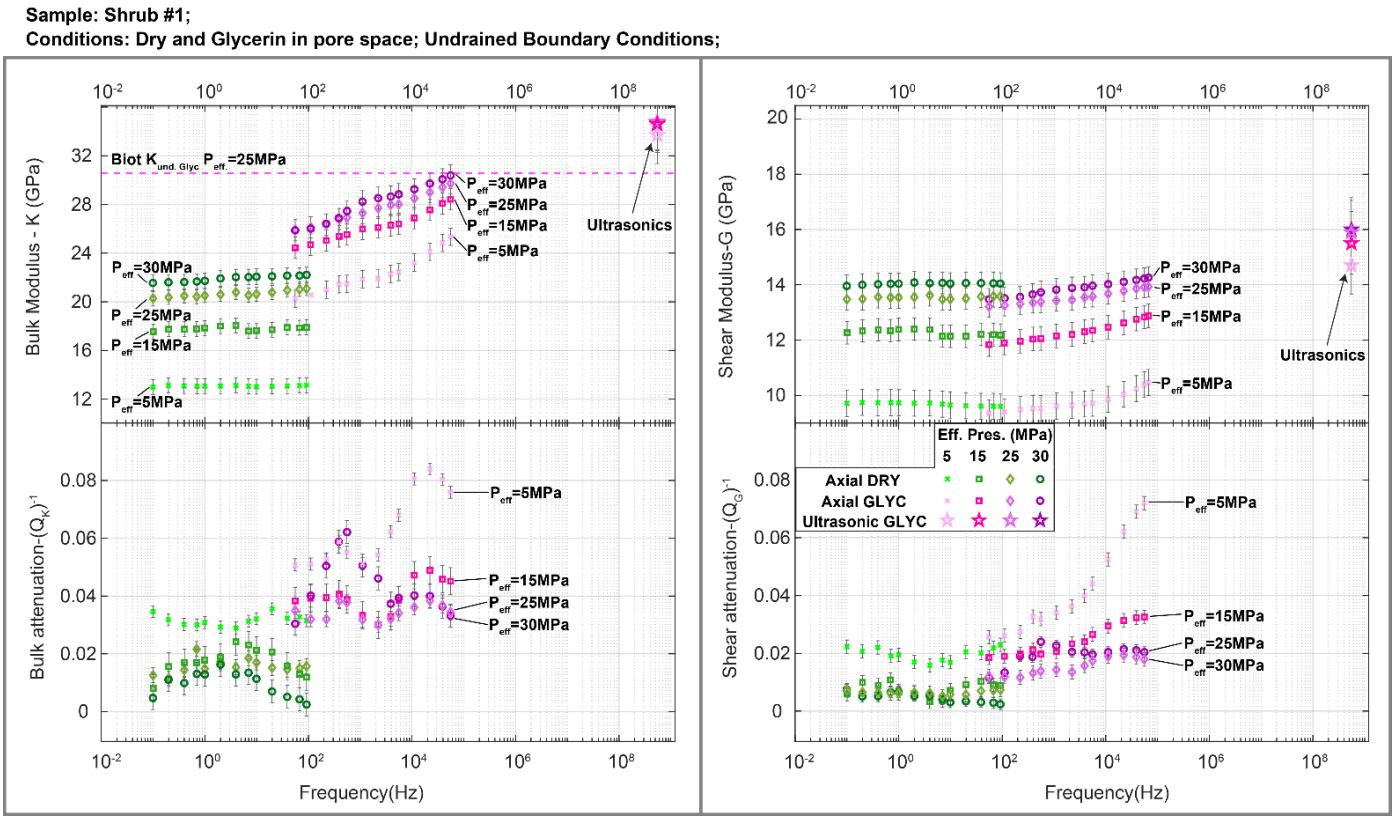

Figure 3.12: Bulk and shear modulus, with their attenuation over a large frequency range (7 10^{-2} to 10^{5} – 10^{6} – 5.5 10^{8} Hz) in dry and glycerin saturated conditions at 4 distinct effective pressures (5, 15, 25 and 30 MPa) for sample Granular #2;

To conclude the experimental results,

i) a high frequency attenuation peak was observed in all three samples, which is pressure dependent. This frequency cutoff is associated with a dispersion and attenuation in the shear modulus. It is interpreted as a squirt-flow mechanism. The frequency cutoff is in the range of 40-80 kHz.

ii) The comparison of the dry bulk modulus derived from the hydrostatic and axial oscillation tests show that granular #1 is isotropic and granular #2 and shrub #1 are not perfectly isotropic.

iii) Finally, a lower frequency attenuation peak was observed in samples granular # 2 and shrub #1, which is less pressure dependent than the high frequency attenuation peak. No dispersion or attenuation on shear is observed for this frequency cut-off. This frequency cut-off is interpreted as a FPD mechanism at mesoscopic scale and will be discussed more thoroughly in section 5.

3.4 Discussion

Two separate attenuation peaks are seen in the experimental results. These peaks are assumed to be caused by two distinct FPD mechanisms: mesoscopic FPD and squirt flow. To explain these, figure 3.13 shows a simplified schematic of the sample in undrained boundary conditions having porosity heterogeneities at the meso- and microscopic scale. This configuration creates a frequency dependent system for a saturated sample with three distinct regimes: undrained (relaxed), mesoscopic (partially relaxed) and unrelaxed. In the undrained frequency regime, fluid has time to flow between both zones. This regime is reached even at low frequencies due to the introduction of microvalves and allows the authors to avoid the drained regime (Pimienta et al.,2017; Borgomano et al.,2020). In this undrained regime, the undrained value is obtained from the drained value using Biot-Gassman equations, with a mean value of the porosity and drained elastic moduli.

The effect of intermittent layers of strata with varying porosity has been shown analytically by Carcione and Picotti (2006) and numerically (e.g. Quintal et al., 2012; Rubino et al., 2009) to create attenuation peaks. Let's assume that sample is made of two zones with different porosity (figure 3.13) with $\Phi_1 > \Phi_2$, where 1 stand for the upper layer, we assume the same drained modulus (K) and the same modulus of the grain K_s in both zones. Then, Skempton coefficient is defined as:

$$B = \frac{\frac{1}{K}-\frac{1}{K_s}}{\frac{1}{K}-\frac{1}{K_s}+\Phi\left(\frac{1}{K_f}-\frac{1}{K_s}\right)}. \quad \ldots (4.1)$$

We get $B_1 < B_2$, it implies that the pore pressure, p_1, for $f > f_1$ in the upper layer is lower than p_2. There is no time for fluid to equilibrate at the sample scale. The frequency cutoff for the mesoscopic flow is $f_1 = D/L^2$, where D is the diffusivity and L in the case of figure 3.13 is half length of the sample. For this frequency cut-off, we do not expect theoretically a change in the shear-modulus.

Finally, in the unrelaxed frequency regime, more compliant saturated cracks (microscopic scale) see an increase in pore pressure, as the fluid in these doesn't have time to escape to stiffer pores. And the frequency cutoff is $f_2 = K\xi^3/\eta$ where the key parameter in this case is the mean crack aspect ratio.

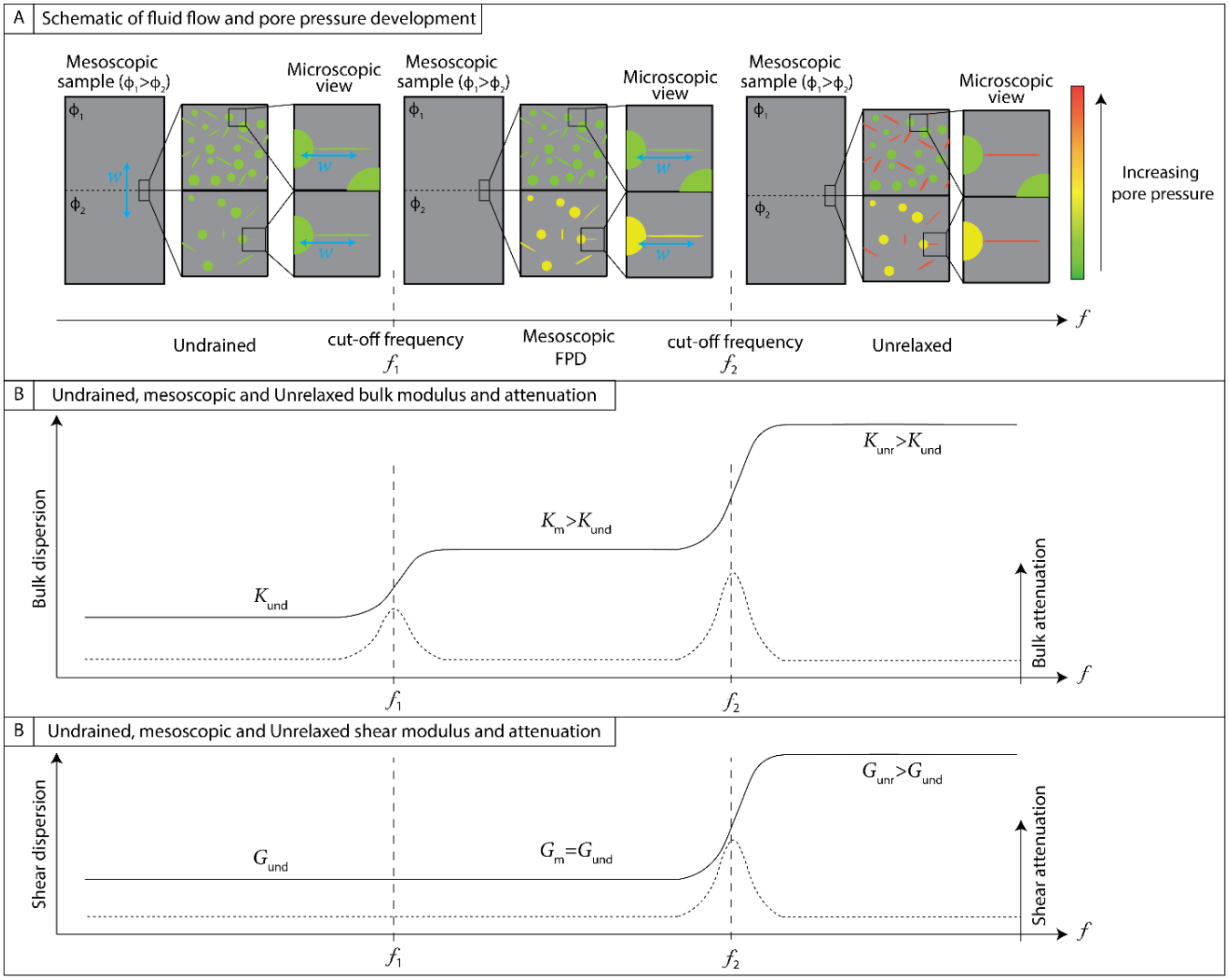

Figure 3.13: A: schematic at different scales of the evolution of pore pressure in the sample between the undrained, mesoscopic and unrelaxed frequency regimes; B: Young's modulus and attenuation between the 3 frequency regimes;

3.4.1 Squirt flow

For all three samples, there are attenuation peaks in the apparent frequency range of 10 to 100 kHz, for the directly measured Young's modulus, as well as, the inferred bulk and shear modulus. These attenuation peaks are reduced with increasing effective pressure and all disappear at the effective pressure of 25 MPa or higher. The dispersion in the respective moduli is also reduced with increasing effective pressure. The non-linear increase in the moduli and ultrasonic wave velocities is commonly associated with the closing of compliant porosity, such as cracks and grain contacts,

of the samples (Walsh, 1965). The observed attenuation and dispersion therefore likely explained by pore scale fluid pressure diffusion from compliant to stiff pores, where compliant pores are progressively closed with increasing effective pressure (Dvorkin et al.,1994; Adelinet et al.,2011).

A plethora of experimental work has been completed on sandstone and carbonate samples saturated with fluids of different viscosity. Particularly in sandstones the dispersion and attenuation has been observed by a number of authors (e.g. Vo-Thanh, 1990, Mikhaltsevitch et al., 2014; Spencer and Shine, 2016; Chapman et al., 2019). Different approaches have been used to quantitatively interpret these observations. Vo-Thanh (1990) used the viscoelastic model of O'Connell and Budianksi (1977). Subramaniyan et al. (2015) used the analytical solution of Gurevich et al. (2010) for squirt flow to interpret the observed attenuation and dispersion in a Fontainebleau sandstone saturated with different water-glycerin mixtures. Chapman et al. (2019) also used the Gurevich et al. (2010) solution and applied it to the observed attenuation and dispersion in the bulk and shear modulus of a glycerin saturated Berea sandstone. Similar observations in carbonate samples are less common (e.g. Adam et al., 2009; Borgomano et al., 2019). Borgomano et al. (2019) was able to create micro cracks needed for squirt flow attenuation by thermally cracking the sample which originally had no squirt flow attenuation. Sun and Gurevich (2020) extended the Gurevich et al. (2010) analytical solution by combining it with the effective medium approach by David and Zimmerman (2012) to extract the crack porosity and crack aspect ratio from pressure dependent measurements of ultrasonic wave velocities. To test this approach Sun and Gurevich (2020) utilized the data from Borgomano et al. (2019), they however only found satisfactory matches between the analytical solution and the experimental data at elevated effective pressures. These papers all helped define squirt flow attenuation and dispersion experimentally and how it can be observed in the lab, mainly, that (i) the dispersion happens in the Young's, shear and bulk moduli and (ii) it is larger at low effective pressures, which is consistent with the results for all three carbonate samples tested in this paper.

Applying the approach of David and Zimmerman (2012) to the pressure dependent p- and s-wave measurements on the three samples in dry conditions, we determined crack aspect ratios of 2.3-3.2×10^{-4}. Using these in Gurevich's (2010) analytical solution, the maximum in attenuation due to squirt flow is predicted at frequencies 1 to 2 orders of magnitude lower than what is observed in our measurements. The discrepancy is likely due to inherent assumptions in the effective medium approach of David and Zimmerman (2012), the idealized geometrical configuration of Gurevich's

(2010) squirt flow model and the experimental procedure. The approach of David and Zimmerman (2012) considers an isotropic rock with a random distribution of cracks which is not consistent with the anisotropy and heterogeneity observed in the three carbonate samples. It should be noted that the aspect ratios are inverted from the p- and s-wave velocities determined form travel time measurements of wave propagating through the entire length of the sample whereas the frequency dependent attenuation and dispersion are determined from local measurements of strain on the sample. The aspect ratios of grain contacts in the vicinity of the strain gauges may be different from those inverted from the velocity measurements given the heterogeneity of the samples.

3.4.2 Mesoscopic flow

The attenuation and dispersion observed at frequencies around 100 Hz for sample granular #2 and shrub #1 seem to be associated with mesoscopic flow, as these samples are heterogeneous. This peak of attenuation is uncommon and has never been reported in the literature, when in perfectly undrained conditions. The critical frequency can be estimated at the first order using $f_1 = D/L^2$. The length between porosity regions was chosen as 30 and 8 mm, for samples granular #1 and shrub #2, respectively, which resulted in a frequency cut off of 140 and 120 Hz, respectively. Looking at the porosity gradient (figure 3.14), there are only 2 zones of varying porosity for granular #2, however there are more zones of varying porosity for shrub #1. This observation is consistent with attributing a larger value of L for sample granular #2 when compared to shrub #1. However, this is a rough estimate and for that reason, a 3D numerical model is developed, using constant petrophysical parameters, apart from the porosity, to investigate in more detail mesoscopic FPD.

3.4.2.1 Numerical model and model results

Model development

COMSOL multiphysics was used to create a numerical model corresponding to the axial oscillation experiments. Biot's (1941) poroelastic quasistatic equations were solved by means of the displacement-pressure formulation (Quintal et al.,2011) within the frequency domain explored experimentally, using:

$$\nabla \cdot \sigma = 0 \,, \qquad \ldots (5.1)$$

$$\nabla \cdot \left(-\frac{k}{\eta}\nabla p_f\right) + \alpha\nabla \cdot (i\omega u) + \frac{I\omega p}{M} = 0 \ , \qquad \ldots (5.2)$$

where u is the solid displacement vector, with 3 dimensional components and σ is the stress tensor,

$$\sigma_{ij} = 2\mu\varepsilon_{ij} + \lambda e\delta_{ij} - \alpha p\delta_{ij} \ , \qquad \ldots (5.3)$$

where δ_{ij}, ε_{ij} and e are the Kronecker delta, components of the strain tensor and cubical dilation given by the strain tensor, respectively. The μ and λ are the shear modulus for the dry frame and Lamé's parameter $\lambda = K_d - 2\mu/3$. The coefficient M is (Biot and Willis, 1957):

$$M = \left(\frac{\phi}{K_f} + \frac{\alpha-\phi}{K_s}\right)^{-1} . \qquad \ldots (5.4)$$

The sample is modeled as a 38 mm diameter and 74 mm height cylinder. The porosity found in the CT scan's greyscale pictures allowed for a determination of porosity dependent on height, z, which is associated to a row of pixels (figure 3.14).

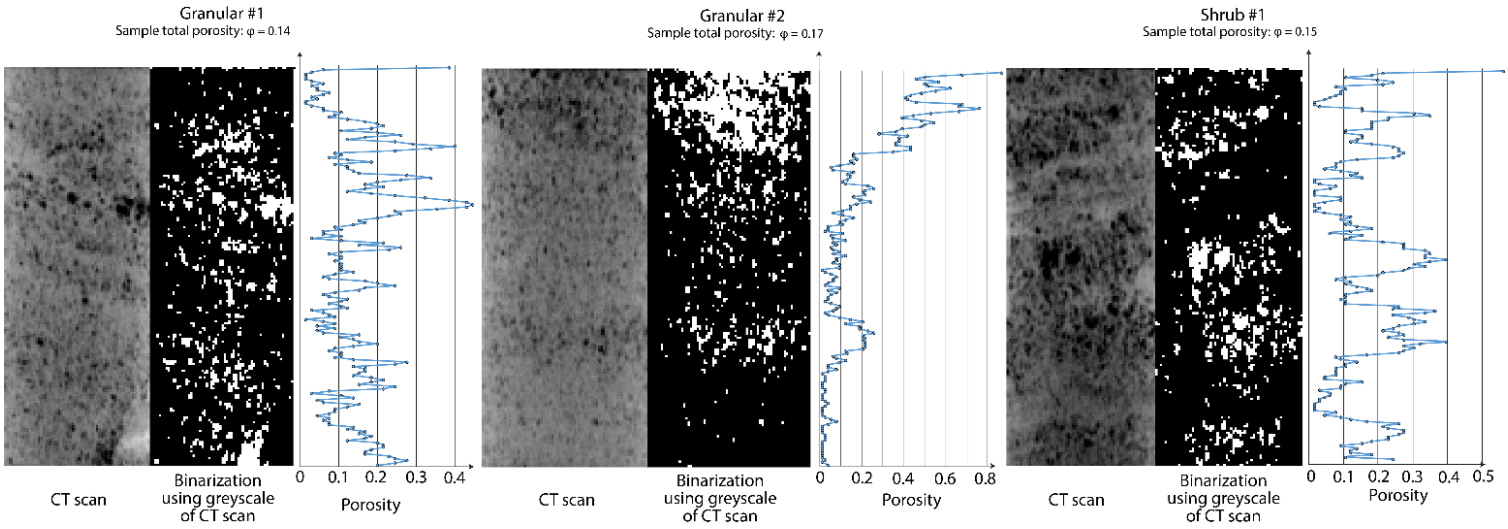

Figure 3.14: CT scan, binarization of the CT scan using greyscale and the porosity height gradient determined from the binarization of the CT scan for samples granular #1, #2 and shrub #1;

Tetrahedral elements are used to create a volumetric mesh within COMSOL multiphysics, then a finite element method is applied using this newly formed mesh to solve for the weak form of equations 5.1 and 5.2. To create undrained boundary conditions, the fluid pressure gradient is set to 0 along the outside limit of the volumetric mesh. An oscillatory axial strain is applied to the top

of the sample equal to 10^{-6}. The bottom of the sample's displacement in the z direction is set to 0. Table 3.2 shows the parameters used for all three samples in the numerical simulations, with the porosity taken using figure 3.14. The bulk and shear modulus were taken from the experimental data at 5 MPa effective pressures. The dynamic viscosity is taken as that of water, since the comparison will be made with the apparent frequency.

Samples	granular 1	granular 2	shrub 1
K_d(GPa)	15	15.4	13
G_d(GPa)	10.5	9.3	9.7
Dry density (kg/m^3)	2247.1	2177.9	2223.6
Permeability (m^2)	4 10^{-15}	16 10^{-15}	1 10^{-15}
$K_{glycerin}$ (GPa)		4.36	
η_{water} (Pa s)		0.001	

Table 3.2: Three carbonate samples properties for numerical simulations;

Numerical model results

Figure 3.15 shows the results for the Young's modulus and attenuation at the strain gauge location using the 3D numerical model with a porosity variation along z for frequencies between 10^{-1} to 10^4 Hz. To simulate the local measurements recorded by a strain gauge, the Young's modulus and attenuation are calculated from the local stress and strain measurements on a 5 mm central stretch, representing the size of a strain gauge. It is important to underline that all parameters in the 3D numerical model are constant apart from the porosity. The blue, green and pink data points represent samples granular #1, #2 and shrub #1, respectively. The Young's modulus increases by 0.2, 0.8 and 1 GPa for samples granular #1, #2 and shrub #1, respectively, when going from low to high frequencies. There is a tiny attenuation peak at 3 10^2 Hz, with a magnitude of 0.004, for granular #1. Granular #2 shows two Young's attenuation peaks at 1 10^2 and 1 10^3 Hz, both with magnitudes of 0.009. Finally, Shrub #1 shows a Young's attenuation peak at 1.5 10^2 Hz with a magnitude of 0.018.

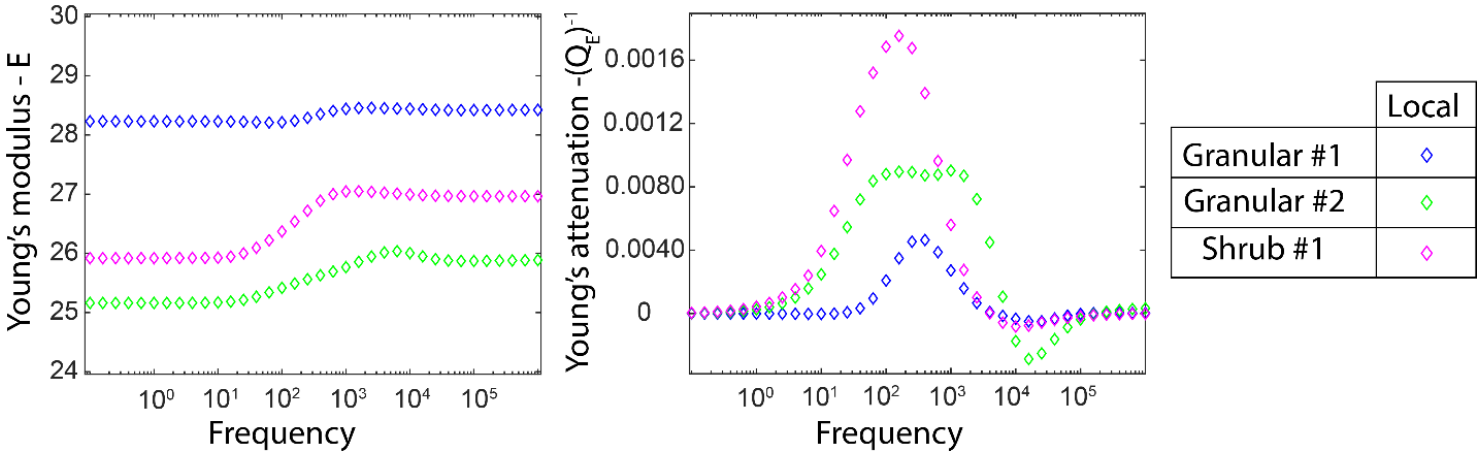

Figure 3.15: Young's modulus and attenuation at the strain gauge location as well as for the whole sample using the 3D numerical model with a porosity gradient along z for frequencies between 10^{-1} to 10^4 Hz;

3.4.2.2 Discussion of numerical and experimental low frequency attenuation results

For samples, granular #2 and shrub #1, there is a distinct attenuation peak, in the experimental results, at a frequency range around 100 Hz, which is not present in granular #1. Looking at the CT scans, it is easy to see that granular #1 has a much more randomly distributed porosity than granular #2 (see figure 3.14). This is in line with the comparison between the bulk modulus using hydrostatic and axial oscillations methods.

For the granular #1 sample, there is close to no dispersion or attenuation in the numerical model which is corroborated by the experimental data.

For the granular #2 sample, at 5 MPa effective pressure when going from low to high frequencies, the Young's modulus increases by 0.9 and 0.8 GPa, for the experimental and numerical results, respectively. For the shrub #1 sample, at 5 MPa effective pressure when going from low to high frequencies, the Young's modulus increases of 0.9 GPa and 1.1 GPa for the experimental and numerical results, respectively. For all three of these samples, the numerical model with porosity gradient gives a good estimation on the dispersion of the elastic moduli.

For granular #2, the experimental data shows an attenuation peak at 100 Hz, with a magnitude of 0.029. The numerical model results show a broad attenuation peak between 100 Hz and 1 kHz, with a magnitude of 0.009. For shrub #1, the experimental results show an attenuation peak at 300 Hz, with a magnitude of 0.036. The numerical model results show an attenuation peak at 200 Hz, with

a magnitude of 0.017. For these two samples, the frequency cutoff is well estimated, however the magnitude of the attenuation peaks underestimated by the numerical model.

Attempts were made to numerically simulate the mesoscopic flow using the same parameters with bulk and shear modulus dependent on height. The bulk and shear were derived from the porosity gradient, using a method from Fortin et al. (2007). However, the numerical results were not improved. This is probably due to the 1D porosity approximation (porosity vs z) made with a 2D representation (CT scan). Some porosity estimates along z were "unrealistic" as they had values higher than 40% (granular #2) which may imply that the size of the REV chosen for the porosity estimation is too small. It should be noted that for granular #2, the mesoscopic attenuation is pressure dependent, whereas the mesoscopic attenuation for shrub #1, is much less pressure dependent. This shows that the parameters which affect the mesoscopic FPD are effected by the change in effective pressure for granular #2 but less so for shrub #1. As porosity will not vary too much, it is most likely due to change in permeability and stiffness of the matrix, related to the samples facies (granular and shrub).

The comparison of the numerical and experimental results, would suggest that the attenuation seen in samples granular #2 and shrub #1 are related to mesoscopic FPD effects. Also, the frequency location of these peaks is within the range of what is reported in the literature Carcionne and Picotti, 2006; Masson and Pride,2007,2014). Indeed, Carcionne and Picotti, (2006) and Masson and Pride (2007,2014) has shown that critical frequency due to mesoscopic FPD effect should be in the 50-500 Hz frequency range, which is consistent with the numerical and experimental results in this work.

3.4.3 Comparison with log measurements

P- and s-wave well log velocity measurements were provided by Total and Petrobas and shown on figure 3.16. These were taken as an average over ~40 cm at a frequency of around 10 kHz. The in situ pressure for all three samples is 85 MPa with a pore pressure of 60 MPa leading to an effective pressure of 25 MPa.

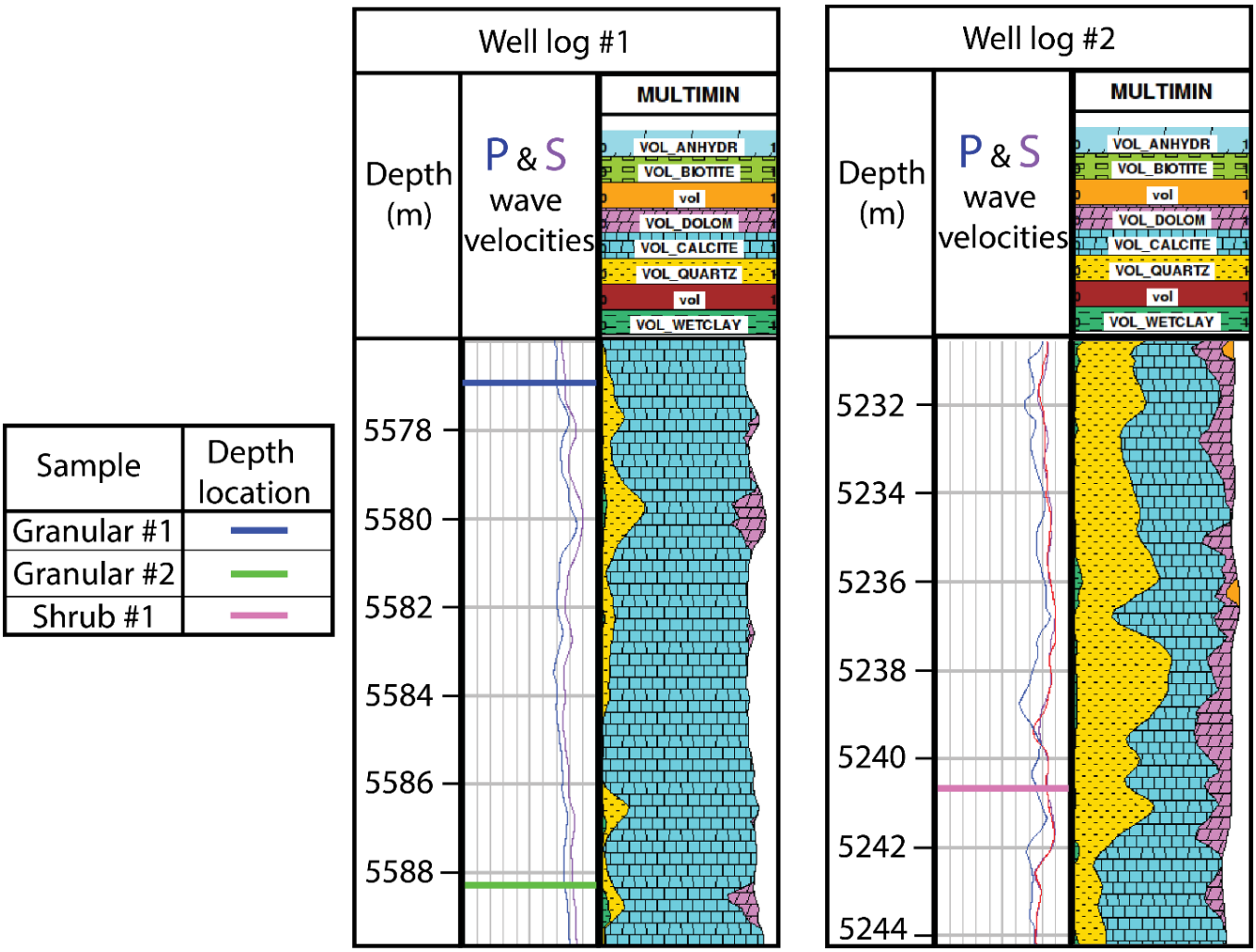

Figure 3.16: P- and s-wave velocities, with chemical composition at depth provided by Total and Petrobras;

Figure 3.17 shows the data collected from the axial oscillation tests in terms of p- and s-wave velocities using equations 3.5, within a frequency range between 10^3 and 10^5. All the data shown is in glycerin saturated conditions with the x, square, diamond and circle shapes representing effective pressures of 5, 15, 25 and 30 MPa, respectively. The large black x represents the p- and s-wave velocities found in situ.

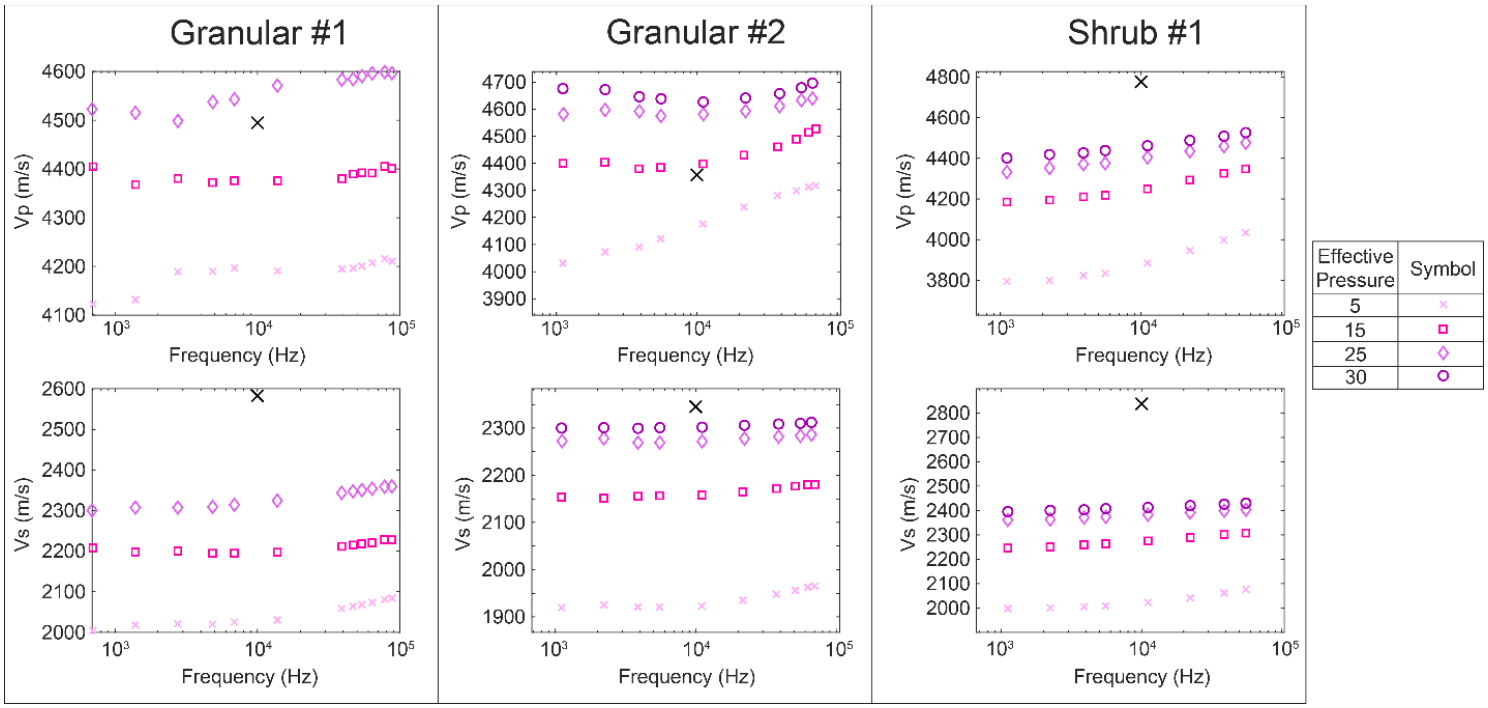

Figure 3.17: Axial oscillation data for all three carbonate samples, converted to P and S wave equivalency over a frequency range (103 to 105 Hz) compared to in situ log well data at the in situ effective pressure of 25 MPa;

For the granular #1 sample, the well log and experimental data, for the in situ effective pressure of 25 MPa, give a p-wave velocity of 4495 and 4543 m/s, respectively, whereas the well log and experimental data give an s-wave velocity of 2583 and 2314 m/s, respectively. The error between the in situ and experimental data is 1.1% and 12.0 % for the p- and s-wave velocities, respectively.

For the granular #2 sample, the well log and experimental data, for the in situ effective pressure of 25 MPa, give a p-wave velocity of 4357 and 4590 m/s, respectively, whereas the well log and experimental data give an s-wave velocity of 2346 and 2276 m/s, respectively. The error between the in situ and experimental data is 5.1 and 3.1 % for the p- and s-wave velocities, respectively.

For the shrub #1 sample, the well log and experimental data, for the in situ effective pressure of 25 MPa, give a p-wave velocity of 4777 and 4405 m/s, respectively, whereas the well log and experimental data give an s-wave velocity of 2838 and 2383 m/s, respectively. The error between the in situ and experimental data is 7.8 and 16.0 % for the p- and s-wave velocities, respectively.

There is a very good agreement between the insitu and experimental data for the two granular samples, with a little more divergence when considering shrub #1. The biggest part of the discrepancy between these measurements is probably due to the length wave difference between the methods. As lab scale, we measured an effective properties of the rock at 8 cm scale, whereas log measurements are effective properties over a length wave $\lambda=v/f\sim$ 45 cm (Bailly et al., 2019).

3.5 Conclusion

Three carbonate samples were tested in dry, brine and glycerin saturated conditions in a large apparent frequency range (7 10^{-2} to 10^{5} – 10^{6} – 5.5 10^{8} Hz) using a triaxial cell in undrained conditions. All three samples had a high frequency attenuation peak around 10 kHz, which was attributed to squirt flow. Two samples, which have slight heterogeneity, had 2 distinct attenuation peaks, the higher of which is attributed to squirt flow and the lower (~100 Hz) which is attributed to mesoscopic FPD effects. A numerical model was made to show that local attenuation can occur between regions of changing porosity. The location of the lower frequency attenuation peak is consistent with mesoscopic FPD effects found in the literature, as well as, with what was found in the numerical model developped in this work. Finally, the insitu data is compared to the experimental data, which shows good correlation.

4. Seismic dispersion and attenuation in fractured fluid-saturated porous rocks: an experimental study with an analytic and computational comparison

This chapter is under press in Rock Mechanics and Rock Engineering: Gallagher A., Fortin J., Borgomano J. V. M., (2022). Seismic dispersion and attenuation in fractured fluid-saturated porous rocks: an experimental study with an analytic and computational comparison.

Abstract

Although different fluid pressure diffusion (FPD) mechanisms caused by fractures have been extensively studied using analytical and numerical methods, there is little to no experimental work completed on them in laboratory conditions. In this paper, hydrostatic stress oscillations (frequency – 0.04 to 1 Hz) are used on an intact and saw cut sample, in dry and water saturated conditions, in a triaxial cell at different effective pressures in undrained conditions. The objective is to study the fracture's effect on the elastic properties of the sample and validate some computational fracture models, that have been explored in the literature. Experimental results highlight dispersion and attenuation in saturated conditions due to the fracture, which diminishes in amplitude as the effective pressure is increased, i.e. as the fracture is closed. From local strain gauge measurements, it is found that there is a local negative phase shift between stress and strain in water saturated conditions for the fractured sample, due to the location of the strain measurements. No attenuation observed in dry conditions. A simple 1D model using mass balance and mechanical equilibrium equations for a linear isotropic poroelastic homogeneous medium give prediction in very good agreement with the experimental results. A 3D model was also developed to allow a comparison between analytic, numerical and experimental results.

4.1 Introduction

Fractures are commonplace in reservoirs. Natural fractures are the consequence of geologic processes (cycle of burial, diagenesis, uplift, tectonic, erosional unloading…) but may also be created due to anthropogenic activities such as geothermal exploitation (Fleuchaus et al., 2017). Even if they only account for a small amount of the total porosity of a geological formation, they may control the reservoir permeability (Walsh, 1981; Paillet et al.,1987) and elastic properties (Matonti et al., 2015; Bailly et al., 2019b); thus a better knowledge of the effect of fractures on the physical properties of a reservoir is fundamental for deep geological repositories (Min et al.,2013), the exploitation of hydrocarbons (Gudmundsson and Løtveit, 2014), CO2 sequestration (Mazumder et al., 2006; Ulven et al., 2014) and geothermal exploitation.

Fractures can be defined as a type of porosity with small aspect ratios which is more compliant than equant pores and as such is more sensitive to stress. As a consequence, elastic properties and thus P- and S- wave velocities are strongly affected by the fracture density, orientation, connectivity and geometry (Walsh, 1981; Brajanovski et al. 2005; Gurevich et al. 2009; Galvin and Gurevich 2009&2015; Quintal et al., 2014; Guo et al. 2018a&2018b, Lissa et al., 2020). The elastic wave velocities for fluid saturated rocks, in the absence of mesoscopic (cm scale) fractures, can be frequency dependent resulting in attenuation and dispersion. This behavior has been shown to be attributed to different mechanisms. One of these fluid pressure diffusion (FPD) mechanisms is at a mesoscopic scale, between different regions and is dependent on the change in properties, such as compressibility, permeability and pore fluid viscosity, between regions (Müller et al., 2010). Heterogeneous rocks and multiple pore fluids can also create volumes of different compressibility which may trigger a similar viscoelastic response (White, 1975). Squirt flow is another FPD mechanism which happens at pore scale, within the representative elementary volume (REV), between stiff and more compliant pores (Batzle et al., 2006; Gurevich et al., 2010). The characteristic frequency is related to the aspect ratio of the different microscopic pores, the elastic properties of the sample and is inversely proportional to the dynamic viscosity of the pore fluid.

In saturated condition, the presence of mesoscopic fractures can also change the elastic properties of samples by promoting dissipation through FPD. This has been shown through analytical modelling (Brajanovski et al. 2005; Gurevich et al. 2009; Galvin and Gurevich 2009&2015), and also through numerical modelling with simple cases of a single fracture and simple stress fields applied (Chapman and Quintal, 2018; Caspari et al. 2019), to slightly more complicated geometries of fractures intersecting each other at 90^{o} (Vinci et al., 2014; Lissa et al., 2020), to even more complex

geometries, such as multiple parallel fractures (Cai et al.,2000; Carcione et al., 2012) or even fractures intersecting at 45º (Quintal et al., 2014). Some work has also been done *in situ* at the Grimsel Test Site in the Swiss alps by Barbosa et al. (2019), who investigated the effect of fractures in a borehole, using a sonic logging tool, which allowed for p- and s-wave velocities as well as their attenuation measurements, with intrinsic background attenuation estimated and removed by studying the intact regions of the borehole.

However, there is a lack of data that investigates in the laboratory, under pressure and in undrained conditions, the frequency dependence of fractured porous rocks. Nakagawa (2013) was able to measure normal and shear fracture attenuation at a range of seismic frequencies (between 1 and 100 Hz) with different axial stresses applied normal to the fracture. This setup was not in a pressure vessel, therefore limiting the stress oscillations to be purely axial and limiting the tests to have a very low pore pressure in the sample to prevent fluid migration between the jacket and the sample. Amalokwu et al. (2014) showed results on man-made intact sandstones and sandstones with aligned penny-shaped voids at different water saturation levels at 40 MPa effective pressure and measurements made at a single frequency of 650 kHz, which showed more attenuation in the sandstone with aligned penny-shaped voids. Amalokwu et al. note however that there can be microstructural differences between the intact and fractured samples due to manufacturing processes, which makes it hard to compare absolute attenuation peaks between both samples.

One needs to be careful regarding the definition of a local and global measurement, in a laboratory setting, when an isotropic medium has a fracture introduced to the sample. As a matter of fact, Chapman and Quintal (2018) investigated numerically the mechanical properties of a fully saturated Berea sandstone sample with a single fracture and distinguished i) the elastic modulus of the whole fractured sample from ii) the apparent elastic modulus of the matrix (local measurement), both affected by the pore pressure variation induced by the fracture. In the second case, the results showed different attenuation peaks depending on where the local strain was measured (more or less close to the fracture). They also show that in this case a negative phase shift between stress and strain is expected.

Finally, one needs to be especially careful that the measured attenuation is related to the fracture and not to other mechanisms like squirt-flow (Gurevich et al.,2010; Chapman et Quintal, 2018), partial saturation (Chapman et al., 2016; Spencer et al., 2016; Chapman et al., 2019), drained-undrained transition (Pimienta et al., 2016) or even mesoscopic FPD (Carcione and Picotti, 2006).

The goal of this work is to validate numerical models by experimentally showing FPD caused by fractures, such as the simulation by Chapman and Quintal (2018). To accomplish this, the elastic properties of an intact sample were monitored during hydrostatic oscillations at a frequency range of 0.04 to 1 Hz in dry and water saturated conditions, with undrained boundaries, and at 3 effective pressures. The effective pressure is defined as the difference between the confining and pore pressure, with the confining and pore pressure defined as the pressure in the triaxial cell and the pressure in the pore fluid of the sample, respectively. The sample was then cut in half, to create a simple known fracture geometry. The fractured sample was then tested again following the same procedure as for the intact sample. Although, the fracture strain cannot be directly measured due to the experimental limitations, we measured the strain in the matrix -affected by pore pressure change due to the fracture- similar to what was investigated in Chapman and Quintal's work (2018), allowing comparisons to numerical models in the literature. Permeability tests were completed on the intact and saw cut sample at varying effective pressures to estimate the hydraulic aperture and stiffness of the fracture in undrained conditions, using innovative microvalves. A 1D model was developed, using the hydraulic aperture and stiffness measured. The model is used to calculate the pore pressure field with frequencies as well as the bulk modulus and attenuation with frequency. In addition, a numerical model was made in COMSOL multiphysics to take into account the 3D geometry and validate the 1D model. Finally, the numerical and analytical models were compared to the experimental data.

4.2 Experimental procedure

The dispersion and attenuation of the bulk modulus was measured using the stress-strain method (Adelinet al. 2011; David et al. 2013; Pimienta et al., 2015), in a TOP Industries™ triaxial cell (figure 1) installed at the ENS Paris geology laboratory (Borgomano et al., 2020). It is outfitted with 3 pumps, two of which are oil filled and control cell pressure and the axial piston, and the final pump is a Quizix dual pump (QX1500HC model), which is water filled and controls upstream and downstream pore pressures in the sample.

Figure 4.1: Top Industry triaxial cell: (left) when cell is closed, (right) cell is open, close up on jacketed sample. Modified after Borgomano et al., 2020;

Four strain gauge pairs are attached to the surface of the sample at mid height (figure 2) and are used to measure local strain during the hydrostatic-stress oscillations. The strain gauge pairs are two directional and have one axial and one radial component at 90° from each other. They have a resistance of 350 Ω and have a gauge length of 5 mm. The sample is held between a top and bottom cap, and is separated from the confining oil by a black neoprene jacket.

The strain gauges and the pressure transducers are connected to the data acquisition system (DAQ), which can record up to a frequency of 4 kHz. The cell pump controls the cell pressure and can reach a maximum pressure of 100 MPa with a hydrostatic oscillating mean amplitude of 0.2 MPa and a minimum and maximum oscillating frequency of 0.001 and 1.3 Hz, respectively.

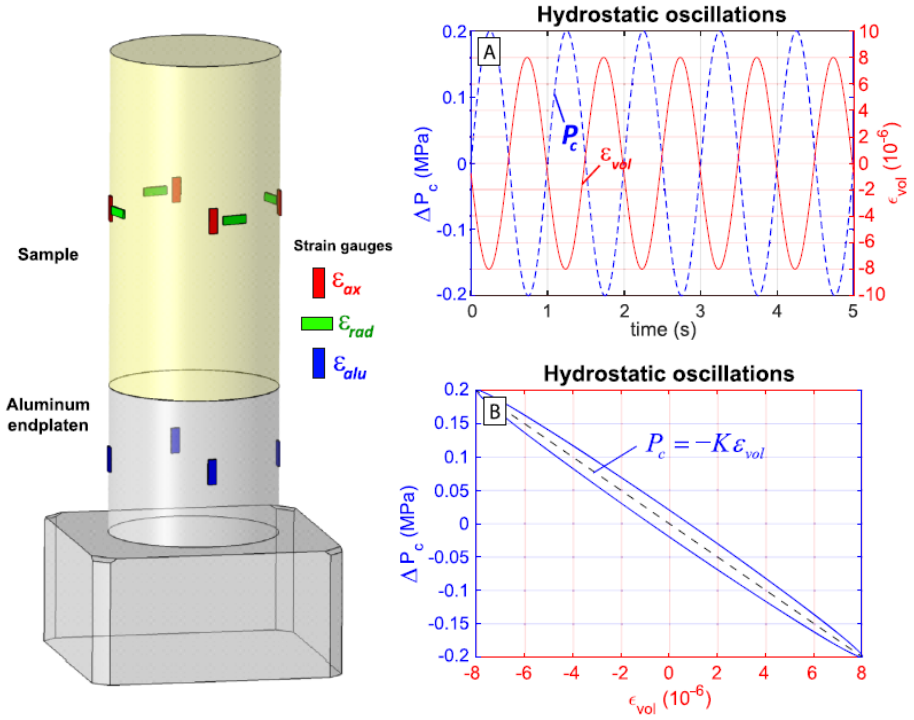

Figure 4.2: Strain gauge positions (left) and typical stress-strain recordings of hydrostatic[(a) and (b)] oscillations (around mean values) on a viscoelastic material. The strains (ε_{ax}, ε_{rad}, ε_{alu}) are each averaged from four strain gauges around the circumference of the sample or aluminum end platen at mid-height. Modified after Borgomano et al., 2020;

It's important to underline that every test completed under pore fluid saturation in this paper was done in undrained conditions. This was accomplished using microvalves which are placed in the bottom and top end platen, which when closed reduce the dead volume to ~ 20 µl. The dead volume can be defined experimentally as the volume of fluid between the inlet and outlet of the sample and the pump or as an excess of water which acts as a fluid reservoir outside of the sample. This implies that the mass of fluid inside the sample during the oscillation is constant, a necessary condition to measure directly the undrained moduli (Fortin and Guéguen, 2021). More details of the experimental set up regarding these microvalves are documented in Borgomano et al. (2020).

4.2.1 Hydrostatic stress oscillations

The confining pump, which is connected to the main chamber of the triaxial cell, is able to oscillate around a confining pressure at a frequency of 0.01 to 1.3 Hz, which is measured using a pressure transducer attached to the main chamber of the triaxial cell using a 1/8" NPT tube. When a sample is put into the triaxial cell, the hydrostatic pressure in the cell is cycled between 5 and 25 MPa three times to ensure all compliant pores are closed. The strain induced by these oscillations are measured

using the strain gauges attached to the sample. The magnitude of the confining pressure oscillation is 0.2 MPa to ensure that the strain is within the linear elastic range ($\varepsilon \sim 10^{-6}$) (Winkler and Murphy III, 1995). The apparent bulk modulus is calculated as:

$$K = \frac{-\Delta P_c}{\varepsilon_{vol}}, \quad \ldots (4.1)$$

where K is the bulk modulus, ΔP_c is the change in confining pressure and ε_{vol} is the volumetric strain. The volumetric strain is calculated as $2\varepsilon_{rad} + \varepsilon_{axial}$, where ε_{rad} and ε_{axial} are the mean values of all strain gauges glued at mid-height on the sample in the axial and radial directions, respectively (figure 2) . Using a MATLAB program, fast fourier transforms (FFTs) are used to determine the stress and strain amplitude for each signal.

4.2.2 Attenuation (Q^{-1})

In the case of porous rocks, the skeleton of the rock itself is none dispersive. However, the pore fluid diffusion induced by a change in the stress field is time-dependent. This can cause dissipation of elastic energy within the sample, similar to that of the rheology of a viscoelastic material (O'Connell and Budiansky, 1977). This anelastic behavior is highlighted in figure 2 B, where the stress-strain curve forms an ellipse, with the area within the ellipse representing the energy lost. This attenuation can be characterized by calculating the phase shift between the stress and the strain, when expressed as a complex stress $\bar{\sigma} = \sigma e^{i(2\pi f t + \phi_\sigma)}$ and complex strain $\bar{\varepsilon} = \varepsilon e^{i(2\pi f t + \phi_\varepsilon)}$ for a dynamic oscillation of frequency f, where ϕ_σ and ϕ_ε are the stress and strain phases.

The stress is related to the strain through its complex modulus $\bar{M}$.

$$\bar{\sigma} = \bar{M}\bar{\varepsilon} \quad \ldots (4.2)$$

The attenuation factor ${Q_M}^{-1}$ is then defined as follows (O'Connell and Budiansky, 1978):

$${Q_M}^{-1} = \frac{Im(\bar{M})}{Re(\bar{M})} = \frac{Im(\bar{\sigma}/\bar{\varepsilon})}{Re(\bar{\sigma}/\bar{\varepsilon})} = \tan(\phi_\sigma - \phi_\varepsilon)\,. \quad \ldots (4.3)$$

To calculate the ${Q_M}^{-1}$, fast Fourier transforms (FFTs) were applied to the stress and strain curves to extract the phases of each, using MATLAB. Using equations (2.1 and 2.3) the attenuation of the bulk modulus can be calculated as:

$${Q_{K_{hyd}}}^{-1} = \tan(\phi_{-\Delta P_c} - \phi_{\varepsilon_{vol}}) \quad \ldots (4.4)$$

4.2.3 Sample characterization

The sample came from Rustrel in the Urgonian Limestone formation in the SE of France (Borgomano et al., 2019). The Rustrel sample was machined from a core into a cylindrical shape with a diameter of 39 mm and a height of 78 mm (figure 3). Using the triple weight method, the porosity, ϕ, of the sample was found to be 16% +- 0.5%. The dry density of the sample is around 2291.5 kg m^{-3}. A thin section was made from a section right above the sample, which was then scanned using a digital microscope (Keyence digital microscope VHX-5000), and a scanning electron microscope (SEM). Figure 3 shows the digital microscope picture (B) which is at a larger scale, with an SEM scan (A) at a smaller scale, as well as pictures of the intact and saw cut samples (C and D). This limestone is made of calcite cement -(b) in figure 3A- surrounding micritic peloidal grains -(a) in figure 3A-; fragments of rudist shells can also be observed.

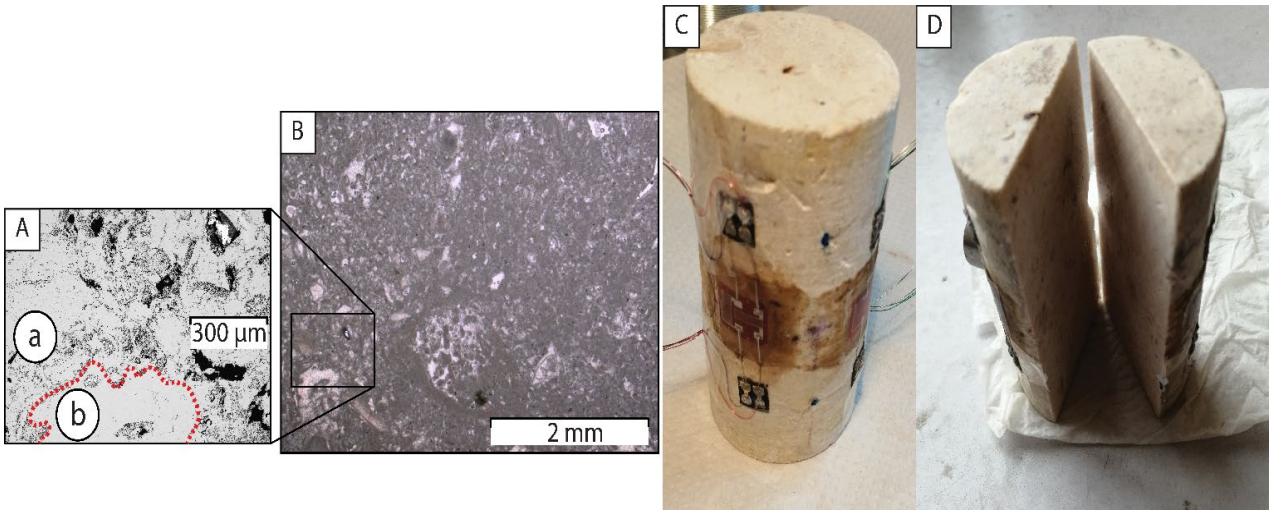

Figure 4.3: (A): SEM scan of the thin section; (B): Digital microscope picture of the same thin section (using Keyence digital microscope VHX-5000); (C)&(D): Intact and sawcut Rustrel samples;

The permeability of the intact sample is 3 10^{-17} m^2 at an effective pressure of 7.5 MPa (table 4.1). After testing the intact sample, it was then cut down its center, along its length using a diamond saw with a width of 2 mm. The permeability of the saw cut sample was measured at varying confining pressures (2, 6, 10, 14, 18, 22 and 26 MPa) using a constant flow rate at the inlet of 1.5 ml/min and having the outlet pressure at 0 MPa. The effective pressure was then calculated by subtracting half the inlet pressure from the confining pressure.

Intact Parameter	Values
Sample length	L = 78 mm
Sample diameter	d = 39 mm
Sample's porosity	ϕ= 0.16
Sample's permeability	K = 3 10^{-17} m^2
Confining oscillation amplitude	P_o= 0.2 MPa
Water Bulk Modulus	K_{wat} = 2.2 GPa
Water viscosity	η_{wat}=10^{-3} Pa s

Table 4.1: Intact Rustrel sample and pore fluid characteristics;

4.2.3 Hydraulic Aperture

The hydraulic aperture of the fracture in the saw cut sample is calculated assuming the total flow rate through the sample (Q_w) is equal to the sum of flow rates i) through the fracture (Q_f) and ii) through sample matrix (Q_m).

$$Q_w = Q_m + Q_f \quad \ldots (4.5)$$

Darcy's law states:

$$Q = \mathrm{A}\frac{\mathrm{k}}{\eta}\frac{\partial \mathrm{P}_f}{\partial \mathrm{z}}, \quad \ldots (4.6)$$

where k is the permeability (m^2), η is the dynamic viscosity of the pore fluid (Pa.s), Q is the flow rate parallel to the fracture ($m^3.s^{-1}$), A is the area of the sample perpendicular to the flow (m^2) and P_f is the pore fluid pressure (Pa). Equation 2.6 was used to calculate the permeability.

Equation 2.6 leads to:

$$k_w A_w = k_m A_m + k_f A_f \quad \ldots (4.7)$$

where k_w, k_m and k_f are the whole sample, matrix and fracture permeability, respectively, and A_w, A_m and A_f are the whole sample, matrix and fracture areas, respectively .

Apart from the permeability of the fracture, each other term in equation 2.7, is known or is a function of the hydraulic aperture (b) of the fracture. In addition, assuming a parallel plate model, the permeability of the fracture can also be related to b and :

$$k_f = \frac{b^2}{12} . \quad \ldots (4.8)$$

Using 2.7 and 2.8, a cubic equation is derived which can be used to infer the hydraulic aperture at varying effective pressures.

4.2.4 Stiffness of the fracture

The normal stiffness of a fracture (Z_n) is defined as (Goodman, 1976):

$$db = \frac{1}{Z_n}(n.d\sigma.n + dP_f), \quad \ldots (4.9)$$

where n is normal to the fracture and σ the applied stress field. Note that in the case of hydrostatic loading equation 2.9 is simplified as

$$db = -\frac{1}{Z_n}(dP_c - dP_f) = -\frac{1}{Z_n}dP , \quad \ldots (4.10)$$

where P_c is the confining pressure and P is the effective pressure.

Knowing the hydraulic aperture at several different effective pressures, m, allows approximation of the fracture stiffness at a given effective pressure P_m : the stiffness is calculated between two loading steps P_{m-1} and P_{m+1},

$$Z_n^m = \frac{P_{m+1} - P_{m-1}}{b_{m-1} - b_{m+1}}, \quad \ldots (4.11)$$

where Z_n^m is the stiffness, b_m is the hydraulic aperture measured at the loading step P_m.

Although efforts were made to simplify the geometry of the fracture, it is important to underline that the stiffness is an estimation of the true mechanical aperture as the parallel plate model (equation 2.8) assumes a continuous aperture along the whole fracture, whereas a more realistic geometry would be a fracture with distinct contact areas along the fractures, which is bound to change with increase in effective pressure. Li et al. (2008) showed that as the effective pressure is increased, the difference between mechanical and hydraulic aperture diverge, due to the creation of more complex and tortuous flow paths.

4.3 Experimental results

In the first part of this section, the hydraulic aperture, permeability and apparent stiffness of the fracture will be shown. The second part shows the experimental results on the elastic properties of the intact and saw cut samples performed at 5, 10 and 20 MPa of effective pressure saturated with air and water. Figure 4 shows a schematic of the intact and saw cut samples, with the coordinate system used in the next sections.

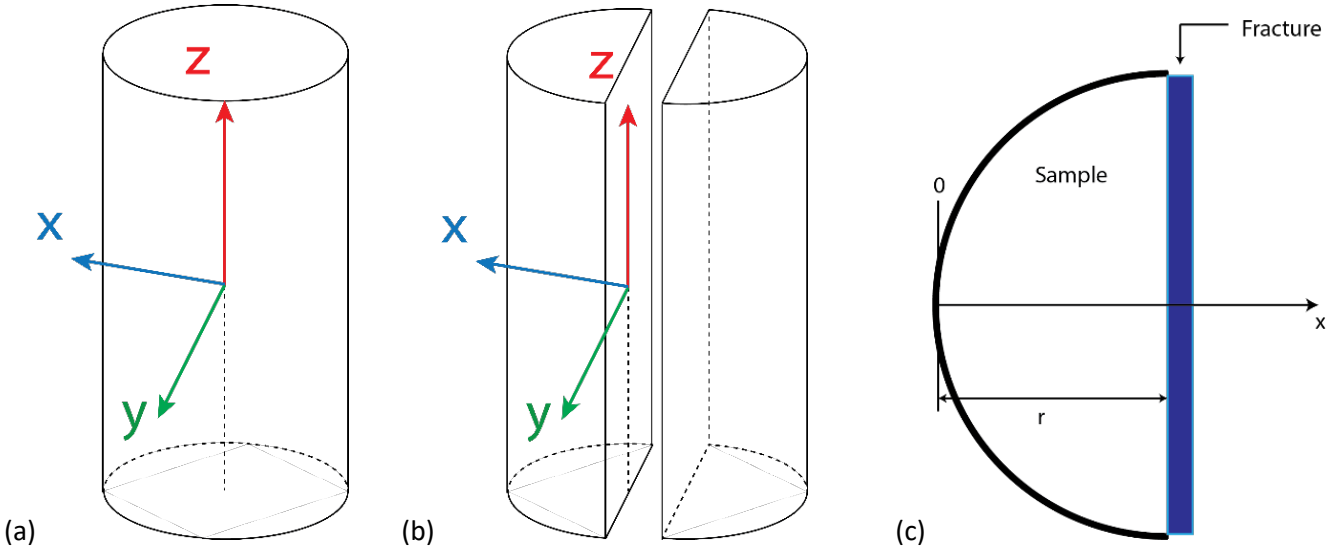

Figure 4.4: Intact (a) and saw cut (b) sample with xyz Cartesian coordinate system; (c) xy representation of saw cut sample;

4.3.1 Hydraulic Measurements

4.3.1.1 Saw cut fracture permeability and hydraulic aperture

Figure 5 shows, in orange, the permeability of the saw cut sample versus the effective pressure. The figure shows that the permeability decreases as confining pressure is increased, i.e. as the fracture is being closed. The permeability of the sample was measured at 7 different effective pressures. Within this range, the permeability dropped by 1.4 orders of magnitude as the effective pressure was increased from 1.8 to 22 MPa.

The hydraulic aperture of the fracture was then calculated following the procedure described in section 2.3, within the same effective pressure range and is shown in blue. Within this range, the hydraulic aperture dropped from 14.5 to 5 µm as the effective pressure was increased from 1.8 to 22

MPa. However, the slope of change in hydraulic aperture is much steeper between 1.8 and 11.6 MPa of effective pressure with a drop in hydraulic aperture from 14.5 to 6.0 µm than it is between 11.6 and 22 MPa of effective pressure with a drop in hydraulic aperture from 6.0 to 5.0 µm. This trend shows that the change in permeability and hydraulic aperture due to change of effective pressure mainly occurs for an effective pressure lower than 12 MPa for this specific man-made fracture.

The intact permeability was measured during saturation and was found to be 3 10^{-17} m^2 at an effective pressure of 7 MPa (orange line in figure 5). This result is in agreement with the study of Borgomano (2018), who showed that between effective pressures of 2.5 and 20 MPa, the permeability of the Rustrel sample changes slightly from 4 10^{-17} to 2.5 10^{-17} m^2.

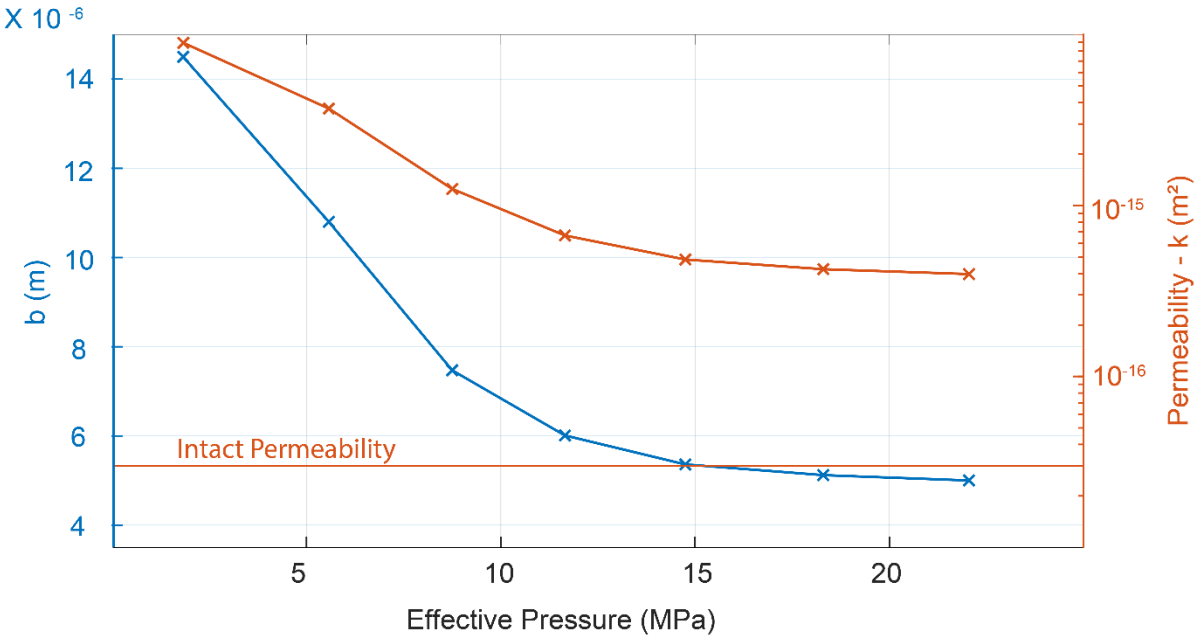

Figure 4.5: 1) left axis: fracture aperture and 2) right axis: permeability log scale versus effective pressure;

4.3.1.2 Stiffness of the fracture versus effective pressure

Figure 6 shows, the change in stiffness of the fracture, versus the effective pressure applied to the sample. The stiffness of the fracture was calculated following the procedure described in section 2.4, which also explains the change in number and magnitude of effective pressure points (see equation 2.11). Within this range, the stiffness of the fracture increased from 9.9 10^{11} to 2.0 10^{13} Pa m^{-1} as the effective pressure was increased from 5.3 to 18.4 MPa, which represents an increase of 1.3 orders of

magnitude. This figure shows, as expected, that the fracture stiffness is increasing exponentially as the effective pressure is increased. Note that the fracture stiffness is obtained through permeability measurements and under the assumption of a parallel plate model, it is thus a rough estimation of the true fracture stiffness. These results will be compared in the discussion to the fracture stiffness obtained using analytical methods developed further on.

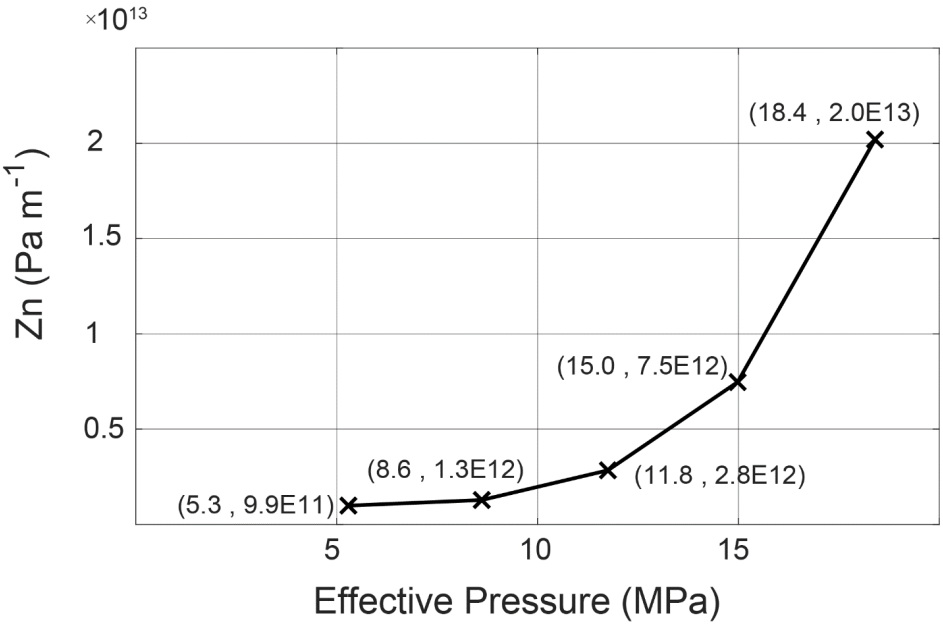

Figure 4.6: Normal stiffness of the fracture (Zn) versus effective pressure;

4.3.2 Hydrostatic measurements

This sub-section focuses on the results derived from the hydrostatic oscillations, which were performed on the dry and water saturated, intact and saw-cut Rustrel sample, at 5, 10 and 20 MPa effective pressures, at a frequency range between 0.04 and 1.1 Hz.

4.3.2.1 Hydrostatic oscillation - Intact sample

Figure 7 shows the results for the hydrostatic oscillations at 5, 10 and 20 MPa effective pressure, in dry and water saturated undrained conditions, for the intact Rustrel sample. The green and blue crosses represent the dry and water intact data, respectively. The bulk modulus for the dry intact data is constant for all frequencies at 25.3, 25.4 and 26.9 GPa for effective pressures of 5, 10 and 20 MPa, respectively. The attenuation for these are close to 0 and are within the precision of our setup (<0.02).

The bulk modulus for the water saturated intact data is constant at all frequencies at around 30.2, 31.1 and 32.6 GPa for effective pressures of 5, 10 and 20 MPa, respectively. The prediction of the water saturated bulk modulus from the dry bulk modulus can be obtained using Gassmann's equation (Gassmann, 1951):

$$K_u = K_d + \alpha\left(\frac{\phi}{K_f} + \frac{(\alpha-\phi)}{K_s}\right)^{-1}, \quad \ldots (4.12)$$

where K_u and K_d are the undrained and dry moduli, K_f the fluid bulk modulus, K_s the solid mineral bulk modulus, ϕ the porosity and α =1-K_d/K_s the Biot coefficient. The predictions of the undrained bulk modulus are given on figure 6 (black lines) using a solid mineral bulk modulus of calcite (77 GPa), which is what is observed in the SEM scan, and are in good agreement with the measured undrained bulk modulus.

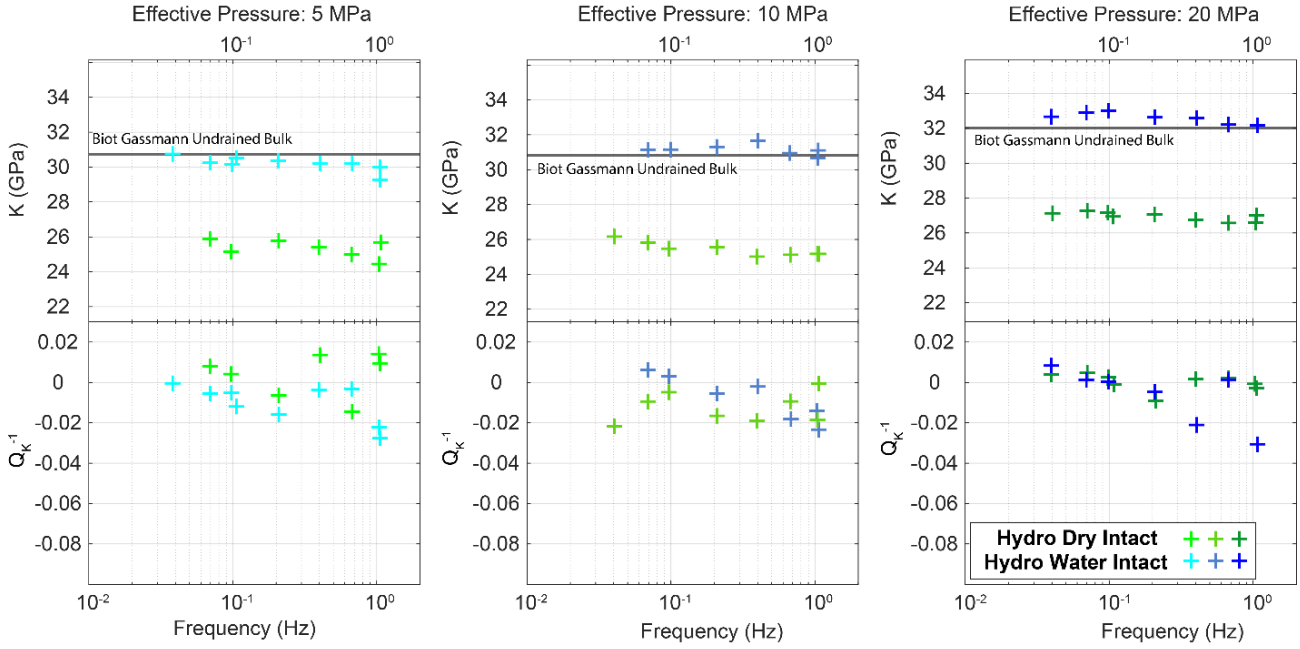

Figure 4.7: Intact Rustrel's dry and water bulk moduli and attenuation at 5, 10 and 20 MPa P_{eff} for axial oscillations. In addition, the prediction of the undrained bulk modulus from Gassmann's equation is plotted. A good match is found between the prediction of Gassmann's equation and the measured undrained bulk moduli;

4.3.2.2 Hydrostatic oscillation - Saw cut sample

Figure 8 shows the results for the hydrostatic oscillations at 5, 10 and 20 MPa effective pressure, in dry and water saturated conditions, for the saw cut Rustrel sample. The green and blue Xs represent the dry and water saw cut data, respectively. The apparent bulk modulus is shown in the top half and

the phase shift is shown in the bottom half. The apparent bulk modulus is calculated in the same way as the bulk modulus for the intact sample. This bulk modulus is not the bulk modulus of the fractured sample, as strains are measured locally by strain gauges glued on the matrix. This apparent bulk modulus is the bulk modulus of the matrix (or background) affected by pore pressure changes induced by the fracture. The phase shift is calculated in the exact same way as for the bulk attenuation for the intact sample, however since the strain measurements are local, it is not the attenuation of the fractured sample, but a phase shift between strain and stress due to the time delay for pore fluid to flow from the fracture to the matrix.

The apparent bulk modulus for the dry saw cut data is constant for all frequencies at 26.7, 28 and 28 GPa for effective pressures of 5, 10 and 20 MPa, respectively. The error band shown in figure 8 is defined using the mean and standard deviation of the dry saw cut phase shift data and is within the typical precision (<0.02) found for dry samples in this setup. This is used to compare to the water saturated data. The bulk moduli for the dry saw cut sample are very close to those obtained in the intact sample; indeed, the bulk modulus is obtained from strain gauges glued on the rock: it is a local measurement.

Under water saturation and for 5 MPa effective pressure, the apparent bulk modulus reaches a peak at the lowest frequency of 0.07 Hz with a value of 36 GPa. The value for the apparent bulk modulus decreases with increasing frequency until 0.4 Hz, at which point it stabilizes around 31 GPa. The phase shift between the stress and strain is negative at low frequencies, with values around -0.08, and increases to 0 at 1 Hz. For 10 MPa effective pressure, again the apparent bulk modulus is at its peak at the lowest frequency of 0.07 Hz with a value of 34.3 GPa. This value decreases with increasing frequency until 0.4 Hz at which point it stabilizes around 32 GPa. The phase shift between stress and strain is negative at low frequencies, with values around -0.02 and increases to 0 at 1 Hz. For 20 MPa effective pressure, the apparent bulk modulus is constant for the full frequency range and there is no attenuation. The dry bulk modulus of the matrix in the saw cut sample is slightly larger by ~1 GPa, than the one measured in the intact sample. This might be due to the extra hydrostatic cycling that the sawcut sample was imposed at the start of every triaxial test, which is common practice to close microcracks; but note that it is also in the error bar of the bulk modulus (~ 1 GPa).

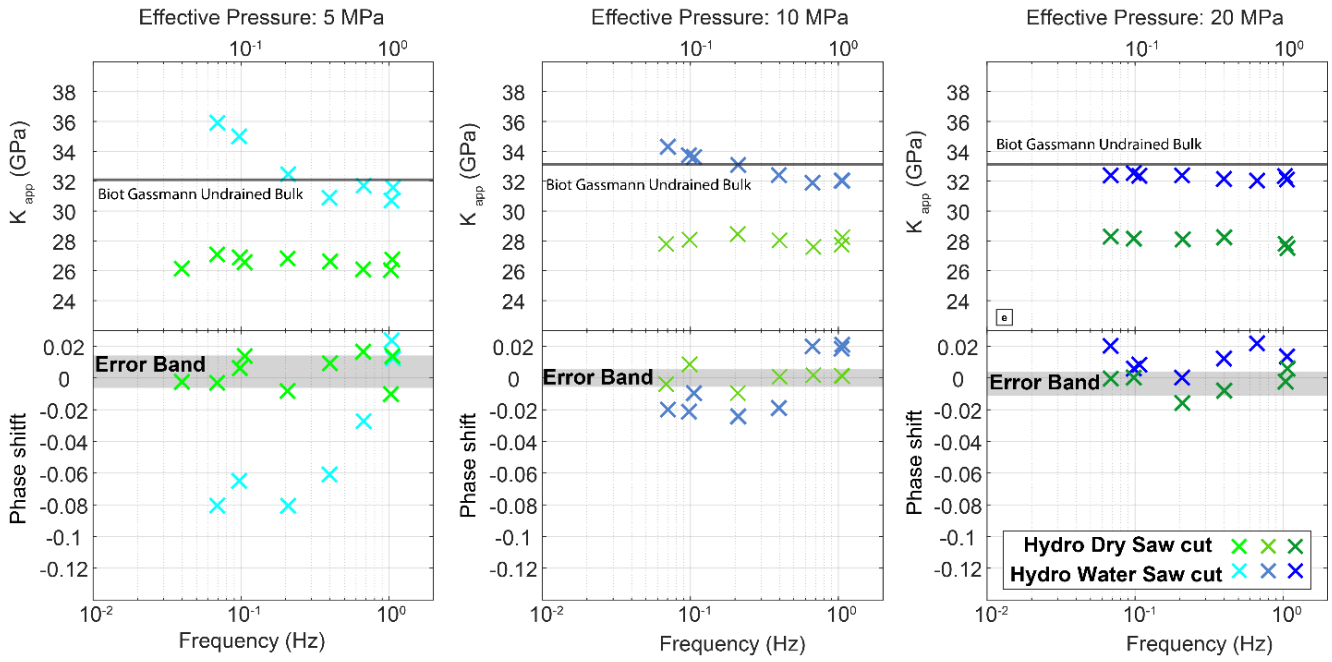

Figure 4.8: Saw cut Rustrel's dry and water saturated bulk modulus and phase shift between stress and stain at 5, 10 and 20 MPa Peff for hydrostatic oscillations;

4.4 Modeling for the saw cut samples

Theoretical models of dispersion due to wave-induced fluid flow between pores and fractures have been developed based on poroelasticity theory (Chapman 2003, Brajanovski et al. 2005, Gurevich et al. 2009). These models show that the characteristic frequency of dispersion depends on the matrix permeability, fluid viscosity, as well as the fracture geometry and properties. The aim, here, is to model the experiment, and in particular the fact that measurements are local measurements obtained by strain gauges, which has not been developed analytically to the authors knowledge. The present approach is consistent with the theory of poroelasticity and, as in the work of Brajanovski et al. (2005), the mechanism behind the dispersion is fluid flow induced between the matrix and the fracture.

4.4.1 Pore pressure

Here we develop a 1D analytic solution along x within the frequency domain (figure 4 c). A mass balance and mechanical equilibrium equation for a linear isotropic poroelastic homogeneous

medium, leads to a partial differential equation which involves the pore fluid pressure (e.g. Rice and Cleary, 1976; Zimmerman, 2000; Guéguen and Boutéca,2004):

$$\frac{\partial p_f}{\partial \mathrm{t}} - \frac{kBK_d}{\eta\alpha(1-\alpha\mathrm{B})}\nabla^2 p_f + \frac{BK_d}{1-\alpha\mathrm{B}}\frac{\partial \varepsilon_v}{\partial \mathrm{t}} = 0\,, \qquad \ldots (4.13)$$

where k, K_d, B, p_f, α and ε_v are the rock's permeability, drained bulk modulus, Skempton's coefficient, pore fluid pressure, Biot's coefficient and the volumetric strain, respectively.

The oscillating hydrostatic pressure is applied so that $P_c(t)$ is sinusoidal and time dependent ($P_c(t) = P_o e^{i\omega t}$). Again, the pore fluid pressure is dependent on the location x (1D model), as well as being time dependent, $\mathrm{p}_f(x,\mathrm{t}) = f(x)\, e^{i\omega t}$. Substituting the oscillating hydrostatic pressure and pore fluid pressure equations into equation 4.1 leads to:

$$f''(x)\frac{ik}{\eta S\omega} + f(x) = B\mathrm{P_o}\,, \qquad \ldots (4.14)$$

where S is the rock's storage coefficient ($S = \alpha/(\mathrm{B}K_d)$). Using the fluid hydraulic diffusivity ($D = k/(S\eta)$), the previous equation can be rewritten as:

$$f''(x)\frac{iD}{\omega} + f(x) = B\mathrm{P_o}\,. \qquad \ldots (4.15)$$

The boundary conditions, at x=0 (at the jacket) and x=r (at the fracture), are used to solve this problem. At x = 0, fluid is not allowed to flow out of the sample, which leads to:

$$\left.\frac{\partial \mathrm{P}_f}{\partial \mathrm{x}}\right|_{x=0} = 0\,. \qquad \ldots (4.16)$$

The second boundary condition states that there is a mass balance between the pore fluid leaving the pore space in the sample and the pore fluid entering the fracture which happens at x = r. The mass of pore fluid, *m*, flowing from the sample to the fracture is given by Darcy's law:

$$\left.\frac{\partial \mathrm{m}}{\partial \mathrm{t}}\right|_{x=r} = -\rho\frac{kA}{\eta}\left.\frac{\partial \mathrm{P}_f}{\partial \mathrm{x}}\right|_{x=r}, \qquad \ldots (4.17)$$

where ρ is the fluid density and *A* is the surface area of the fracture in the y-z plane. The change of pore fluid mass in the fracture is related to the pore fluid pressure, and the volume change of the fracture:

$$\frac{\partial \rho\mathrm{V}}{\partial \mathrm{t}} = \rho\frac{V}{K_f}\frac{\partial \mathrm{P}_f}{\partial \mathrm{t}} + \rho\frac{\partial \mathrm{V}}{\partial \mathrm{t}}\,, \qquad \ldots (4.18)$$

where V is half of the fracture volume and K_f the fluid bulk modulus. The volume change of the fracture is related to the change in its aperture, *b,* and can be expressed as $dV = A\ db/2$. In addition db is related to the fracture's normal stiffness, Z_n (equation 2.10).

Thus combining 4.5, 4.6 and 2.10, leads to the boundary condition at x=r:

$$S_1 \frac{\partial \mathrm{P}_f}{\partial \mathrm{t}}\Big|_{x=r} - \frac{A}{2Z_n}\frac{\partial \mathrm{P}_c}{\partial \mathrm{t}}\Big|_{x=r} + \frac{kA}{\eta}\frac{\partial \mathrm{P}_f}{\partial \mathrm{x}}\Big|_{x=r} = 0 \text{ , with } S_1 = \frac{V}{K_f} + \frac{A}{2Z_n} \approx \frac{A}{2Z_n} \ . \quad \ldots (4.19)$$

In the estimation of S_1, the compressibility of the fluid can be neglected in comparison to the fracture stiffness. Using both boundary conditions, the pore fluid pressure $\mathrm{p}_f(\mathrm{x},\mathrm{t})$ can be solved:

$$P_f(x,t) = P_o e^{i\omega t}\left(B + \cosh\sqrt{\frac{i\omega}{D}}x\left[\frac{1-B}{2Z_n S\sqrt{\frac{D}{i\omega}}\sinh\sqrt{\frac{i\omega}{D}}r + \cosh\sqrt{\frac{i\omega}{D}}r}\right]\right). \quad \ldots (4.20)$$

Equation 4.8 highlights the characteristic frequency $f_f \propto \frac{D}{r^2}$, which is the time needed for the pore pressure to equilibrate between the fracture and pores (Brajanovski et al. 2005).

In the limit case of low frequency $w \to 0$, equation 4.8 reduces to :

$$P_f(x,t) = P_o\left(B + \frac{1-B}{1+2SZ_n r}\right). \quad \ldots (4.21)$$

In this case, frequencies are low enough to allow equilibration of the fluid pressure between fracture and pores.

In the limit case of high frequency $\omega \to \infty$, equation 4.8 reduces to :

$$P_f(x<r,t) = BP_o e^{i\omega t} \text{and } P_f(r,t) = P_o e^{i\omega t}. \quad \ldots (4.22)$$

At high frequencies the fluid has no time to move from pores in the matrix into the fractures, or vice versa. In this case the pore pressure in the matrix (related to the Skempton coefficient) is lower than the pore pressure in the fracture.

Figure 9 a) shows the evolution of the pore pressure in the sample during hydrostatic oscillations, using equation 4.8, from x=0 to r, at frequencies of 10^{-4}, 10^{-1}, 10^{0}, 10^{1} and 10^{4} Hz. The sample characteristics used for this model are given in Table 4.2. At a frequency of 10^4 Hz, the pore pressure in the sample is constant at $p_f = B\Delta P_c$ =53 kPa and the pore pressure in the fracture reaches $\Delta P_c =$ 0.2 MPa. As the frequency of the applied stress oscillations is reduced, the pore pressure in the fracture decreases, indeed the pressure has time to percolate through the sample, causing a higher

pore pressure throughout the sample matrix. The pore pressure found near the jacket (at x=0) is found to be 53 kPa, when the applied frequency is 10^4 Hz. As the frequency is reduced to quasi static conditions, the pore pressure found near the jacket increases to its highest value of 90.7 kPa (using 4.10). Figure 9 (B) shows the pore pressure evolution versus frequency at r= 0 (where strain gauges are glued) and 2 cm (inside the fracture). At low frequencies, the pore pressure in the whole sample is equilibrated and equal to 90.7 kPa, then as the frequency is increased, the pore pressure decreases at the strain gauge location and increases in the fracture.

Sample Characteristics for 1D Model	Values
Stiffness of Fracture – Z_n(m Pa^{-1})	0.75 10^{12}
Dry Bulk Modulus – K_d (GPa)	26
Matrix Permeability – k (m^2)	10^{-17}
Porosity - ϕ	0.16
Skempton's coefficient - B	0.2407

Table 4.2: 1D model sample characteristics;

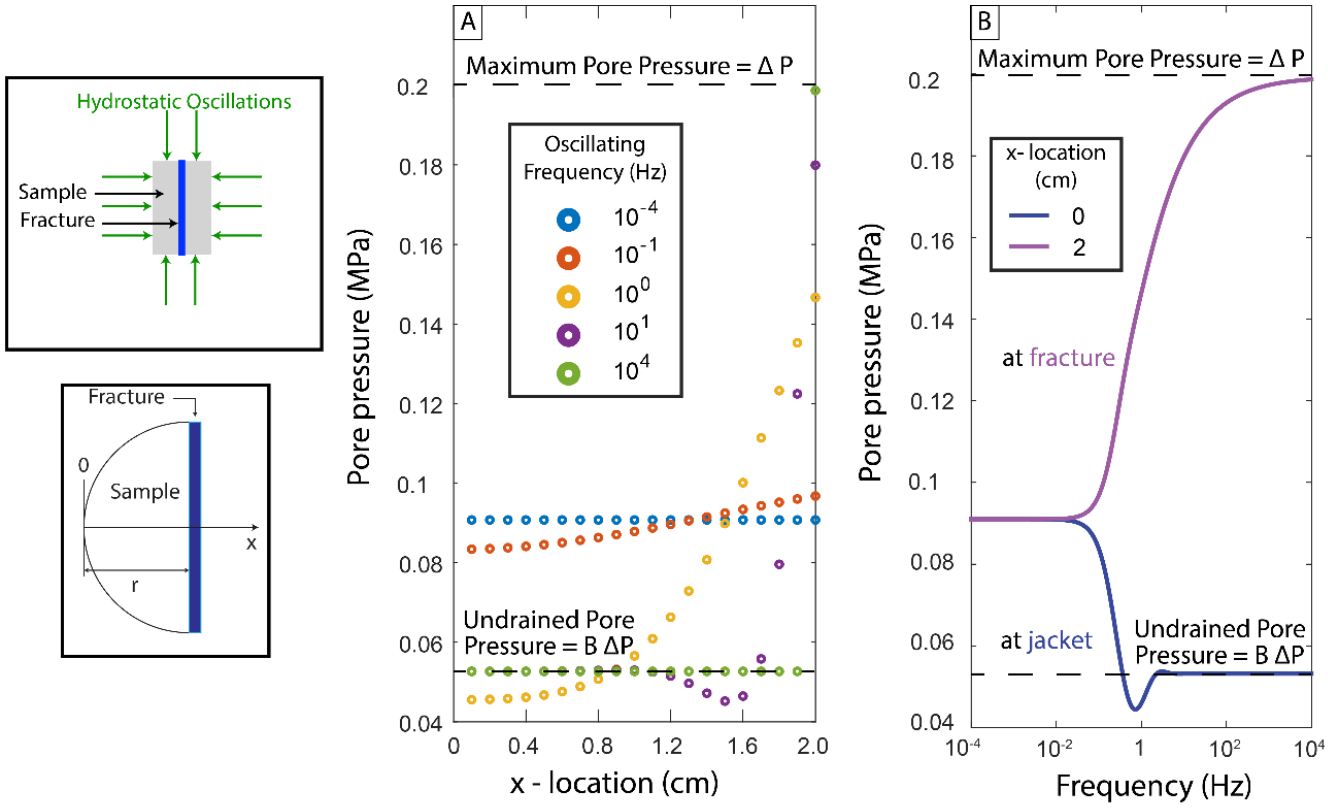

Figure 4.9: Pore pressure versus x-location and pore pressure versus frequency (at x=0 and 2 cm);

4.4.2 Apparent bulk modulus

Recalling that the volumetric strain is given by:

$$\varepsilon_v(x,t) = -\frac{1}{K_d}\left[P_c(t) - \alpha\, p_f(x,t)\right]. \quad \ldots (4.23)$$

The local apparent bulk modulus measured by the strain gauge at x=0 is calculated using equation 4.8:

$$K_{matrix} = -\frac{P_0 e^{i\omega t}}{\varepsilon_v(0,t)} = \frac{K_d}{\left\{1-\alpha\left(B+\left[\frac{1-B}{2Z_n S\sqrt{\frac{D}{iw}}\sinh\sqrt{\frac{i\omega}{D}}r+\cosh\sqrt{\frac{i\omega}{D}}r}\right]\right)\right\}}. \quad \ldots (4.24)$$

In the limit case of high frequency ($\omega \to \infty$),

$$K_{matrix} = \left[\frac{K_d}{1-B\alpha}\right] = K_u, \quad \ldots (4.25)$$

which is simply the undrained bulk modulus. In this limit case, the bulk modulus measured by the strain gauge is not affected by the fracture.

In the limit case ($\omega \to 0$), the local apparent bulk modulus is :

$$\frac{1}{K_{matrix}} = \frac{1}{K_u} - \frac{\alpha(1-B)}{K_d(1+2SZ_n r)}. \quad \ldots (4.26)$$

In this case, the bulk modulus measured by the strain gauge is larger than the undrained bulk modulus, as the pore pressure in the matrix is higher.

4.4.3 Bulk modulus of the fractured sample

The overall goal here is not to develop a complete model for P-wave dispersion of a porous rock containing a fracture. Such analytical models can be found in Chapman (2003) or Brajanovski et al. (2005). Here the aim is to show that a negative phase shift for the apparent bulk modulus predicted in section 4.2 is in agreement with a positive bulk attenuation of the fracture sample. First of all, as the matrix is an isotropic elastic solid, the fractured sample is a transversely isotropic elastic solid. However, it is still possible to define a bulk modulus of the fracture sample, K_{fr}, defined as:

$$P - \alpha P_f = -K_{fr}\frac{\Delta V}{V}, \quad \ldots (4.27)$$

where V is the volume of the fractured sample.

Let's consider the bulk modulus, K_{fr}, of the fractured sample in the fluid saturated case, in the limit case of high frequency $w \to \infty$ equations 2.10, 4.13 and 4.15 leads to

$$K_{fr} = K_u, \quad \ldots (4.28)$$

which is the same as if there was no fracture; in agreement with previous results (Brajanovski et al. 2005).

Let's consider the bulk modulus, K_{fr}, of the fractured sample in the fluid saturated case, in the limit case of low frequency $w \to 0$ equations 2.10, 4.14 and 4.15 leads to

$$\frac{1}{K_{fr}} = \frac{1}{K_u} - \frac{\alpha(1-B)^2}{K_d\, B(1+2SZ_n r)} = \frac{1}{K_u} - \frac{\alpha(1-B)^2}{K_d\, B+\alpha 2Z_n r}. \quad \ldots (4.29)$$

Figure 10 shows in solid and dashed lines the theoretical predictions of the apparent matrix bulk modulus (at x=0) and the bulk modulus of the fractured sample for different value of the normal fracture compliance and using the poroelastic constants given in table 4.3. At high frequency, the moduli are not affected by the fracture and converge to the undrained bulk modulus. As the frequency increases the bulk modulus of the fracture sample increases, in agreement with Brajanovski et al. (2005). The trend of the apparent bulk modulus of the matrix shows an opposite trend which decreases as the frequency increases. Note that using the low frequency bulk modulus value, and equations 4.14 or 4.17 it is possible to directly infer the fracture compliance, knowing the poroelastic properties of the rock.

One needs to remember that the evolution of the apparent matrix bulk modulus is related to the pore fluid migrating from the fracture to the pore volume. This creates theoretically an unusual negative phase shift between stress and strain (figure 10b), which is not seen when looking at the attenuation of the bulk modulus of the fractured sample (figure 10 c).

4.4.4 1D analytical versus 3D computational

The 1D analytical model allows to understand the mechanisms behind the dispersion and attenuation of the apparent matrix bulk modulus. However, the 1D model is a geometrically simplified version of the fractured cylindrical sample. To take into account the 3D geometry of the experiment, the dispersion and attenuation caused by the fluid pressure diffusion is modelled numerically in COMSOL by solving Biot's (1941) poroelastic quasistatic equations in the frequency domain, using the displacement-pressure formulation (Quintal et al., 2011). These equations are:

$$\nabla \cdot \sigma = 0 \,, \qquad \ldots (4.30)$$

$$\nabla \cdot \left(-\frac{k}{\eta}\nabla p_f\right) + \alpha\nabla \cdot (i\omega u) + \frac{I\omega p}{M} = 0 \,, \qquad \ldots (4.31)$$

where u is the vector of solid displacement, with components in the x, y and z directions, and σ is the stress tensor,

$$\sigma_{ij} = 2\mu\varepsilon_{ij} + \lambda e\delta_{ij} - \alpha p\delta_{ij} \,, \qquad \ldots (4.32)$$

where δ_{ij}, ε_{ij} and e are the Kronecker delta, components of the strain tensor and cubical dilation given by the strain tensor, respectively. The μ and λ are the shear modulus for the dry frame and Lamé's parameter $\lambda = K_d - 2\mu/3$. The coefficient M is (Biot and Willis, 1957)

$$M = \left(\frac{\phi}{K_f} + \frac{\alpha-\phi}{K_s}\right)^{-1} . \qquad \ldots (4.33)$$

The fractured sample is modeled with an intact matrix and a fracture having a higher permeability, porosity and compliance. The drained bulk modulus for the fracture was calculated using the normal stiffness of the fracture multiplied by the aperture. We also take into account a fracture shear modulus, estimated and taken as half the value of the drained bulk modulus, according to the study of Lubbe et al. (2008) on a carbonate limestone. The geometry is made of two half cylinders (matrix), with a rectangular cuboid in between both halves (fracture). The width of the rectangular cuboid is equal to the diameter of the cylinder at 40 mm. The height of the fracture is equal to the height of the cylinder and was taken as 80 mm. The fracture aperture has little effect in the analytical model or numerical model as long as the aperture is smaller than 1.1 10^{-3} m (equation 4.7) and sensitivity tests were done on the effect of aperture. The model was run at an aperture of 2 10^{-4} m with sensitivity tests run at 10^{-6} m. The parameters used for the intact and fracture volumes are summarized in table 4.3.

	Intact	Fracture
Grain bulk modulus (GPa)	K_s = 77	K_s = 77
Grain density (kg/m^3)	ρ_s = 2710	ρ_s = 2710
Porosity	ϕ= 0.16	ϕ= 0.9
Permeability (m^2)	k = 10^{-17}	k = 10^{-12}
Drained bulk modulus (GPa)	K_d = 28	K_d = 0.2, 0.52, 4

Drained shear modulus (GPa)	μ_d = 14	μ_d = 0.1, 0.26, 2
Fluid bulk modulus (GPa)	K_f = 2.2	K_f = 2.2
Fluid density (kg/m^3)	ρ_f= 1000	ρ_f= 1000
Fluid viscosity (Pa s)	$\eta_{wat}=10^{-3}$	$\eta_{wat}=10^{-3}$

Table 4.3: Material properties for the poroelastic equations used in COMSOL multiphysics, with bulk and shear modulus shown for 3 different scenarios similar to effective pressures of 5, 10 and 20 MPa, respectively;

COMSOL multiphysics is used to create a volumetric mesh with tetrahedral elements and the weak form of equations 4.19 and 4.20 are solved, using a finite element method. The gradient of fluid pressure is set to 0 along the outside boundary, creating undrained boundary conditions. To induce the hydrostatic pressure, an oscillatory radial stress amplitude of 2 10^5 Pa is applied along the curved surface of the cylinder and fracture. An oscillatory stress amplitude of 2 10^5 Pa is applied to the top of the cylinder in the negative z direction and to the bottom of the cylinder in the positive z direction.

Figure 10 shows the 1D analytical solution and 3D COMSOL multiphysics results of the apparent matrix bulk modulus (at location x = 0) and the bulk modulus of the fracture sample versus frequency, for 3 fracture stiffness's: 1 10^{12}, 2.6 10^{12} and 2 10^{13} Pa m^{-1}. The solid and dashed lines show the 1D analytical model results. The Os and Xs are for the 3D numerical model completed in COMSOL multiphysics. The solid line and Os are for local measurements at the "strain gauge" location. The dashed line and Xs are for global measurements, i.e. matrix and fracture. The black, blue and red colors represent the solution at a normal compliance of 1, 2.6 and 20 10^{12} Pa m^{-1}, respectively.

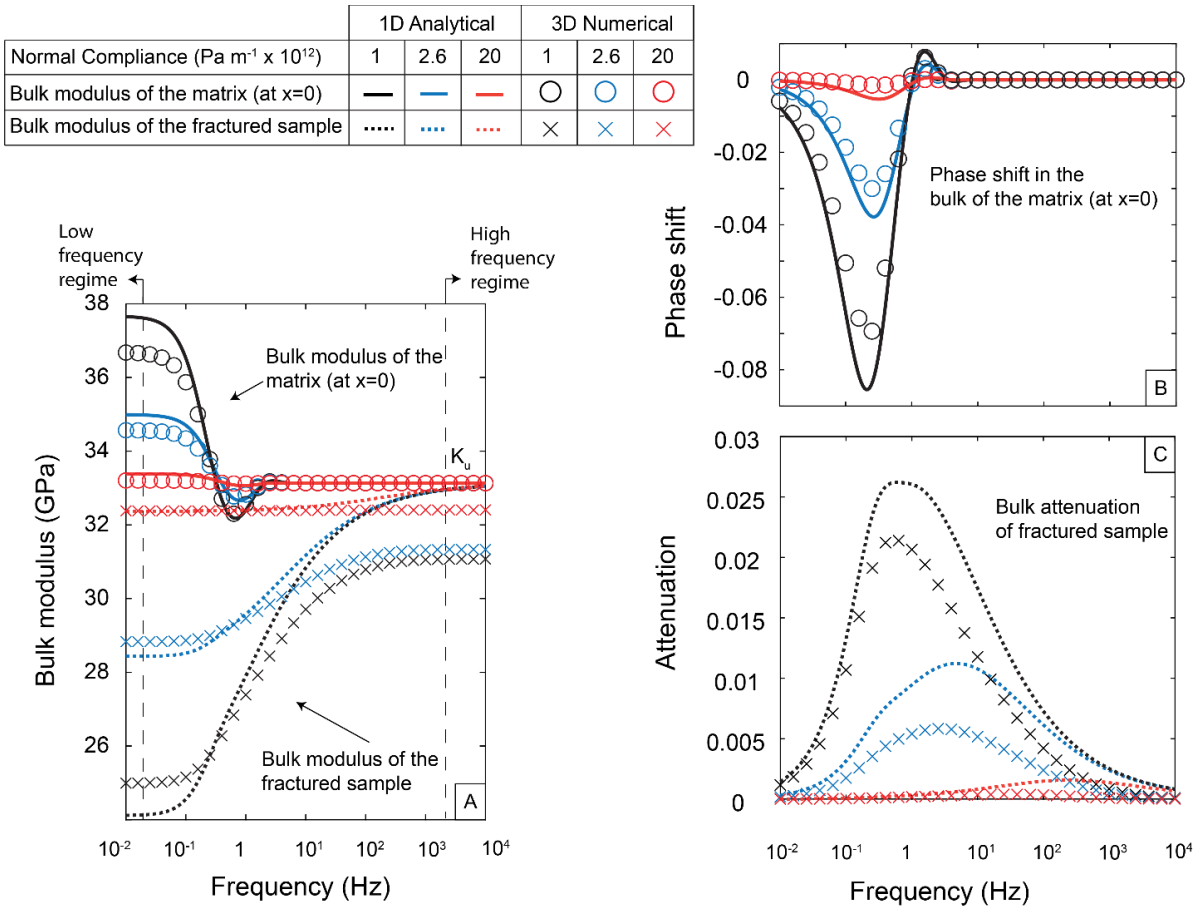

Figure 4.10: Bulk Modulus of local measurement (x=0) and of whole fractured sample versus frequency, with associated phase shift and attenuation versus frequency;

In the low frequency regime, below 10^{-2} Hz, the bulk modulus of the fractured sample is smaller than the apparent matrix bulk modulus. In the high frequency regime above 10^{3} Hz, the apparent matrix bulk modulus are equal and constant at K_u (equation 4.13). Overall there is a good consistency between the 1D model and the 3D numerical model: for the apparent matrix modulus, the low frequency moduli for the 1D analytical model are 37.6, 35 and 33.2 GPa for a fracture stiffness of 1 10^{12}, 2.6 10^{12} and 2 10^{13} Pa m^{-1}, respectively, whereas for the 3D numerical model these values are 36.7, 34.6 and 33.2 GPa. For the bulk modulus of the fractured sample, the low frequency moduli for the 1D analytical model are 24.1, 28.4 and 32.8 GPa for a fracture stiffness of 1 10^{12}, 2.6 10^{12} and 2 10^{13} Pa m^{-1}, respectively, whereas for the 3D numerical model these values are 25, 28.8 and 32.4 GPa.

The critical frequency for the attenuation for the 1D analytical model and 3D analytical model also match well. The amplitude of the attenuation (fractured sample) for the 1D analytical model are 0.026, 0.011 and 0.001 for fracture stiffness of 1 10^{12}, 2.6 10^{12} and 2 10^{13} Pa m^{-1}, respectively,

whereas for the 3D numerical model these values are 0.021, 0.006 and 0.000. The amplitude of the phase shift (apparent matrix modulus) for the 1D analytical model is -0.085, -0.038 and -0.005 for a fracture stiffness of 1 10^{12}, 2.6 10^{12} and 2 10^{13} Pa m^{-1}, respectively, whereas for the 3D numerical model these values are -0.069, -0.0307 and -0.001.

Small differences between the 1D and 3D models are expected as the solution for pore pressure propagation in the 3D numerical model is more intricate, taking into account the complex geometry of the sample, whereas the 1D analytical model is simplistic. That being underlined, the critical frequency is the same for both the 1D and 3D models, both models predict almost the same negative phase shift for the apparent matrix bulk modulus, and both models show an apparent matrix bulk modulus that converges at K_u in the high frequency regime.

In the high frequency, and for the fractured sample, the modulus converges to a value smaller than K_u for the 3D simulation. This is due to the aperture not being small enough: when modelling with a smaller aperture (10^{-6} m), the 3D numerical model converges to K_u, which is not shown, since the length of the sample has to be greatly reduced to create a model that could be run on the servers without crashing the system. This is further highlighted by the increase in high frequency apparent matrix bulk modulus, with an increase in fracture stiffness, as the fracture stiffness comes closer to the matrix stiffness.

4.4.5 Comparing experimental results with the 1D analytical model

Figure 11 shows the results presented in figure 7, with the solution to the 1D analytical model, as well as the solution for the 3D numerical model. The sample properties for the 1D and 3D models can be seen in table 4.4. The drained bulk modulus is taken from figure 7. The fracture stiffness was calculated using the low frequency regime (equation 4.14) for the 1D analytical model, and was adjusted, in the 3D model, to fit the experimental data (it is the only unknown parameter).

	1D analytical			3D computational		
Sample Characteristics	Sample Effective Pressure (MPa)					
	5	10	20	5	10	20
Stiffness of Fracture – Z_n(Pa m^{-1})	1 10^{12}	2.6 10^{12}	5 10^{13}	0.7 10^{12}	1.8 10^{12}	3.5 10^{13}
Drained Bulk Modulus – K_d (GPa)	26	28	28	26	28	28
Matrix Permeability – k (m^2)	10^{-17}					
Porosity - ϕ	0.16 .					

Table 4.4: 1D and 3D model sample characteristics;

Figure 11 shows that the experimental data is in good agreement with the 1D analytical and 3D numerical models. The inferred value for the fracture stiffness are given in table 4.4. The fracture stiffness increases as effective pressure increases. The 1D and 3D models predict the same order of magnitude for the fracture stiffness, however the 1D model slightly overestimates the fracture stiffness, and for the three effective pressures a ratio of ~0.7 is found between the fracture stiffness used from the 3D model to the one deduced from the 1D model. As the 3D model takes into account the geometry of the problem, it is probably a better approximation of the stiffness of the fracture. The 1D model is analytical, catches the mechanisms behind dispersion and attenuation, and is easy to use to interpret the experimental data.

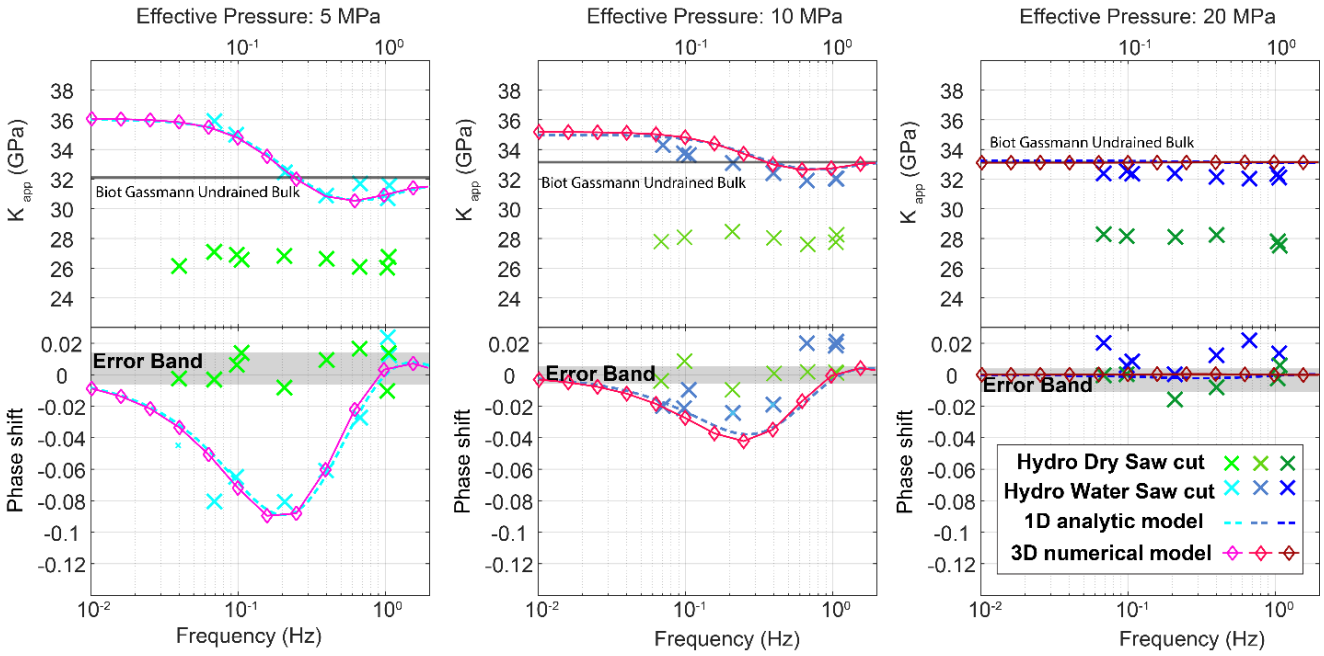

Figure 4.11: Experimental results for hydrostatic oscillations with the predictions of the 1D model superimposed;

4.5 Discussion

In this paper, the permeability of the sample was used to calculate the hydraulic aperture of the fracture. For a saw cut sample with the fracture running parallel to the flow path, there is an expected decrease in permeability when the effective pressure is increased, which has been shown experimentally by others (Kluge et al., 2017; Blöcher et al.,2019) and is consistent in this work. The flow rates used for the hydraulic aperture never exceeded 2.5 10^{-8} m^3/s, which is well below the Reynolds number threshold for laminar flow and the fracture is relatively flat and parallel as it was cut using a diamond saw, however there is certainly partial contact between both halves of the sample, meaning the parallel plate model is not completely met. The stiffness of the fracture calculated using this method has an error of 1, 33 and 92 %, at effective pressures of 5, 10 and 20 MPa, when compared to the stiffness calculated from the 1D analytical model, and 41, 4 and 26 % when compared to the fracture stiffness from the 3D numerical model. The 3D numerical model is in better agreement with the hydraulic measurements of fracture stiffness, than the 1D analytical model. Li et al. (2008) showed that the error between hydraulic aperture and real aperture are on an order of 2.

The pore pressure model presented in section 4.2, shows the trend of pore pressure along the x axis depending on the applied hydrostatic frequency. The pore pressure in the pore matrix is highest at low frequencies and lowest at high frequencies, the opposite is true for the fluid pressure in the fracture. At high frequencies (10^3 Hz and above), the pore pressure in the fracture does not have time to dissipate into the matrix. This is analogous to squirt flow attenuation mechanisms, for which fluid does not have the time to equilibrate between pores and cracks. Note however that in the case of a fracture medium, poroelasticity can be applied as the pore pressure is equilibrated at a REV scale, which is not the case for squirt flow. In addition, the cut-off frequency related to squirt flow is typically at a much higher frequency range (> 10 kHz), whereas in this case the frequency cut-off is:

$$f \approx \frac{4D}{L^2} \quad \ldots (4.34)$$

where L is the distance between 2 fractures (or 2 times the distance r in our experiments), and thus typically occurs at low frequency. The distance between the fractures (and thus the fracture density) is a key parameter to estimate the frequency cut-off. This can be shown by using the 1D analytical model developed and changing the value of r. When changing r from 2 to 4 to 8 cm, the cutoff frequency goes from 0.85 to 0.32 to 0.12 Hz with the attenuation magnitude going from 0.076 to 0.048 to 0.025, respectively. This is consistent with the numerical models developed by Hunziker et al. (2018) which has shown that an increase in fracture density does increase the magnitude and cut off frequency of the attenuation caused by FPD from the fracture to the pore space.

Figure 10 and 11 show that the critical frequency for the FPD from the fracture to the matrix changes depending on the fracture stiffness, with an increase in critical frequency as the fracture stiffness increases. The importance of the location of the strain measurement is highlighted in figure 10, the local strain measurement shows a critical frequency which is smaller than that of the critical frequency for the whole sample. The importance of the location of strain measurement has been shown numerically before by Chapman and Quintal (2018), with a change in the cut-off frequency depending on the location of where the strain measurement was taken. A negative phase shift was also shown in their work, when the attenuation was measured locally at a set distance from a fracture. This negative phase shift is shown experimentally in figure 11, at lower effective pressures, as the strain gauges used here are local measurements, which shows the effect the fracture has on the local strain measurements. The ‘global’ bulk strain measurements would be needed, to calculate directly the bulk dispersion and attenuation of the fractured sample. The 1D model in this paper (figure 11), as well as the numerical model in Chapman and Quintal (2018), show that although some local

measurements can create a negative phase shift between the stress and strain, the 'global' bulk attenuation is still positive. However, this work shows that it is possible to calculate the fracture stiffness by inversion through the apparent matrix bulk modulus, and then predict the bulk modulus and attenuation of the fractured sample.

The dispersion caused by the fracture decreases in magnitude with an increase in effective pressure. This is expected as the fracture closes when there is an increase in effective pressure. When using the 1D model, the amplitude of the attenuation is sensitive to the stiffness of the fracture, which decreases with an increase of effective pressure. This implies that dispersion and attenuation related to fractures mainly occurs in shallow reservoirs, or during fluid injection as the effective pressure is increased leading to opening of pre-existing fractures.

4.6 Conclusion

With the addition of innovative microvalves, a set of hydrostatic oscillation tests was performed on an intact and saw cut cylindrical sample at frequencies between 0.07 and 1 Hz in purely undrained conditions. As expected, the intact sample showed no dispersion for dry or water saturated conditions. Permeability tests were performed at a large range of effective pressures to measure hydraulic aperture and stiffness of the man-made fracture. Using the local strain measurements during the hydrostatic oscillations, the apparent matrix bulk modulus and phase shift were measured. At an effective pressure of 5 MPa, the apparent matrix bulk modulus decreased from 36 at low frequency to stabilize at 31 GPa at higher frequencies and a maximum local negative phase shift of -0.08 was recorded, with the cut-off frequency at ~0.2 Hz. At an effective pressure of 15 MPa, the local bulk modulus again decreased with increase in frequency, however only by 2.6 GPa from 34.6 to 32 GPa and a maximum local negative phase shift of -0.02 was recorded, with a cut-off frequency at ~0.35 Hz. At an effective pressure of 20 MPa, there was no change in local bulk modulus and no phase shift.

A 1D analytical model and 3D numerical model, for hydrostatic oscillations on a fractured sample, were developed and fit well the experimental data, which implies a fracture to matrix leak-off. The models give insight on how a negative phase shift can be observed locally, and how the fracture stiffness can be measured. It underlines also the importance of fracture stiffness and the location of the strain measurements on the cut-off frequency and the magnitude of the phase shift.

5. Frequency-dependent attenuation caused by FPD due to interconnected fractures: Experimental evidence and numerical modeling

5.1 Introduction

The study of wave-induced fluid pressure diffusion (FPD) has been shown analytically (Chapman, 2003; Brajanovski et al. 2005; Gurevich et al. 2009) and numerically (Quintal et al., 2014; Hunziker et al., 2018; Jänicke et al., 2019; Lissa et al., 2021) to be a crucial factor in understanding seismic energy dissipation in fractured media.

Numerically, there has been substantial advancements in not only the interaction between fractures and pore space (Caspari et al.,2019), but fractures and fractures (Vinci et al., 2014; Lissa et al., 2020). These theoretical and numerical studies on fractures help understand how these react depending on their orientation (Guo and Gurevich, 2020), the parameters of the matrix (Brajanovski et al.,2005; Vinci et al.,2014), or even how fractures interact with each other (Quintal et al.,2014). For simpler geometries, analytical models have been used as a benchmark to compare to numerical models. However, very little work has been done experimentally. Nakagawa (2013), measured normal and shear fracture attenuation, under uniaxial stress applied normal to the fracture. The sample was jacketed and the pore pressure was in a slight vacuum to prevent the fluid from moving between the jacket and sample. The frequency range was between 1 and 100 Hz. Amalokwu et al. (2014) synthesized two sandstone samples, one with aligned penny-shaped voids and the other without, and tested these at 40 MPa at a frequency of 650 kHz. Their results showed that the sample with the synthesized fractures had more attenuation. These experiments were revisited in 2017 by Amalokwu et al., where a Gassmann equation was applied and used to predict the dispersion due to squirt flow, at different water saturations ranging from 0 to 1.

The goal in this paper is to create an experimental setup which can easily be validated using a numerical approach, and highlights **fracture to fracture** fluid pressure diffusion (FPD). This will be done using a traditional triaxial cell outfitted with new microvalves to obtain undrained conditions and an eddy gauge which can measure global strain of the sample. A cylindrical sample of a very low permeability Solnhofen limestone was cut twice using a diamond saw. These cuts were done horizontally and vertically, so the cuts intersect in the center of the volume, and create a “Swiss

cross". The cell is also outfitted with an axial oscillator which can oscillate between 10^{-2} and 10^{3} Hz. The idea is to monitor the dispersion caused by the attenuation due to fluid flowing from the horizontal fracture, which is being squished due to the axial oscillations, to the vertical fracture which in this case acts as a small dead volume. Due to the low permeability, there should be little to no fluid migration to the pore space of the matrix, highlighting fracture to fracture FPD. It is important to make sure that the attenuation measured is indeed related to the FPD between the fractures and no other mechanisms. Also, some permeability tests were performed at a range of effective pressures to calculate the hydraulic aperture and estimate roughly the vertical fractures stiffness. Finally, a 3D numerical model of the experiment was made to compare experimental and numerical results.

5.2 Experimental procedure

A TOP Industries™ triaxial cell is used to pressurize and saturate the sample (Borgomano et al., 2020). Two pumps are oil filled and control the cell pressure and axial piston, respectively. One Quizix dual precision pump (QX1500HC model), is used to regulate upstream and downstream pore pressure in the sample. The pore fluid used in this paper is 98% glycerin with product specification as Glycérol ≥98%, GPR RECTAPUR® provided by VWR Chemicals. Glycerin is used as it has a higher dynamic viscosity than water, which allows for the observation of FPD at lower frequencies. The cell is outfitted with microvalves in both the top and bottom end platten, when these are closed, the dead volumes are reduced to ~ 20 µl, creating undrained boundary conditions. Further details on the microvalves are presented in Borgomano et al. (2020) paper. An eddy gauge sensor was developed to measure global axial strain.

5.2.1 Axial oscillations

For the axial oscillation test, first the cell pressure pump brings the sample to a pre-determined confining pressure. A piezoelectric actuator is then sandwiched in between the sample and axial piston with a small deviatoric stress applied (5 MPa) through the axial piston to ensure proper contact. The actuator is fed by an electronic signal which causes an oscillatory volume change in the actuator. This creates an oscillatory stress propagation in the column. The stress is calculated using:

$$\sigma_{ax} = \varepsilon_{alu} E_{alu}, \quad \ldots (5.1)$$

where σ_{ax} is the axial stress in the column, E_{alu} is the Young's modulus of the aluminum bottom plate and ε_{alu} is the axial strain in the aluminum bottom plate. Four strain gauge pairs are attached

to the bottom aluminum plate and are used to measure ε_{alu}. Knowing E_{alu} ,the axial stress can be calculated.

5.2.2 Eddy gauge sensor

An eddy gauge sensor is a sensor which is fed by an alternate current, which in turn creates a magnetic field around the sensor. A conductive material, a small aluminum cylinder in this case, was chosen to be a target (see figure 5.1). The magnetic field will generate an eddy current in the target based on the distance (x) between the sensor and the target as well as the resistivity (ρ), the electric permeability (μ) of the target and the frequency (f) of the alternating current. Due to the creation of an eddy current in the target, the impedance (Z) of the coil in the sensor will change. The change in impedance in the coil can be seen in equation 2.2, which was shown by Wang and Fend (2013).

$$Z_{Eff} = [R_c + R_E(x, \rho, \mu, f)] + j\omega[L_c + L_e(x, \rho, \mu, f)] \quad \ldots (2.2)$$

R_c and L_c are the inherent resistance and inductance of the sensor. R_e and L_e are the change in resistance and inductance due to eddy current being generated. The frequency of the alternating current is constant, and the resistivity and permeability of the target are known. The temperature can change the inductance and resistivity but this can be accounted for (Wang and Feng, 2013). For our specific use, the temperature is stable at 21 °C.

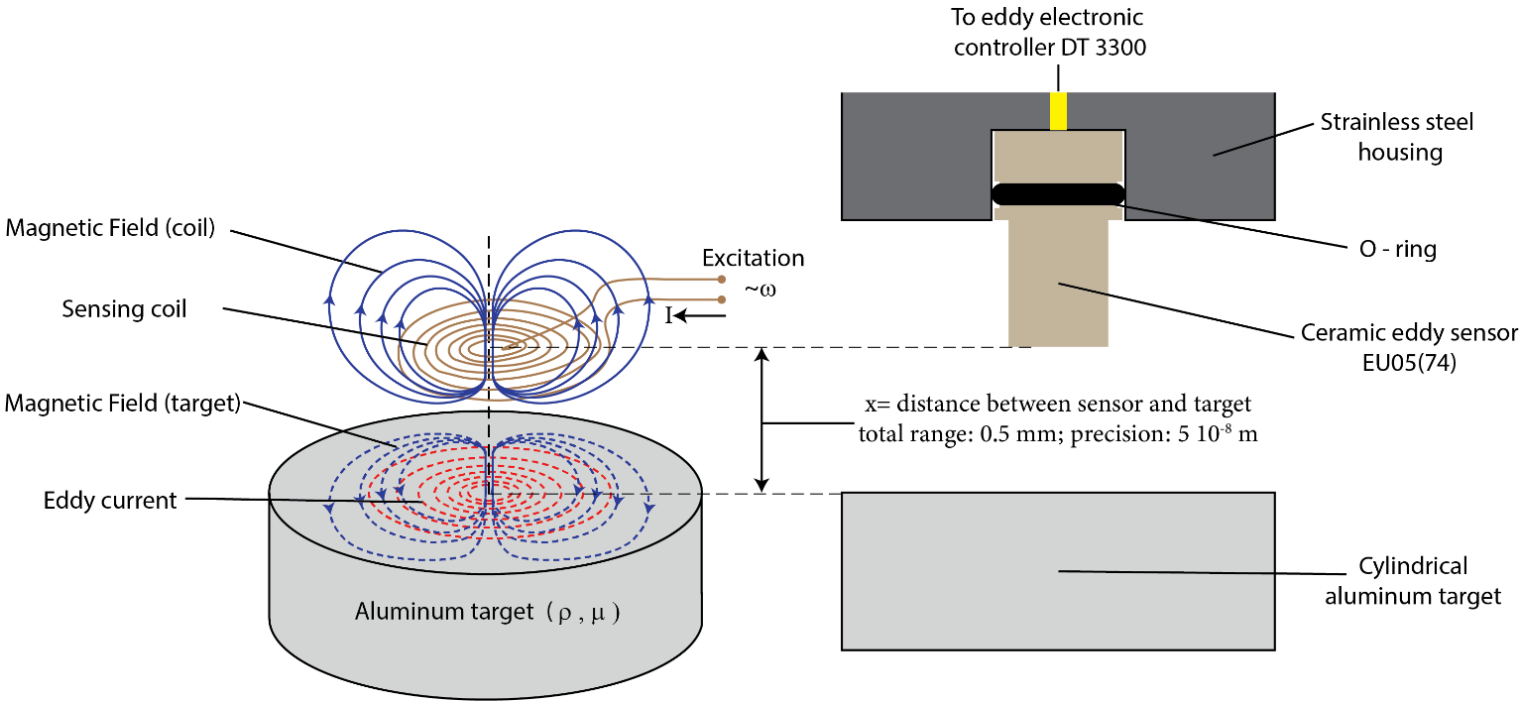

Figure 5.1: left: Working principals of eddy gauge sensor; right: Schematic of eddy gauge implementation in high pressure triaxial cell;

Eddy gauge sensors are relatively new, reliable and are being used both in the industry (Cardwell et al., 2008; García-Martín et al., 2011) and in academia (Ying et al.,2007; Zainal Abidin et al., 2011; Wang et al., 2013). Eddy gauge sensors main advantage is that it implements a non-contact system.

The eddy gauge sensor that was used at ENS is the EU 05(74) with a DT3300 controller provided by Micro-epsilon™. The sensor has a total range of 0.5 mm with a precision of $5X10^{-8}$ m and has a working temperature range of 0 to 60 ^{o}C. The eddy gauge sensor is used axially along the sample length to measure the axial deformation of the sample, as well as, the bottom and top metal caps.

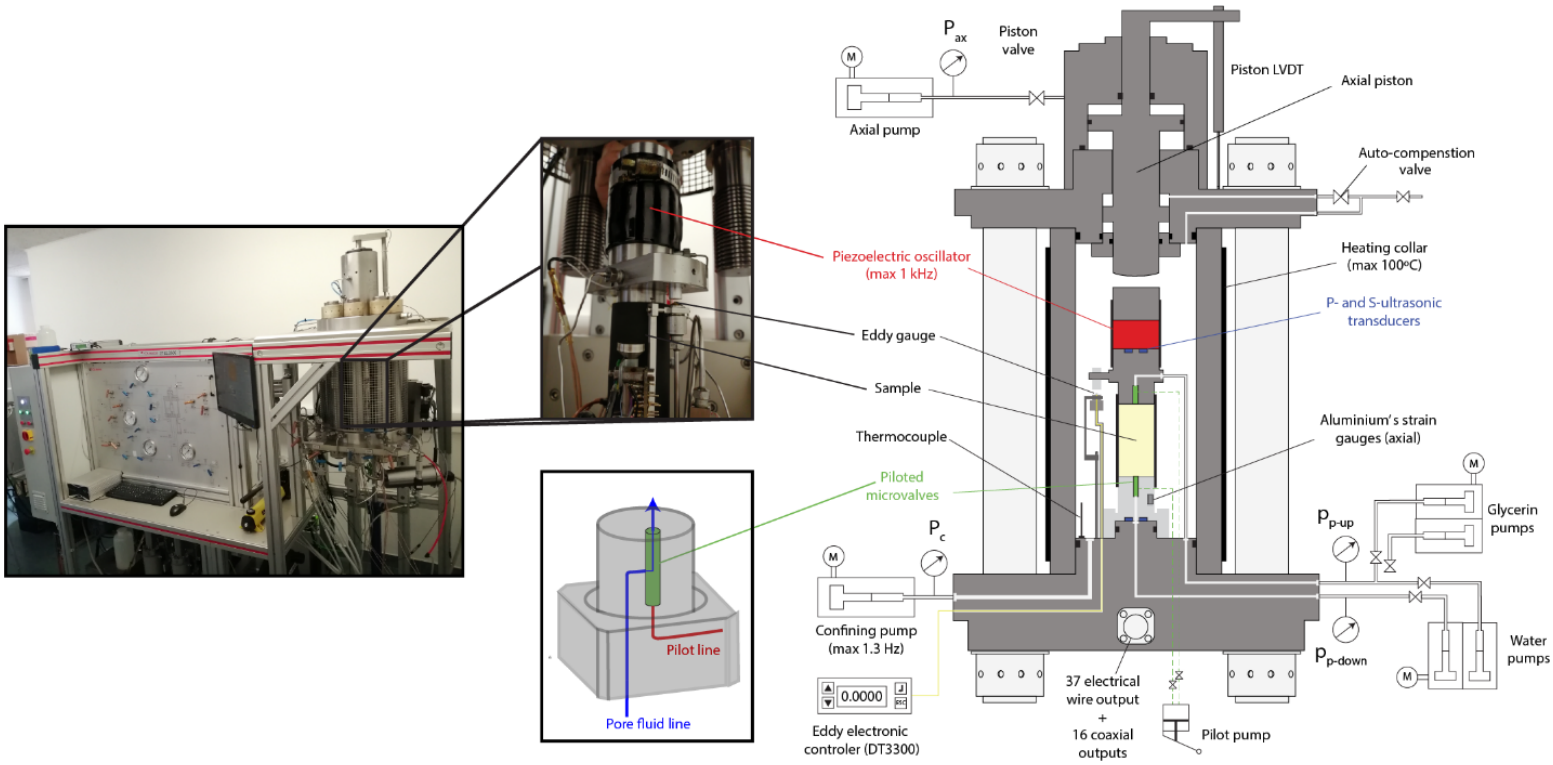

Figure 5.2: Picture of TOP Ind. triaxial cell, jacketed sample and schematic of microvalve and whole triaxial cell system (modified from Borgomano);

The compliance of the system ($S_{sys.}$) is calculated using:

$$S_{sys.} = \frac{\varepsilon_{eddy\ gauge}}{\sigma_{ax}} \quad , \qquad \ldots (5.2)$$

with:

$$\varepsilon_{eddy\ gauge} = \frac{\Delta l_{eddy}}{l_{system}}, \qquad \ldots (5.3)$$

where $\varepsilon_{eddy\ gauge}$ is axial strain measured by the eddy gauge, Δl_{eddy} is the eddy displacement and l_{system} is the length of the system (147 mm), which includes the metal bottom and top caps. Assuming there is no dispersion at the largest effective pressure of 25 MPa, since the fracture is completely closed, and the system is perfectly elastic, a correction ($Cor.$) is calculated for the compliance as follows:

$$Cor. = S_{sys.} - S^{40\ Hz} \ , \qquad \ldots (5.4)$$

where $S_{sys.}$ is the compliance matrix of the system at an effective pressure of 25 MPa and $S^{40\ Hz}$ is the compliance of the system at an effective pressure of 25 MPa and a frequency of 40 Hz. This

correction removes small frequency dependent changes in compliance due to the eddy gauge sensor, which was observed. The correction is applied at each effective pressure following:

$$S_{new} = S - Cor.\,, \qquad \ldots (5.5)$$

where S_{new} is the compliance of the column (sample, aluminum bottom cap and steel top cap), without the frequency effect of the eddy gauge and S is the compliance of the system at each effective pressure.

Finally, the elastic modulus (E) is calculated from the compliance

$$E = \frac{1}{S_{new}}\,, \qquad \ldots (5.6)$$

and is normalized with the elastic modulus at an effective pressure of 25 MPa using:

$$\hat{E} = \frac{E}{E^{25\,MPa}}\,, \qquad \ldots (5.7)$$

where $\hat{E}$ is the normalized elastic modulus and $E^{25\,MPa}$ is the elastic modulus at 25 MPa.

As the eddy displacement also reads the displacement in the bottom and top cap, which includes a small part in aluminum and stainless steel, the normalization is ideal to highlight dispersion caused by the FPD, since elastic properties of the metal column are frequency independent.

5.2.4 Normalized Young's attenuation

The attenuation of the Young's modulus (${Q_E}^{-1}$) is calculated using (O'Connell and Budiansky, 1978):

$${Q_E}^{-1} = \frac{Im(\bar{E})}{Re(\bar{E})} = \frac{Im(\bar{\sigma}/\bar{\varepsilon})}{Re(\bar{\sigma}/\bar{\varepsilon})} = \tan(\phi_{\sigma_{ax}} - \phi_{\varepsilon_{sample}}). \qquad \ldots (5.8)$$

Again, it is assumed the fracture is closed and therefore there is no attenuation at an effective pressure of 25 MPa, consequently a corrected attenuation (${Q_E}^{-1}{}_{cor.}$) is calculated, as follows:

$${Q_E}^{-1}{}_{cor.} = {Q_E}^{-1} - {Q_E}^{-1}{}_{Eff.P.=25\,MPa}\,, \qquad \ldots (5.9)$$

where ${Q_E}^{-1}{}_{Eff.P.=25\,MPa}$ is the attenuation at an effective pressure of 25 MPa. This correction gives an attenuation of 0 at all frequencies at an effective pressure of 25 MPa, which is consistent with the correction made with the Young's modulus.

5.2.5 Kramer-Kronig's relationship

To verify that the normalized Young's modulus and normalized Young's attenuation is causal, the Kramers-Kronigs relation (Nowick and Berry,1972) is applied to the linear interpolation of the normalized Young's modulus to determine the imaginary part of this, following:

$$Im(\bar{E}) = \frac{2}{\pi}\int_0^{\infty}\left[Re\left(\overline{E(\alpha)}\right) - Re\left(\overline{E(r)}\right)\right]\frac{\omega d\alpha}{\omega^2-\alpha^2}, \quad \ldots (5.10)$$

where $Re\left(\overline{E(\alpha)}\right)$ is the linear interpolation of the real part of the normalized Young's modulus, $Re\left(\overline{E(r)}\right)$ is the relaxed real part of Young's modulus given by the high-frequency limit of $Re\left(\overline{E(\alpha)}\right)$, α is the integration variable, and ω is the angular frequency.

5.2.6 Hydraulic Aperture

To calculate the hydraulic aperture of the vertical fracture, it is assumed that there is no flow taking place through the matrix ($Q_m = 0$) due to the low permeability of the sample and that the flowrate through the sample (Q_w) is equal to the flowrate through the fracture (Q_f).

$$Q_w = Q_f \quad \ldots (5.11)$$

Darcy's law states:

$$Q = \mathrm{A}\frac{\mathrm{k}}{\eta}\frac{\partial \mathrm{P}_f}{\partial \mathrm{z}}, \quad \ldots (5.12)$$

where k is the permeability (m^2), η is the dynamic viscosity of the pore fluid (Pa.s), Q is the flow rate through the fracture ($m^3.s^{-1}$), A is the area of the sample perpendicular to the flow (m^2) and P_f is the pore fluid pressure (Pa).

Using a parallel plate model, the hydraulic aperture (b) can be calculated as follows:

$$b = \sqrt{12 * k_f}. \quad \ldots (5.13)$$

In addition:

$A = b * D$,

where D is the diameter, then:

$$b = \sqrt[3]{\frac{12*Q*\eta}{D\frac{\partial P_f}{\partial z}}}. \quad \ldots (5.14)$$

5.2.6 Vertical fracture stiffness calculations

A rough estimation of the stiffness of the vertical fracture was measured by calculating the hydraulic aperture at multiple effective pressures. The change in effective pressure between two points represents a loading step, m, and the difference between the hydraulic aperture between these shows the displacement normal to the fracture. The normal stiffness of a fracture is defined by (Goodman, 1976):

$$Z_n^m = \frac{P_{m+1} - P_{m-1}}{b_{m-1} - b_{m+1}}, \quad \ldots (5.15)$$

where Z_n^m is the hydraulic stiffness, b_m is the hydraulic aperture measured at the loading step P_m. It is important to underline that it is a rough estimation as the true mechanical aperture is not the hydraulic aperture which is inferred from the parallel plate model.

5.3 Sample preparation

For this study, the underlying research goal was to use the innovative eddy gauge to capture attenuation effects of fracture to fracture FPD. To ensure that this effect is isolated, a Solnhofen limestone cylindrical sample was chosen, as it has a very low permeability, which eliminates the FPD effects from the fracture to the matrix of the sample, in the frequency range chosen. This section first describes the sample, then the method used to create two fractures in a Swiss cross formation.

5.3.1 Solnhofen limestone

In the geological formation known as Altmühltal lies Solnhofen limestone. This limestone was formed in a basin which was around 30 by 70 km, in southern Germany. It was created by a micritic carbonate mud (Koch, 2007). The basin held multiple lagoons which had limited access to open sea and could get isolated, creating low oxygen zones. This made it less likely for predators to roam around, and for this reason, if an animal perished in these lagoons, they were not eaten and were left to settle whole in the carbonate mud. For this reason, Solnhofen limestone is a well-known formation as it often preserves some of the best quality fossils.

Solnhofen limestone is 99.9% calcite with it's grain size shown to be around 5 μm and a measured density around 2663 kg/m^3 (Robertson,1955; Heard, 1960; Baud et al., 2000). Baud et al. (2000) show the intact Young's modulus to be around 60 GPa, with its Poisson's ratio, porosity and its intrinsic compressibility to be 0.34, 3% and 1.6 10^{-11} Pa^{-1}, respectively. Its permeability is estimated to be below 10^{-18} m^2 (Koch, 2007). The characteristics of the sample are tabulated in table 5.1.

5.3.2 Swiss cross - Fracture preparation

An intact cylindrical sample of Solnhofen limestone, with a radius of 40 mm and height of 80 mm, was centrally saw cut down its length, using a diamond saw. Then, these halves were marked and cut again around it's center. The new dimensions of the sample are shortened in height and width perpendicular to the fracture by 3 mm, due to the sawcut. Each section was marked (1 through 4), then was sanded (400 grit) along the inside surface, then each section was placed and held together using transparent tape. This was done to keep all parts aligned during the mounting process. Small drops of epoxy were applied to chipped corners to reduce dead volumes.

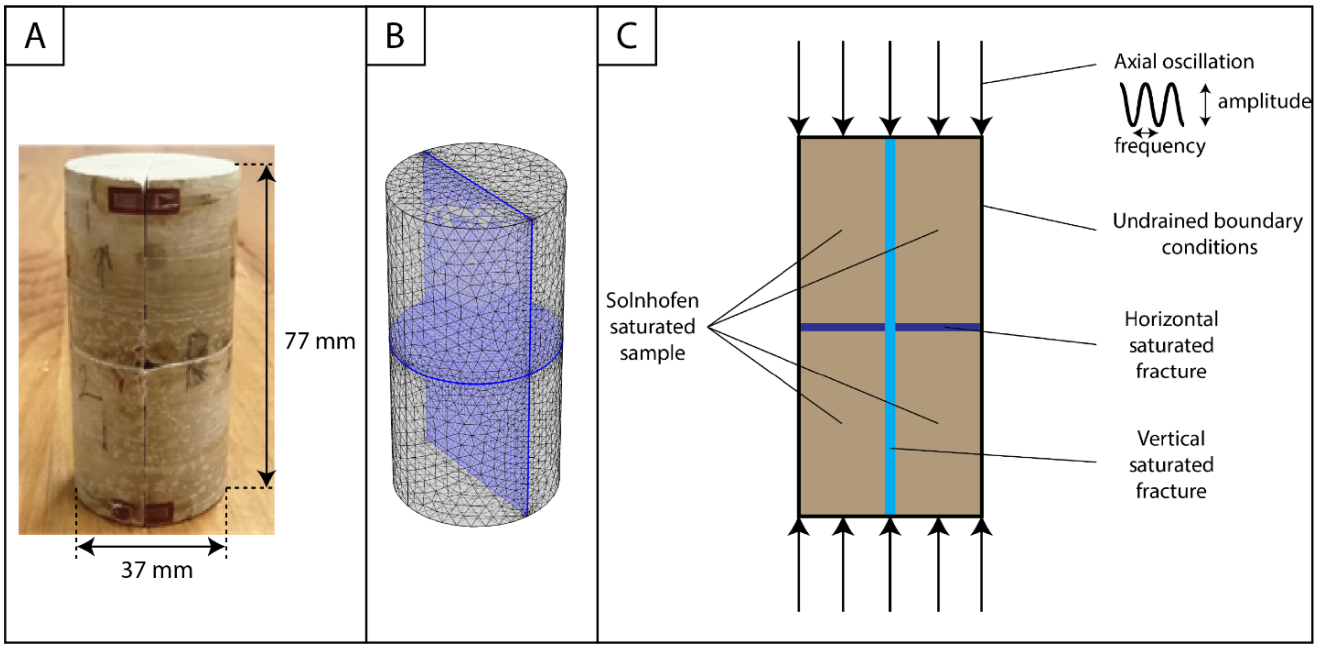

Figure 5.3: (A) Solnhofen limestone sample with Swiss cross fracture and shortened dimensions; (B) Picture of the meshing used for the numerical simulation, with fracture highlighted in blue; (C) Schematic of Solnhofen limestone sample with Swiss cross fracture during experiment;

5.4 Results

5.4.1 Swiss Cross - Young modulus versus frequency

Figure 5.4 shows the normalized Young's modulus of the Swiss cross Solnhofen sample, in undrained glycerin saturated conditions, at effective pressures of 5, 10, 15, 20 and 25 MPa. The circles represent the data collected from the eddy gauge. The lines show the linear interpolation.

At the lowest frequency recorded of $2\ 10^{-1}$ Hz, the normalized Young's modulus increases from 0.71 to 1 for effective pressure of 5 and 25 MPa, respectively.

At the highest frequency recorded of $4\ 10^{1}$ Hz, the normalized Young's modulus increases from 0.86 to 1 for effective pressure of 5 and 25 MPa, respectively. This increase in Young's modulus is smaller than the lower frequency case.

At 5 MPa effective pressure, the normalized Young's modulus goes from 0.71 to 0.86 at frequencies of $2\ 10^{-1}$ and $4\ 10^{1}$ Hz, respectively.

At 20 MPa effective pressure, the normalized Young's modulus goes from 0.95 to 0.99 at frequencies of $2\ 10^{-1}$ and $4\ 10^{1}$ Hz, respectively. This represents a large decrease in dispersion, when compared to the 5 MPa effective pressure case.

At 25 MPa effective pressure, the normalized Young's modulus does not change with frequency as the fracture is assumed to be completely closed.

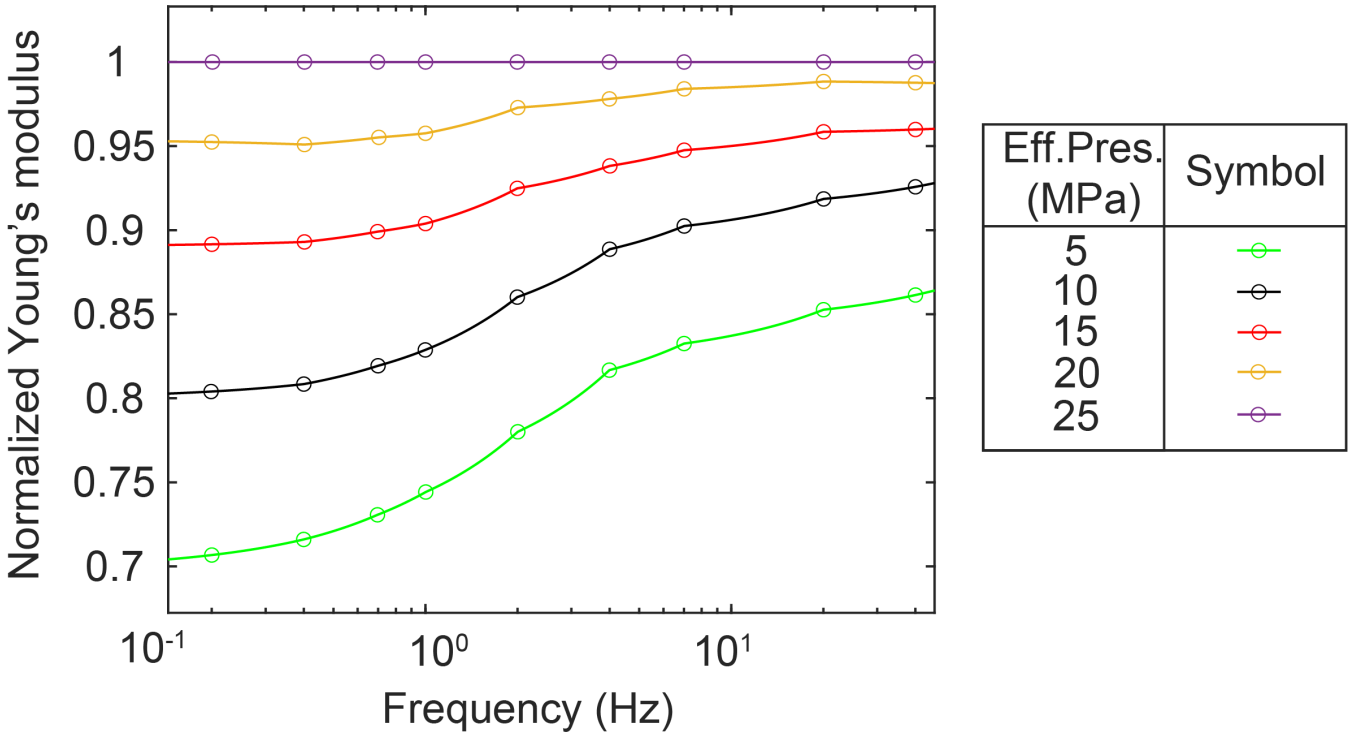

Figure 5.4: Normalized Young's modulus versus frequency of Solnhofen sample with Swiss cross fracture in undrained glycerin saturated conditions at 5, 10, 15, 20 and 25 MPa effective pressures;

5.4.2 Swiss Cross - Young's attenuation versus frequency

Figure 5.5 shows the normalized Young's attenuation of the Swiss cross Solnhofen sample using both the eddy gauges (circles) and Kramer-Kronig's relationship (dotted lines), in undrained glycerin saturated conditions at effective pressures of 5, 10, 15, 20 and 25 MPa.

As the data is normalized using the attenuation at an effective pressure of 25 MPa, the attenuation for 25 MPa effective pressure is 0. The highest attenuation, at effective pressures of 5, 10, 15 and 20 MPa using the eddy gauge data are 0.073, 0.052, 0.026 and 0.018, respectively, at a frequency of 2 Hz, for each effective pressure. These results were validated using the Kramers-Kronigs method on the linear interpolation of the Young's modulus. The highest attenuation, at effective pressures of 5, 10, 15 and 20 MPa using the Kramers-Kronigs method are 0.081, 0.060, 0.033 and 0.019, respectively, at frequencies of 1.80, 1.78, 1.75 and 1.67 Hz, respectively. There is a slight trend, for the critical frequency to shift to lower frequencies, as the effective pressure is increased.

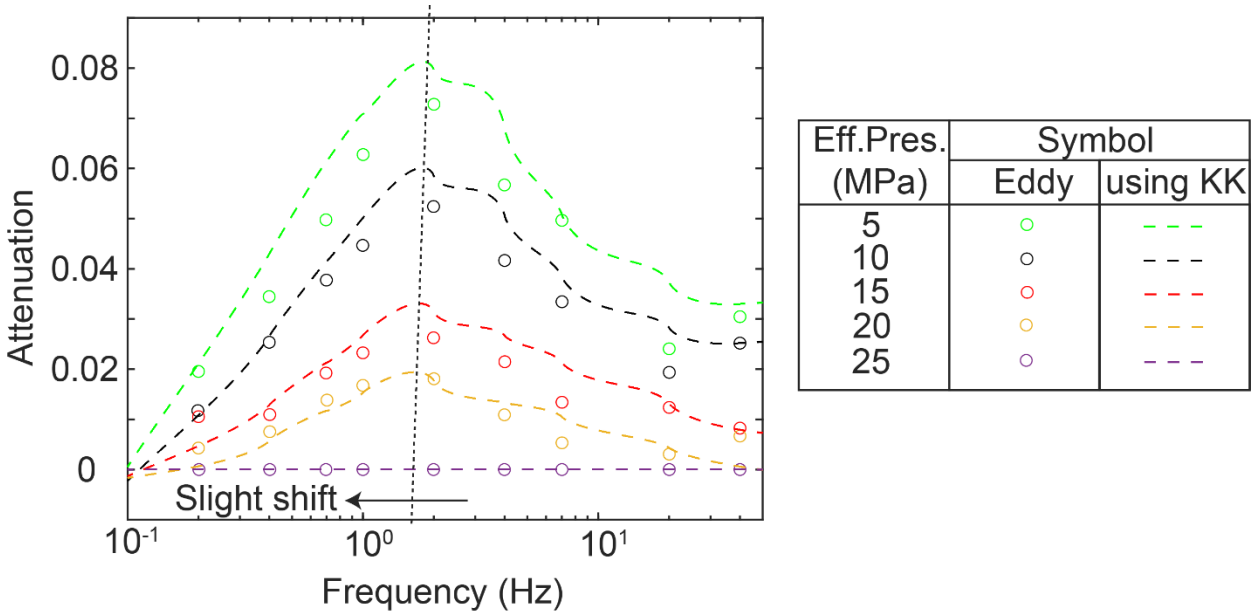

Figure 5.5: Normalized attenuation of Young's modulus versus frequency of Solnhofen sample with Swiss cross fracture in undrained glycerin saturated conditions at 5, 10, 15, 20 and 25 MPa effective pressures, using eddy gauge and using Kramer-Kronigs relationship;

5.4.3 Permeability and hydraulic aperture

Figure 5.6 shows the evolution of the permeability and hydraulic aperture with the effective pressure. As the effective pressure increases from 1 to 29 MPa, the permeability decreases from 4.6 10^{-11} to 4.0 10^{-12} m^2, and the hydraulic aperture decreases from 2.3 10^{-5} to 6.9 10^{-6} m. This correlation is expected since the fractures close as the pressure is increased.

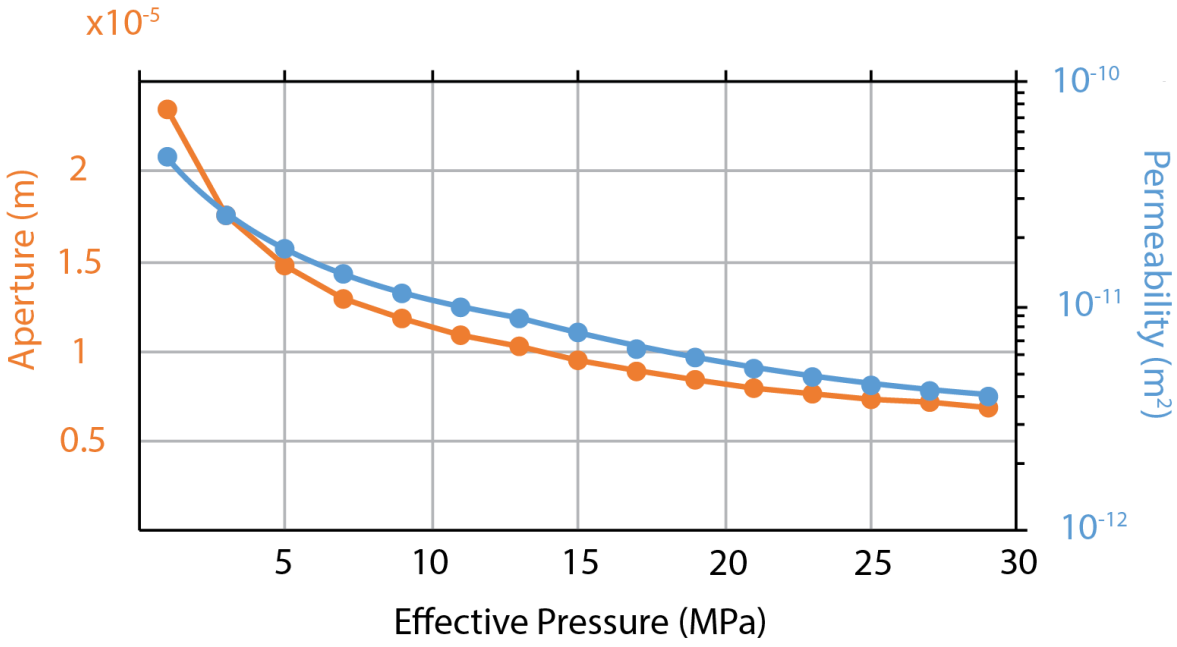

Figure 5.6: Hydraulic aperture and permeability versus effective pressure;

5.4.4 Fracture Stiffness

Figure 5.7 shows the vertical fracture stiffness, calculated from the hydraulic aperture versus effective pressure. The fracture stiffness is shown to increase, in an exponential fashion, as the effective pressure is increased. At 3 MPa effective pressure the vertical fracture stiffness is found to be 4.5 10^{11} Pa m^{-1}. At 27 MPa effective pressure the vertical fracture stiffness increases to 9.4 10^{12} Pa m^{-1}. It should be noted that the horizontal fracture is deformed by the confining pressure as well as the deviatory axial stress applied to it, for that reason, it should be stiffer. A reasonable estimate of the horizontal fracture stiffness would be to use the vertical fracture stiffness at 5 MPa higher effective pressure, as the differential stress, between the radial and axial stress, is fixed to 5 MPa.

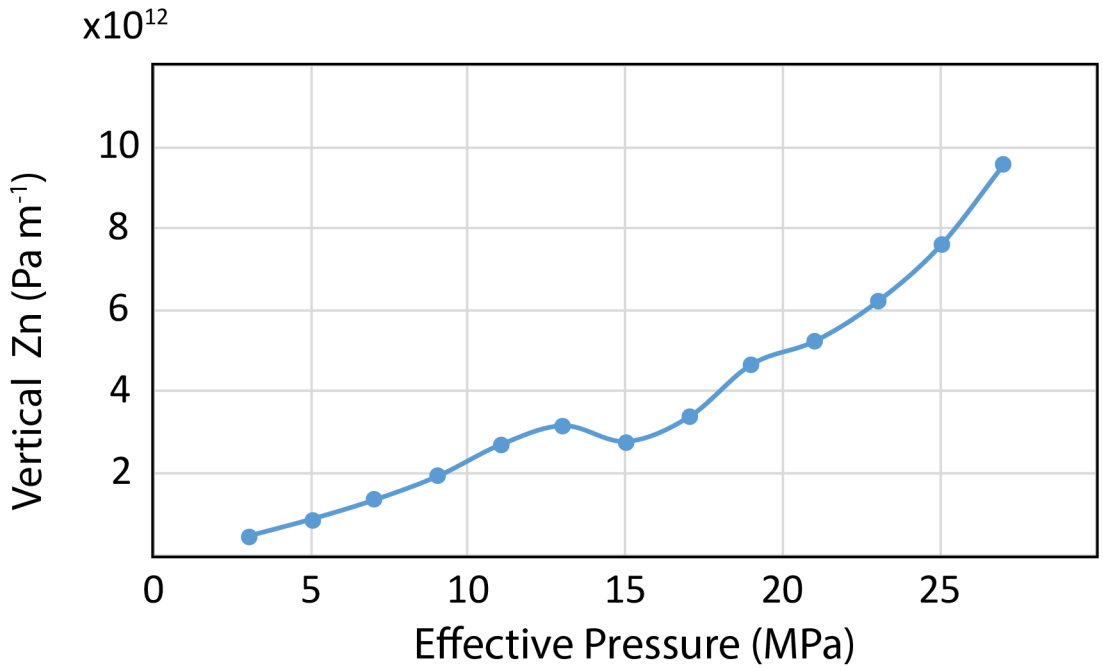

Figure 5.7: Vertical fracture stiffness versus effective pressure;

5.5 Numerical Model

5.5.1 Model development

A numerical model is made using COMSOL to compare to the experimental data. This is done by solving Biot's (1941) poroelastic quasistatic equations using the displacement-pressure formulation (Quintal et al., 2011) in the frequency domain, as follows:

$$\nabla \cdot \sigma = 0\,, \qquad \ldots (5.16)$$

$$\nabla \cdot \left(-\frac{k}{\eta}\nabla p_f\right) + \alpha\nabla \cdot (i\omega u) + \frac{I\omega p}{M} = 0\ , \qquad \ldots (5.17)$$

where u is the vector of solid displacement, with components in the x, y and z directions, α is the Biot coefficient and σ is the stress tensor,

$$\sigma_{ij} = 2\mu\varepsilon_{ij} + \lambda e\delta_{ij} - \alpha p\delta_{ij}\ , \qquad \ldots (5.18)$$

where δ_{ij}, ε_{ij} and e are the Kronecker delta, components of the strain tensor and cubical dilation given by the strain tensor, respectively. The μ and λ are the shear modulus for the dry frame and Lamé's parameter $\lambda = K_d - 2\mu/3$. The coefficient M is (Biot and Willis, 1957)

$$M = \left(\frac{\phi}{K_f} + \frac{\alpha - \phi}{K_s}\right)^{-1} . \quad \ldots (5.19)$$

The sample is modeled with two distinct zones: an (i) intact zone and a (ii) fractured zone. The intact zone has the characteristics of the intact Solnhofen limestone. The fractured zone is modeled assuming a very high permeability and porosity. Using the normal compliance (stiffness^{-1}) estimate calculated previously, the shear compliance can be inferred knowing that the ratio of the normal over shear compliance of carbonate limestones is found to be 0.5 by Lubbe et al. (2008), over a large range of effective pressures. Then the dry p-wave and s-wave modulus can be calculated using (Nakagawa and Schoenberg, 2007):

$$H = b * Z_n \text{ and } G = b * Z_t , \quad \ldots (5.20)$$

where H and G are the p- and s-wave moduli, respectively, and S_n and S_t are the normal and shear compliance, respectively. Then the bulk modulus can be calculated using:

$$K = H - {}^{4}/_{3}\, G. \quad \ldots (5.21)$$

The intact zones are modeled with four half cylinders, which are held apart by the fracture aperture, all space between the intact zones are considered fractured zones. The total height of the model is 77 mm, the total diameter is 40 mm. The parameters used for the intact and fractured zones are presented in table 5.1. The fracture stiffness in the numerical model at each effective pressure is assumed to be the same for the horizontal and vertical fractures, using the estimate of the horizontal fracture from the hydraulic measurements.

	Intact	Fracture		
		5 MPa	15 MPa	25 MPa
Grain bulk modulus (GPa)	K_s = 75		K_s = 75	
Grain density (kg/m^3)	ρ_s = 2663		ρ_s = 2663	
Porosity	ϕ= 0.03		ϕ= 0.99	
Permeability (m^2)	k = 10^{-18}	k = 1 10^{-12}	k = 5.5 10^{-12}	k = 4 10^{-12}
Drained bulk modulus (GPa)	K_d = 60	K_d = 0.13	K_d =0.33	K_d =1.33
Drained shear modulus (GPa)	G_d = 21.5	G_d = 0.20	G_d = 0.50	G_d =2.00
Fluid bulk modulus (GPa)		K_{glyc} = 3.4		
Fluid density (kg/m^3)		ρ_{glyc}= 1260		
Fluid viscosity (Pa s)		η_{glyc}=10^0		

Table 5.1: Material properties for the poroelastic equations used in COMSOL multiphysics;

Tetrahedral elements are used to create a volumetric mesh (figure 5.3) within COMSOL multiphysics, then a finite element method is applied using this newly formed mesh to solve for the weak form of equations 5.1 and 5.2. An axial strain oscillation is applied to the top surface with 0 axial displacement set to the bottom surface. The sides of the cylinders are free to move with undrained conditions fixed.

5.5.2 Comparing experimental results to numerical model

Figure 5.8 shows the normalized bulk modulus from the experimental results as well as the numerical results. The numerical normalized Young's modulus results are presented for effective pressures of 5, 15 and 25 MPa, which is shown in green, red and purple diamonds, respectively. The numerical simulation shows a total dispersion of 0.13, 0.06 and 0.03 for effective pressures of 5 and 15 MPa, respectively.

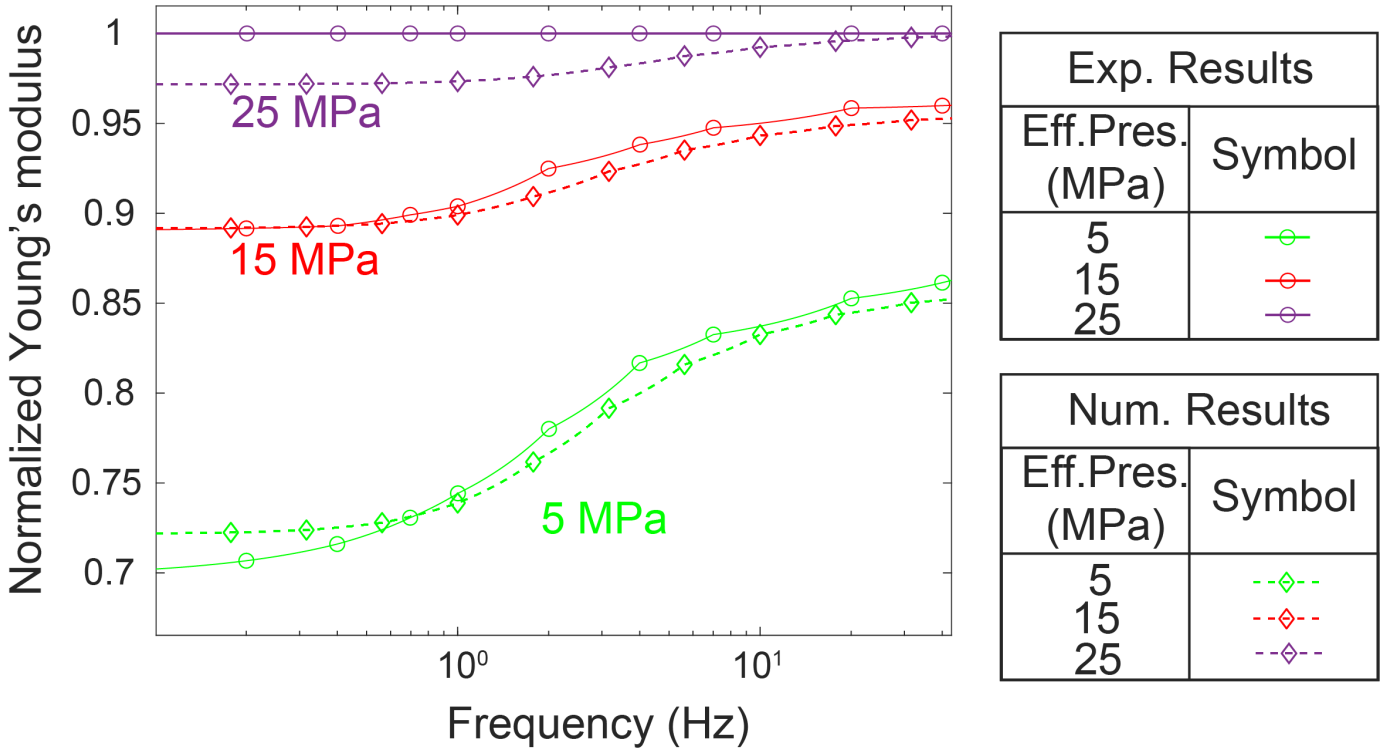

Figure 5.8: Normalized Young's modulus versus frequency of Solnhofen sample with Swiss cross fracture in undrained glycerin saturated conditions at 5, 10, 15, 20 and 25 MPa effective pressures for experimental results and at 5,15 and 25 MPa effective pressures for numerical model results;

Figure 5.9 shows the attenuation from the experimental results as well as the numerical results. The numerical Young attenuation results are presented for effective pressures of 5, 15 and 25 MPa, which is shown in green, red and purple diamonds, respectively. The maximum attenuation reached, for an

effective pressure of 5 MPa, is 0.071, with the critical frequency around 2.5 Hz. The maximum attenuation reached, for an effective pressure of 15 MPa, is 0.029, with the critical frequency around 2.5 Hz. The maximum attenuation reached, for an effective pressure of 25 MPa, is 0.012, with the critical frequency around 4.4 Hz. The numerical simulations are in good agreement with the experimental data.

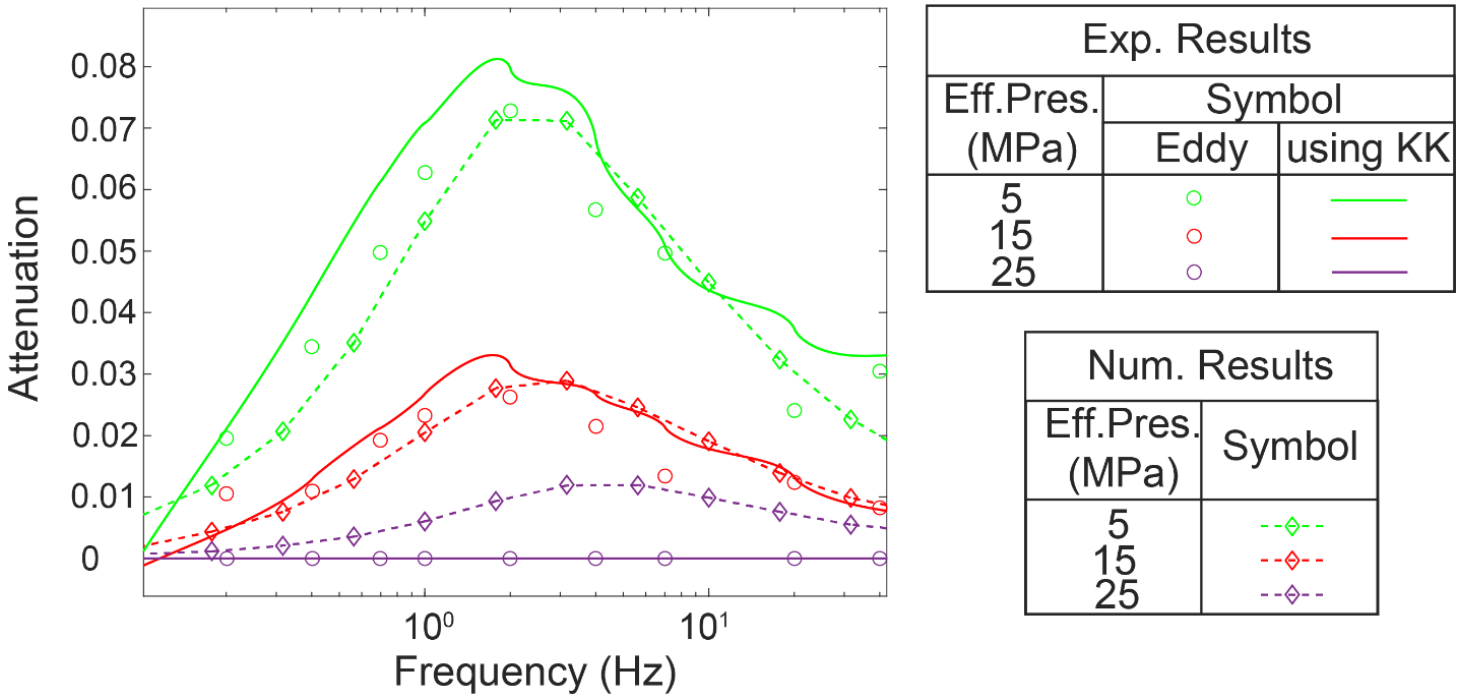

Figure 5.9: Normalized Young's attenuation versus frequency of Solnhofen sample with Swiss cross fracture in undrained glycerin saturated conditions at 5, 15 and 25 MPa effective pressures, using eddy gauge and using Kramer-Kronigs relationship, with the Young's attenuation versus frequency of the numerical simulation under the same conditions at effective pressures of 5, 15 and 25 MPa;

5.6 Discussion

Figure 5.4 shows the normalized Young's modulus of the Swiss cross Solnhofen sample, in undrained glycerin saturated, conditions at effective pressures of 5, 10, 15, 20 and 25 MPa. At 25 MPa effective pressure, the normalized Young's modulus does not change with frequency as the fracture is assumed to be completely closed and there is no attenuation. At 20 MPa effective pressure, the normalized Young's modulus goes from 0.95 to 0.99 at frequencies of 2 10^{-1} and 4 10^{1} Hz, respectively. At 5 MPa effective pressure, the normalized Young's modulus goes from 0.71 to 0.86 at frequencies of 2 10^{-1} and 4 10^{1} Hz, respectively. There is a trend of increase in dispersion with decrease in effective pressure which is associated to the FPD between both fractures (horizontal and vertical), as their compliances are largest at low effective pressures. This is corroborated by the 3D

numerical fracture to fracture simulation completed using the estimated fracture stiffness and aperture values found from permeability measurements, as well as the petro physical properties of the sample.

Others work such as Vinci et al. (2014) and Lissa et al. (2020) showed numerically the importance of the FPD between two fractures and was able to show the effect that changing of geometry fracture has on the FPD, however, a direct comparison has never been shown between numerical and experimental work. This stepping stone can help validate future numerical work on fracture FPD for work using finite element modelling.

Although fracture to fracture FPD was not directly solved for analytically, FPD from matrix to fracture has been shown analytically through Brajanovski et al. (2005), Gurevich et al. (2009) and Galvin and Gurevich (2009&2015) works, and shows that the stiffness of a fracture is increased when reaching the critical frequency through effective medium theory, which is consistent with the results presented here.

At the lowest frequency recorded of 2 10^{-1} Hz, the normalized Young's modulus increases from 0.71 to 1 for effective pressure of 5 and 25 MPa, respectively. This increase in Young's modulus is attributed to i) to the matrix compressibility and ii) the horizontal fracture stiffening.

At the highest frequency recorded of 4 10^{1} Hz, the normalized Young's modulus increases from 0.86 to 1 for effective pressure of 5 and 25 MPa, respectively. At this frequency, fluid has not time to flow from the fracture to fracture, therefore, the fracture compressibility is equal to the glycerin's compressibility.

Thus the global displacement is equal to the displacement of the matrix plus the displacement of the fracture (third term) and simplifying to obtain the following equivalence:

$$\frac{1}{E^*} = \frac{1}{E^{intact}} + \frac{e}{E_g L} \sim \frac{1}{E^{intact}} \quad \ldots (5.22)$$

where E^*, E^{intact} and E_g is the Young's modulus of the whole sample, intact part of the sample and the glycerin, respectively, e is the mechanical aperture and L is the length of the sample. Equation 6.1 represents the axial compliance of the fractured sample.

This is in agreement Brajanovski et al. (2009) who showed that the effect the fracture has, at high frequencies, on the compliance of the whole sample becomes nil (granted large enough spacing).

Therefore, the increase in normalized Young's modulus (0.14) in the highest frequency regime, when going from 5 to 25 MPa effective pressure, is mostly attributed to the change in the matrix compressibility (closure of preexisting cracks).

Looking at figure 5.5, which shows the attenuation of the fractured sample at varying effective pressures, there is a slight trend, for the critical frequency to shift to lower frequencies, as the effective pressure is increased. This follows the estimation for the frequency cut off for a fractured medium:

$$f \approx \frac{4D}{L^2}, \quad \ldots (5.23)$$

where D is the hydraulic diffusivity and L is the distance between 2 fractures (constant here). As the hydraulic diffusivity is directly related to the permeability and bulk modulus of the fracture, the slight decrease in critical frequency suggests that the permeability decreases at a larger rate than the bulk modulus of the fracture for the same step increase in effective pressure.

Looking at figures 5.8 and 5.9, there is very good agreement between the experimental and numerical data for effective pressures of 5 and 15 MPa. For an effective pressure of 25 MPa, there is a slight discrepancy between the numerical model and experimental results of 0.03 and 0.012 for the normalized Young's modulus at low frequencies and Young's attenuation at the attenuation peak, respectively. The first explanation can be due to a too small estimate of fracture stiffness, from the experimental hydraulic measurement, for the numerical input. When a fracture stiffness is changed from $1\ 10^{13}$ to $2\ 10^{13}$ Pa/m, the difference between the experimental and numerical model drops down to 0.01 and 0.004 for the normalized Young's modulus at low frequencies and Young's attenuation at the attenuation peak, respectively, which means this might be a better estimate. The second explanation can be due to the fact that the fracture is not in fact completely closed, at 25 MPa but is closed at a slightly larger effective pressure, meaning there is a slight fracture compliance at 25 MPa and the experimental dispersion and attenuation is not nil but a value slightly larger.

The numerical results were obtained for an aperture of $2\ 10^{-4}$ m, as that is the computing limit of the system used, with smaller apertures creating an increase in nodes due to smaller mesh sizing. In addition, according to Brajanovski et al. (2009) the aperture is not a key parameter that controls the amount of dispersion and attenuation. A control test was outsourced (use of stronger computers) to study a numerical model with an aperture of $2\ 10^{-5}$ m, which is the measured hydraulic aperture. The results give the same values of magnitude of attenuation and dispersion, but show an attenuation peak with a critical frequency shifted down by one order of magnitude. This discrepancy can be due to (i) the hydraulic aperture not being analogous to the mechanical aperture, (ii) the simplicity of a

constant fracture aperture not considering fracture roughness or contact areas,. Lissa et al. (2020) completed numerical models on the attenuation mechanisms between fracture to fracture FPD and found that when comparing a fracture with and without contact areas, the case with contact areas had the critical frequency increase by 1 to 2 orders of magnitude, depending on the geometry, which could explain the lower critical frequency in the outsourced constant aperture test.

Although the exact determination of the aperture could be beneficial for direct comparisons of the frequency cut-off, due to the properties of the Solnhofen limestone (impermeable) and undrained conditions of the test, it is clear that the attenuation recorded is due to fracture to fracture FPD, and the prediction of the numerical modelling is in agreement in term of dispersion and attenuation.

5.7 Conclusion

A very low permeability Solnhofen limestone cylindrical sample was saw cut twice horizontally and vertically at mid height to create a “Swiss cross” formation. Axial oscillations were performed, in a large frequency range (10^{-1} to 4 10^{2} Hz), on the glycerin saturated sample in a triaxial cell, at 5, 10, 15, 20 and 25 MPa effective pressures, under undrained conditions. Hydraulic measurements were made to measure permeability and roughly estimate the fractures aperture and stiffness. The axial strain was measured using an innovative eddy gauge which allowed for normalized Young’s modulus and attenuation measurements. FPD between both fractures were shown, with the largest dispersion on the normalized Young’s modulus and Young’s attenuation of 0.15 and 0.073, respectively, at an effective pressure of 5 MPa. This dispersion and attenuation was shown to be sensitive to effective pressure. It is predicted that the decrease in dispersion and attenuation, when increasing effective pressure, is caused by the fracture stiffening which is corroborated by the 3D numerical simulation results.

6. Conclusion and perspectives

The goal of this thesis is to use the experimental facilities at the ENS geology laboratory to study the elastic properties of carbonate samples in a large frequency range and understand the mechanisms behind the attenuation peaks observed due to viscous fluid flow between different types of heterogeneities. The triaxial cell used for all experiments in this manuscript allows for three types of tests, described previously. These methods combined with the use of specific types of pore fluids allowed for a large apparent frequency range to be studied. Unique to the setup at ENS are two technical improvements which were made at the start of my doctoral work, which include (i) a pair of microvalves inserted at the inlet and outlet of the sample and (ii) a global axial eddy gauge. These advancements allowed for the observation of specific FPD attenuation mechanisms which have previously only been theorized or observed in numerical simulations.

6.1 Mesoscopic FPD and pore scale squirt flow experiment with takeaways

Three carbonate samples, originating from a pre salt formation, were tested. An attenuation mechanism at 40 kHz apparent frequency was observed in all three samples. This is assumed to be caused by squirt flow at the pore scale as there is dispersion in both shear and bulk moduli and it is pressure dependent. Usually, in similar setups, a drained-undrained frequency regime is observed around 10 Hz. However, the microvalves remove any attenuation that would be caused by the drained-undrained regime, as the pore volume is kept constant. This advancement allowed for a clear attenuation peak to be observed around 100 Hz, in the heterogeneous samples. This second peak was identified as mesoscopic FPD between regions of varying porosity. There was no shear attenuation caused by the mesoscopic FPD which is consistent with the literature (White, 1975). Also, a simple numerical model was developed, for the mesocopic FPD, which revealed similar critical frequencies and magnitudes of the attenuation peaks observed experimentally. The model assumed the same dimensions of samples used with elastic properties mimicking what was calculated during the tests, however a 1D porosity gradient was applied by analyzing a 2D slice for each sample of the CT scans made available by TOTAL and Petrobras.

There have been some interesting attenuation peaks observed experimentally caused by mesoscopic FPD due to heterogeneity in the pore fluid (Alemu et a.,2013; Tisato et al., 2015; Chapman et al., 2021). However, there has been no experimental work, until now, showing attenuation caused by

mesoscopic heterogeneity in the porosity, which is shown analytically by Carcione and Picotti (2006) to be just as impactful. Also, comparisons between the laboratory and in situ p- and s-wave measurements are in good agreement with each other.

In retrospect, when studying heterogeneous samples, it would be ideal to complete a full 3D CT scan to create a 3D map of the sample's porosity. This would allow for a more accurate representation in the numerical models of the sample. During the numerical simulations, it was found that the attenuation peak shifted depending on the location of the measurement. With this in mind, it could be beneficial to experimentally measure the local strain at multiple heights on a heterogeneous sample to explore how the attenuation peaks moved depending on location. This exercise could help improve models, deepen our understanding of the mechanics behind this viscous fluid flow and help create more robust 3D numerical models, which could be used to help define the subsurface remotely through elastic wave propagation.

6.2 Fracture to background FPD experiment with takeaways

A carbonate cylindrical sample, from Rustrel in the SE of France, was also tested when it was intact and after a vertical saw cut was made along its length. This series of tests were done in dry and water saturated conditions, using hydrostatic oscillations, at frequencies between 0.04 and 1 Hz and at three effective pressures. The strain measurements were done locally and a negative phase shift between the stress and strain was observed for the saw cut sample in the water saturated conditions, at the lower effective pressures. At the highest effective pressure, the same sample had no attenuation as the fracture was closed. A 1D analytical model and 3D numerical model were developed which both confirmed that although the pore pressure in the compliant fracture increases at high frequencies, a slight decrease in pore pressure is seen in the matrix, which creates a slight local decrease in bulk modulus with increase in frequency. In this study, the experimental data is well described by both models. The 1D model was ideal to get a quick first order estimation of the normal compliance of the fracture and the 3D model corroborated the results from the analytical model and can allow different geometries to be explored.

This work is important as it shows how significant the location of measurements can be, and how the fluid connects all parts of a rock, and by monitoring its behavior, local measurements can be used to infer global properties.

In retrospect, it could be interesting to repeat a similar experiment with global strain measurements, to record both the global positive attenuation and local negative phase shift between the stress and

strain, at the same time. As the local responses can be used to infer elastic properties of the fracture, the global measurements would help to create a more accurate method of deducing these results.

6.3 Fracture to fracture FPD experiment with takeaways

A relatively impermeable (10^{-18} m^2) Solnhofen limestone was used to investigate FPD that can be caused by two fractures in contact with each other. Many numerical simulations have been made studying this configuration, however never has this been measured experimentally (Rubino et al., 2013; Quintal et al., 2014). Typically, fracture to fracture FPD occurs at higher frequencies (Vinci et al., 2014) therefore glycerin was used as a pore fluid to increase the apparent frequency of the system. The Solnhofen sample was cut twice down its length and height, creating a "Swiss cross" formation. This series of tests were completed at multiple effective pressures using axial oscillations, at frequencies between 0.2 and 40 Hz. The strain measurements were completed using the eddy gauge, which is a global axial measurement and the normalized Young's modulus and attenuation were measured. An attenuation peak was found at a frequency of 2 Hz, which increased in amplitude with a decrease in effective pressure. A numerical model was made to simulate this experiment, with a really good match between the experimental and numerical dispersion and attenuation, when using an aperture of $2\ 10^{-4}$ m.

These findings are remarkable, as this simple fracture formation has been heavily leaned upon when studying fractures to fracture FPD numerically, however, has not been measured experimentally in the lab.

In retrospect, it could be beneficial to scan the roughness of both fractures, to better simulate the roughness and contact points in the fracture numerically, which could lead to a better approximation of the experimental results (Lissa et al., 2020). Another idea would be to create multiple synthetic un dispersive glass samples, which are equally impermeable and have them all saw cut in the same manner; after which different roughness's could be applied. Each unique finish could be scanned with known fracture geometries. Next the experimental results from the same test could be compared to a numerical model with a better knowledge of fracture contact areas and roughness.

In this manuscript, the experimental results completed on carbonate samples corroborated analytical and numerical results which have been available for years. This achievement helps us truly understand the underlying physics behind FPD mechanisms related to heterogeneities, giving confidence in what models to move forward with and great insight into how to interpret log well measurements as well as seismic signals.

Bibliography

Adam, L., Batzle, M., & Brevik, I. (2006). Gassmann's fluid substitution and shear modulus variability in carbonates at laboratory seismic and ultrasonic frequencies. *Geophysics*, *71*(6), F173-F183.

Adam, L., Batzle, M., Lewallen, K. T., & van Wijk, K. (2009). Seismic wave attenuation in carbonates. *Journal of Geophysical Research: Solid Earth*, *114*(B6).

Adelinet, M., Fortin, J., Guéguen, Y., Schubnel, A., & Geoffroy, L. (2010). Frequency and fluid effects on elastic properties of basalt: Experimental investigations. *Geophysical Research Letters*, *37*(2).

Adelinet, M., Fortin, J., & Guéguen, Y. (2011). Dispersion of elastic moduli in a porous-cracked rock: Theoretical predictions for squirt-flow. *Tectonophysics*, *503*(1-2), 173-181.

Alemu, B. L., Aker, E., Soldal, M., Johnsen, Ø., & Aagaard, P. (2013). Effect of sub-core scale heterogeneities on acoustic and electrical properties of a reservoir rock: a CO2 flooding experiment of brine saturated sandstone in a computed tomography scanner. *Geophysical Prospecting*, *61*(1), 235-250.

Alonso-Zarza, A. M., & Tanner, L. H. (2009). *Carbonates in continental settings: facies, environments, and processes*. Elsevier.

Amalokwu, K., Best, A. I., Sothcott, J., Chapman, M., Minshull, T., & Li, X. Y. (2014). Water saturation effects on elastic wave attenuation in porous rocks with aligned fractures. *Geophysical Journal International*, *197*(2), 943-947.

Amalokwu, K., Papageorgiou, G., Chapman, M., & Best, A. I. (2017). Modelling ultrasonic laboratory measurements of the saturation dependence of elastic modulus: new insights and implications for wave propagation mechanisms. *International Journal of Greenhouse Gas Control*, *59*, 148-159.

Anselmetti, F. S., & Eberli, G. P. (1993). Controls on sonic velocity in carbonates. *Pure and Applied geophysics*, *141*(2), 287-323.

Anselmetti, F. S. (1994). *Physical properties and seismic response of carbonate sediments and rocks* (Doctoral dissertation, ETH Zurich).

Anselmetti, F. S., & Eberli, G. P. (1999). The velocity-deviation log: a tool to predict pore type and permeability trends in carbonate drill holes from sonic and porosity or density logs. *AAPG bulletin*, *83*(3), 450-466.

Anselmetti, F. S., & Eberli, G. P. (2001). Sonic velocity in carbonates—A combined product of depositional lithology and diagenetic alterations.

Bailly, C., Adelinet, M., Hamon, Y., & Fortin, J. (2019a). Combined controls of sedimentology and diagenesis on seismic properties in lacustrine and palustrine carbonates (Upper Miocene, Samos Island, Greece). *Geophysical Journal International*, 219, 1300–1315.

Bailly, C., Fortin, J., Adelinet, M., & Hamon, Y. (2019b). Upscaling of elastic properties in carbonates: A modeling approach based on a multiscale geophysical data set. *Journal of Geophysical Research: Solid Earth*, *124*(12), 13021-13038.

Bailly, C., Kernif, T., Hamon, Y., Adelinet, M., & Fortin, J. (2022). Controlling factors of acoustic properties in continental carbonates: Implications for high-resolution seismic imaging. *Marine and Petroleum Geology*, 137.

Barbosa, N. D., Caspari, E., Rubino, J. G., Greenwood, A., Baron, L., & Holliger, K. (2019). Estimation of fracture compliance from attenuation and velocity analysis of full-waveform sonic log data. *Journal of Geophysical Research: Solid Earth*, *124*(3), 2738-2761.

Batzle, M., & Wang, Z. (1992). Seismic properties of pore fluids. *Geophysics*, *57*(11), 1396-1408.

Batzle, M. L., Han, D. H., & Hofmann, R. (2006). Fluid mobility and frequency-dependent seismic velocity—Direct measurements. *Geophysics*, *71*(1), N1-N9.

Baud, P., Schubnel, A., & Wong, T. F. (2000). Dilatancy, compaction, and failure mode in Solnhofen limestone. *Journal of Geophysical Research: Solid Earth*, *105*(B8), 19289-19303.

Baud, P., Reuschlé, T., Ji, Y., Cheung, C. S., & Wong, T. F. (2015). Mechanical compaction and strain localization in Bleurswiller sandstone. *Journal of Geophysical Research: Solid Earth*, *120*(9), 6501-6522.

Bear, J. (1972). *Dynamics of Fluids in Porous Media*, 784 p., American Elsevier Publishing Company, New York.

Biot, M. A. (1941). General theory of three-dimensional consolidation. *Journal of applied physics*, *12*(2), 155-164.

Biot, M. A. (1956). Theory of propagation of elastic waves in a fluid-saturated porous solid. II. Higher frequency range. *The Journal of the acoustical Society of america*, *28*(2), 179-191.

Biot, M. A., & Willis, D. G. (1957). The elastic coefficients of the theory of consolidation.

Biot, M. A. (1962). Mechanics of deformation and acoustic propagation in porous media. *Journal of applied physics*, *33*(4), 1482-1498.

Birch, F. (1960). The velocity of compressional waves in rocks to 10 kilobars: 1. *Journal of Geophysical Research*, *65*(4), 1083-1102.

Blanchard, T. D., & Delommot, P. (2015). An example of the measurement and practical applications of time-lapse seismic attenuation. *Geophysics*, *80*(2), WA25-WA34.

Blöcher, G., Kluge, C., Milsch, H., Cacace, M., Jacquey, A. B., & Schmittbuhl, J. (2019). Permeability of matrix-fracture systems under mechanical loading–constraints from laboratory experiments and 3-D numerical modelling. *Advances in Geosciences*, *49*, 95-104.

Bohacs, K. M., Carroll, A. R., Neal, J. E., Mankiewicz, P. J., Gierlowski-Kordesch, E. H., & Kelts, K. R. (2000). Lake-basin type, source potential, and hydrocarbon character: an integrated sequence-stratigraphic-geochemical framework. *Lake basins through space and time: AAPG Studies in Geology*, *46*, 3-34.

Borgomano, J. V. M., Pimienta, L., Fortin, J., & Guéguen, Y. (2017). Dispersion and attenuation measurements of the elastic moduli of a dual-porosity limestone. *Journal of Geophysical Research: Solid Earth*, *122*(4), 2690-2711.

Borgomano, J. V., Fortin, J., & Guéguen, Y. (2017). Elastic dispersion and attenuation in fully saturated sandstones: Role of mineral content, porosity, and pressures. *Journal of Geophysical Research: Solid Earth*, *122*(12), 9950-9965.

Borgomano, J. V. M. (2018). *Dispersion of elastic moduli of saturated carbonates: Experimental study and modelisation* (Doctoral dissertation, Ph. D. thesis, PSL Research University, Paris, France).

Borgomano, J. V., Fortin, J., & Guéguen, Y. (2019a). Cracked, porous rocks and fluids: Moon and earth paradox. *Minerals*, *9*(11), 693.

Borgomano, J. V., Pimienta, L. X., Fortin, J., & Guéguen, Y. (2019b). Seismic dispersion and attenuation in fluid-saturated carbonate rocks: Effect of microstructure and pressure. *Journal of Geophysical Research: Solid Earth*, *124*(12), 12498-12522.

Borgomano, J. V., Gallagher, A., Sun, C., & Fortin, J. (2020). An apparatus to measure elastic dispersion and attenuation using hydrostatic-and axial-stress oscillations under undrained conditions. *Review of Scientific Instruments*, *91*(3), 034502.

Bosart, L. W., & Snoddy, A. O. (1927). New Glycerol Tables1. *Industrial & Engineering Chemistry*, *19*(4), 506-510.

Brajanovski, M., Gurevich, B., & Schoenberg, M. (2005). A model for P-wave attenuation and dispersion in a porous medium permeated by aligned fractures. *Geophysical Journal International*, *163*(1), 372-384.

Brajanovski, M., Müller, T. M., & Parra, J. O. (2010). A model for strong attenuation and dispersion of seismic P-waves in a partially saturated fractured reservoir. *Science China Physics, Mechanics and Astronomy*, *53*(8), 1383-1387.

Cai, J. G., & Zhao, J. (2000). Effects of multiple parallel fractures on apparent attenuation of stress waves in rock masses. *International Journal of Rock Mechanics and Mining Sciences*, *37*(4), 661-682.

Carcione, J. M., Helbig, K., & Helle, H. B. (2003). Effects of pressure and saturating fluid on wave velocity and attenuation in anisotropic rocks. *International Journal of Rock Mechanics and Mining Sciences*, *40*(3), 389-403.

Carcione, J. M., & Picotti, S. (2006). P-wave seismic attenuation by slow-wave diffusion: Effects of inhomogeneous rock properties. *Geophysics*, *71*(3), O1-O8.

Carcione, J. M., Santos, J. E., & Picotti, S. (2012). Fracture-induced anisotropic attenuation. *Rock mechanics and rock engineering*, *45*(5), 929-942.

Cardwell, D. N., Chana, K. S., & Russhard, P. (2008, January). The use of eddy current sensors for the measurement of rotor blade tip timing: sensor development and engine testing. In *Turbo Expo: Power for Land, Sea, and Air* (Vol. 43123, pp. 179-189).

Caspari, E., Novikov, M., Lisitsa, V., Barbosa, N. D., Quintal, B., Rubino, J. G., & Holliger, K. (2019). Attenuation mechanisms in fractured fluid-saturated porous rocks: a numerical modelling study. *Geophysical Prospecting*, *67*(4-Rock Physics: from microstructure to seismic signatures), 935-955.

Cleary, M. P. (1978), Elastic and dynamic response regimes of fluid-impregnated solids with diverse microstructures, International Journal of Solids and Structures, 14(10), 795–819.

Chapman, M. (2003). Frequency-dependent anisotropy due to meso-scale fractures in the presence of equant porosity. *Geophysical prospecting*, *51*(5), 369-379.

Chapman, S., Tisato, N., Quintal, B., & Holliger, K. (2016). Seismic attenuation in partially saturated Berea sandstone submitted to a range of confining pressures. *Journal of Geophysical Research: Solid Earth*, *121*(3), 1664-1676.

Chapman, S., Quintal, B., Tisato, N., & Holliger, K. (2017). Frequency scaling of seismic attenuation in rocks saturated with two fluid phases. *Geophysical Journal International*, *208*(1), 221-225.

Chapman, S., & Quintal, B. (2018). Numerical analysis of local strain measurements in fluid-saturated rock samples submitted to forced oscillations. *Geophysics*, *83*(5), MR309-MR316.

Chapman, S., Borgomano, J. V., Yin, H., Fortin, J., & Quintal, B. (2019). Forced oscillation measurements of seismic wave attenuation and stiffness moduli dispersion in glycerine-saturated Berea sandstone. *Geophysical Prospecting*, *67*(4-Rock Physics: from microstructure to seismic signatures), 956-968.

Chapman, S., Borgomano, J. V., Quintal, B., Benson, S. M., & Fortin, J. (2021). Seismic Wave Attenuation and Dispersion Due to Partial Fluid Saturation: Direct Measurements and Numerical Simulations Based on X-Ray CT. *Journal of Geophysical Research: Solid Earth*, *126*(4), e2021JB021643.

David, E. C., & Zimmerman, R. W. (2012). Pore structure model for elastic wave velocities in fluid-saturated sandstones. *Journal of Geophysical Research: Solid Earth*, *117*(B7).

David, E. C., Fortin, J., Schubnel, A., Guéguen, Y., & Zimmerman, R. W. (2013). Laboratory measurements of low-and high-frequency elastic moduli in Fontainebleau sandstone. *Geophysics*, *78*(5), D369-D379.

Dunn, K. J. (1987). Sample boundary effect in acoustic attenuation of fluid-saturated porous cylinders. *The Journal of the Acoustical Society of America*, *81*(5), 1259-1266.

Dvorkin, J., Nolen-Hoeksema, R., & Nur, A. (1994). The squirt-flow mechanism: Macroscopic description. *Geophysics*, *59*(3), 428-438.

Dvorkin, J., Mavko, G., & Nur, A. (1995). Squirt flow in fully saturated rocks. *Geophysics*, *60*(1), 97-107.

Eberli, G. P., Baechle, G. T., Anselmetti, F. S., & Incze, M. L. (2003). Factors controlling elastic properties in carbonate sediments and rocks. *The Leading Edge*, *22*(7), 654-660.

Fett, T., Munz, D., & Thun, G. (2002). Young's modulus of soft PZT from partial unloading tests. *Ferroelectrics*, *274*(1), 67-81.

Fleuchaus, P., & Blum, P. (2017). Damage event analysis of vertical ground source heat pump systems in Germany. *Geothermal Energy*, *5*(1), 1-15.

Fortin, J., Stanchits, S., Dresen, G., & Guéguen, Y. (2006). Acoustic emission and velocities associated with the formation of compaction bands in sandstone. *Journal of Geophysical Research: Solid Earth*, *111*(B10).

Fortin, J., Guéguen, Y., & Schubnel, A. (2007). Effects of pore collapse and grain crushing on ultrasonic velocities and Vp/Vs. *Journal of Geophysical Research: Solid Earth*, *112*(B8).

Fortin, J., & Guéguen, Y. (2021). Porous and cracked rocks elasticity: Macroscopic poroelasticity and effective media theory. *Mathematics and Mechanics of Solids*, *26*(8), 1158-1172.

Freytet, P., & Verrecchia, E. P. (2002). Lacustrine and palustrine carbonate petrography: an overview. *Journal of Paleolimnology*, *27*(2), 221-237.

Galvin, R. J., & Gurevich, B. (2009). Effective properties of a poroelastic medium containing a distribution of aligned cracks. *Journal of Geophysical Research: Solid Earth*, *114*(B7).

Galvin, R. J., & Gurevich, B. (2015). Frequency-dependent anisotropy of porous rocks with aligned fractures. *Geophysical Prospecting*, *63*(1), 141-150.

García-Martín, J., Gómez-Gil, J., & Vázquez-Sánchez, E. (2011). Non-destructive techniques based on eddy current testing. *Sensors*, *11*(3), 2525-2565.

Gassmann, F. (1951). Elastic waves through a packing of spheres. *Geophysics*, *16*(4), 673-685.

Goodman, R. E. (1976). Methods of geological engineering in discontinuities of rocks: west, St. *Paul, Minn*.

Gomez, C. T., Dvorkin, J., & Vanorio, T. (2010). Laboratory measurements of porosity, permeability, resistivity, and velocity on Fontainebleau sandstones. *Geophysics*, *75*(6), E191-E204.

Gudmundsson, A., & Løtveit, I. F. (2014). Sills as fractured hydrocarbon reservoirs: examples and models. *Geological Society, London, Special Publications*, *374*(1), 251-271.

Guéguen, Y., & Boutéca, M. (Eds.). (2004). *Mechanics of fluid-saturated rocks*. Elsevier.

Guo, J., Germán Rubino, J., Barbosa, N. D., Glubokovskikh, S., & Gurevich, B. (2018a). Seismic dispersion and attenuation in saturated porous rocks with aligned fractures of finite thickness: Theory and numerical simulations—Part 1: P-wave perpendicular to the fracture plane. *Geophysics*, *83*(1), WA49-WA62.

Guo, J., Germán Rubino, J., Barbosa, N. D., Glubokovskikh, S., & Gurevich, B. (2018b). Seismic dispersion and attenuation in saturated porous rocks with aligned fractures of finite thickness: Theory and numerical simulations—Part 2: Frequency-dependent anisotropy. *Geophysics*, *83*(1), WA63-WA71.

Guo, J., & Gurevich, B. (2020). Frequency-dependent P wave anisotropy due to wave-induced fluid flow and elastic scattering in a fluid-saturated porous medium with aligned fractures. *Journal of Geophysical Research: Solid Earth*, *125*(8), e2020JB020320.

Gurevich, B., Brajanovski, M., Galvin, R. J., Müller, T. M., & Toms-Stewart, J. (2009). P-wave dispersion and attenuation in fractured and porous reservoirs–poroelasticity approach. *Geophysical Prospecting*, *57*(2), 225-237.

Gurevich, B., Brajanovski, M., Galvin, R. J., Müller, T. M., & Toms-Stewart, J. (2009). P-wave dispersion and attenuation in fractured and porous reservoirs–poroelasticity approach. *Geophysical Prospecting*, *57*(2), 225-237.

Gurevich, B., Sadovnichaja, A. P., Lopatnikov, S. L., & Shapiro, S. A. (1998). Scattering of a compressional wave in a poroelastic medium by an ellipsoidal inclusion. *Geophysical Journal International*, *133*(1), 91-103.

Gurevich, B., Makarynska, D., de Paula, O. B., & Pervukhina, M. (2010). A simple model for squirt-flow dispersion and attenuation in fluid-saturated granular rocks. *Geophysics*, *75*(6), N109-N120.

Han, T., Liu, B., & Sun, J. (2018). Validating the theoretical model for squirt-flow attenuation in fluid saturated porous rocks based on the dual porosity concept. *Geophysical Journal International*, *214*(3), 1800-1807.

Haldorsen, H. H., & Lake, L. W. (1984). A new approach to shale management in field-scale models. *Society of Petroleum Engineers Journal*, *24*(04), 447-457.

Hart, D. J., & Wang, H. F. (1995). Laboratory measurements of a complete set of poroelastic moduli for Berea sandstone and Indiana limestone. *Journal of Geophysical Research: Solid Earth*, *100*(B9), 17741-17751.

Heard, H. C. (1960). Transition from brittle fracture to ductile flow in Solenhofen limestone as a function of temperature, confining pressure, and interstitial fluid pressure.

Hunziker, J., Favino, M., Caspari, E., Quintal, B., Rubino, J. G., Krause, R., & Holliger, K. (2018). Seismic attenuation and stiffness modulus dispersion in porous rocks containing stochastic fracture networks. *Journal of Geophysical Research: Solid Earth*, *123*(1), 125-143.

Jackson, I., & Paterson, M. S. (1993). A high-pressure, high-temperature apparatus for studies of seismic wave dispersion and attenuation. *Pure and Applied Geophysics*, *141*(2), 445-466.

Jackson, I., Schijns, H., Schmitt, D. R., Mu, J., & Delmenico, A. (2011). A versatile facility for laboratory studies of viscoelastic and poroelastic behaviour of rocks. *Review of Scientific Instruments*, *82*(6), 064501.

Jaeger, J. C., Cook, N. G., & Zimmerman, R. (2009). *Fundamentals of rock mechanics*. John Wiley & Sons.

Jänicke, R., Quintal, B., Larsson, F., & Runesson, K. (2019). Identification of viscoelastic properties from numerical model reduction of pressure diffusion in fluid-saturated porous rock with fractures. *Computational Mechanics*, *63*(1), 49-67.

Johnson, D. L. (2001). Theory of frequency dependent acoustics in patchy-saturated porous media. *The Journal of the Acoustical Society of America*, *110*(2), 682-694.

Johnston, D. H., & Toksöz, M. N. (1980). Ultrasonic P and S wave attenuation in dry and saturated rocks under pressure. *Journal of Geophysical Research: Solid Earth*, *85*(B2), 925-936.

King, M. S., Marsden, J. R., & Dennis, J. W. (2000). Biot dispersion for P-and S-wave velocities in partially and fully saturated sandstones. *Geophysical Prospecting*, *48*(6), 1075-1089.

Kluge, C., Blöcher, G., Milsch, H., Hofmann, H., Nicolas, A., Li, Z., & Fortin, J. (2017). Sustainability of fractured rock permeability under varying pressure. In *Poromechanics VI* (pp. 1192-1199).

Kobayashi, Y., & Mavko, G. (2016). Variation in P-wave modulus with frequency and water saturation: extension of dynamic-equivalent-medium approach. *Geophysics*, *81*(5), D479-D494.

Koch, R. (2007). Sedimentological and petrophysical characteristics of Solnhofen monument stones lithographic limestone: A key to diagenesis and fossil preservation. *Neues Jahrbuch für Geologie und Paläontologie-Abhandlungen*, 103-115.

Lee, M. W., & Collett, T. S. (2009). Unique problems associated with seismic analysis of partially gas-saturated unconsolidated sediments. *Marine and Petroleum Geology*, *26*(6), 775-781.

Li, B., Jiang, Y., Koyama, T., Jing, L., & Tanabashi, Y. (2008). Experimental study of the hydro-mechanical behavior of rock joints using a parallel-plate model containing contact areas and artificial fractures. *International Journal of Rock Mechanics and Mining Sciences*, *45*(3), 362-375.

Lissa, S., Barbosa, N. D., Caspari, E., Alkhimenkov, Y., & Quintal, B. (2020). Squirt flow in cracks with rough walls. *Journal of Geophysical Research: Solid Earth*, *125*(4), e2019JB019235.

Lissa, S., Barbosa, N. D., & Quintal, B. (2021). Fluid pressure diffusion in fractured media: The role played by the geometry of real fractures. *Journal of Geophysical Research: Solid Earth*, *126*(10), e2021JB022233.

Lubbe, R., Sothcott, J., Worthington, M. H., & McCann, C. (2008). Laboratory estimates of normal and shear fracture compliance. *Geophysical Prospecting*, *56*(2), 239-247.

Lucia, F. J. (1995), Rock-Fabric/Petrophysical Classification of Carbonate Pore Space for Reservoir Characterization, AAPG Bulletin, 79(9), 1275–1300.

Madonna, C., & Tisato, N. (2013). A new seismic wave attenuation module to experimentally measure low-frequency attenuation in extensional mode. *Geophysical Prospecting*, *61*(2-Rock Physics for Reservoir Exploration, Characterisation and Monitoring), 302-314.

Mallet, C., Fortin, J., Guéguen, Y., & Bouyer, F. (2013). Effective Elastic Properties of Cracked Solids: An Experimental Investigation. *International journal of fracture*, *182*(2).

Mallet, C., Fortin, J., Guéguen, Y., & Bouyer, F. (2015). Brittle creep and subcritical crack propagation in glass submitted to triaxial conditions. *Journal of Geophysical Research: Solid Earth*, *120*(2), 879-893.

Masson, Y. J., & Pride, S. R. (2007). Poroelastic finite difference modeling of seismic attenuation and dispersion due to mesoscopic-scale heterogeneity. *Journal of Geophysical Research: Solid Earth*, *112*(B3).

Masson, Y. J., & Pride, S. R. (2011). Seismic attenuation due to patchy saturation. *Journal of Geophysical Research: Solid Earth*, *116*(B3).

Masson, Y. J., & Pride, S. R. (2014). On the correlation between material structure and seismic attenuation anisotropy in porous media. *Journal of Geophysical Research: Solid Earth*, *119*(4), 2848-2870.

Matonti, C., Guglielmi, Y., Viseur, S., Bruna, P. O., Borgomano, J., Dahl, C., & Marié, L. (2015). Heterogeneities and diagenetic control on the spatial distribution of carbonate rocks acoustic properties at the outcrop scale. *Tectonophysics*, *638*, 94-111.

Mavko, G., & Nur, A. (1975). Melt squirt in the asthenosphere. *Journal of Geophysical Research*, *80*(11), 1444-1448.

Mavko, G. M., & Nur, A. (1979). Wave attenuation in partially saturated rocks. *Geophysics*, *44*(2), 161-178.

Mavko, G., & Jizba, D. (1991). Estimating grain-scale fluid effects on velocity dispersion in rocks. *Geophysics*, *56*(12), 1940-1949.

Mavko, G., T. Mukerji, and J. Dvorkin (2009), The rock physics handbook: Tools for seismic analysis of porous media, Cambridge university press.

Mazumder, S., Karnik, A. A., & Wolf, K. H. A. (2006). Swelling of coal in response to CO2 sequestration for ECBM and its effect on fracture permeability. *Spe Journal*, *11*(03), 390-398.

Mikhaltsevitch, V., Lebedev, M., & Gurevich, B. (2011). A low-frequency laboratory apparatus for measuring elastic and anelastic properties of rocks. In *SEG Technical Program Expanded Abstracts 2011* (pp. 2256-2260). Society of Exploration Geophysicists.

Mikhaltsevitch, V., Lebedev, M., & Gurevich, B. (2014). A laboratory study of low-frequency wave dispersion and attenuation in water-saturated sandstones. *The Leading Edge*, *33*(6), 616-622.

Mikhaltsevitch, V., Lebedev, M., & Gurevich, B. (2016). Validation of the laboratory measurements at seismic frequencies using the Kramers-Kronig relationship. *Geophysical Research Letters*, *43*(10), 4986-4991.

Min, K. B., Lee, J., & Stephansson, O. (2013). Implications of thermally-induced fracture slip and permeability change on the long-term performance of a deep geological repository. *International Journal of Rock Mechanics and Mining Sciences*, *61*, 275-288.

Morlet, J., Arens, G., Fourgeau, E., & Glard, D. (1982). Wave propagation and sampling theory—Part I: Complex signal and scattering in multilayered media. *Geophysics*, *47*(2), 203-221.

Müller, T. M., Gurevich, B., & Lebedev, M. (2010). Seismic wave attenuation and dispersion resulting from wave-induced flow in porous rocks—A review. *Geophysics*, *75*(5), 75A147-75A164.

Murai, Y., Kawahara, J., & Yamashita, T. (1995). Multiple scattering of SH waves in 2-D elastic media with distributed cracks. *Geophysical Journal International*, *122*(3), 925-937.

Murphy III, W. F., Winkler, K. W., & Kleinberg, R. L. (1986). Acoustic relaxation in sedimentary rocks: Dependence on grain contacts and fluid saturation. *Geophysics*, *51*(3), 757-766.

Nakagawa, S., & Schoenberg, M. A. (2007). Poroelastic modeling of seismic boundary conditions across a fracture. *The Journal of the Acoustical Society of America*, *122*(2), 831-847.

Nakagawa, S., Kneafsey, T. J., Daley, T. M., Freifeld, B. M., & Rees, E. V. (2013a). Laboratory seismic monitoring of supercritical CO2 flooding in sandstone cores using the Split Hopkinson Resonant Bar technique with concurrent X-ray computed tomography imaging. *Geophysical Prospecting*, *61*(2-Rock Physics for Reservoir Exploration, Characterisation and Monitoring), 254-269.

Nakagawa, S. (2013b, January). Low-frequency (< 100 Hz) dynamic fracture compliance measurement in the laboratory. In *47th US Rock Mechanics/Geomechanics Symposium*. American Rock Mechanics Association.

Nicolas, A., Fortin, J., Regnet, J. B., Dimanov, A., & Guéguen, Y. (2016). Brittle and semi-brittle behaviours of a carbonate rock: influence of water and temperature. *Geophysical Journal International*, *206*(1), 438-456.

Nowick, A. S., and B. S. Berry (1972), Anelastic relaxation in crystalline solids, Materials Science Series, Academic Press, London.

O'Connell, R. J., & Budiansky, B. (1977). Viscoelastic properties of fluid-saturated cracked solids. *Journal of Geophysical Research*, *82*(36), 5719-5735.

O'Connell, R. J., & Budiansky, B. (1978). Measures of dissipation in viscoelastic media. *Geophysical Research Letters*, *5*(1), 5-8.

O'Donnell, M., Jaynes, E. T., & Miller, J. G. (1981). Kramers–Kronig relationship between ultrasonic attenuation and phase velocity. *The Journal of the Acoustical Society of America*, *69*(3), 696-701.

Pace, A., Bourillot, R., Bouton, A., Vennin, E., Galaup, S., Bundeleva, I., Patrier P. & Visscher, P. T. (2016). Microbial and diagenetic steps leading to the mineralisation of Great Salt Lake microbialites. *Scientific Reports*, *6*(1), 1-12.

Palmer, I. D., & Traviolia, M. L. (1980). Attenuation by squirt flow in undersaturated gas sands. *Geophysics*, *45*(12), 1780-1792.

Paffenholz, J., & Burkhardt, H. (1989). Absorption and modulus measurements in the seismic frequency and strain range on partially saturated sedimentary rocks. *Journal of Geophysical Research: Solid Earth*, *94*(B7), 9493-9507.

Paillet, F. L., Hess, A. E., Cheng, C. H., & Hardin, E. (1987). Characterization of fracture permeability with high-resolution vertical flow measurements during borehole pumping. *Groundwater*, *25*(1), 28-40.

Parra, J. O. (2000). Poroelastic model to relate seismic wave attenuation and dispersion to permeability anisotropy. *Geophysics*, *65*(1), 202-210.

Panza, E., Agosta, F., Rustichelli, A., Vinciguerra, S. C., Ougier-Simonin, A., Dobbs, M., & Prosser, G. (2019). Meso-to-microscale fracture porosity in tight limestones, results of an integrated field and laboratory study. *Marine and Petroleum Geology*, *103*, 581-595.

Pimienta, L., Fortin, J., & Guéguen, Y. (2014). Investigation of elastic weakening in limestone and sandstone samples from moisture adsorption. *Geophysical Journal International*, *199*(1), 335-347.

Pimienta, L., Fortin, J., & Guéguen, Y. (2015a). Bulk modulus dispersion and attenuation in sandstones: Bulk modulus dispersion and attenuation. *Geophysics*, *80*(2), D111-D127.

Pimienta, L., Fortin, J., & Guéguen, Y. (2015b). Experimental study of Young's modulus dispersion and attenuation in fully saturated sandstones. *Geophysics*, *80*(5), L57-L72.

Pimienta, L., Fortin, J., & Guéguen, Y. (2016a). Effect of fluids and frequencies on Poisson's ratio of sandstone samples. *Geophysics*, *81*(2), D183-D195.

Pimienta, L., Borgomano, J. V. M., Fortin, J., & Guéguen, Y. (2016b). Modelling the drained/undrained transition: Effect of the measuring method and the boundary conditions. *Geophysical Prospecting*, *64*(4-Advances in Rock Physics), 1098-1111.

Pimienta, L., Fortin, J., Borgomano, J. V., & Guéguen, Y. (2016c). Dispersions and attenuations in a fully saturated sandstone: Experimental evidence for fluid flows at different scales. *The Leading Edge*, *35*(6), 495-501.

Pimienta, L., Borgomano, J. V., Fortin, J., & Guéguen, Y. (2017). Elastic dispersion and attenuation in fully saturated sandstones: Role of mineral content, porosity, and pressures. *Journal of Geophysical Research: Solid Earth*, *122*(12), 9950-9965.

Pride, S. R., Berryman, J. G., & Harris, J. M. (2004). Seismic attenuation due to wave-induced flow. *Journal of Geophysical Research: Solid Earth*, *109*(B1).

Quintal, B., Steeb, H., Frehner, M., & Schmalholz, S. M. (2011). Quasi-static finite element modeling of seismic attenuation and dispersion due to wave-induced fluid flow in poroelastic media. *Journal of Geophysical Research: Solid Earth*, *116*(B1).

Quintal, B., Steeb, H., Frehner, M., Schmalholz, S. M., & Saenger, E. H. (2012). Pore fluid effects on S-wave attenuation caused by wave-induced fluid flow. *Geophysics*, *77*(3), L13-L23.

Quintal, B. (2012). Frequency-dependent attenuation as a potential indicator of oil saturation. *Journal of Applied Geophysics*, *82*, 119-128.

Quintal, B., Jänicke, R., Rubino, J. G., Steeb, H., & Holliger, K. (2014). Sensitivity of S-wave attenuation to the connectivity of fractures in fluid-saturated rocks. *Geophysics*, *79*(5), WB15-WB24.

Rice, J. R., & Cleary, M. P. (1976). Some basic stress diffusion solutions for fluid-saturated elastic porous media with compressible constituents. *Reviews of Geophysics*, *14*(2), 227-241.

Riding, R. (2000). Microbial carbonates: the geological record of calcified bacterial–algal mats and biofilms. *Sedimentology*, *47*, 179-214.

Robertson, E. C. (1955). Experimental study of the strength of rocks. *Geological Society of America Bulletin*, *66*(10), 1275-1314.

Rubino, J. G., Ravazzoli, C. L., & Santos, J. E. (2009). Equivalent viscoelastic solids for heterogeneous fluid-saturated porous rocks. *Geophysics*, *74*(1), N1-N13.

Rubino, J. G., & Holliger, K. (2013). Research note: Seismic attenuation due to wave-induced fluid flow at microscopic and mesoscopic scales. *Geophysical Prospecting*, *61*(4), 882-889.

Rubino, J. G., Müller, T. M., Guarracino, L., Milani, M., & Holliger, K. (2014). Seismoacoustic signatures of fracture connectivity. *Journal of Geophysical Research: Solid Earth*, *119*(3), 2252-2271.

Sarout, J., Nadri, D., Delle Piane, C., Esteban, L., Dewhurst, D., & Clennell, M. B. (2012, December). Multi-physics and multi-scale characterization of shale anisotropy. In *AGU Fall Meeting Abstracts* (Vol. 2012, pp. MR23D-06).

Sarout, J. (2012). Impact of pore space topology on permeability, cut-off frequencies and validity of wave propagation theories. *Geophysical Journal International*, *189*(1), 481-492

Shapiro, S. A. (2003). Elastic piezosensitivity of porous and fractured rocks. *Geophysics*, *68*(2), 482-486.

Spencer Jr, J. W. (1981). Stress relaxations at low frequencies in fluid-saturated rocks: Attenuation and modulus dispersion. *Journal of Geophysical Research: Solid Earth*, *86*(B3), 1803-1812.

Spencer Jr, J. W., & Shine, J. (2016). Seismic wave attenuation and modulus dispersion in sandstones. *Geophysics*, *81*(3), D211-D231.

Subramaniyan, S., Quintal, B., Madonna, C., & Saenger, E. H. (2015). Laboratory-based seismic attenuation in Fontainebleau sandstone: Evidence of squirt flow. *Journal of Geophysical Research: Solid Earth*, *120*(11), 7526-7535.

Sun, C., Tang, G., Zhao, J., Zhao, L., & Wang, S. (2018). An enhanced broad-frequency-band apparatus for dynamic measurement of elastic moduli and Poisson's ratio of rock samples. *Review*

of Scientific Instruments, *89*(6), 064503.

Sun, C., Tang, G., Zhao, J., Zhao, L., Long, T., Li, M., & Wang, S. (2019). Three-dimensional numerical modelling of the drained/undrained transition for frequency-dependent elastic moduli and attenuation. *Geophysical Journal International*, *219*(1), 27-38.

Sun, Yongyang, and Boris Gurevich. "Modeling the effect of pressure on the moduli dispersion in fluid-saturated rocks." *Journal of Geophysical Research: Solid Earth* 125.8 (2020): e2019JB019297.

Szewczyk, D., Bauer, A., & Holt, R. M. (2016). A new laboratory apparatus for the measurement of seismic dispersion under deviatoric stress conditions. *Geophysical Prospecting*, *64*(4-Advances in Rock Physics), 789-798.

Takei, Y., Fujisawa, K., & McCarthy, C. (2011). Experimental study of attenuation and dispersion over a broad frequency range: 1. The apparatus. *Journal of Geophysical Research: Solid Earth*, *116*(B9).

Thomsen, L. (1995). Elastic anisotropy due to aligned cracks in porous rock1. *Geophysical Prospecting*, *43*(6), 805-829.

Tisato, N., & Madonna, C. (2012). Attenuation at low seismic frequencies in partially saturated rocks: Measurements and description of a new apparatus. *Journal of Applied Geophysics*, *86*, 44-53.

Tisato, N., & Quintal, B. (2013). Measurements of seismic attenuation and transient fluid pressure in partially saturated Berea sandstone: evidence of fluid flow on the mesoscopic scale. *Geophysical Journal International*, *195*(1), 342-351.

Tisato, N., Quintal, B., Chapman, S., Podladchikov, Y., & Burg, J. P. (2015). Bubbles attenuate elastic waves at seismic frequencies: First experimental evidence. *Geophysical Research Letters*, *42*(10), 3880-3887.

Ulven, O. I., Storheim, H., Austrheim, H., & Malthe-Sørenssen, A. (2014). Fracture initiation during volume increasing reactions in rocks and applications for CO2 sequestration. *Earth and Planetary Science Letters*, *389*, 132-142.

Vinci, C., Renner, J., & Steeb, H. (2014). On attenuation of seismic waves associated with flow in fractures. *Geophysical Research Letters*, *41*(21), 7515-7523.

Vo-Thanh, D. (1990). Effects of fluid viscosity on shear-wave attenuation in saturated sandstones. *Geophysics*, *55*(6), 712-722.

Walsh, J. B. (1965), The effect of cracks on the compressibility of rocks, Journal of Geophysical Research, 70(2), 381–389.

Walsh, J. B. (1981, October). Effect of pore pressure and confining pressure on fracture permeability. In *International Journal of Rock Mechanics and Mining Sciences & Geomechanics Abstracts* (Vol. 18, No. 5, pp. 429-435). Pergamon.

Wang, H., & Feng, Z. (2013). Ultrastable and highly sensitive eddy current displacement sensor using self-temperature compensation. *Sensors and Actuators A: Physical*, *203*, 362-368.

Winkler, K., & Nur, A. (1979). Pore fluids and seismic attenuation in rocks. *Geophysical Research Letters*, *6*(1), 1-4.

Winkler, K. W., & Murphy III, W. F. (1995). Acoustic velocity and attenuation in porous rocks. *Rock physics and phase relations. A Handbook of physical constants*, 20-34.

White, J. E. (1975). Computed seismic speeds and attenuation in rocks with partial gas saturation. *GEOPHYSICS*, *40*(2), 224–232.

Yin, W., & Peyton, A. J. (2007). Thickness measurement of non-magnetic plates using multi-frequency eddy current sensors. *Ndt & E International*, *40*(1), 43-48.

Yin, H., Borgomano, J. V., Wang, S., Tiennot, M., Fortin, J., & Guéguen, Y. (2019). Fluid substitution and shear weakening in clay-bearing sandstone at seismic frequencies. *Journal of Geophysical Research: Solid Earth*, *124*(2), 1254-1272.

Yin, W., & Peyton, A. J. (2007). Thickness measurement of non-magnetic plates using multi-frequency eddy current sensors. *Ndt & E International*, *40*(1), 43-48.

Zainal Abidin, I. M. (2011). *Modelling and experimental investigation of eddy current distribution for angular defect characterisation* (Doctoral dissertation, Newcastle University).

Zhang, Y., Nishizawa, O., Kiyama, T., & Xue, Z. (2015). Saturation-path dependency of P-wave velocity and attenuation in sandstone saturated with CO2 and brine revealed by simultaneous measurements of waveforms and X-ray computed tomography images. *Geophysics*, *80*(4), D403-D415.

Zhao, L., Tang, G., Sun, C., Zhao, J., & Wang, S. (2021). Dual attenuation peaks revealing mesoscopic and microscopic fluid flow in partially oil-saturated Fontainebleau sandstones. *Geophysical Journal International*, *224*(3), 1670-1683.

Zimmerman, R. W. (2000). Coupling in poroelasticity and thermoelasticity. *International Journal of Rock Mechanics and Mining Sciences*, *37*(1-2), 79-87.

RÉSUMÉ

Quelle est la principale différence entre l'étude d'un échantillon de roche en laboratoire, à l'échelle centimétrique, et l'étude d'un affleurement rocheux sur le terrain, à l'échelle kilométrique ? Un affleurement rocheux peut inclure des hétérogénéités qui ne seront pas présentes dans un échantillon de roche, comme des fractures, des paramètres hétérogènes variables ou même des couches rocheuses complètement différentes, pour ne mentionner que quelques exemples. Dans quelle mesure les propriétés déterminées à l'échelle centimétrique peuvent-elles être utilisées pour trouver des propriétés à l'échelle du terrain ? Pour aider à répondre à cette question, plusieurs tests de laboratoire sont développés et réalisés pour mieux caractériser les fractures et les hétérogénéités

MOTS CLÉS

Physique et mécanique des roches, vitesse élastiques, carbonates, hétérogénéité

ABSTRACT

What is the main difference between studying a rock sample in the lab, at the centimeter scale, and studying a rock outcrop in the field, at the kilometer scale? A rock outcrop can include heterogeneities that will not be present in a rock sample, such as fractures, varying heterogeneous parameters or even completely different rock layers, to name a few. How than can properties determined at the centimeter scale be used to find properties at the field scale? To help answer this question, multiple laboratory tests are developed and performed to better characterize fractures and mesoscopic heterogeneities, which will allow data extrapolated from the laboratory to be applied to field scale parameters.

KEYWORDS

Rock physics, wave velocity, carbonates, heterogeneity